2018

FACIES ARCHITECTURE AND CONTROLS ON RESERVOIR BEHAVIOR IN THE TURONIAN WALL CREEK MEMBER OF THE FRONTIER FORMATION, POWDER RIVER BASIN, WYOMING

Nathan M. La Fontaine
University of Montana, Missoula

FACIES ARCHITECTURE AND CONTROLS ON RESERVOIR BEHAVIOR IN THE TURONIAN WALL CREEK MEMBER OF THE FRONTIER FORMATION, POWDER RIVER BASIN, WYOMING

By

NATHAN MICHAEL LA FONTAINE

Bachelor of Science, Cal Poly, San Luis Obispo, CA, 2015

Thesis

presented in partial fulfillment of the requirements
for the degree of

Master of Science
in Geosciences

The University of Montana
Missoula, MT

May 2018

Approved by:

Scott Whittenburg, Dean of The Graduate School
Graduate School

Marc S. Hendrix, Committee Chair
Department of Geosciences

Michael H. Hofmann, Committee Co-Chair
Department of Geosciences

Payton Gardner
Department of Geosciences

John Bardsley
Department of Mathematical Sciences

La Fontaine, Nathan, M.S., Spring 2018 Geosciences

Facies Architecture and Controls on Reservoir Behavior in the Turonian Wall Creek Member of the Frontier Formation, Powder River Basin, Wyoming

Chairperson: Marc S. Hendrix

Co-Chairperson: Michael H. Hofmann

Inter-well heterogeneities influencing fluid migration in deltaic reservoirs are controlled by lateral lithofacies changes and vertical complexities such as low permeability thin-beds. Subsurface tools often cannot predict the spatial and stratigraphic organization of these architectural elements, nor their influence on effective reservoir properties and connectivity. This study integrates sedimentological, stratigraphic, and fluid simulation data to 1) document the facies architecture and depositional evolution of the Turonian Wall Creek Member (WCM) of the Frontier Formation, and 2) quantify the role of multi-scale stratigraphic heterogeneity on reservoir behavior. Upscaled permeability properties derived from fluid simulation of nested, small-scale facies models condition the observed architecture within a 500m x 715m geocellular model.

Key surfaces recognized across the study area separate the WCM into three depositional sequences, each of which contain multiple parasequences that form the geomodel framework. Sequence 1 consists of a top-truncated package of river-dominated delta lobes, interpreted as highstand deposits (HST1); sequence 2 is made of wave-dominated delta sandstones deposited during subsequent highstand (HST2); sequence 3 consists of heterolithic tidal bar deposits of a tidally-influenced delta (LST). Detailed mapping of the HST1/HST2 show the spatial distribution of intra-parasequence lithofacies is largely controlled by their proximity to high energy conditions above wave-base and near distributary channels.

Modelling results show that permeability of the fine-grained component within heterolithic deposits is the most critical parameter in reservoir behavior. In wave-dominated environments, relatively simple bed geometries of thin-beds induce low vertical permeability. Conversely, more architecturally complex tidal deposits maintain better vertical connectivity but limited horizontal permeability. Flow compartmentalization on any scale happens only when thin-beds are assumed to be impermeable barriers; mud drapes with lower clay content act only as flow baffles. Fine-scale heterogeneities carry through as controlling factors in geomodel (500m x715m) reservoir simulations. In the wave-dominated setting, continuous horizons of low vertical permeability facies delineate parasequence-scale flow units. Within individual parasequences, the lithofacies distribution plays an important role on effective permeability pathways and total volume in place. Results from this outcrop-to-geomodel study can be applied to WCM reservoirs in the subsurface and used as guidance to build more accurate geomodels in other basins.

Acknowledgements

Foremost, I would like to express my sincere gratitude to my advisor Michael Hofmann for his expertise, encouragement, and guidance over the course of this project. Along with the opportunity to take part in such a rewarding educational experience, I'm grateful for the myriad of opportunities to attend and present at conferences, field trips, and other professional events as a part of this research. Thank you also to my co-advisor Marc Hendrix, who I could always count on for great discussions and encouragement, and of course for his excellent classes. Thank you also to my two other committee members, Payton Gardner and John Bardsley, for their valuable thoughts, guidance, and time throughout this thesis.

Thanks to Tuan Le and Todd Hoffman of the Montana Tech Petroleum Engineering group. Their contributions and insight into reservoir modelling have been invaluable these last two years, and they were a pleasure to work with.

Thank you to the faculty and fellow graduate students at the University of Montana. Special thanks to my lab partners Clayton Schultz and John Zupanic for introducing me to Missoula and our research group. John, thanks for kicking off the Frontier Formation study and for acquainting me with the outcrops. Thank you also to my field assistant Mike Arthur for fearlessly subjecting himself to a rattlesnake infested study location with me.

Special thanks to Isabellah von Trapp for her unfailing support and encouragement, and for the abundance of great memories throughout our time in Missoula. Thank you also to my family for their support of my academic and professional goals.

Lastly, thank you to SM Energy for generously supporting my research and education at the University of Montana.

Table of Contents

I. Introduction

Ancient deltaic systems form a vital component of the world's hydrocarbon reservoirs, yet their stratigraphic architectures and associated controls on fluid migration pathways are notoriously difficult to predict (Tyler and Finley 1991; Slatt 2006; Gani and Bhattacharya, 2007). This is largely due to the heterolithic nature of these deposits, which develop under the multitude of dynamic, countering forces at the continental and marine interface (Bhattacharya 2006; Shepherd 2009). In recent years, a growing number of outcrop analog studies have focused on better understanding and quantifying the stratigraphic architecture and process variability within deltaic and shallow marine deposits (e.g. Hampson, 2000; Gani and Bhattacharya, 2007; Lee et al., 2007; Olariu et al., 2010; Deveugle et al., 2011; Olariu et al., 2012; Ahmed et al., 2014; Feldman et al., 2014). Particularly with the recent rise in digital outcrop model (DOM) datasets, such reservoir-scale studies provide important three-dimensional information on facies distributions, depositional geometries, and typical geobody (i.e. channels, barforms, sheets, etc.) dimensions that can be drawn on in analogous subsurface reservoir definition (e.g. Pringle et al., 2004; Enge et al., 2007; Atlas et al. 2009; Rarity et al. 2014; Rittersbacher et al., 2014). Taken a step further, flow simulation of outcrop-conditioned geocellular models highlights important architectural controls on reservoir behavior by capturing facies-based volume estimates and permeability pathways that are not often incorporated into simple layer-cake grids (Willis and White, 2000; White et al., 2004; Atlas et al., 2009; Sech et al., 2009; Deveugle et al., 2014; Graham et al., 2015).

Though essential in understanding larger-scale reservoir characteristics, such architectural studies may not fully capture the substantial role of fine scale heterogeneities on fluid flow. Below the scale of inter-well spacing, often as low as 40 acres in onshore

conventional reservoirs and ~50m (150ft) in unconventional reservoirs (e.g. QEP Investor Report 2011; Lalehrokh and Bouma 2014; Corrizo Annual Report 2016; EOG Annual Report 2016), heterogeneities exist as thin, fine-grained interbeds, commonly referred to in the geomodeling community as "stochastic shales" due to their short length and common treatment as randomly distributed elements (e.g. Begg and King, 1985; Haldorsen and Chang, 1986; Burton and Wood 2013). The presence of these low-permeability beds fundamentally determines how a reservoir drains by influencing reservoir connectivity, making their representation in upscaled reservoir models essential (Tyler and Finley 1991; Willis and White 2000; Larue and Friedmann, 2001; Grammer et al., 2004; Wood 2004; Ringrose et al., 2005; Sech et al. 2009; Deveugle et al., 2011; Burton and Wood, 2013; Alpak and Barton 2014; Massart et al. 2016).

Quantitative analog studies help resolve the character of these multi-scale heterogeneities, but they rarely measure and directly contrast their respective influences on reservoir behavior. Moreover, the efforts doing so have historically focused on non-deltaic settings (e.g. Jones et al. 1995; Keogh et al. 2014; Norhdal et al. 2014). In an effort to fill this void, this research adopts a multi-scale, outcrop-based modelling approach to quantify the impact of pore-, bed-, facies- and sequence stratigraphic heterogeneities in a mixed-influence deltaic reservoir. The Turonian Wall Creek Member (WCM) of the Frontier Formation is well suited for determining these controls in a 3D framework, as superb, 3D exposures are present on the western limb of the Powder River Basin (PRB) in Wyoming. In addition, the PRB has been a prolific hydrocarbon producer since the late 1800s (WSGS 2014), and interest in the WCM has been renewed with modern advances in drilling technology (Fluckiger et al. 2015), providing the means of immediately testing the findings of this study on a subsurface problem.

Results from this study 1) quantify temporal and spatial variation in facies architecture and associated reservoir connectivity within a well-defined stratigraphic framework, 2) quantify and highlight the relative impact on fluid flow exerted by multiple scales of stratigraphic hierarchy, and 3) demonstrate a flow-based upscaling workflow that represents fine-scale (~cm) heterogeneities in a coarse-grid reservoir model. Outcomes of these efforts are integrated and represented in a high resolution, 500m x 715m geocellular model built in Petrel, marking the applied culmination of this thesis.

II. Geologic Setting

The study area is located in the Tisdale Anticline at Wall Creek Road (WCR) along the western margin of the Powder River Basin (PRB), south of Kaycee, Wyoming (Figure 1). The PRB is an asymmetric tectonic basin, extending from central Wyoming to southern Montana. Major tectonic subsidence started as part of the Laramide deformation during the Late Cretaceous (Campanian) and ceased in the Paleogene (Eocene) (Dickinson 1978; Decelles 2004). Contemporaneous uplifting occurred around the PRB, encompassing the modern day Miles City Arch to the north, the Laramie Mountains to the south, the Black Hills to the east, and the Bighorn Mountains and Tisdale Anticline to the west (Figure 1).

The Cenomanian-Turonian Frontier Formation was deposited as an east-southeastward prograding clastic wedge on the Cretaceous Western Interior Seaway's (KWIS) western margin (McGookey et al. 1972; Bhattacharya and Willis 2001; Figure 1). In the western PRB, the Frontier Formation overlies on the Mowry Shale, with its basal contact designated by the Clay Spur Bentonite dated at 97.17 ± 0.69 Ma (Obradovich 1993). It is overlain by the Cody Shale, which is separated by a significant, regionally correlative marine flooding surface (Willis et al. 1999). The Frontier Formation locally consists of three unconformity bounded members: the lower Belle Fourche, the middle Emigrant Gap, and the upper Wall Creek Member (Merewether 1979; Bhattacharya and Willis 2001), which is the focus of this study.

A wide assortment of depositional interpretations given to the Wall Creek Member underscores its complexity and laterally heterogeneous character in outcrop and well logs. Early workers interpreted offshore bars (e.g. Tillman and Almon, 1979; Tillman and Merewether, 1994), offshore sand ridges (Winn, 1983), and offshore shelf delta plumes (Winn, 1991), but recent work placing these deposits into a sequence-stratigraphic framework conclude their origin

as deltaic sediments deposited at maximum shoreline regression during lowstand (e.g. Bhattacharya and Willis 2001; Sadeque 2006; Zupanic 2017). Sediments were deposited in a low-accommodation, gently sloping basin floor, far from the rapidly subsiding foredeep to the west (Pang and Nummendal, 1995; Hamlin, 1996; Decelles and Giles, 1996; Bhattacharya and Willis. 2001). This depositional setting was prone to top-truncation by marine ravinement during subsequent transgression, explaining the lack of terrestrial facies and isolated nature of these deposits (Bhattacharya and Willis 2001).

Laterally, the WCM exhibits dramatic changes in morphological character throughout the western PRB. In the Raptor Ridge and western Tisdale Anticline region, seven distinct, shoaling upward parasequences separated by marine flooding surfaces have been identified in outcrop and subsurface correlations (Bhattacharya et al., 2003; Sadeque 2006). These basinward thinning, lensoid-shaped parasequences are not ubiquitously present in all areas due to autocyclic delta switching processes (Howell et al. 2003; Sadeque 2006; Sadeque et al., 2009) (Figure 2). Superimposed upon this depositional heterogeneity, regional variation in parasequence architecture and isopach trends are commonly attributed to basinal changes brought about by embryonic Laramide expression (e.g. Howell et al. 2003; Sadeque 2006). The outcrops discussed in this thesis lie in the northern reaches of WCM deposition, where amalgamated sand bodies and decreased isopach thicknesses evidently define a region of reduced accommodation space (Sadeque et al. 2009). The outcrops appear to largely belong to Parasequence (PS) 4 originally reported in *Sadeque, 2006* (Figure 2); however, multiple, potentially unmapped or uncorrelated parasequences are internally evident, as demonstrated in this study.

III. Methods and Materials

Integration of sedimentological, stratigraphic, and fluid simulation data governed the construction of a static geocellular model of the WCM. The geomodel is purposed to capture geologic heterogeneities at the inter-well, bed- (~1-50m) and intra-parasequence scales (20m-1km), within a framework composed of more regional parasequence- (>1km), and sequence stratigraphic intervals (>1km). The latter two scales are only partially represented, as they extend far from the localized study location. Additionally, fluid simulations of the geomodel and internally nested facies models quantify the respective influences on effective reservoir permeability and sweep efficiency exerted by each level of heterogeneity. This chapter details the various facets of the data collection and model building methodology, and is summarized in the workflow of Figure 3.

Stratigraphic description and interpretation

Fieldwork was conducted at outcrops around the Wall Creek Road in the Tisdale Anticline, south of Kaycee, Wyoming (Figures 1, 4). An approximately 1 km^2 study area was chosen in which the WCM is cut by a series of intersecting canyons, offering excellent exposure in both the depositional dip and strike orientations. Nine stratigraphic sections were measured at ~150m intervals providing cm-scale constraint of facies distribution (Figure 4; Appendix A). Data captured at each stratigraphic section included bed thickness and lateral continuity, grain size, bioturbation (ichnofauna and abundance), paleoflow indicators, and sedimentary structures. These field measurements formed the base to organize the stratigraphy of the WCM into lithofacies (Figure 5)**.** All stratigraphic measurements were recorded using a Jacob's Staff and/or a 15 cm ruler. Grain size was observed and recorded in the field using a hand lens and a common grain size card. Paleocurrent was typically measured parallel to cross-beds or the short-axis of

ripples using a standard Brunton Compass. Bilinparl directional indicators such as petrified logs or groove casts were also measured when present. High resolution photographs shot using a Canon DSLR camera recorded lithofacies at each measured section for reference and were later used to constrain detailed facies maps. Additionally, this study integrated four measured sections of *Zupanic, 2017* from within or in close proximity to the study area. Measured section logs assisted in both elucidating a sequence stratigraphic framework and its internal facies distribution.

Petrographic description

Observing variation in grain size and grain sorting was key in interpreting the location of a tidal bar parasequence boundary incorporated in the final geomodel. Thus, 13 hand samples were collected in the field across interpreted tidal bar stacking surfaces (approximately 10-15 cm increments), and selected samples were sent to a commercial vendor for production of thin sections. Basic, qualitative petrographic description of the thin sections augmented preliminary field observations by ensuring subtle but significant grain size transitions (e.g. upper fine sand to lower medium sand) indicative of a tidal bar parasequence boundary were accurately recorded.

Digital Outcrop Model Construction and Interpretation

Photogrammetric, or Structure from Motion (SFM), methods were used to construct a complete digital outcrop model of the $1km^2$ study area. This procedure, performed using Agisoft PhotoScan, generates a 3D point cloud by calculating an object's (i.e., outcrop's) geometry as a function of angular variation between photographs taken from different perspectives. To provide the input for the DOM construction, a combined ~6,000 photos representing all outcrop faces in the study area were methodologically taken at various horizontal and vertical angles, with at least 60% overlap between consecutive photos, following a commonly cited data density requirement

(e.g. Baltsavias 1999). To minimize the computational workload and maximize processing speeds, pre-processing of all photos was required, and consisted of applying a mask to all portions of photos that would not be a part of the model (e.g. foreground vegetation, sky, etc.; (Appendix D). The models were then constructed in a series of steps, each of which only considered photographic data without a mask applied: identifying and matching points (pixels) between photos, building a point cloud with each point representing XYZ information, connecting points into a triangulated irregular network (TIN), and draping a photographic texture over the network (Figure 6). Even with pre-processing, initial photogrammetric model file sizes exceeded the computational limitations of the lab computers. Consequently, 28 sub-models of outcrop faces (with smaller file sizes) were built and later merged into 6 continuous models. Each sub-model typically represented an outcrop face of 100-150m, and often took more than 24 hours to fully process. The 6 merged models represented outcrops ranging from ~250-900m long; the combined outcrop lengths included in the final set of models is about 3.5 km.

Photogrammetrically produced 3D point clouds do not have internal geo-referencing or scaling capabilities like those of LiDAR. Therefore, it was necessary to provide both scale and a coordinate system to the digital outcrop models using geographic data gathered in the field. To collect this data, a field assistant and I conducted a survey using a laser range-finding Leica TS06 total station and a standard surveying prism reflector. First, an initial, starting position of the Leica total station was determined using a handheld GPS, providing an initial basepoint for the survey. The total station was then oriented by rotating its viewpoint to north, as measured by a declination-adjusted Brunton compass, and manually setting its azimuth to 0°0’0”. Using a series of built-in leveling tools, the total station was then adjusted to horizontal. After the initial set-up, a collection of 52 ground control points (GCPs), represented by 15x5 cm strips of bright

blue tape, were placed on all outcrops within the study area. The surveying prism was then placed at each visible GCP, and the XYZ location of these points were measured and calculated relative to the known position of the total station. The total station was strategically relocated multiple times during the survey so that all GCP positions could be captured in as few steps as possible, minimizing any associated error. To ensure the total station positioning maintained its validity after any relocation, the set-up process was repeated and the azimuth and distance of known points (i.e. GCPs or previous total station positions) were calculated, so the new position could be triangulated. Ground control points on outcrop were easily identifiable in the outcrop models' photographic drapes; point data at these locations were manually assigned known UTM coordinates gathered during the total station survey (Appendix B). While some error in the surveying and georeferencing process is present (e.g. spatial variation between surveying prism and outcrop face GCP, variation between image pixel selected as GCP and the exact portion of the 15 cm blue strips measured in the field, GPS resolution, error between surveying station location points, etc.), this process provided sub-meter geospatial constraint to the final DOM, and was deemed satisfactory for the modelling procedure.

Upon their initial production, the 6 digital outcrop models were imported into Virtual Reality Geological Studio (VRGS), a data visualization and interpretation package mainly used to collect quantitative stratigraphic or structural data using point cloud or TIN data sets, often in the form of LiDAR (Light Detection and Ranging) or SFM-produced digital outcrop models. Each of the six outcrop models were placed in one single coordinate system, and could consequently be viewed and interpreted together in VRGS. All quantitative data collection for the geocellular modelling took place here, and consisted of traced polylines with UTM coordinate information. Data collection was focused to providing stratigraphic horizon inputs for

Petrel model frameworks as well as a statistical database for geobody dimensions (e.g. bed or mud drape lengths and widths). Within this statistical database, geobody measurements were divided into depositional strike- and dip- categories, based on the orientation of outcrops from which measurements came from and their relation with mean paleo-transport data taken during fieldwork. As each outcrop was not perfectly in line with the mean depositional strike and dip data, measurements gathered this way likely have a considerable element of uncertainty. However, the large number of measurements added to the statistical database increases confidence in results, and effectively highlighted architectural anisotropies statistically evident. Such information was drawn on largely to educate stochastic modelling parameters (discussed in the geocellular modelling methods section). All interpretations used as modelling inputs were exported and transferred to the geomodelling software Petrel as ASCII data.

Facies Architecture Quantification

Detailed facies maps of the well exposed, lower stratigraphic intervals (basal ~15m) were made using photopanoramas of all outcrop faces included in the final geocellular models. These maps relied on measured section facies constraint (e.g. grain size, sorting, sedimentary structures, bioturbation level, etc.) and visual interpretation of bed geometry (e.g. tabular, erosive) and sedimentary structures (e.g. cross-bedding, planar lamination, hummocky cross-stratification) within photographs. Three visually identifiable map facies (MF1, MF2, and MF3) were included in these maps and each facies grouping was assigned a unique color (Figure 5). All facies maps were then uploaded into an open-source, quantitative image analysis platform (Figure 7; bcgsc.ca). This software produces comprehensive pixel color (RGB) statistics for any given image and outputs accurate proportions of representative color clusters. For each facies map, the relative proportions of MF1 (yellow), MF2 (green), and MF3 (red) were measured.

Undesired color outputs resulting from background noise in images or transitional pixel colors at the edges of primary facies were omitted, and proportions were normalized for the three primary facies. I isolated facies map segments corresponding to the lowermost 6 reservoir zone divisions within the geomodel and repeated this process for each outcrop map; facies proportions gathered in this way highlighted both vertical and lateral trends in facies architecture. Such trends were mapped and used as a primary data source for stochastic property distribution parameters, which is discussed further in the results chapter.

Geocellular modelling

All geocellular modelling was performed in Schlumberger Petrel, a comprehensive software platform used in the energy industry for 3D data visualization, interpretation, mapping and reservoir modelling. Construction of a geocellular model effectively capturing the Wall Creek reservoir architecture involved three primary steps, each requiring iterative integration between Petrel and VRGS data inputs. This process consisted of 1) building the field scale (500m x 715m x 15m) sequence-stratigraphic model, separated into zones representing genetic depositional packages (parasequence- scale) and facies- based flow units 2) capturing the impact pore- and bed-scale heterogeneities impart on fluid migration through fluid simulation of five cm- resolution facies models, and 3) populating the sequence-stratigraphic model with upscaled properties (K_X,K_Y,K_V) spatially distributed according to facies architectural trends gathered in the facies mapping phase. Fluid simulation of the final model was performed by collaborators in the petroleum engineering group at Montana Tech, marking the culmination of the project.

Geomodel framework construction

In order to maximize confidence of modelling results, the location and perimeter of the complete geomodel were chosen where the greatest 3D outcrop data constraint exists. Surfaces

interpreted to be of significance in controlling reservoir behavior were interpolated in Petrel from VRGS data points, and separate the model into distinct building blocks or zones. Interpreted parasequences were logically chosen to comprise these building blocks, owing to their nature as relatively conformable successions of genetically related beds bounded by marine flooding surfaces (Van Wagoner, et al. 1988). Such divisions may be mappable in the subsurface, and thus could delineate analogous reservoir model zonation. Additionally, laterally extensive (km+) intra-parasequence facies transitions further divide the geocellular model, as such transitions often mark distinct changes in physical properties and can delineate hydraulic flow units (Slatt 2006).

All geomodel framework surfaces were created in two primary steps. First, each surface was interpolated using all available data points, using the "convergent interpolation" method. Out of the available options in Petrel, this method produced the most realistic and smooth surface while still honoring all of the imported data points. However, surface extrapolation trends in the far reaches away from these data points (i.e. model horizon corners and edges) tended to exhibit dramatic bends that were geologically unrealistic. To address this, a second, planar surface averaged to all data points for its respective horizon was constructed. The first surface was then applied a trend associated with the planar surface, while still maintaining the original convergent interpolation and hard data constraint. This process effectively "straightened out" the corners and/or edges of surfaces with undesired extrapolations.

Due to structural deformation between outcrops in the study location, two outcrop faces (outcrops "C" and "F") and all of their associated data points exhibited slightly varying plunge and dip trends than the remainder of the data. As a result, surfaces, maps, and reservoir zones interpolated using these points exhibited unwanted bends and kinks that had a visible impact on

surrounding zone isopachs, and could not be corrected by simply flattening the model onto a surface. To best represent true stratigraphic geometries, some manual data-processing was required to artificially reconstruct outcrop structural trends and remove such artifacts. This correction process consisted of 1) isolating Petrel data points belonging to problematic outcrops, for each independent surface of the final geomodel 2) creating an average, planar surface constrained to these points, 3) determining the angular difference between this surface and a planar surface conditioned to all other data points of the same dataset, 4) applying a rotation of this angle to the problematic data points around their collective barycenter, using the point-editing software MeshLab, and 5) splicing the uncorrected data with the rotated points in Petrel (Appendix D). This process was repeated for each surface that included data points from the two problematic outcrops. Point sets from the westernmost outcrop "C" required a rotation of 7.46° toward the east, while points from the middle outcrop "F" required a rotation of 1.6° toward the east and 1.04° toward the south.

As individual horizon data sets were rotated independently, their respective rotation points had slight variation, causing some local thinning or thickening in zone isopachs that may have had a minimal effect on reservoir model results. In future work, this process could be improved by extracting a bulk point cloud data set containing points from all surface horizons, at each problematic outcrop, and rotating this point cloud as a single unit. The updated point cloud would then need to be partitioned and spliced back into the respective datasets. Such a process would ensure a single point of rotation for all horizon data sets in question. Nevertheless, apart from a few, relatively small anomalies in the final horizons, the described workflow sufficiently subtracted unwanted artifacts from the geomodel and provided the means to more independently test stratigraphic controls on fluid migration.

Facies Modelling:

The final, coarse geomodel was built so that its total cell count was 78,890, with individual cell dimensions ranging from 10x10x1m to 10x10x3m. This grid arrangement was chosen so that the Petrel Reservoir Engineering fluid simulator at Montana Tech could run smoothly given their local computational constraints, while still capturing intra-parasequence scale facies architecture. At a higher resolution, bed-scale heterogeneities existed in all facies of the study area as thin, inter-well scale, fine-grained drapes. To capture these complexities and their effective impact on directional permeability in the coarse model grid cells, 5 high resolution facies models were built for fluid simulation and results were used in subsequent flow-based upscaling. These models (Figure 5; models A-E) capture and test outcrop constrained fine-grained thin bed networks within 1) thin, interbedded sands and silt beds (F1), and 2) thin, interbedded sand and silt deposits (F1) stacking up into parallel laminated storm deposits (F2), and 3) stacked heterolithic tidal facies (F4 and F5). Of the five facies observed in the field, F3 is the single lithofacies that was not discretely modelled. Final geomodel cell population of F3 (GM4) adopted the results from facies modelling of F5, a very similar litho-facies. The facies models range from 15-25 meters in length and width, 1-3 meters in height, and have cell dimensions of 30-75cm in length and width, and thicknesses of ～1-3 cm (Appendix D).

Each model was built using the same methodology and constrained to similar data sets (Figure 8). The corners of well-exposed outcrops provided 3D constraint of bedding geometries and were used to gather data for each facies model. At each site, a framework of discontinuous mud drapes was interpreted within the DOM and imported into Petrel. Ellipsoid surfaces were then extrapolated to approximate the average dimensions of fine-grained drapes as measured in the field. Statistical dimensions drawn in on this step are organized by facies and separated into

strike and dip orientations to capture anisotropies related to bed geometries (Appendix H). Combined with these dimensional parameters and outcrop control, surfaces maintained geologic realism by honoring geometric trends associated with the underlying bedding. Surfaces representing erosive, scouring bedding planes were applied a parabolic trend, whereas tabular beds were applied a planar trend. Geological rules were then applied so that younger surfaces truncate older surfaces, creating an interconnected network of fine-grained thin-beds. The level of connectivity within these networks varied between the different facies architectures modelled.

After its initial construction, a transmissibility multiplier (TM), a mathematical representation of permeability reduction, was applied to all grid cells cut by the shale surface network. The thin, vertical cell dimensions of each model represented each mud drape as a 1-3 cm thick surface, and intra-drape thickness variation was not accounted for. An associated TM value between 0-1 imparts a linear reduction in permeability to the cells it crosses; a value of 1 has no impact on fluid flow and is essentially "invisible" to the model, TM=0 represents 100% reduction, or "no-flow" through the cell, and a TM of 0.5 represents a 50% reduction of permeability. Collaborative fluid simulation studies of facies models intersected by the TM networks resulted in directional effective permeability values used as inputs for the upscaled model cells. Models were simulated at 6500 or 7500 psi to represent analogous subsurface pressures. During this modelling procedure, injection and production wells were placed on opposing sides of the grids, and permeability was measured in all K_X, K_Y, and K_V orientations using Darcy's Law. Sensitivity testing varying TM values between 0-1 within the same facies model provided a proxy to understand the role of pore-scale controls on flow.

With thin, cm-scale cell thicknesses, the facies modelling process used herein effectively captured the complex geometry of shale interbeds as well as the surrounding sand connectivity.

Representative effective volumes (REV's) of individual facies were not empirically defined in the modelling procedure; however, each model was built to a scale that could sufficiently capture the typical dimensions of the respective heterogeneities tested.

Property Population

Within the field-scale geomodel, each zone was stochastically populated with geomodel facies (GM) properties (Figure 5) according to four primary inputs. These constraints included 1) upscaled property inputs (K_X, K_Y, K_V) derived from the flow-based upscaling of high resolution (cm-scale) facies models, 2) deterministically defined geometric facies trends based on the depositional model interpreted from facies relationships and sequence stratigraphic observations (i.e. facies distributed relative a sediment point source according to underlying delta lobe isopach morphologies), 3) "upscaled well log" data, in the form of deterministically assigned geomodel facies placement directly representing outcrop observations, and 4) vertical and lateral facies proportion trends statistically derived from outcrop facies panels produced at all outcrop locations. The “upscaled well log” data provided hard constraint for the model, by ensuring the facies arrangement directly observable in outcrop was incorporated into stochastic property distributions. The term is used in Petrel for any form of discretely defined facies data, and does not necessarily require true well or pseudo-well data inputs. Instead, this data was created by importing an XYZ point set representing polylines intersecting a non-background facies (traced within VRGS), and assigning the point set respective facies codes in Petrel (Figure 9). Any cells cut by the point set were then assigned the non-background facies while a constant background facies could be maintained.

Object-based and texture-based property modelling methods (i.e. multi-point statistics), often used to capture architecture such as fluvial or deltaic distributary channel systems, were

deemed unnecessary for the geomodel, as the geometry of WCM architectural elements (i.e. HST1 delta lobe, HST2 shoreface parasequence, LST tidal bars) was discretely captured as reservoir model zones. Additionally, internal 'geobodies' such as the local presence of GM3 or GM4 facies within a dominant GM1 background, typically had isotropic dimensions or existed at a spatial resolution approximately the size of a single grid cell. As a result, such bodies did not require representation as an 'object', as such a unit would merely take the form of a single cell.

Therefore, pixel-based stochastic modelling methods, which use indicator variograms to assign properties on a cell-by-cell basis (Ringrose and Bentley, 2016), were applied to distribute discrete facies throughout the individual zones. Depending on the modelling needs of the individual zone, Sequential Indicator Simulation (SIS) and/or Truncated Gaussian with Trends algorithms were applied. SIS is the most common pixel-based modelling method, and traditionally gives good model results in subsurface reservoir models with many closely-spaced wells or well-to-well correlations (Ringrose and Bentley, 2016). It is also good for handling complex well-conditioning cases, and avoids the 'funneling' effect that can unrealistically concentrate geobodies into inter-well regions of object-based models (Ringrose and Bentley, 2016). The density of data gathered from this outcrop study exceeds that of even the most tightly spaced wells, and the facies "upscaled log" data is likely more complex than that produced by horizontal wells, making the SIS algorithm a suitable method selection. Its main drawback, a general assumption of no lateral or vertical trends of element distribution, was addressed by superimposing spatial facies probability trends (gathered through the facies mapping phase) to the stochastic algorithm.

In contrast to other, more architecturally simple zones, Zone 1-HST1 consists of increased facies heterogeneity related to the local position within a small fluvial delta lobe.

Consequently, spatial trends derived from facies maps alone could not adequately distribute properties in a manner consistent with the depositional model. For this zone, the Truncated Gaussian with Trends algorithm was employed to map distinct facies "belts", organized and separated based on delta lobe isopach contours (Appendix D). Each facies "belt" was then individually populated with facies properties using the SIS algorithm. Statistics for each facies belt were derived from outcrop facies diagrams with positions located within the respective contoured belts. By using this method, facies distribution followed a trend contouring around a deltaic point source, and placed greater proportions of more proximal facies toward the axial position on the delta lobe.

In all cases, variogram values for facies distribution were estimated based on the average lateral continuity of facies measured in facies maps, as well as the lateral correlation of overall trends across outcrops in the study area (Appendix I). Such values were found by measuring the lateral extent of all non-background facies deposits in the DOM and calculating their average. Isotropic lateral variogram ranges of 10-20m were applied in all cases. All stochastically derived outputs were quality checked to ensure an accurate representation of the observed field data.

Geomodel Simulation

Upon initial production of the detailed outcrop geomodel, a second, identical geomodel was produced and disassociated with the 1) facies distribution identified in outcrop, and 2) effective K_X, K_Y, and K_V reservoir properties gained through facies simulation. This proxy model was built to represent a 'layer cake' reservoir representation that might be extrapolated from subsurface data, and only included parasequence- scale architecture. Comparison of fluid simulation results between these models elucidated the importance of outcrop-constrained, intra-parasequence scale facies distribution and bed-scale architectures on reservoir behavior. Next,

each of the original two models were copied and then flattened on a prominent flooding surface extending across the entirety of the field area. This organization minimized structural effects produced by the dip of the Tisdale Anticline outcrops on fluid flow, further highlighting stratigraphic- as well as structural controls on fluid flow.

Identical fluid simulation scenarios of each of the four models tested various well configuration and completion strategies (Figure 10). First, a series of four simulations placed four, 500 foot lateral wells in North-South and West-East trending orientations along two stratigraphic horizons. Each well was positioned so that its mid-point lie directly at the map-view center of the geomodel. The upper wells were positioned in the topmost zone (Zone 8) of the geomodel, while the lower wells were placed at the top of a parasequence near the stratigraphic center of the model. Each of these scenarios simulated flow with and without fractures, using both TM=0 and TM=0.5 upscaled data inputs. Fracture parameters used included seven fracture stages, at a 250 foot fracture spacing, 200 foot fracture length, and 50 foot fracture heights. Second, three vertical wells were placed in the direct center and SW and NE corners of the geomodels. These corners were chosen as they were located at the topographically highest and lowest points in the structurally dipping model. Each vertical well simulation tested cases of TM=0 and TM=0.5 upscaled data inputs, with a) completion in all zones and b) only the uppermost zone perforated. Comparison between all modelling outcomes were used to describe the importance of stratigraphic architecture on flow. A total of 84 simulations were performed on the models; the nomenclature used to identify the simulations is included with simulation results in Appendix G. Readers are referred to the collaborative thesis *Le 2017* for a more detailed description of engineering parameters within the fluid simulation procedures.

IV. Results

A. Facies Analysis

Facies

Sedimentary facies are distinguished by lithology, bed thickness and geometry, grain size, sedimentary structures, and ichnofauna (diversity and abundance) (Figure 5). Interpretations of associated depositional processes and environments are included for each facies in the subsequent Facies Association section.

Facies 1: Thin interbedded sandstone and siltstone/mudstone.

Facies 1.1. Laterally continuous (100s m) thinly interbedded sandstone and siltstone/mudstone

Facies 1.1 is present locally at the base of the WCM, where beds' clinoformal geometries toe out into the underlying muddy sediments. This facies consists of tan to reddish, fine-grained sandstone beds with tabular geometries and sharp bases. Internal structure commonly consists of massive, plane-parallel lamination and rare ripple-lamination. Interbedded deposits of (<1cm) siltstone or mudstone commonly separate thick (2-30cm) sandstone beds. Upward grading of massive to parallel-laminated sandstone, or parallel-laminated to ripple-laminated sandstones are interpreted to compose Ta-Tb and Tb-Tc Bouma sequences (Bouma, 1962). In outcrop, F1.1 has a distinctively greater degree of carbonaceous woody material found interspersed within sandstone beds. The bioturbation index is generally very low, ranging from 0-2, and more commonly 0-1. Ichnofacies of sandstone deposits include *Skolithos* and *Ophiomorpha*, and interbedded fine-grained deposits contain *Planolites, Thallasinoides, and Palaeophycus*. Chert pebbles floating in matrix are sometimes present. Beds are commonly 100s of meters long and generally stacks upward into F2.2, F2.3, and/or F3.

Facies 1.2. Discontinuous (10s m) thinly interbedded sandstone and siltstone/mudstone

This facies, the most common in the study location, consists of thin, discontinuous fine-grained sand beds interbedded with siltstone and mudstone drapes. In comparison with F1.1, F1.2 is less well sorted and has a higher clay content. Beds are massive or parallel laminated with sharp, sometimes erosional basal contacts. The tops of individual sandstone beds are often capped by wave ripples. Observed ichnofauna include *Skolithos, Ophiomorpha, Arenicolites, Planolites, Thallasinoides, Terebellina, Palaeophycus,* and *Rosselia*. The Bioturbation Index is higher in this sub-facies than in F1.1, as low as 1 but more commonly 2-3. Multiple petrified logs are present in these deposits, typically in horizons interfingering with F2. Facies 1.2 generally stacks upward or is laterally interbedded with F2 and F3. Sandstone bed continuity ranges from 1s to 10s of meters, while sandstone thicknesses are typically 2-5 cm. Siltstone and mudstone interbeds are typically <1cm thick.

Facies 2: Parallel laminated sandstone

Facies 2.1. Swaley cross-stratified sandstone (SCS)

Facies 2.1 consists of tan to reddish, very fine to fine-grained, well sorted sandstones with beds ranging from ~5-25+ cm thick. SCS beds commonly exhibit multiple orders of truncating low-angle planar lamina sets, with laminae gradually flattening higher in the bed. Beds have sharp basal contacts that are often highly erosive and scour into underlying sediments. Common basal lags of pebbles, bivalve imprints, ammonites, and rip-up clasts are present. Highly concentrated carbonaceous plant material is sometimes present in lag but otherwise this facies has little woody debris. B.I. is typically 0-2, with *Skolithos, Ophiomorpha,* and

Arenicolites being the dominant traces in SCS deposits. This facies is typically well cemented in the study area and often laterally transitions into Facies 1.2 and F2.3, and occasionally F2.2.

Facies 2.2: Hummocky cross-bedded sandstone (HCS)

Facies 2.2 consists of tan to red, very fine to fine-grained sandstone exhibiting antiformal, low-angle planar lamination. HCS beds typically exhibit sharp basal contacts and relatively thin bed thicknesses (~5-15 cm). Bioturbation ranges from 1-3, and dominant traces are *Skolithos, Ophiomorpha* and *Arenicolites*. This facies is rarely encountered in the study area, but is typically associated with F1, F2.1 or F2.3.

Facies 2.3. Low-angle planar laminated sandstone

Facies 2.3 consists of tan to red, very fine to fine-grained, well-sorted sandstone with horizontal to low-angle planar lamination. Beds are often sharp at the base and rippled at their tops, and do not locally exhibit the diagnostic swale or hummock of Facies 2.1 and 2.2. This facies is often preferentially cemented and associated with SCS in the study area. Observed ichnofauna include *Skolithos, Ophiomorpha,* and *Arenicolites*. Bioturbation ranges from 0-2.

Facies 3: Planar and trough cross-bedded sandstone

This facies consists of fine to lower medium-grained, planar and trough-cross bedded sandstone with rare mud-draped foresets and rare mud rip-up clasts. Beds range from 5-30 cm thick and have erosive basal contacts. Bioturbation is typically 0-1 and consists of *Skolithos* in sandstones and rare *Planolites* in associated thin mud beds. It is vertically interbedded with F1.2 and rarely F1.1, and very commonly transitions laterally to F2.

Facies 4: Heterolithic, wavy and flaser bedding

F4 consists of wavy to lenticular bedded, alternating thin (cm-scale) sandstone and mudstone/silty mudstone deposits, with rare, thick mud beds up to ~10cm thick. Convoluted bedding is rarely present, and mud rip-up clasts are sometimes observed in thin, interbedded sandstones. F4 exhibits little bioturbation (BI=0-2) and, where present, consists of only *Planolites* and *Palaeophycus*. It is most commonly found at the base of coarsening upward successions, underlying thick accumulations of F5.

Facies 5: Heterolithic trough and planar cross-bedded sandstone

This facies consists of upper fine to lower medium-grained, cross-bedded sandstone with very common mud-draped foresets and bed boundaries. Deposits consist of aggradational, lenticular beds typically 10-30 cm thick, with erosive, undulating basal boundaries. Beds are organized in a shingled stacking pattern, and their lateral extents are typically 10-30 m. Sedimentary structures include ripples, convoluted bedding, rip-up clasts and reactivation surfaces. Bioturbation is 0-1 with only rare observations of *Skolithos.* F5 is commonly interbedded with facies 4, and composes the majority of the upper ~2/3 of the WCM in the study area.

Facies Associations

FA1: Fluvial-Dominated Lower Delta Front Facies Association: F1.1 and F2

Description

FA1 primarily consists of F1.1 deposits, which gradationally stack upward into- or interfinger with F2. It is characterized by progradational stacking patterns exhibiting clinoformal

geometries dipping to the south-southwest. Facies are organized into two distinct, lobate architectural elements with aggregate paleoflow data trending to the south. The lobate, discontinuous architectures hosting FA1 are the most heterogeneous of any observed sedimentary package.

Interpretation

FA1 is interpreted to represent deposition in a fluvial-dominated, wave-influenced distal deltaic environment. The presence of gravity flow deposits with preserved partial Bouma sequences were generated by either the collapse of sediment accumulations near the edge of the delta top, or by direct charging of gravity flows (hyperpycnal flows) by river plumes. The latter interpretation is preferred as such dense, coarse sediment-laden undercurrents likely entrained the abundant plant materials that may have otherwise escaped into suspension. The associated, overall low BI in this FA corroborates a river-fed source, in which high sedimentation rates and/or a stressed water column led to the impoverished ichnofauna community (MacEachern et al., 2005; Sadeque et al. 2009; Buatois and Mángano, 2011; Ashworth et al. 2015). Additionally, the presence of *Skolithos* and *Cruziana* ichnofacies mirrors the episodic and alternating low and high energy conditions along a fluvial influenced delta front. The laterally continuous, clinoformal beds of FA1, and their collective position within a mapped, lobate sediment package, further indicate progradation of a fluvial delta with little wave- or tide- reworking. When present, the minor association of storm-generated F2 facies indicates deposition below fair weather wave base and above storm wave base. The outermost, distal deposits of FA1 solely consist of F1 and thus indicate a position on the lower delta front below or very near storm-wave base.

FA2: Wave-Dominated Lower Delta Front Facies Association: F1.2 and F2

Description

FA2 primarily consists of F1.2 deposits interfingered with sparse F2.2 or F2.3 beds. F1.2 beds are laterally continuous over a scale of 1s-10s of meters. F1.2 beds are massive to planar bedded, with decreased sorting quality relative to the F1.1 deposits. F2.2 deposits (HCS) are most common in this FA. FA2 shows a dominant southerly paleoflow trend, and has the greatest bioturbation levels of any facies association, corresponding to both the *Skolithos* and *Cruziana* ichnofacies.

Interpretation

Sedimentary characteristics of FA2 clearly indicate deposition by dominantly wave-processes with little fluvial influence. Increased bioturbation (BI: 1-3) is attributed to more normal marine salinity and low sedimentation rates compared to FA1. The abundant, massive beds may have formed by suspension settle-out or represent partial Bouma (Ta) sequences (Bouma, 1962). Planar laminated F1.1 sandstone beds indicate deposition by traction processes, and may represent thin tempestites or hyperpycnal flow deposits. Such high-energy processes are supported by the observed *Skolithos* ichnofacies within sandstone beds. The common wave ripples and discontinuous, pinch-and-swell bed architecture within FA2 is attributed to wave-reworking of the deposits, while the rare occurrence of HCS suggests infrequent or low-magnitude storm surge deposition in an otherwise lower energy setting near wave-base. Interbedded mud and silt drapes are burrowed by the *Cruziana* ichnofacies and record the low-energy settle out of suspended load during quiescent periods. The observed stacking patterns demonstrate significant storm influence in a storm-wave dominated delta front, hereafter referred

to as a shoreface setting, but do not necessarily represent a storm-dominated succession, which can be solely composed of amalgamated HCS with little to no bioturbation (Buatois and Mángano, 2011).

FA3: Wave-Dominated, Middle Delta Front Facies Association: F2 and F3

Description

The wave-dominated middle delta front facies association (FA3) is highly prevalent in the lower ~1/3 of the WCM, and comprised of mainly planar laminated sandstone (F2) and planar cross-bedded to trough cross-bedded sandstone (F3). Included within F2 are its three sub-facies divisions: swaley cross-stratified sandstone (F2.1), hummocky cross-stratified sandstone (F2.2), and low-angle planar laminated sandstone (F2.3). Each sub-facies is typically found at the tops of bedsets composed of FA2. Where present, F3 is always interbedded with F2. Similar to FA1 and FA2, paleoflow data has a dominant southerly component.

Interpretation:

Each sub-facies of F2 and F3 are interpreted to represent storm-generated deposition in the middle delta front to shoreface setting (Figure 11). Facies 2.1 (SCS) and 2.2 (HCS) observations strongly resemble diagnostic traits of the idealized sequence of hummocky cross stratification proposed in *Dott, 1982*, including antiformal hummocks and erosive synformal swales, multiple orders of truncating laminae, rich plant detritus concentrations, and basal horizons of pebbles, shells, and rip-up clasts. Erosive basal bed boundaries, the absence or generally low clay content, and a dominant *Skolithos* ichnofacies suggests rapid, high-energy deposition. These beds likely formed in the WCM when strong storm waves and unidirectional currents stripped fine sand from the beach or upper shoreface and transported it to its deeper

setting (Grant and Madsen, 1979; Vincent et al., 1982; Swift and Figueiredo, 1983; Snedden et al., 1988; Dumas 2006). Upon transport to the deeper setting, sands infilled localized scours produced by storm-wave orbitals on the delta front. Scours were incrementally filled, as demonstrated by the upwardly decreasing dip of SCS laminae. Coarse basal material in SCS deposits represents the remaining lag after storm winnowing and before the subsequent infill, while mud chips likely indicate erosion of the underlying beds during rapid sand deposition.

HCS deposits are present in FA3 but more often associated with FA1 and FA2. As HCS is preserved best in deep settings with sedimentation rates sufficiently high enough to preserve bathymetrically expressive hummocks (Dumas 2006), its decreased proportion within FA3 indicates a more shallow-water environment relative to FA1 and FA2. Facies 2.3 (low-angle planar sandstone) present within FA3 strongly resembles Facies 2.1/2.2, with its well-sorted, planar lamination and association with F1. It is likely that these deposits also represent HCS/SCS deposition but no swales or hummocks were immediately visible at the measured sections. As hummock or swale wavelengths can be very long (averaging ~19m, measured up to 75m in the study area) it is possible that their identification in the field was missed or not possible due to outcrop cover.

When associated with F1.2, F3 is interpreted to represent asymmetric, migrating bedforms that deposited further landward on the shoreface as the product of greater unidirectional currents. The consistently southward paleo-transport direction exhibited by these deposits is shared with that of both F1 and F2. This uniformity suggests that these bedforms do not represent upper shoreface deposits, which would likely exhibit net shoreward transport (Swift et al., 1991; Dumas and Arnott. 2006), but rather were positioned in a more proximal part of the middle shoreface or wave dominated delta front. In all cases, the dominance of the

Skolithos ichnofacies, coupled with a lack of significant *Cruziana* traces, demonstrates an overall higher energy environment in FA3 than that observed in FA1 or FA2, consistent with a storm-dominated, middle shoreface setting (MacEachern and Pemberton, 1992; Pemberton *et al.*, 2001; Buatois and Mángano 2011). Higher in the overall succession, an increased proportion of F3 makes up FA3 intervals, demonstrating an overall progradational stacking pattern of shoreface sediments.

FA4: Upper Delta Front facies association: F1.1, F2, and F3

Description:

The upper delta front facies association is marked by the presence of medium-grained F3 deposits stacking on top of or laterally changing to fine-grained F1.1 and F2. This association is rare and occurs only at the outcrop "B-WCR10" and "H-East" sections. Bioturbation levels are distinctively low (BI=0-1) for this FA. Paleoflow is dominantly southward with significant westward and eastward components as well.

Interpretation

FA4 is composed of successions of trough cross-bedded sandstone with mud chips deposited on foresets, overlying or laterally transitioning into both F1.1 beds with partial Bouma sequences (Ta-Tb), and F2 deposits of marine (wave) influence. All observed deposits have increased levels of woody material, reflecting their riverine sources. The generally southward-directed paleoflow reflects a sediment source to the north or northeast, consistent with the overall coarsening of facies (F3) in this direction. The subordinate paleoflow components ranging from west to east are the result of changing lateral bedform migration in a distal terminal distributary channel (TDC) environment. No distinct, downcutting channel margin was definitively

identified, and the interpretation of a channel at WCR-10 is based largely on the mixed-influence facies association as well as its diagnostic position within the overall lobe. In general, the character of FA4 strongly resembles other TDCs, which are defined by similar facies associations, minimal topographic expression, and subtle incision into previous deposits (Olariu and Bhattacharya 2006).

The sub-kilometer proximity of the northern lobe (and its presumed TDC) to the southern lobe TDC deposits (~500m) agrees well with modern river-dominated delta TDC spacing (Olariu and Bhattacharya, 2006). The relatively small dimensions of the two mapped lobes likely reflects a setting of short recurrence intervals between lobe shifting events, owing to a locally low-accommodation setting. The TDC's and their respective lobes likely coalesce to form a more regional scale delta that encompasses the entire distributary system.

FA5: Tidal Bar facies association F4 and F5

Description:

FA5 consists of two primary facies: heterolithic, wavy and flaser bedding (F4), and heterolithic trough and planar cross-bedded sandstone (F5). These facies are arranged in gradationally coarsening upward successions, with the mud-rich, heterolithic F4 passing upward into F5. Within each cycle, the sand content, sorting, and grain size of F5 generally increases upward. The tops of individual successions are commonly capped by an abrupt transition back into F4. Bioturbation ranges from 0-1, and consists of an impoverished community of rare *Skolithos* in sandstones and *Planolites* and *Palaeophycus* in the fine-grained deposits. Paleotransport direction is dominantly to the southeast, in contrast to the other FAs which have a more southerly trend.

Interpretation

Progradational stacking patterns, stressed ichnofauna, and an abundance of tidal indicators within the heterolithic F4 and F5 indicate deposition as migrating tidal dunes. Sands were likely transported as bedload during flood and ebb stages to form migrating, cross-bedded dunes, while the finer cohesive sediments were transported as suspended load and deposited during calmer, slack tide conditions (Wang 2012). The prevailing southerly paleoflow of FA5 is generally consistent with all other facies associations, and likely indicates ebb- dominated transport (Figure 11) directly from the riverine sediment source. Fine-grained drapes delineate bed boundaries, and represent the toesets of forward-migrating dunes. Reactivation surfaces within cross-bed foresets capture laminae-scale unconformities that formed as the result of shifting orientations or magnitudes of unidirectional current. The distinctly impoverished trace fossil assemblage supports a tidal environment with brackish, salinity stressed waters (Buatois and Mángano, 2011).

Cyclical, upward-coarsening facies successions within FA5 strongly resembles facies models for progradational tidal bars or compound dunes deposited in front of a tidally influenced delta (Dalyrmple and Rhodes, 1995; Willis and Gabel 2003; Burton 2013; Feldman 2014; Eide et al. 2016). The concentration of F4 at the base of cycles likely represents deposition in the sand-starved bar toesets or troughs between tidal bars. Here, current velocities and/or wave energy are lower than at bar crests, and only occasional bedload transport of sand interrupts the suspension fallout of mud (Dalyrmple and Rhodes, 1995; Burton 2013; Eide et al. 2016). The coarser grained bar-tops, in contrast, likely had a greater degree of fine sediment winnowed away due to the strong tidal and/or wave energy.

No intertidal deposits are recognized in FA5, likely either due to an overall sedimentary position in a more distal location on the delta front, or to erosional destruction of once-present bar tops. A lack of major channel-like features within this facies, coupled with what appears to be a convex upward morphology displayed by the best constrained tidal bar (Figure 12) suggest the tidal bars have minimal basal erosion, and were locally deposited in a distal setting of little to no valley confinement (Burton 2013). The latter is in turn supported by a marine assemblage of ichnofauna described in regionally correlative deposits (*Zupanic, 2017).* The transition from FA2 to FA5 appears both sharp and gradational across the field area. At the scale of study, it is unclear if the observed truncation of underlying deposits is the product of regional erosion or more localized, erosive scour during bedform migration. In general, the local signature of the WCM tidal bars share a strong resemblance with those described in other Frontier deposits (Sadeque et al. 2009; Feldman et al. 2014) and the more well documented Sego Sandstone (e.g. Willis and Gabel, 2001; Willis and Gabel, 2003; Wood 2004; Birkhead 2005; Burton 2013; Legler et al., 2014).

B. Sequence Stratigraphic Framework

Sequence stratigraphy divides stratigraphic intervals into genetically related depositional sequences (Catuneanu, 2006), thereby delivering the predictive capacity necessary to constrain sedimentary geometries and regional facies trends within reservoir models. This section details the local sequence stratigraphic model by first describing the six key sequence stratigraphic surfaces (A-F) and their relation to the observed facies stacking patterns. The surfaces are then related to the WCM systems tracts and sequences.

Surfaces

Surface A – Parasequence Boundary

Surface A is present near the base of the WCM and marks the top surface of a parasequence interpreted as delta lobe deposits (Figure 13). Ubiquitously present at the top of this succession is a fine-grained, heavily bioturbated *Glossifungites* horizon that dips into the basal shale at an angle of ~2° (Figure 13). This is interpreted to mark a flooding event in which active sedimentation ceased due to a delta lobe abandonment. The parasequence below surface A is composed of a progradationally stacked FA1 and FA4, while the surface is onlapped by beds of FA1 and FA3, with the former only present at the WCR-9 and WCR-13 locality. The onlapping beds are interpreted to be part of a second delta lobe (parasequence) that was deposited laterally offset and immediately to the north of the first parasequence. I interpret surface A to be a sub-regional parasequence boundary that separates two stacked delta lobes of a fluvial dominated delta.

Surface B - Transgressive Surface of Erosion-Maximum Flooding Surface (TSE-MFS)

Surface B is a sharp contact truncating the underlying beds of the fluvial dominated delta lobes (FA1, FA4) from overlying wave dominated delta and shoreface deposits (FA2 and FA3). A good example of surface B is observed at the WCR-6 section, where dipping clinoforms of the northern delta lobe are truncated by the sharp surface B. To the south, at the southeastern delta lobe, surface B becomes conformable with surface A. The sharp and horizontal contact of surface B is interpreted as a transgressive surface of marine erosion that occurred during a minor transgressive episode in the study area. As the underlying F1.1 and overlying F1.2 deposits represent a setting in either the middle to lower delta front or shoreface, a significant shift in

shoreline position compared to the underlying fluvial dominated delta deposits did not occur across the surface. However, the distinct switch in sediment transport processes from fluvial dominated to wave dominated, and the presence of this surface throughout the study area, suggests that surface B is a more regionally observable and significant surface.

Surface C: Parasequence Boundary

Surface C is present throughout the study area and separates middle shoreface (wave dominated delta) deposits from overlying, lower shoreface (wave dominated delta) deposits. Although this facies change only represents minor shifts in shoreline position, the reservoir properties of these two facies associations are distinctly different and therefore the surface is recognized as a sub-regional parasequence boundary. The recognition of this boundary might bare more weight for the geomodel part of this study then the distinction of depositional environments or the regional correlation of surfaces.

Surface D: Parasequence Boundary

Surface D is recognized across the entire study area as a sharp contact separating some of the most proximal middle shoreface deposits (FA3) from overlying lower deposits (FA2). This contact marks one of the most significant shifts in shoreline position within the wave dominated lower part of the WCM, and is interpreted as a significant regional flooding surface, and the top of a parasequence. This flooding surface is one of the flattest surfaces in the study area and is used as a datum for most cross sections in this study (Figure 16).

Surface E: Sequence Boundary

This surface, regionally correlated in *Zupanic, 2017*, is locally preserved as an erosional contact separating underlying FA2 and overlying FA5 deposits (Figure 16). When mapped,

surface E appears to show an undulatory nature across the field site, and locally extend within a decimeter of the HST2-PS2 surface at outcrop "C" and "G". The surface is the most regionally significant within the WCM, as it marks a regional shift in external influence from a wave dominated environment to a tidally influenced environment.

Surface F: Parasequence Boundary

This surface lies within a thick succession of FA5, and commonly separates underlying F5 deposits from overlying, mud-rich F4 deposits. Both above and below the surface, facies commonly stack upward from F4 to F5. The surface is easily observed across the field area by a distinct weathering pattern, as underlying sandy deposits are better cemented and less eroded than the immediately overlying fine-grained deposits (Figure 17). The juxtaposition of more distal, mud-rich heterolithic F4 sediments directly on top of proximal, sand rich deposits of F5 is interpreted as a flooding surface and the top of a parasequence.

Systems Tracts

Three major systems tracts are locally recognized within the Wall Creek sandstone. These systems tracts are termed HST1, HST2, and LST, and each are the sole element locally preserved as a part of their respective 4th order sequences (*Zupanic, 2017*).

Sequence 1: HST1

The coarsening upward succession of the fluvial dominated delta (FA1, FA4) at the base of the WCM is interpreted as HST1. The exact position of the basal contact of HST1 is unknown due to the gradual transition from the underlying WCM siltstone to the WCM sandstone. The southerly dipping delta front clinoforms toe out into the underlying siltstones, and it is inferred that the downlap surface of these clinoforms is the basal contact of HST1. The upper contact of

HST1 is well defined and is marked by the transgressive surface of marine erosion (surface B) truncating the delta clinoforms, and separating the fluvial dominated deposits of HST1 from the overlying wave dominated deposits of HST2. Within the HST1, two delta lobe parasequences are evident. Surface A separates the southeastern delta lobe from the second delta lobe to the north. Increased vertical and lateral facies heterogeneity, attributable to the shifting depositional position on these two distinct delta lobes, characterizes this systems tract (Figure 18). Increased proportions of F3 and F2 are present at WCR-10, coinciding with the thickest deposits of HST1, interpreted as the most axial position on the southeastern delta lobe. Here, greater unidirectional current energy distributed sediment in terminal distributary channels and/or mouth bar assemblages. The HST1 sediments rapidly pinch out in the westernmost outcrops of the study area, bringing about a local thickness change of 3.5m between WCR-10 and WCR-7. Observed facies relationships coupled with the preservation of mounded deltaic lobes suggest deposition in a fluvial dominated delta setting. This fluvial dominance observed during HST1 is in stark contrast to the subsequent systems tracts that are strongly influenced by wave- and tidal currents.

Sequence 2: HST2

The merged TSE and MFS (Surface B) separates the HST1 from the HST2. The HST2 is bounded at its top by the regional sequence boundary (Surface E). Here a thick storm-wave dominated shoreface succession is preserved, demonstrating a significant shift in basin dynamics from the prominent fluvial influence observed in HST1. Progradational stacking patterns of FA2 transitioning upward into FA3 characterize this interval, preserving a cyclical sedimentary position between lower and middle shoreface environments. In contrast to the laterally continuous delta front deposits of the HST1 that show little evidence of reworking, the prominence of highly erosive, storm-generated deposits (SCS/HCS) and interbedded, pinch-and-

swell facies demonstrates strong storm-wave influence. HST2 is composed of three distinct progradationally stacked parasequences that are separated by minor flooding surfaces (surface C and surface D). HST2-PS1 is largely capped by F2 deposits, whereas HST2-PS2 preserves a far greater proportion of F3 in its upper horizons, illustrating a progradational stacking pattern of parasequences. The onset of a third parasequence is recognized as a transition back into lower delta front sediments (F1.2) directly overlying HST2-PS2, but this package is very thin in the study area, due to incision of the overlying sequence boundary (surface E).

Similar to the underlying deltaic HST1, the HST2 quickly thins toward the west (Figure 19). This thinning is largely accommodated in the HST2-PS1 interval, which decreases in thickness by ~3m between WCR-9 and WCR-7. Additionally, thickening and thinning of this package has a largely inverse relationship with the underlying HST1 isopach, suggesting compensational stacking of depositional centers.

Sequence 3: LST

Surface E, interpreted as a regional sequence boundary due to its significant erosional and undulating profile across the western PRB margin (Zupanic, 2017), marks the base of the LST. The LST is composed of a thick package of tidally influenced delta sediments (FA5) that are generally coarsening, consistent with observations from nearby subsurface gamma ray logs that also show a coarsening upward log pattern (Figure 20). The beds overlying the inferred SB are very heterolithic and contain the coarsest sediments in the study area, as well as the largest bedforms (FA5). The facies characteristics of these deposits, combined with the erosional nature of the basal SB, suggest that a significant relative drop in sea level resulted in a basinward shift of the shoreline. The tidal character of FA5 suggests that the sea level lowering and the

associated narrowing of the KWIS might have amplified tidal currents along an embayed shoreline, a mechanism observed in modern and ancient analogs (e.g. Steel et al., 2012).

Progradationally stacked tidal bars are interpreted to be the main architectural element present in the LST, and are themselves defined by a coarsening upward, heterolithic facies association. Successions of migrating tidal dunes are preserved as stacked sequences of interbedded F4 and F5; variation in N/G within the facies is attributed to proximal-distal position within the regional-scale tidal bars. Increased erosion of outcrops in the western portion of the study location make mapping the complete WCM impossible; however; the lowermost tidal bar of the succession is mapped as far west as the WCR-5 measured section, providing sufficient constraint for extrapolation across the geomodel. This bar, bounded at its top by the LST-PS1 surface, shows a gradual southwestward thickening.

C. Facies Quantification

Using the quantitative image analysis approach outlined in Chapter III, the spatial distribution of lithofacies was characterized for each zone of the geomodel. These zones, shown in Figure 21, directly relate to regional, intra-parasequence facies transitions, and/or interpreted parasequence/sequence boundaries. Isopachs of each zone are included in Figure 22. Given the observational scale difference between measured section and photograph-based facies mapping, the three visually distinctive facies mapped (MF1, MF2, MF3) were not further subdivided into their associated sub-facies in the diagrams. The relative proportions of these three facies were quantified for each zone at each outcrop included in the final geomodel (outcrops C-G; Figure 4). This section presents the statistical results and spatial trends of each zone's mapping results; the driving mechanisms for any associated facies trends are included in the subsequent discussion

chapter. For each zone, outcrop results are listed in a roughly west-east direction; all facies diagrams discussed are included in Appendix C.

Zone 1 – HST1

The basal zone of the geomodel captures the architectural heterogeneity and proximal-distal facies relationships within a fluvial-dominated delta (HST1). Out of the two delta lobes recognized in the study area, the geomodel primarily captures deposits of the southeastern lobe. However, as previously mentioned, the toesets of the northern lobe are included in the western portion of the model boundaries. Zone 1 is bounded at its base by the lower contact of the WCM sandstone, and at its top by 1) the HST1-PS1 surface (surface A) and 2) the TSE-MFS (surface B), where it is interpreted to truncate and merge with the HST-PS1. Onlapping deposits observed directly above the SE delta lobe surface at WCR-9 and WCR-13 are interpreted to belong to the northern lobe, but are included in zone 2 due to a prominent shift in facies proportions, discussed in the *Zone 2* section.

Zone 1 is not present at outcrop "C" and thus does not have any associated facies statistics. The deltaic package begins to appear as a thin bedset at the base of outcrop "D". Here, zone 1 is composed of 100% F1.1 (MF1) gravity flow deposits, which have a southerly paleoflow and are likely sourced from the northern delta lobe. This homogenous facies architecture continues ~150m east to the WCR-5 ridge (outcrop "F"); a transition begins to occur at the WCR-8 section (outcrop "G"), where very thin trough cross-beds appear in the otherwise MF1 dominated zone.

At the WCR-4 section (outcrop "H" - West), facies are again composed of 100% MF1. The exposed interval of this zone is only a few meters wide and does not provide high quality

data, but the presence of a measured section (WCR-4) does provide clear facies constraint. Moving eastward into the SE lobe depocenter, the "H-East" and "B-WCR10" outcrop sections exhibit a significant increase in MF3, with 17.47% and 26.34% respectively.

At the southern end of outcrop "B" (B-South), Zone 1 consists of 62.37% MF1 and 32.49% MF2, while MF3 is reduced to only 5.14% of the total volume. Moving ~100m northward, the WCR-13 section (B-North) preserves the lateral pinching out of zone 1, delineated by the HST1-PS1 delta lobe flooding surface descending toward the underlying prodelta muds. Here, facies proportions are 86.17% MF1, 10.89% MF2, and 2.95% MF3. Clearly, the thicker and more proximal or axial position on the local delta lobe preserves increased facies variety, whereas distal and lateral positions on the lobe are dominated by MF1 deposits.

Zone 2 – HST1

Zone 2 is a present only locally within the geomodel, bounded at its base by the HST1-PS1 (surface A), and at its top by the TSE-MFS (surface B). It is partitioned from the underlying zone 1, as it represents a genetically unique sediment package that onlaps and fills the interlobe spaces of the underlying delta lobe topography. Additionally, internal facies characteristics are dramatically different, with a significant increase in MF2 (Appendix C). This is first observed at outcrop "B"-North, where 49.22% MF1, 49.4% MF2, and 1.38% MF3 are documented. To the south, a thick accumulation of MF2 is present at the outcrop "H-West" section; this is interpreted to belong to the same depositional package and is composed of 100% MF2. This same facies composition continues past outcrop "G", but the zone dies out before reaching outcrop "F", where the HST1-PS1 is directly overlain by the HST2 (Appendix C).

Zone 3 – HST2

Zone 3 is present in all outcrops of the study area, but exhibits significant thickness variation and facies distribution. It is bounded at its base by the TSE-MFS (surface B) and at its top by the HST2-PS1 (surface C) horizon. At the WCR-7 outcrop, zone 3 is dramatically thinner than it is in the east, and it is composed of 44.24% MF2 and 55.30% MF1 (Appendix C). At outcrop "D" MF2 makes up 84.03% of the zone, with the remaining 15.97% consisting of MF1. Moving eastward, MF2 is reduced to 28.43% of the zone at the outcrop "F" and 39.55% at outcrop "G. The nearby "H-West" section is made up of 64.19% MF1 and 35.81% MF2, while "H-East" is made of 78.66% MF1 and 21.34% MF2. Lastly, the "B" outcrops range from 66.72%-73.07% MF1 while the remainder is composed of MF2.

The general increase in F2 proportions in the west can be related to the overall thinning of the zone. F1 typically composes the basal part of the zone in the east, and F2 commonly delineates the top of the parasequence. It appears that the westward thinning of this zone is accommodated in the lower part of the parasequence, as the upper horizon of concentrated F2 is still observed at the western outcrops (Figure 21; Appendix C). As a result, this sedimentary thinning is associated with a reduction of MF1, which effectively increases the relative proportion of MF2 in zone 3.

Zone 4 – HST2

Zone 4 is bounded at its base by the HST2-PS1 (surface C) and at its top by a distinct, intra-parasequence facies transition. This geomodel horizon marks the field-wide, intra-parasequence transition from MF1 to MF3/MF2 (Figure 21; Appendix C). Measured facies proportions are highly consistent within this zone. The western outcrop "C" ridge is composed of

86.88% MF1, 9.96% MF2, and 3.16% MF3, while outcrop "D" measured 83.31% MF1, 7.04% MF3, and 3.16% MF2. The F3 and much of the F2 at these outcrops occur along a horizon about midway up in the zone; this facies horizon is not present elsewhere in the study area. Moving eastward, MF1 makes up 92.64%, 96.54%, 92.56%, and 92.94% at the "F", "G", "H-West", and "H-East" localities, respectively (Appendix C). The "B-WCR-10" section is a slight anomaly, with only 81.79% of the outcrop composed of MF1, but this is likely attributable to its very small exposure that hosts a large F2 scour. Finally, the "B-South" and "B-North" sections are made up of 90.58% MF1 and 93.61 MF1, respectively. At each of these locations, MF2 accounts for the remaining ~3-19% of the outcrops.

Zone 5 – HST2

Zone 5 is an intra-parasequence zone partitioned on the basis of a significant facies transition at its base, and the prominent HST2-PS2 flooding surface (surface D) at its top (Figure 21). The zone is present in all outcrops captured in the geomodel, and consists of low-angle planar bedded sandstone (MF2) and trough cross-bedded sandstone (MF3). Uncertainty is mainly related to misinterpreting the apparent dip of trough cross beds as low angle planar sandstones. As these two facies are the sole components in this interval, only the percentages of MF3 are given; the remainder belongs to MF2. MF3 makes up 31.49%, 58.25%, 97.89%, and 33.57% of the zone at the "C", "D", "F", and "G" sections (Figure 4). The "H-West", "H-East", and "B-WCR-10" sections measure 32.94%, 16.25%, and 44.20% MF3. Moving northward, MF3 accounts for 21.06% of the zone at "B-South" and 21.06% at "B-North".

Zone 6 – HST2

The final zone of the geomodel that incorporated facies maps is bounded by the HST2-PS2 flooding surface (surface D) at its base and the S.B. (surface E) at its top (Figure 21). This zone is homogeneous across the entire study area. At all locations, it is composed of 100% MF1.

Zones 7 and 8 - LST

Zones 7 and 8 consist of interbedded facies 4 and 5 that stack to form a tidal bar in the overlying LST. This interval was not discretely mapped like zones 1-6. While bed-scale facies heterogeneity increases dramatically within these deposits, the distribution of lithofacies within the mapped tidal bar is generally more homogeneous and widespread, in contrast to the more heterogeneous stacking architecture of underlying deposits. Thus, these zones were effectively modelled by integrating facies-scale fluid simulation results into a simpler, layer cake zone approach.

D. Geocellular Modelling

Facies model simulation results

Five high-resolution (cm scale cell thickness), outcrop constrained grids capture flow behavior sensitivity to bed-scale heterogeneities, or "stochastic shales" (Haldorsen and Lake 1984; Begg and King, 1985). Effective permeability results from these models were analyzed and used as direct input for upscaled cells in the field-scale geomodel, discussed further in the following section (Figure 3). Facies model 'A' captures the impact on fluid migration exerted by thin-beds within a sequence of F1, while models 'B' and 'C' capture the commonly observed, upward transition between F1 and F2 (Figure 5). Two stacked, nested grids (models 'D' and 'E') capture heterogeneities within facies 4 and 5 (Figure 5); the two grids share identical bounding surfaces as zones 7 and 8 in the geomodel. The fluid simulation of each of the five listed grids

incorporated sensitivity tests toward 1) variation in sand permeability values, and 2) variation in transmissibility multiplier values, which represent the permeability of interbedded silt and mudstones. In all cases reservoir pressure ΔP was standardized at 6500 or 7500 psi.

Potential variation from subsurface rock properties by telogenetic alteration made outcrop-sourced porosity and permeability measurements less than ideal for this study. Instead, these inputs were gathered from analogous core facies in proprietary PRB subsurface data (Appendix E). The mean or median value of individual lithofacies were typically used as baseline property inputs. Models 'D' and 'E' are exceptions, in which sensitivity testing incorporated representative sandstone porosity and permeability values from a different well, and calculated by the collaborating group at Montana Tech. All model parameters and results described in this section are included in the respective section of Appendix F.

Model 'A'

Model 'A' captures a ~1m interval of F1, the most common lithofacies of the HST1 and HST2 (Appendix F: Tables A-B). The lateral dimension of this grid are 15m x 11.5m, and the vertical cell resolution is ~1cm. Background cells representing sand deposits were given a permeability input of k=0.001 mD and Φ=0.0403. Cells cut by fine-grained drapes compose 7.51% of the grid, and were assigned transmissibility impedance values ranging from 0 to 1, with 0 being representative of a flow barrier (100% flow reduction) and 1 being representative of full flow (0% reduction). The highest observed flow reduction of 97.88% occurred in the vertical direction during case 1, in which fine-grained drapes were assigned TM=0. In this same case, K_X and K_Y were only reduced by 9.75% and 8.73%, respectively. In case 2, fine-grained drape impedance was reduced to 70% (TM=0.3), which may be more realistic of a baffling layer.

Consequently, K_V reduction dropped significantly to 12.97%, while K_X and K_Y were reduced to 5.28% and 3.62%, respectively.

Slight horizontal anisotropy is demonstrated in these simulations, as K_X (depositional strike) permeability is consistently reduced to a greater degree than its K_Y (depositional dip) counterpart in all five cases. Additionally, considerable vertical permeability anisotropy is present in all cases; however, K_V and K_X reduction values do converge at about TM=0.7 (30% permeability reduction in fine-grained drapes). Nevertheless, K_V reduction is consistently greatest of the three orientations, in all simulated cases.

Model 'B'

Model 'B' represents a 1.88m thick interval composed of an F1 bedset (54.9% of grid) overlain by an erosive, scouring bed F2 deposit, which is in turn overlain by an erosive, planar bedded F2 deposit (45.1% of grid). The complete, isotropic dimensions of the F2 scour are captured within the margins of the grid. Three primary simulation scenarios varied F2 property inputs while maintaining constant F1 properties of Φ=0.0329% and k=0.0015 mD (Appendix F: Tables C-H). The F2 property inputs used range from the highest 0.003 mD and k=0.0578% values of scenario 1, to the low-case scenario 3 values of Φ=0.0403% and 0.001 mD. This modelling design was chosen as F2 shows a wide range of porosity and permeability values in the subsurface, possibly due to diagenetic alteration, whereas F1 is notably more consistent. In this light, the three modelling scenarios act to capture fluid behavior sensitivity toward the observed variation in subsurface F2 properties. Within each of the three aforementioned scenarios, five cases tested TM networks assigned to values of 0, 0.3, 0.5, 0.7, and 1. Cells cut by the TM network compose 13.7% of the model 'B' grids.

In scenario 1, F2 cells were assigned property values of Φ=0.0578 % and k=0.003 mD. Results illustrate a significant anisotropy between horizontal and vertical permeability. In the extreme, TM=0 (no-flow) scenario, K_V was completely reduced by 100%. In contrast, K_X and K_Y were both reduced approximately 31-32%. This anisotropy remains consistent up until 0.7 TM, where K_V permeability reduction converges with that of both K_X and K_Y (Appendix F). Notably, in all cases, horizontal permeability appears highly isotropic; variation between K_X and K_Y is <1% in all cases.

Scenario 2 (F2 values: Φ=0.0451% and k=0.002 mD) and scenario 3 (F2 values: Φ=0.0403% and k=0.001) test settings of incrementally decreased reservoir quality of F2. Results from both scenarios exhibit similar overall trends as those of scenario 1. Vertical permeability reduction is consistently greatest in all cases, but converges with K_X and K_Y values at TM=0.7. Again, horizontal permeability remains highly isotropic. Albeit minimal, the greatest contrast in K_X and K_Y is observed in case 1 of scenario 3, where a TM=0 value produces a difference of 2.73% between the two values.

Model 'C'

The third facies model has identical dimensions and vertical cell resolution as model 'B', and is located in a slightly offset position within the same stratigraphic interval. Thus, many of the surface inputs are shared between the two models. However, the large F2 scour that is completely captured within the prior model is only partially represented in model 'C'. As a result, the overall proportion of F1 is increased to 56%, providing another variable with which to examine flow sensitivity. Identical variation in F2 rock properties was tested in the three model 'C' scenarios. Again, for each scenario, a range of TM values between 0 and 1 were simulated. All listed results correspond to respective TM values of 0, 0.3, 0.5, 0.7, and 1.

Similar to model ‘B’ simulation results, flow reduction was greatest in the K_V direction in the TM=0 case of all three model ‘C’ scenarios, where vertical permeability was completely destroyed (Appendix F: Tables I-N). K_V reduction was consistently greatest, but these values did converge to within 1 percentage point of the K_X and K_Y reduction values, in each of the three scenarios. A slight horizontal anisotropy is apparent at no-flow thin-bed conditions (TM=0), as effective permeability reduction is consistently greater in the y-direction than x-direction counterparts. The contrast between the K_X and K_Y increases from about 1% to near 5% between scenario 1 and scenario 3, corresponding to incrementally decreased F2 cell permeability and porosity inputs. However, at all TM values greater than TM=0, which more realistically represent baffling effects, there is little contrast in permeability between the two orientations.

Model ‘D’

Facies model ‘D’ captures bed-scale heterogeneities associated with a 3m package of F4 and F5 (Appendix F: Tables O-R). Heterolithic, tidally influenced cross-bedded and wavy-bedded facies form tidal dunes, which make up the bed-scale architecture of these deposits. The geometrically complex muddy toesets of migrating tidal dunes are the primary bed-scale heterogeneities captured in model ‘D’. The overall grid dimensions are 25x15x3 m with a cell sizes of 50x75x3 cm. This resolution effectively represents the geometry and connectivity associated with the LST heterolithic sediments, which is far more complex than the majority of underlying wave-dominated delta deposits. Cells cut by the TM network make up 15.4% of the total grid volume for model ‘D’.

Three modelling scenarios of this grid architecture varied reservoir pressure, sand permeability, and thin-bed transmissibility values (Appendix F, Tables O-T). The first, base scenario included four cases (Appendix F, Tables O-P), all of which incorporated high quality

end-member reservoir sandstone values of Φ=0.0665 and k=0.1789 mD. Variables tested included TM values of 0 and 1, which were each simulated with a ΔP of 6500 psi and 7500 psi. Change in reservoir pressure had little impact on permeability values; likewise, TM values of 1 (used as a baseline to quality check modelling results) had no impact on results. However, baseline K_V was still substantially lower than its horizontal counterparts, likely due to the preferential fluid migration (and faster rates) parallel to the well arrangements. With TM=0 (no-flow), K_X reduction averaged 15.48%, K_Y reduction averaged 13.66%, and K_V was reduced by 66.05%.

Next, a constant ΔP of 6500 psi was applied, and the TM was varied between 0 and 1 in 0.1 increments, with the aim of quantifying the effect of lithological contrast between the coarse and fine-grained portion of heterolithic sediments. Results demonstrate a highly linear relationship between lithological contrast represented by lower TM values, and effective permeability reduction. This relationship fails at 0.1 TM in the K_X and K_Y results, and around 0.5 TM in the K_V results. At these levels of transmissibility impedance, effective permeability begins to be reduced at an increased rate. These results also show that, with very low lithological contrast (TM≥0.8), permeability reduction is greater in the horizontal direction than the vertical direction. In all other cases, K_V reduction is substantially higher (Appendix F, Tables Q-R).

A final, shorter modelling scenario simulated fluid migration through the same grid using three varying pairs of porosity and permeability values gathered from the subsurface core data used to populate models A-C. These values represent a much ‘tighter’ sandstone, with permeability multiple orders smaller than that of the initial two scenarios. The three cases of tested permeability values between 0.002 and 0.003 mD, and porosity values between 4.29 and

4.74%. A constant TM=1 was applied in each simulation. Results from the three cases are identical; K_X was reduced by 15.48%, K_Y was reduced by 13.66%, and K_V decreased by 66.05%.

Model 'E'

The fifth high-resolution facies model was built directly above model 'D', to capture ~2 meters of coarser grained, better sorted F5 deposits. The upper bounding surface of this grid is interpreted as sub-regional parasequence boundary, as it is directly overlain by muddier heterolithic sediments belonging to a younger tidal bar. Similar to the underlying model, this grid captures the fine-grained drapes of stacked tidal dunes. However, field observations show that bar top facies are coarser, better sorted and have less overall mud content. Fluid simulation of this grid was intended to capture the impact of this intra-parasequence variation on effective flow properties within a tidal bar. Model 'E' simulation scenarios are identical to those of model 'D'. The grid dimensions are 25x15x2m with a 50x75x2 cm cells, and the TM network composes 15.4% of the grid. The thinner cell thicknesses in model 'E' was accommodated by the smaller overall grid size (2m thick vs 3m thick model 'D').

The initial base scenario included four cases, all of which incorporated high end-member reservoir sandstone values of Φ=0.0665 and k=0.1789 mD. Variables tested included TM values of 0 and 1, which were each simulated with a ΔP of 6500 and 7500 psi. Change in reservoir pressure, as well as TM values of 1, had little or no impact on permeability values. With TM=0, K_X reduction averaged 33.16%, K_Y reduction averaged 38.91%, and K_V was reduced by 89.73%.

The subsequent scenario maintained a ΔP of 6500 psi, with 10 cases of TM varied between 0 and 1 in 0.1 increments. The relationship between TM and effective permeability is similar in all cases to those of model 'D'; permeability decreases in a linear fashion at TM values

between 1 and 0.1 for the K_X and K_Y orientations, and between 1 and ~0.6 in the K_V orientation (Appendix F: Tables S-Z). Notably, a significantly greater overall reduction in permeability is measured for each orientation compared to that of the underlying model. Similar to model 'D', K_V reduction is slightly less than K_X or K_Y reduction when TM≥0.9, but rapidly increases at values <0.9.

A final scenario simulated fluid flow using sandstone property inputs taken from PRB core data. Identical properties tested in model 'D' were used, including 1: Φ=4.74%; 0.002 mD, 2: Φ=4.91%, 0.003 mD, and 3: Φ=4.29%, 0.002 mD. TM=0 was again applied for each simulation. Again, results were consistent in all cases: K_X was reduced approximately 33.2%, K_Y was reduced by 38.91%, and K_V was reduced by 89.73%.

Field Geomodel Simulation Results

Four field scale (500m x 715m) geomodels were built, incorporating different orientations (tilted vs. flattened) and datasets (upscaled permeability properties and intra-parasequence facies architecture vs. subsurface proxy representing parasequence architecture and original core permeability values; Figure 10). Fluid simulation of field-scale geologic models and their corresponding subsurface proxy models incorporated a series of seven well configurations (Figure 10). Within each configuration, both TM=0 and TM=0.5 upscaled facies properties and various well completion strategies were employed. Results from the structurally dipping models are presented first, followed by results from the flattened stratigraphic models. Lateral well results are shown in tables 1-3, and all model simulation data is included in Appendix G. All cumulative production values listed are in stock tank barrels (stb) after five simulated years.

Structural Models; Lateral Well Configurations

At TM=0 (unfractured), cumulative production spanned from 4,372 stb to 22,824 stb (Table 1). With fractures applied, production ranged from 5,079 stb to 33,069 stb (Table 2). In both sets of simulations, production was far greater with wells placed in the LST. Additionally, both W-E trending wells outperformed their N-S counterparts. At TM=0.5, these large production discrepancies ceased: production ranges within the unfractured scenario converged to 38,500-44,123 stb, while fractured simulations yielded 41,888-48,824 stb. In contrast to its poor performance at TM=0, the lower W-E trending well recorded the greatest production in the unfractured scenario. Upon fracking, production was greatest for wells placed in the upper horizon, and in wells trending W-E.

Similar production values as those from the 0.5 TM outcrop model simulation were achieved in the proxy model, which output 39,588-43,771 stb in the unfractured case and 41,600-52,183 stb with fractures. In both instances, production was greatest with well placement in the LST. Regardless of the zone, W-E trending wells outperformed their N-S counterparts. Compared with the TM=0.5 outcrop model simulation, production from wells placed in the LST are ~8% higher in the proxy model, while the production from lower wells decrease by 1-7%.

Structural Models; Vertical Well Configurations

In all instances, vertical well configurations dramatically underperformed lateral well arrangements (Appendix G). Total production ranged from 426 to 2,929 stb at TM=0, and 760 to 4,934 stb at TM=0.5. In the proxy model, production ranged from 825 to 4,155 stb. In all cases, the well placed in the thick center of the model, perforating all zones, significantly outperformed all other wells. This was consistently followed by the NE and then SW wells with all zones

perforated. As expected, production decreased heavily when wells only perforated the tidal bar top (zone 8) in the LST. With this completion strategy, the center well always had higher production than the wells placed in the corner of the models.

Flattened Models; Lateral Well Configurations

At TM=0 and with no fractures, cumulative production in the flattened outcrop model ranged from a low of 3,152 to 22,909 stb (Table 3). When compared with the analogous structural model, the performance of the W-E trending horizontal wells placed in the middle of HST2 (base of HST2-PS2) declined by ~33%, while all other wells slightly improved. With the addition of fractures, production at TM=0 increased to a range of 6,368 and 34,280 stb. Fractures were critical for the lower, W-E trending well (HST2), causing a 140% surge in production. In contrast, the remaining three wells' production improved by 16-49%.

As in the analogous structural models, the disparity between well configuration completion strategies is greatly diminished at TM=0.5. In no-frac scenarios, production spanned from 38,562 to 44,749 stb, while the incorporation of fractures boosted production to a range of 42,003 and 50,077 stb (Tables A, C). Fractures augmented flow in the upper wells by ~18-22% while only improving the lower wells by ~1.5-4% (Table B). Again, W-E trending laterals consistently outperformed their N-S counterparts placed in the same horizon.

Production from the flattened proxy model was similarly high, with values ranging from 39,684 to 44,092 stb in unfractured simulations (Table C). In contrast to the other earlier modelling scenarios, both of the W-E trending wells outperformed the N-S wells in these cases. The introduction of fractures boosted production to a range of 40,779 to 53,473 stb, the latter of which was the greatest observed production of all simulations. Additionally, the more consistent

relationship of upper wells outperforming lower wells returned in these cases. Similarly, W-E trending laterals consistently produced greater quantities than the corresponding N-S well of the same horizon.

Flattened models; Vertical Well Configurations

As expected, vertical well configurations greatly underperformed the lateral well arrangements (Appendix G). Total production ranged from a nominal 428 (Appendix G; VNEU0) to 2,953 stb (VCA0) in TM=0 cases, and 760 (VSWU0.5) to 4,380 (VCA0.5) in TM-0.5 cases. In both TM cases, reservoir optimization was achieved with 1) well placement in the center of the model, and 2) perforation of all zones. Similar to the TM=0.5 case, production from the proxy model ranged from 823 ((Px)VSWU) to 4,156 stb ((Px)VCA).

Compared to the structurally dipping models, production varied by negligible quantities in the proxy model and TM=0 simulations. Likewise, at TM=0.5, the majority of production variation was negligible between the two model orientations. The center well arrangement completing in all zones is the only exception, where production decreased by 11% in the flattened model.

V. Discussion

Evolution of WCM Facies Architecture and Subsurface Implications

Phase 1: Highstand Systems Tract 1:

The basal package of the WCM comprises a wave-influenced, river-dominated delta system. Gravity flow deposits along low angle dipping clinoforms are the dominant facies and represent delta front deposits. Laterally, these transition into planar laminated storm-beds, as well as trough cross-bedded sandstones interpreted as terminal distributary channels and/or distal mouth bar deposits. Results from net sand isopachs, spatial facies mapping, and lap-out relationships indicate the presence of two delta lobes, separated by surface A (Figure 13). Each lobe is interpreted as a spatially confined parasequence within a larger progradational system.

HST1 facies architecture and the lobate morphology indicate controlling factors to be a mix of mainly fluvial and wave processes. Gravity flow deposits are largely preserved undisturbed in the lower delta front deposits (F1.1) that accumulated below the storm wave base. Storm influenced deposits (F2) become more prevalent in the upper reaches of the clinoforms and eventually transition into trough cross-beds (F3) that are interpreted as distal distributary channel or mouth bar deposits (Appendix C) Abrupt thickening near depocenters subjected local deposits to increased wave influence, and likely corresponds to a hydrodynamic zone in which fluvial current transport capacity was largely dissipated. Above Surface A, concentrated storm facies indicate a sediment-starved region between delta lobes. Lastly, a secondary control on HST1 architecture appears to be exerted by stratigraphically controlled seafloor topography in place prior to delta deposition. This is evidenced by lateral variation in thickness between the WCM sandstone and an underlying marker horizon of offshore mudstone (Figure 23; MFS1 of *Zupanic, 2017*); additional field data is required to better support this inference.

The presence of low-angle clinoforms that gradually toe out into the underlying mud suggests rapid, but not abrupt, advancement of the system. This is in contrast to some previous interpretations, which place a sharp forced regressive surface at the base of the WCM (Willis 2003; Zupanic 2017). Regionally, the two delta lobes mark the onset of the widespread progradation of the WCM depositional system, and likely indicate a relative drop in sea level. The onset of this regional regression is generally attributed to a 3rd order glacio-eustatic lowstand (Sadeque 2006; Zupanic 2017). Due to the highly localized scale of the basal parasequences, autocyclic lobe switching processes may have been controlled by high-frequency changes in sediment equivalent to 5th order Milankovitch cycles. However, it is possible these deposits represent even shorter periods of time, as short recurrence intervals (<100 years) of similar scale TDC bifurcation and avulsion has been documented in modern deltas (Olariu and Bhattacharya 2006).

As most detailed studies of the WCM utilized subsurface datasets or focused on outcrops of the Raptor Ridge and Murphy Creek localities (e.g. Winn 1991; Lee et al. 2005; Sadeque 2006; Gani and Bhattacharya 2007), the HST1 has not been previously identified at WCR. Knowledge of this distinct sedimentary package at the base of the WCM can benefit interpretations and predictions of nearby reservoir architecture. Additionally, the types of surfaces bounding the HST1 (TSE and MFS, surface B) are generally regional in nature, and can form through-going seismic reflectors or have distinctive log character, potentially enabling future workers to correlate the basal package into the subsurface. Basinward, this horizon may transition into a condensed section of organic shale deposited during the sediment-starved transgressive systems tract. The presence of such low-permeability strata may act as an effective barrier and compartmentalize the reservoir into distinct units lacking pressure communication.

Phase 2: Highstand Systems Tract 2:

After an inferred re-organization in the depositional system, the fluvial dominated HST1 was replaced by deposits with indications of widespread and sustained wave and storm influence (FA2, FA3) that are prevalent in HST2. Deposits of discontinuous, thinly interbedded sandstone and siltstone (FA2) are interpreted as wave-reworked, lower delta front deposits transported by gravity flows or suspension settleout. These beds stack upward into thick deposits of HCS/SCS and cross-bedded facies (FA3), marking a more proximal position on the middle shoreface. The stacking pattern of the above facies suggest that at least two complete and one partial parasequence are present in the HST2, each separated from the underlying parasequence by a flooding surface (Surface C and D). Isopach trends show that the HST2-PS1 compensationally stacked into a small sub-basin controlled by the underlying topography of 1) the HST1 delta system to the east, and 2) the western bathymetric high in place prior to WCM sand deposition. As a result, the lower F1.2 beds of HST2-PS1 are missing at WCR-7, and the WCM takes the form of a sharp-based, storm-dominated shoreface (Figure 23). Along with this underlying seafloor topography, HST2 facies architecture is controlled by a westward increase in wave influence, as evidenced by the presence of FA3 in the west. These trends are shared by HST1-PS1 and HST-PS2, indicating continually shallower water depths to the west.

Simple onlapping of a topographically complex seafloor does not fully explain this along-strike variation in wave influence (Figure 23). Proximal-distal facies relationships may account for these trends if the shoreline existed to the west, but this setting is not supported by FA2 and FA3's southerly paleoflow data. Early movement of the Tisdale Anticline is thus proposed as a possible source for these anomalies. Gentle uplift would have tilted the low-accommodation seafloor to the east and raised the western portion of the seabed into the path of stronger wave

orbitals. Such proto-Laramide activity, demonstrated as a control on regional unconformities and parasequence architecture in Cenomanian Frontier deposits, has been regularly proposed as an influence on WCM deposition (Howell et al. 2003; Sadeque 2006; Vakarelov 2006; Vakarelov and Bhattacharya, 2009). The observed facies relationships and isopach trends at WCR are potentially congruent with these inferences, and may support more regional work constraining the timing of Laramide movement and WCM deposition.

Regionally, the shift in depositional environment from the fluvial-dominated HST1 marks a transgression-regression event, potentially forced by sediment supply changes associated with 4th order Milankovitch scale cycles. Again, no high resolution age constraint or petrographic data is available to infer any tectonic or eustatic controlling mechanisms, but the presence of inferred 5th order parasequences in both the HST1 and HST2 provides a qualitative sense of its temporal and spatial scale. The shift from fluvial to wave regimes also demonstrates a hierarchically greater process than that of the 5th order parasequence cycles, which share similar traits within their respective systems tracts. Lastly, the package is largely correlative to the inferred 4th order, regional HST2 package of *Zupanic, 2017*.

Phase 3: Lowstand Systems Tract

The upper WCM package is composed of cycles of heterolithic, wavy to lenticular bedded deposits that stack upward into coarser grained heterolithic cross-beds. The architecture, heterolithic lithofacies, ichnofacies, and stacking pattern of these deposits all support their interpretation as progradational tidal bars. At this scale of study, complete bars are not captured and observed facies architecture is controlled solely by the stratigraphic position within the bars. A significant shift in paleoflow toward the southeast indicates the deltaic source relocated to the northwest.

Tidal incision at the sequence boundary was in response to a relative lowering of base level, and the overlying LST marks the uppermost 4th order systems tract of the WCM (Zupanic, 2017). Little variation in petrologic composition above and below the S.B. (surface E) suggest this is not a tectonically driven event (Zupanic, 2017), but rather a consequence of eustatic changes. While nominal tectonic activity may have locally influenced the stacking patterns and facies distribution of these deposits, large-scale tectonic adjustment of the hinterland (sediment sources) to the west is not apparent. Tidal bars compose the LST's 5th order depositional elements, with cyclical stacking patterns attributed to high-frequency changes in sediment supply or lateral bar migration. The shifting position of the deltaic source to the northwest may be the product of restriction and embayment of the shoreline. An embayment may have also formed in response to older sedimentary topography or tectonic forcing, as demonstrated in younger Frontier deposits (Bhattacharya and Willis, 2001). In all cases, the paleoflow trends, facies stacking patterns, and bar geometries presented here can be drawn on to augment paleogeographic interpretations and analogous reservoir architecture definition.

Architectural Controls on Fluid Migration

Pore-scale heterogeneities

As no thin-bed petrophysical data was collected in this study, published permeability values of fine-grained sediments are drawn on to link the TM network to a range of lithologies. Permeability of fine-grained sediments varies widely due to heterogeneous factors like particle morphology, sorting, packing, orientation, diagenetic history, and thermal maturation (e.g. Young et al., 1964; Boggs 1992; Neuzil, 1994; Lewis et al. 2006). As a result, early literature extends a broad range to shale permeability, typically between 0.01 nD and 1 µD (e.g. Brace, 1980; Best and Katsube 1995; Revil and Cathles 1999). Recent, more advanced efforts

quantifying unconventional shale reservoir properties yield similarly wide ranges. Notable examples include the Barnett Shale: 2.3 nD-0.096 µD (Heller et al. 2014; Bhandari et al. 2015), Eagle Ford: 5 nD-0.012 mD, Marcellus: 20 nD-55 nD, and the Montney: 0.0085 mD-0.0135 mD (Heller et al. 2014). Siltstone values, less prevalent in literature, yield values ranging from .001 mD to as high as 3.35 mD (Brace, 1980; Best and Katsube 1995). Likewise, intermediate end-members of sandy-shale and clayey-sands, measured from the Pleistocene Gulf of Mexico, yield a range between ~0.01 mD-5 mD, and ~1D-5D, respectively (Revil and Cathles 1999). Baseline sandstone permeability inputs used in the WCM geomodel range from 0.0015 mD to 0.003 mD, measured from core samples (Appendix E). Therefore, TM=0.1 end-members represent a range of 0.00015-0.0003 mD thin-beds, TM=0.5 represents a range of 0.00075 mD-0.0015 mD, and TM=0.9 represents 0.00135-0.0027 mD. Each of these values falls within the aforementioned range of shale and siltstone values, providing the means to semi-quantitatively connect these results to the underlying geology.

Base-case modelling simulations at TM=0 capture fine-grained drapes equivalent to the nanodarcy range of permeability, many orders of magnitude lower than the host sandstone. Thus, the mud-rich heterolithic deposits of the HST1 and LST are likely best characterized by TM=0 or TM ≤0.1. Higher values like TM=0.5 may better represent the system when factors such as bioturbation and intra-mud drape sandstone amalgamation increase sand connectivity. The stressed ichno-facies of both the HST1 and LST deltas suggest little to no enhancement of connectivity by biological processes. However, silt was observed within mud drapes, and it is likely that there are levels of sandstone amalgamation not captured in the facies models. In contrast to delta deposits, the interbedded drapes within the wave-dominated HST2 contain increased levels of siltstone rather than mudstone. Additionally, a far greater level of

bioturbation is present within the HST2, most notably in the form of vertical *Arenicolites* burrows connecting sandstone beds at mud drape interfaces. Such burrows, present throughout the study location, likely buffer the effect of the widespread siltstone and mudstone drapes. This combination of factors suggests higher TM values (i.e. TM=0.5) may better represent the shoreface deposits.

In all depositional environments, results of TM sensitivity tests collectively demonstrate that the permeability of the fine-grained component within a heterolithic system is a critical parameter in the reservoir's effective properties. An increase of the thin-bed TM network from 0.0-0.1 (10% of sandstone permeability) highlights this importance, as it commonly doubles the effective permeability of the reservoir facies (Appendix F; Tables R, X). Furthermore, a gradual increase of TM is of far greater importance in the determination of K_V than K_H (Appendix F; Tables B, G, N, R, X). If the ratio between peak values in a bimodal grain size distribution can be determined, these results can improve estimates of effective directional permeability for a given heterolithic system.

Bed-scale architectural anisotropies

Wave-influenced facies

Except at very high TM values (usually above TM=0.8-0.9) vertical permeability unfailingly decreased more than its horizontal counterparts in fluid simulation (Appendix F; Tables B, G, N). These results are consistent with the expected outcomes, and are attributed to the nature of horizontal geological stratification that generally produces the same result (e.g. Lisham 1970; Slatt 2006; Manzocchi et al. 2008; Green and Ennis-King 2009). Although F1 thin beds were greater in the strike orientation, model 'A's negligible horizontal anisotropy and

minimal K_H reduction demonstrates the horizontal, relatively planar bedding geometries of F1 do not effectively compartmentalize flow laterally in any direction. Low K_V results are broadly similar to other studies modelling distal heterolithics, which exhibited very low to no vertical permeability (e.g. Deveugle et al. 2011; Graham et al. 2015). In the river-dominated HST1, the extent of interbedded impermeable drapes may be 100s of meters, and the K_V / K_H anisotropy may consequently increase. Along with the expected decrease in K_V, FA1 clinoforms may shunt flow updip (Willis and White, 2000; Howell et al., 2008; Olariu et al. 2010; Graham et al. 2015). While cells of Zone 1 were inclined to represent such geometries, it is unclear if this had a significant impact on fluid flow.

Complex, scouring surfaces increased architectural heterogeneity within the wave influenced deposits of models 'B' and 'C'. Intersections of horizontal F1 shales and F2 scours produced small, effective compartments that inhibited lateral fluid flow. Additionally, the greater spatial extent of middle shoreface F2 drapes completely masked each grid, and is the source for their 100% K_V reduction. When compared with model 'A', the lower effective permeability values calculated for models 'B' and 'C', coupled with their increased porosity/permeability baseline inputs, demonstrate the overarching control of bed-scale architecture on this scale of effective reservoir behavior. In this case, modelling results show that the bedding geometries of the "better" reservoir facies of the HST, as might be characterized from core data, actually inhibit flow (Appendix F; Tables G, N). Overall, wave-influenced beds in the study area have greatly reduced vertical permeability and have a minimal effect on horizontal permeability reduction. These anisotropic trends may be magnified at the tops of parasequences, where F2 beds often extend greater distances than underlying F1 deposits.

Tidally influenced facies

The understanding of effective permeability within tidally influenced heterolithic deposits (F4 and F5) has been of great interest in the petroleum industry, and various mathematical and modelling techniques have been employed to improve its estimation (e.g. Jackson et al., 2003; Willis et al., 2004; Jackson et al., 2005; Ringrose et al. 2005; Nordhal and Ringrose, 2007; Burton 2011; Alpak and Barton, 2014). Recent, surface-based modelling efforts have shown that the distribution and connectivity of mudstone in tidal dune toesets have a greater impact on permeability than the distribution of mudstone drapes in dune foresets (Massart et al., 2016). At the time of this writing, no known studies had used a DOM dataset to directly capture the geometry and connectivity of these dune toesets in fluid simulation. Observations of anisotropic tidal shale dimensions (depositional strike > depositional dip) educated an initial hypothesis that preferential fluid migration pathways, constrained by these shale geometries, would be reflected by significantly anisotropic K_H ($K_X > K_Y$) reservoir behavior.

This hypothesis is rejected by model 'D' results and supported by model 'E' results at TM=0, while the remaining increments of the sensitivity tests (TM=0.1 to 1) output largely isotropic results. This does not conclusively demonstrate significant permeability anisotropy within a tidal bar element. However, greater measured mud drape anisotropies in the tidal bar top (Appendix H) are consistent with increased $K_X > K_Y$ anisotropy of model 'E'. Results show that within a tidal bar, upward changes in mud drape geometries may cause an equivalent increase in permeability anisotropy (Appendix F, Table X). However, this relationship is only valid when mud drapes are equivalent to TM=0; with minimal introduction of transmissibility, tidal deposits behave isotropically. At all TM values, the large increase in overall K_H reduction in model 'E' is

likely due to the greater abundance of mud drapes than that of model 'D'. When compared with modelling results of wave-influenced facies, the greater rate of vertical fluid migration in models 'D' and 'E' indicate tidal shale networks maintain increased levels of tortuous upward fluid pathways due to the amalgamation of coarse grained tidal dunes. In contrast, horizontal permeability is lower in tidal settings due to the same complex bedding geometries (Appendix F, Tables R, X).

Reservoir scale controls on fluid migration and production implications

Flow modeling results suggest that stratigraphic heterogeneities are the dominant control on fluid flow in the WCM. When bed-scale heterolithics exhibit high lithologic contrast (TM=0), vertical permeability within parasequence-scale facies architecture is the key determinant in the WCM reservoir production (Figure 24, Tables A-C). This is evidenced by the significant decrease in well production in unfractured outcrop models compared to analogous production from unfractured TM=0.5 and subsurface proxy counterparts (Tables A-C). The tops of HST2-PS1 (Zone 3) and HST2-PS2 (Zone 5) consist of laterally extensive GM2 and/or GM3 deposits in the upscaled outcrop models. As a result, these horizons compartmentalize the geomodels into three units with little to no communication (Figure 10). Sensitivity to both intra-parasequence architecture and low-angle structural dip is greatest in these simulations and in the HST, due to the presence of low K_V wave-dominated facies (Figure 24). In the equivalent high permeability models (TM=0.5 and proxy), GM2 and/or GM3 cells consisted of universally greater K values that were highly beneficial for cumulative production.

When bed-scale heterogeneities have minimal permeability contrast with the bulk reservoir facies (TM=0.5), the outcrop models and corresponding proxy models behave similarly (Tables A, B). Low-angle structural dip is an insignificant factor on flow (Tables A, B). Small

variation in cumulative production is primarily attributed to the intra-parasequence facies distribution unresolvable in the subsurface proxy representation. The relatively minor impact of this inter-well architecture may be more pronounced in settings of highly variable facies properties; however, the petrophysical similarity of lithofacies suggest this type of uncertainty may be insignificant to production (flow) in analogous subsurface reservoir definition. The heterogeneous distribution of GM2, 3, and 4 present in Zone 4 maintains some control over production from the HST lateral wells, but is far less important at TM=0.5. (Figure 10).

Well Configuration and Completion Strategy

In all cases, lateral wells are more productive than vertical well arrangements. Increased production of the LST by west-east trending wells is not attributed to a stratigraphic effect. Instead, the slightly longer dimensions of the geomodel in this orientation provided increased reservoir availability (Figure 10). As production variation between the two oriented wells targeting the LST tidal bar is minimal (~6.5%) with no induced fractures, any anisotropies in flow migration produced by bed-scale architecture are likely negligible. If the entire system is characterized by low TM values, wells should avoid parasequence-scale K_V barriers of the HST2 and instead target tidal facies with the greatest reservoir availability. HST barriers are composed of laterally continuous intervals of FA3, represented in the geomodels by upscaled K_V=0 values attained from fluid simulation of models 'B' and 'C' (Appendix F). Paleotransport direction is insignificant in well placement at the scale of this geomodel, as demonstrated by the minimal K_X/K_Y permeability anisotropies in tidal facies (Appendix F, Tables R, X). However, the geomodel only captures a small window within a regional tidal bar (Figure 11); the elongate geometry of tidal bars would require consideration for planning of a full lateral.

If the depositional system is better characterized by TM=0.5 upscaled properties, optimized well placement should target the tops of shoreface parasequences and laterally continuous intra-parasequence horizons of middle shoreface deposits. Again, K_H anisotropy is insignificant and the thickness of the reservoir is instead a more important factor in well placement. It is worth noting that if fractures are incorporated, well production can be up to ~10% greater in the LST than the best-case HST well. The best HST well captures the anomalous horizon of FA3 in the west, which may be difficult or impossible to predict in the subsurface. The more homogenous architecture encountered by the N-S trending HST well is likely a more probable result for a subsurface well, but produces ~24% less than the fractured LST well (Tables A-C).

As stated in the discussion on pore-scale heterogeneities, TM=0 and TM=0.5 may better characterize the HST1/LST deltaics and the HST2 shoreface, respectively. This necessitates a cross examination of well performance at TM=0 in the LST and at TM=0.5 in the HST. With no fractures, laterals wells placed in the HST produce up to 44,749 stb, while wells fracturing the LST produce a maximum of 34,280 stb at TM=0 (Tables A, C). As the permeability of deltaic packages is overestimated in TM=0.5 simulations, future work partitioning TM=0/0.5 upscaled properties into the different systems tracts is needed to confirm these inferences.

Drawbacks of modelling methodologies

Along with direct, deterministic outcrop constraint attained from digital outcrop model datasets, strengths of the high resolution facies models include their incorporation of 1) average mud drapes dimensions 2) realistic bedding geometries, and 3) geological rules of truncation, all of which help capture and test fluid flow against bed-scale architecture at the most accurate degree possible. Supporting the validity of these modelling methods, simulation results largely

agree with pre-modelling expectations based on geological observations. Nevertheless, identification of this workflow's drawbacks can educate the methodologies of future, similar studies.

First, the semi-quantitative link between TM and lithology is uncertain. Future work quantifying the relative permeabilities within heterolithic facies can help constrain the selection of TM for heterolithics in the WCM and other analogous systems. Secondly, fluid simulation of facies models assumed normal, laminar flow conditions, and did not consider non-Darcy flow behavior that may characterize tight sandstone reservoirs. Such variation in flow dynamics may produce significant changes to overall fluid flow paths and should be considered in future work. Thirdly, the facies modelling workflow can be improved upon that used here by quantifying and integrating the representative elemental volume (REV) into facies model dimensions, as outlined in other studies quantifying architectural controls on fluid flow (e.g. Bear 1972; Jackson et al. 2003; Ringrose et al. 2005; Norhdal and Ringrose 2008; Massart et al. 2016). In this thesis, the dimensions of models A-E were chosen to be close to- or greater than the average mud drape dimension for the incorporated litho-facies, while also maintaining an appreciable level of 3D outcrop constraint. A better understanding of individual facies REV would especially improve confidence in the TM=0 geomodel simulation results for models 'B' and 'C'. The upscaled properties of parasequence-scale barriers compartmentalizing flow are conditioned to these model simulation results, which at K_V=0, are likely not representative in all scenarios. With some thin-bed transmissibility, bed geometry variation, and processes of bioturbation and amalgamation providing secondary connectivity, it is likely that these horizons have K_V not incorporated in the TM=0 simulations. Nevertheless, in this study, these values can still be related to common diagenetic trends; the observed low-permeability HST2 horizons may

exemplify laterally persistent zones of cementation like that observed in outcrop. Such trends can commonly mark the tops of parasequences (Taylor et al. 1995) and may be present in the subsurface, adding to the value of these results.

Next, it is acknowledged that this study did not account for a variety of other heterogeneities that can have an effect on flow. Foremost, individual facies porosity and permeability were simplistically defined, as each GM facies consisted of a constant set of petrophysical properties. This was the case in both facies-scale and field- scale models. Small variation of TM values in facies models highlights the importance of the contrast between lithology properties on fluid flow; likewise, variation in intra-facies permeability and grain fabric may have provided pore-scale, conducive fluid pathways not present in geomodel simulations. Additional complexities include natural fractures and diagenetic alterations. Such omissions were purposefully not included 1) so the impact of primary stratigraphic heterogeneity on fluid flow could be isolated and discretely quantified, and 2) due to time limitations for the project. It is acknowledged that their presence in a subsurface reservoir may dramatically alter the results of this study. Outcrops were noted to contain natural fractures that might be present to a lesser extent in the PRB subsurface. Such fractures, if present, may generate vertical permeability pathways. Similarly, depending on the processes at work, diagenetic alteration may both create and destroy reservoir porosity and permeability.

Summary of Geologic Implications

The role of pore- and bed-scale architecture on fluid flow varies between wave- and tidally- influenced facies. Bioturbation and increased silt content within wave-influenced deposits likely generate higher transmissibility in thin-beds and relatively high K_V/K_H ratios. In the absence of these factors, fine-grained bedding geometries are likely to produce lower K_V/K_H

ratios similar to those observed in the tidal facies deposits. Tidal thin-bed geometries may impose greater K_H anisotropy, but this does not exert a key control on overall reservoir behavior. In contrast to the more planar architecture of wave-influenced facies, complex tidal shale networks are less effective in reducing vertical sandstone connectivity due to the higher degree of sandstone amalgamation in those deposits.

Within both shoreface parasequences and tidal bar parasequences, upward variation in thin-bed character and associated permeability anisotropy can be predicted. Namely, K_X/K_Y mud drape dimensions and permeability anisotropy increases within tidal bars, and both K_V and K_H decrease upward in the transition from the lower- to middle wave-dominated shoreface. The latter is due to more spatially extensive and complex bedding geometries of middle shoreface storm deposits.

At low TM, widespread K_V barriers of parasequence-scale facies architecture control fluid flow by compartmentalizing the reservoir. At higher TM, the role of intra-parasequence scale facies distribution is greater. Minimal structural dip and intra-parasequence architecture may be more important when low K_V facies are prominent. In a subsurface dataset lacking the high resolution, 3D control of outcrop, optimized, low-risk well development strategies are more likely to take place in thick stratigraphic accumulations within the tidal LST, where facies heterogeneity and distribution are easier to predict.

VII. Conclusions:

1. The Wall Creek Member at Wall Creek Road exhibits a complex coarsening upward succession of stacked deltaic deposits. These deposits are organized in systems tracts of multiple sequences, and include 1) a basal river-dominated delta (HST1), overlain by 2) a storm-wave dominated delta or shoreface (HST2), and 3) a tidally influenced delta (LST).

2. Results from high resolution geomodeling reveal a strong facies dependency on flow behavior that also carries through to the upscaled geomodel and reservoir simulations. In general, it is observed that the permeability of fine-grained thin-beds or mud drapes have an outsized influence on the overall reservoir behavior.

3. Thin, laterally continuous mudstone beds in the wave-dominated, distal shoreface setting have the greatest negative effect on vertical permeability and a minimal impact on fluid migration pathways laterally. Conversely, the more complex stratigraphic architectures of heterolithic tidal facies maintain better vertical connectivity but decrease horizontal permeability more effectively.

4. The effect of flow anisotropy measured in the high resolution facies models carries through to the upscaled geomodel, and defines flow-units at the parasequence scale. The presence of laterally continuous, wave-dominated delta facies with little vertical permeability divides the geomodel into distinct compartments lacking pressure communication. When bed-scale heterogeneities are less effective controls on fluid flow (higher thin-bed transmissibility), such compartmentalization does not exist.

5. The presence of structural tilt can also impact reservoir behavior. In the WCM model this is most obvious in the wave-dominated facies, which exhibit little to no vertical

permeability. Consequently, fluid migration pathways are more sensitive to gravity driven processes than tidal facies, which behave more homogenously due to their decreased K_V/K_H anisotropy.

6. When the geomodel is vertically compartmentalized, intra-parasequence facies distribution is an important control on permeability pathways and total volumes in place. This heterogeneity is only a minor factor in overall production when bed-scale mud drapes act as permeable baffles and no compartmentalization is present.

VII. References

Ahmed, S., Bhattacharya, J. P., Garza, D. E., & Li, Y. (2014). Facies architecture and stratigraphic evolution of a river-dominated delta front, Turonian Ferron Sandstone, Utah, USA. Journal of Sedimentary Research, 84(2), 97-121.

Alpak, F. O., & Barton, M. D. (2014). Dynamic impact and flow-based upscaling of the estuarine point-bar stratigraphic architecture. *Journal of Petroleum Science and Engineering*, *120*, 18–38. https://doi.org/10.1016/j.petrol.2014.05.020

Anna, L. O., 2009, Geologic assessment of undiscovered oil and gas in the Powder River Basin Province: U.S. Geological Survey Digital Data Series DDS–69–U, 93 p.

Armstrong, F. C., and Cressman, E. R., 1963, the Bannock Thrust Zone, southeastern Idaho: U. S. Geological Survey Professional Paper 374-J, 22 p.

Armstrong, R. L., 1968, Sevier orogenic belt in Nevada and Utah: Geological Society of America Bulletin, v. 79, p. 429–458.

Ashworth, P. J., Best, J. L., & Parsons, D. R. (2015). Fluvial-Tidal Sedimentology (Vol. 68). Elsevier.

Atlas, H., Fabuel-perez, I., Hodgetts, D., & Redfern, J. (2009). A new approach for outcrop characterization and geostatistical analysis of a succession using digital outcrop models : Upper Triassic Oukaimeden Sandstone Formation , central, *6*(6), 795–827. https://doi.org/10.1306/02230908102

Baltsavias, Emmanuel P. "A comparison between photogrammetry and laser scanning." *ISPRS Journal of photogrammetry and Remote Sensing* 54.2 (1999): 83-94.

Bear, J. 1972. Dynamics of Fluids in Porous Media. Elsevier, New York

Begg, S. H., & King, P. R. (1985, January 1). Modelling the Effects of Shales on Reservoir Performance: Calculation of Effective Vertical Permeability. Society of Petroleum Engineers. doi:10.2118/13529-MS

Best, M. E., & Katsube, T. J. (1995). Shale permeability and its significance in hydrocarbon exploration. The Leading Edge, 14(3), 165-170.

Bergman, K. M., and R.G.Walker, 1988, Formation of Cardium E5 erosion surface, and associated deposition of conglomerate; Carrot Creek field, Cretaceous Western Interior seaway, Al- berta, in D.P. James and D. A Leckie, eds., Sequences, stratigraphy, sedimentology, surface and subsurface: Canadian Society of Petroleum Geologists Memoir 15, p.15–24

Bhandari, A. R., Flemings, P. B., Polito, P. J., Cronin, M. B., & Bryant, S. L. (2015). Anisotropy and stress dependence of permeability in the Barnett shale. Transport in porous media, 108(2), 393-411. Bhattacharya, J. P., & Willis, B. J. (2001). Lowstand deltas in the Frontier Formation, Powder River Basin, Wyoming: implications for sequence stratigraphic models. AAPG bulletin, 85(2), 261-294.

Bhattacharya, J.P., Howell, C.D. Jr., Gani, M. R., White C.D., 2003, Facies Architecture of Topographically controlled, Top-truncated, Mixed-influenced Delta Lobes, Frontier Formation, Powder River Basin, Wyoming, U.S.A.: UTD Quantitative Sedimentology Consortium Field Trip Guide, July 31-August 3, 2003, 99p.

Bhattacharya, J. (2003). Sedimentology. *Encyclopedia of Sediments and Sedimentary Rocks*, 145–152. https://doi.org/10.1007/978-1-4020-3609-5

Bhattacharya, J.P., Howell, C.D. JR., Gani, M. R., White, C.D., 2003, Facies Architecture of Topographically controlled, Top-truncated, Mixed-influenced Delta Lobes, Frontier Formation, Powder River Basin, Wyoming, U.S.A.: UTD Quantitative Sedimentology Consortium Field Trip Guide, July 31-August 3, 2003, 99p.

Bhattacharya, J.P., 2006, Deltas, In: Walker, R.G., and Posamentier, H., (eds.) Facies Models revisited, SEPM Special Publication, v. 84, p.237-292.

Bhattacharya, J. P., Copeland, P., Lawton, T. F., & Holbrook, J. (2016). Estimation of source area, river paleo-discharge, paleoslope, and sediment budgets of linked deep-time depositional systems and implications for hydrocarbon potential. Earth-Science Reviews, 153, 77-110.

Birkhead, Stanley Scott (2005). Architecture of the upper Sego Sandstone, Book Cliffs, Utah. Master's thesis, Texas A&M University. Texas A&M University. Available electronically from http://hdl.handle.net /1969.1/3326.

Bouma, A. H. (1962). Sedimentology of some flysch deposits: a graphic approach to facies interpretation. Elsevier Pub. Co..

Brace, W. F. (1980, October). Permeability of crystalline and argillaceous rocks. In International Journal of Rock Mechanics and Mining Sciences & Geomechanics Abstracts (Vol. 17, No. 5, pp. 241-251). Pergamon.

Buatois, L. A., & Mángano, M. G. (2011). Ichnology: Organism-substrate interactions in space and time. Cambridge University Press.

Burton, D., & Wood, L. J. (2013). Geologically-based permeability anisotropy estimates for tidally-influenced reservoirs using quantitative shale data. *Petroleum Geoscience*, *19*(1), 3–20. https://doi.org/10.1144/petgeo2011-004

Cobban, W. A., Merewether, E. A., Fouch, T. D., and Obradovich, J. D., 1994, Some Cretaceous shorelines in the western interior of the United States, in Caputo, M. V., Peterson, J. A., and Franczyk, K. J., editors, Mesozoic systems of the Rocky Mountain region, U.S.A.: Denver, Colorado, Rocky Mountain Section SEPM, p. 393–414.

Corrizo Co., 2016 Annual Report, p. 9, from Corrizo Co. Investor Relations website, http://www.eogresources.com/investors/reports/2016/EOGR_2016_Annual_Report.pdf

Craddock, W. H., Drake, II, R. M., Mars, J. C., Merrill, M. D., Warwick, P. D., Blondes, M. S., … Lohr, C. D. (2012). Geologic Framework for the National Assessment of Carbon Dioxide Storage Resources ─ Powder River Basin, Wyoming, Montana, South Dakota, and Nebraska. *Geologic Framework for the National Assessment of Carbon Dioxide Storage Resources: U.S. Geological Survey Open-File Report 2012─1024─B*, 30. https://doi.org/10.1016/j.ijggc.2012.09.018

Dalrymple, R.W., and Rhodes, R.N., 1995, Estuarine dunes and bars, in G.M.E. Perillo, ed., Geomorphology and sedimentology of estuaries: New York, Elsevier Science, p. 359-422.

Davis Jr, R. A. (2012). Tidal signatures and their preservation potential in stratigraphic sequences. In *Principles of tidal sedimentology* (pp. 35-55). Springer Netherlands.

Davis, T. L., Benson, R. D., Roche, S. L., & Talky, D. (1997). 4-D, 3-C seismology and dynamic reservoir characterization—a geophysical renaissance. In SEG Technical Program Expanded Abstracts 1997 (pp. 880-882). Society of Exploration Geophysicists.

DeCelles, P. G. (2004). Late Jurassic to Eocene evolution of the Cordilleran thrust belt and foreland basin system, western U.S.A. *American Journal of Science*, *304*(2), 105–168. https://doi.org/10.2475/ajs.304.2.105

DeCelles, P. G., and K. A. Giles, 1996, Foreland basin systems: Basin Research, v. 8, p. 105–123.

Deveugle, P. E. K., Jackson, M. D., Hampson, G. J., Farrell, M. E., Sprague, A. R., Stewart, J., & Calvert, C. S. (2011). Characterization of stratigraphic architecture and its impact on fluid flow in a fluvial-dominated deltaic reservoir analog: Upper Cretaceous Ferron Sandstone Member, Utah. *AAPG Bulletin*, *95*(5), 693–727. https://doi.org/10.1306/09271010025

Dickinson, W.R., 1974, Plate tectonics and sedimentation, in Dickinson, W.R., ed., Tectonics and sedimentation: Society of Economic Paleontologists and Mineralogists Special Publication 22, p. 1–27

Dickinson, W. R., & Snyder, W. S. (1978). Plate tectonics of the Laramide orogeny. *Geological Society of America Memoir*, *151*, 355–366. https://doi.org/10.1130/MEM151-p355

Dixon, J. S., 1982, Regional structural synthesis, Wyoming salient of the western overthrust belt: American Association of Petroleum Geologists Bulletin, v. 66, p. 1560–1580.

Dolton, G. L., Fox, J. E., & Clayton, J. L. (1990). Petroleum geology of the Powder River basin, Wyoming and Montana (No. 88-450-P). US Geological Survey.

Downey, Joe S., and George A. Dinwiddie. *The regional aquifer system underlying the Northern Great Plains in parts of Montana, North Dakota, South Dakota, and Wyoming; summary*. No. 1402-A. 1988.

Duke, W. L., Arnott, R. W. C., & Cheel, R. J. (1991). Shelf sandstones and hummocky cross-stratification: new insights on a stormy debate. *Geology*, *19*(6), 625-628.

Dumas, S., Arnott, R.W.C., and Southard, J.B., 2005, Experiments on oscillatory and combined-flow bed forms: implications for interpreting parts of the shallow marine sedimentary record: Journal of Sedimentary Research, v. 75, p. 501–513.

Dumas, S., & Arnott, R. W. C. (2006). Origin of hummocky and swaley cross-stratification—The controlling influence of unidirectional current strength and aggradation rate. *Geology*, *34*(12), 1073-1076.

Enge, H. D., Buckley, S. J., & Howell, J. A. (2007). From outcrop to reservoir simulation model : Workflow and procedures, (6), 469–490. https://doi.org/10.1130/GES00099.1

EOG Co., 2016 Annual Report, p. 5, from EOG Cp. Investor Relations website, http://www.eogresources.com/investors/reports/2016/EOGR_2016_Annual_Report.pdf

Ericksen, M. C., & Slingerland, R. (1990). Numerical simulations of tidal and wind-driven circulation in the Cretaceous Interior Seaway of North America. *Geological Society of America Bulletin*, *102*(11), 1499–1516. https://doi.org/10.1130/0016-7606(1990)102<1499:NSOTAW>2.3.CO;2

Feldman, H. R., Fabijanic, J. M., Faulkner, B. L., & Rudolph, K. W. (2014). Lithofacies, parasequence stacking, and depositional architecture of wave-to tide-dominated shorelines in the Frontier Formation, western Wyoming, USA. Journal of Sedimentary Research, 84(8), 694-717.

Fluckiger, S. D., Hennes, A. M., Zawila, J.S., Hofmann, M. H., (2015). Predicting Reservoir Heterogeneity in The Upper Cretaceous Frontier Formation in The Western Powder River Basin – An Integrated Stratigraphic, Sedimentologic, Petrophysical, and Geophysical Study. Unconventional Resources Technology Conference. San Antonio, TX; 20-22 July 2015.

Galloway, W.E., 1975. Process framework for describing the morphologic and stratigraphic evolution of deltaic depositional systems. In: Broussard, M.L. (Ed.), Deltas, Models for Exploration. Houston Geological Society, Houston, TX, pp. 87–98

Gani, M. R., & Bhattacharya, J. P. (2007). Basic Building Blocks and Process Variability of a Cretaceous Delta: Internal Facies Architecture Reveals a More Dynamic Interaction of

River, Wave, and Tidal Processes Than Is Indicated by External Shape. *Journal of Sedimentary Research*, *77*(4), 284–302. https://doi.org/10.2110/jsr.2007.023

Graham, G. H., Jackson, M. D., & Hampson, G. J. (2015). Three-dimensional modeling of clinoforms in shallow-marine reservoirs: Part 1. Concepts and application. AAPG Bulletin, 99(6), 1013-1047.

Graham, G. H., Jackson, M. D., & Hampson, G. J. (2015). Three-dimensional modeling of clinoforms in shallow-marine reservoirs: Part 2. Impact on fluid flow and hydrocarbon recovery in fluvial-dominated deltaic reservoirs. AAPG Bulletin, 99(6), 1049-1080.

Grammer, G.M., P.M. Harris, and G. P. Eberli, 2004, Integration of outcrop and modern analogs in reservoir modeling: Overview with examples from the Bahamas, *in* Integration of outcrop and modern analogs in reservoir modeling: AAPG Memoir 80, p. 1-22

Grant, W. D., & Madsen, O. S. (1979). Combined wave and current interaction with a rough bottom. Journal of Geophysical Research: Oceans, 84(C4), 1797-1808.

Green, C. P., & Ennis-King, J. (2010). Vertical permeability distribution of reservoirs with impermeable barriers. Transport in Porous Media, 83(3), 525-539.Goodbred, Jr, S. L., & Saito, Y. (2012). Tide-dominated deltas. In *Principles of Tidal Sedimentology* (pp. 129-149). Springer Netherlands.

Haldorsen, H. H., & Lake, L. W. (1984). A new approach to shale management in field-scale models. Society of Petroleum Engineers Journal, 24(04), 447-457.

H. Haldorsen, Helge & M. Chang, David. (1986). Notes on stochastic shales: from outcrop to simulation model.. Reservoir characterization. 445-485. 10.1016/B978-0-12-434065-7.50020-4.

Hale, L.A., 1960, Frontier Formation—Coalville, Utah, and nearby areas of Wyoming and Colorado, in Overthrust Belt of southwest Wyoming: Wyoming Geological Association Fifteenth Annual Field Conference Guidebook, p. 137–146

Hamlin, H.S., 1996, Frontier Formation stratigraphy on the Moxa Arch, Green River basin, Wyoming: The Mountain Geologist, v.33, p. 35–44.

Hampson, G. J. (2000). Discontinuity surfaces, clinoforms, and facies architecture in a wave-dominated, shoreface-shelf parasequence. Journal of Sedimentary Research, 70(2).

Heller, R., Vermylen, J., & Zoback, M. (2014). Experimental investigation of matrix permeability of gas shales. AAPG bulletin, 98(5), 975-995. Howard, J. D. (1978). Sedimentology and trace fossils.

Howell C.D., Bhattacharya, J.P., Robinson, A.B., and Griffin, W.R., 2003, Topographically controlled, mixed-influence top-truncated deltas: Turonian Wall Creek Member, Frontier Formation, Powder River Basin, Wyoming, U.S.A (abstract): American Association of Petroleum Geologists, Annual Convention, Abstract Volume, 81 p

Jackson, M. D., Muggeridge, A. H., Yoshida, S., & Johnson, H. D. (2003). Upscaling permeability measurements within complex heterolithic tidal sandstones. Mathematical Geology, 35(5), 499-520.

Jones, A., Doyle, J., Jacobsen, T., & Kjønsvik, D. (1995). Which sub-seismic heterogeneities influence waterflood performance? A case study of a low net-to-gross fluvial reservoir. Geological Society, London, Special Publications, 84(1), 5-18.

Jordan, T. E., 1981, Thrust loads and foreland basin evolution, Cretaceous, western United States: American Association of Petroleum Geologists Bulletin, v. 65, p. 2506–2520

Josh, M., Esteban, L., Delle Piane, C., Sarout, J., Dewhurst, D. N., & Clennell, M. B. (2012). Laboratory characterisation of shale properties. *Journal of Petroleum Science and Engineering*, *88*, 107-124.

Kaufmann, E.G., 1985, Cretaceous evolution of the Western interior basin of the United States, in, L.M. Pratt, E.G. Kaufmann, and F.B. Zelt, eds., SEPM 2nd Annual Midyear Meeting, Golden, Colorado: Field Trip Guidebook, P. IV-XIII.

Keogh, K. J., Leary, S., Martinius, A. W., Scott, A. S. J., Riordan, S., Viste, I., … Howell, J. (2014). Data capture for multiscale modelling of the Lourinhã Formation, Lusitanian Basin, Portugal: an outcrop analogue for the Statfjord Group, Norwegian North Sea. *Geological Society, London, Special Publications*, *387*(1), 27–56. https://doi.org/10.1144/SP387.11

Kirschbaum, M. A., & Roberts, L. N. (2005). Stratigraphic framework of the Cretaceous Mowry Shale, Frontier Formation and adjacent units, southwestern Wyoming Province, Wyoming, Colorado, and Utah. US Geological Survey Southwestern Wyoming Province Assessment Team, Petroleum systems and geologic assessment of oil and gas in the southwestern Wyoming province, Wyoming, Colorado, and Utah: US Geological Survey digital data series DDS, 69.

Lalehrokh, F., & Bouma, J. (2014, September). Well spacing optimization in eagle Ford. In SPE/CSUR Unconventional Resources Conference–Canada. Society of Petroleum Engineers.

Larue, D. K., and F. Friedmann, 2001, Stratigraphic uncertainty in field development studies: A conceptual modeling approach: The Leading Edge, v. 20, p. 28-33.

Lee, K., McMechan, G. a., Gani, M. R., Bhattacharya, J. P., Zeng, X., & Howell, C. D. (2007). 3-D Architecture and Sequence Stratigraphic Evolution of a Forced Regressive Top-Truncated Mixed-Influenced Delta, Cretaceous Wall Creek Sandstone, Wyoming, U.S.A. *Journal of Sedimentary Research*, *77*(4), 303–323. https://doi.org/10.2110/jsr.2007.031

Legler, B., Hampson, G. J., Jackson, C. A., Johnson, H. D., Massart, B. Y., Sarginson, M., & Ravnås, R. (2014). Facies relationships and stratigraphic architecture of distal, mixed tide- and wave-influenced deltaic deposits: Lower Sego sandstone, western Colorado, USA. *Journal of Sedimentary Research*, *84*(8), 605-625.

Lewis, M. A., Cheney, C. S., & O Dochartaigh, B. E. (2006). Guide to permeability indices.

Li, H., & White, C. D. (2003). Geostatistical models for shales in distributary channel point bars (Ferron Sandstone, Utah): From ground-penetrating radar data to three-dimensional flow modeling. *AAPG Bulletin*, *87*(12), 1851–1868. https://doi.org/10.1306/07170302044

Lishman, J. R. (1970). Core permeability anisotropy. Journal of Canadian Petroleum Technology, 9(02).

MacEachern, J.A., Bann, K.L., Bhattacharya, J.P., & Howell Jr, C.D. (2005). Ichnology of deltas: organism responses to the dynamic interplay of rivers, waves, storms, and tides.

MacEachern, J. A., Raychaudhuri, I., & Pemberton, S. G. (1992). Stratigraphic applications of the Glossifungites ichnofacies: delineating discontinuities in the rock record.

Manzocchi, T., Carter, J. N., Skorstad, A., Fjellvoll, B., Stephen, K. D., Howell, J. A., ... & Cole, J. (2008). Sensitivity of the impact of geological uncertainty on production from faulted and unfaulted shallow-marine oil reservoirs: objectives and methods. Petroleum Geoscience, 14(1), 3-15.

Martinius, a. W., Ringrose, P.S., Brostrom, C., Elfenbein, C., Naess, a., and Ringas, J.E., 2005, Reservoir challenges of heterolithic tidal sandstone reservoirs in the Halten Terrace, mid-Norway: Petroleum Geoscience, v. 11, p. 3–16, doi: 10.1144/1354-079304-629.

Massart, B.Y.G., Jackson, M.D., Hampson, G.J., Johnson, H.D., Legler, B., and Jackson, C.A.-L., 2016, Effective flow properties heterolithic, cross-bedded tidal sandstones: Part 1. Surface-based modeling: AAPG Bulletin, v. 100, p. 697–721, doi: 10.1306/02011614221.

McGookey, D. P., compiler, 1972, Cretaceous System, in Mallory, W. W., editor, Geologic atlas of the Rocky Mountain region: Denver, Rocky Mountain Association of Geologists, p. 190–228.

McIlroy, D. (2004). Ichnofabrics and sedimentary facies of a tide-dominated delta; Jurassic Ile Formation of Kristin Field, Haltenbanken, offshore mid-Norway. *Geological Society Special Publications*, *228*, 237–272. https://doi.org/10.1144/GSL.SP.2004.228.01.12

Merewether, E. A., W. A. Cobban, and E. T. Cavanaugh, 1979, Frontier Formation and equivalent rocks in eastern Wyoming: The Mountain Geologist, v. 16, p. 67-101.

M'Gonigle, J.W., Dalrymple, G.B., and Holmes, C.W., 1995, Single-crystal 40Ar/39Ar ages for rocks in the lower part of the Frontier Formation (Upper Cretaceous), southwest Wyoming: The Mountain Geologist v. 32, p. 47–53.

Neuzil, C.E. (1994). How permeable are clays and shales? *Water resources research*, *30*(2), 145-150

Nordahl, K., Ringrose, P. S., & Wen, R. (2005). Petrophysical characterization of a heterolithic tidal reservoir interval using a process-based modelling tool. *Petroleum Geoscience*, *11*(1), 17–28. https://doi.org/10.1144/1354-079303-613

Nordahl, K., & Ringrose, P. S. (2008). Identifying the representative elementary volume for permeability in heterolithic deposits using numerical rock models. Mathematical geosciences, 40(7), 753-771.

Nordahl, K., Messina, C., Berland, H., Rustad, a. B., & Rimstad, E. (2014). Impact of multiscale modelling on predicted porosity and permeability distributions in the fluvial deposits of the Upper Lunde Member (Snorre Field, Norwegian Continental Shelf). *Geological Society, London, Special Publications*, *387*(1), 85–109. https://doi.org/10.1144/SP387.10

Obradovich, J. 1993. A Cretaceous time scale, *in* Kauffman, E.G., and W. G. E. Caldwell. "The Western Interior Basin in space and time." *Evolution of the Westerns Interior Basin: Geological Association of Canada, Special Paper* 39 (1993): 1-30

Olariu, C., Steel, R. J., Dalrymple, R. W., & Gingras, M. K. (2012). Tidal dunes versus tidal bars: The sedimentological and architectural characteristics of compound dunes in a tidal seaway, the lower Baronia Sandstone (Lower Eocene), Ager Basin, Spain. *Sedimentary Geology*, *279*, 134–155. https://doi.org/10.1016/j.sedgeo.2012.07.018

Olariu, C., Steel, R. J., & Petter, A. L. (2010). Delta-front hyperpycnal bed geometry and implications for reservoir modeling: Cretaceous Panther Tongue delta, Book Cliffs, Utah. AAPG bulletin, 94(6), 819-845.

Pang, M., and Nummedal, D., 1995, Flexural subsidence and basement tectonics of the Cretaceous Western Interior Basin, United States: Geology, v. 23, p. 173–176.

Posamentier, H.W., G.P.Allen, D. P.James, and M. Tesson, 1992, Forced regressions in a sequence stratigraphic frame- work: concepts, examples, and exploration significance: AAPG Bulletin, v.76, p. 1687–1709.

Price. R. A. 1973. Large-scale gravitational flow ofsupracrustal rocks, southcrn Canadian Rockies. In: Gravity and Tectonics (edited by DeJong, K. A. & Scholten, R.). Wiley, New York, 491-502.

Prince, C. M., Steele, D. D., Zelaya, R., & Devier, C. A. (2011). Shale diagenesis and permeability: Examples from the Barnett Shale and the Marcellus Formation. Search and Discovery Article, 50372, 22.

Pringle, J. K., Westerman, A. R., Clark, J. D., Drinkwater, N. J., & Gardiner, A. R. (2004). 3D high-resolution digital models of outcrop analogue study sites to constrain reservoir model uncertainty: an example from Alport Castles, Derbyshire, UK. Petroleum Geoscience, 10(4), 343-352.

QEP Energy Co., 2012 Northern Region Report, November 2011, Web. http://media.corporate-ir.net/Media_Files/IROL/23/237732/QEPEnergy_NorthernRegion_QEPAnalystDay_Nov2011.pdf

Rajput, S., & Thakur, N. K. (2016). *Geological Controls for Gas Hydrates and Unconventionals*. Elsevier.

Rarity, F., Van Lanen, X. M. T., Hodgetts, D., Gawthorpe, R. L., Wilson, P., Fabuel-Perez, I., & Redfern, J. (2014). LiDAR-based digital outcrops for sedimentological analysis: workflows and techniques. Geological Society, London, Special Publications, 387(1), 153-183.

Rhodes, R. L. (2015). Interpreting Variability in the Depositional History of the Wall Creek Member, Frontier Formation, Powder River Basin, Wyoming, USA. University of Wyoming.

Revil, A., & Cathles, L. M. (1999). Permeability of shaly sands. Water Resources Research, 35(3), 651-662.

Ringrose, P., Nordahl, K., & Wen, R. (2005). Vertical permeability estimation in heterolithic tidal deltaic sandstones. *Petroleum Geoscience*, *11*(1), 29–36. https://doi.org/10.1144/1354-079303-614

Ringrose, P. S., Martinius, a. W., & Alvestad, J. (2008). Multiscale geological reservoir modelling in practice. *Geological Society, London, Special Publications*, *309*(1), 123–134. https://doi.org/10.1144/SP309.9

Ringrose, P., & Bentley, M. (2016). *Reservoir model design.* Springer

Rittersbacher, A., Howell, J. a., & Buckley, S. J. (2014). Analysis Of Fluvial Architecture In the Blackhawk Formation, Wasatch Plateau, Utah, U.S.A., Using Large 3D Photorealistic Models. *Journal of Sedimentary Research*, *84*(2), 72–87. https://doi.org/10.2110/jsr.2014.12

Rodosta, Traci, et al. "US Department of Energy's regional carbon sequestration partnership initiative: Update on validation and development phases." *Energy Procedia* 4 (2011): 3457-3464.

Royse, F., Jr., Warner, M. A., and Reese, D. L., 1975, Thrust belt structural geometry and related stratigraphic problems Wyoming-Idaho-northern Utah, in Bolyard, D. W., editor, Deep drilling frontiers of the central Rocky Mountains: Denver, Rocky Mountain Association of Geologists, p. 41–54.

Sadeque, J. (2006). Regional Reservoir Compartmentalization Within Offlapping, Top-truncated, Mixed-influenced Deltas, Wall Creek Member, Frontier Formation, Powder River Basin, Wyoming. ProQuest.

Sadeque, J., Bhattacharya, J. P., Maceachern, J. A., & Howell, C. D. (2009). Differentiating amalgamated parasequences in deltaic settings using ichnology: an example from the Upper Turonian Wall Creek Member of the Frontier Formation, Wyoming.

El Sayed, A. M. A., Abuseda, H., & El Sayed, N. A. (2017). Petrophysical study of Szolnok Formation, Endrod gas field, Hungary. Egyptian Journal of Petroleum, 26(1), 189-202.

Sech, R. P., Jackson, M. D., & Hampson, G. J. (2009). Three-dimensional modeling of a shoreface-shelf parasequence reservoir analog: Part 1. surface-based modeling to capture high-resolution fades architecture. *AAPG Bulletin*, *93*(9), 1155–1181. https://doi.org/10.1306/05110908144

Shepherd, M., 2009, Deltaic Reservoirs, *in* M. Shepherd, Oil field production geology: AAPG Memoir 91, p. 279-288.

Slatt, R. M. (2006). *Stratigraphic Reservoir Characterization for Petroleum Geologists, Geophysicists, and Engineers - Origin, Recognition, Initiation, and Reservoir Quality*. *Developments in Petroleum Science* (Vol. 61). https://doi.org/10.1016/B978-0-444-56365-1.00013-4

Slattery, J. S., Cobban, W. A., Mckinney, K. C., Harries, P. J., & Sandness, A. L. (1996). Early Cretaceous To Paleocene Paleogeography of the Western Interior Seaway : the Interaction of Eustasy and Tectonism, (August), 22–60. https://doi.org/10.13140/RG.2.1.4439.8801

Snedden, J. W., Nummedal, D., & Amos, A. F. (1988). Storm-and fair-weather combined flow on the central Texas continental shelf. *Journal of Sedimentary Research*, *58*(4).

Soeder, D. (2011, September). Petrophysical Characterization of the Marcellus & Other Gas Shales. In AAPG Eastern Section Meeting.

Steel, R. J., Plink-Bjorklund, P., & Aschoff, J. (2012). Tidal deposits of the Campanian Western Interior Seaway, Wyoming, Utah and Colorado, USA. In *Principles of Tidal Sedimentology* (pp. 437-471). Springer Netherlands.

Swift, D. J., Figueiredo Jr, A. G., Freeland, G. L., & Oertel, G. F. (1983). Hummocky cross-stratification and megaripples: a geological double standard?. *Journal of Sedimentary Research*, *53*(4).

Swift, D.J.P., Oertel, G., Tillman, R., and Thorne, J., eds., 1991, Shelf sand and sandstone bodies; geometry, facies and sequence stratigraphy: Oxford, UK, International Association of Sedimentologists

Taylor, K. G., Gawthorpe, R. L., & Van Wagoner, J. C. (1995). Stratigraphic control on laterally persistent cementation, Book Cliffs, Utah. Journal of the Geological Society, 152(2), 225-228.

Tillman, R. W., & Almon, W. R. (1979). Diagenesis of Frontier formation offshore bar sandstones, Spearhead Ranch field, Wyoming.

Tillman, R. W., & Merewether, E. A. (1994). Field guide for valley-fill, estuarine and shelf ridge sandstones, mid-Cretaceous Frontier Formation, central Wyoming. Rocky Mountain Section (SEPM).

Tolman, R. C., Simons, J. W., Petrie, D. H., Nygaard, K. J., Clingman, S., & Farah, A. M. (2009, January). Method and Apparatus for Simultaneous Stimulation of Multi-Well Pads. In SPE Hydraulic Fracturing Technology Conference. Society of Petroleum Engineers.

Tyler, N., Finley, R.J., 1991. Architectural controls on the recovery of hydrocarbons from sandstone reservoirs. In: Miall, A.D., Tyler, N. (Eds.). The Three- Dimensional Facies Architecture of Terrigenous Clastic Sediments and Its Implications for Hydrocarbon Discovery and Recovery. SEPM Concept in Sedimentology and Paleontology, vol. 3, pp. 1–5

Vincent, C. E., Stolk, A. and Porter, C. F. C., Sand suspension and transport on the Middelkerke Bank (southern North Sea) by storms and tidal currents. Marine Geology 150, 113-129, 1998

Walker, R.G., 1995, Sedimentary and tectonic origin of a trans- gressive surface of erosion: Viking Formation, Alberta, Can- ada: Journal of Sedimentary Research, v.B65, p. 209–221.

Wallace, Kerstan J., et al. "Regional CO2 sequestration capacity assessment for the coastal and offshore Texas Miocene interval." *Greenhouse Gases: Science and Technology* 4.1 (2014): 53-65.

Wang, P. (2012). Principles of sediment transport applicable in tidal environments. In Principles of Tidal Sedimentology (pp. 19-34). Springer Netherlands.

White, C. D., Willis, B. J., Dutton, S. P., Bhattacharya, J. P., & Narayanan, K. (2004). Sedimentology, statistics, and flow behavior for a tide-influenced deltaic sandstone, Frontier Formation, Wyoming, United States. *AAPG Memoir*, *80*, 129–152.

Willis, B.J., & Gabel, S. (2001). Sharp-based, tide-dominated deltas of the Sego Sandstone, Book Cliffs, Utah, USA. *Sedimentology*, *48*(3), 479-506.

Willis, B.J., and Gabel, S. L. (2003). Formation of deep incisions into tide-domintated river deltas: implications for the stratigraphy of the Sego Sandstone, Book Cliffs, Utah, USA. *Journal of Sedimentary Research*, *73*(2), 246-263.

Willis, B. J., & White, C. D. (2000). Quantitative Outcrop Data for Flow Simulation. *Journal of Sedimentary Research*, *70*(4), 788–802. https://doi.org/10.1306/2DC40938-0E47-11D7-8643000102.31865D

Winn Jr, R. D., Stonecipher, S. A., & Bishop, M. G. (1983). Depositional environments and diagenesis of offshore sand ridges, Frontier Formation, Spearhead Ranch Field, Wyoming. The Mountain Geologist.

Winn, R.D., JR., 1991, Storm deposition in marine sand sheets: Wall Creek Member, Frontier Formation, Powder River Basin, Wyoming: Journal of Sedimentary Petrology, v. 61, p. 86-101.

Wood LJ (2004) Predicting tidal sand reservoir architecture using data from modern and ancient depositional systems, integration of outcrop and modern analogs in reservoir modeling. AAPG Mem. 80:45-66

WSGS. (2014). Powder-River-Basin Oil and gas geology, production, and future development.

Young, A., Low, P.F., & McLatchie, A.S. (1964). Permeability studies of argillaceous rocks. *Journal of Geophysical Research*, *69*(20), 4237-4245

Zupanic, J., Hofmann, M. H. (2016). *Stratigraphic Architecture and Facies Distribution Within the Wall Creek Member of the Frontier Formation, Western Powder River Basin, Wyoming.* AAPG Datapages/Search and Discovery Article #90259 ©2016 AAPG Annual Convention and Exhibition, Calgary, Alberta, Canada, June 19-22, 2016.

Zupanic, John, "Lateral Heterogeneity and Architectural Analysis of the Wall Creek Member of the Upper Cretaceous (Turonian) Frontier Formation" (2017). Graduate Student Theses, Dissertations, & Professional Papers. 11033. https://scholarworks.umt.edu/etd/11033

VIII. Figures

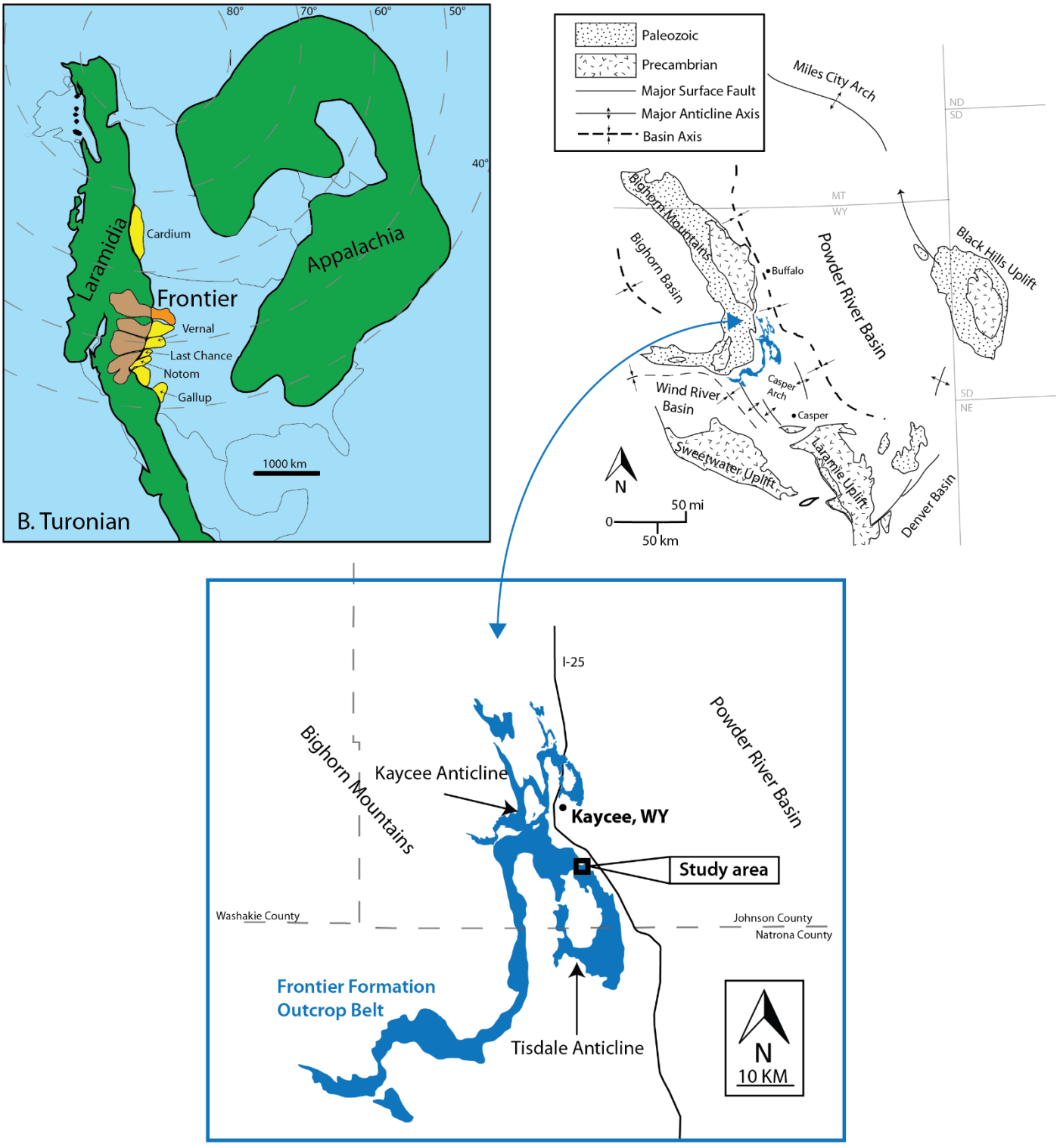

Figure 1: Top left: *North American Turonian Paleogeography, showing the position of the Frontier (orange) and other major delta systems (yellow) along the Cretaceous Western Interior Seaway. Modified from Bhattacharya et al. 2016.* ***Top right:*** *Map of the Powder River Basin and surrounding geologic structures. Modified from Dolton et al. 1990.* ***Bottom:*** *Frontier Formation outcrop belt along the western margin of the Powder River Basin. Modified from Gani and Bhattacharya, 2006.*

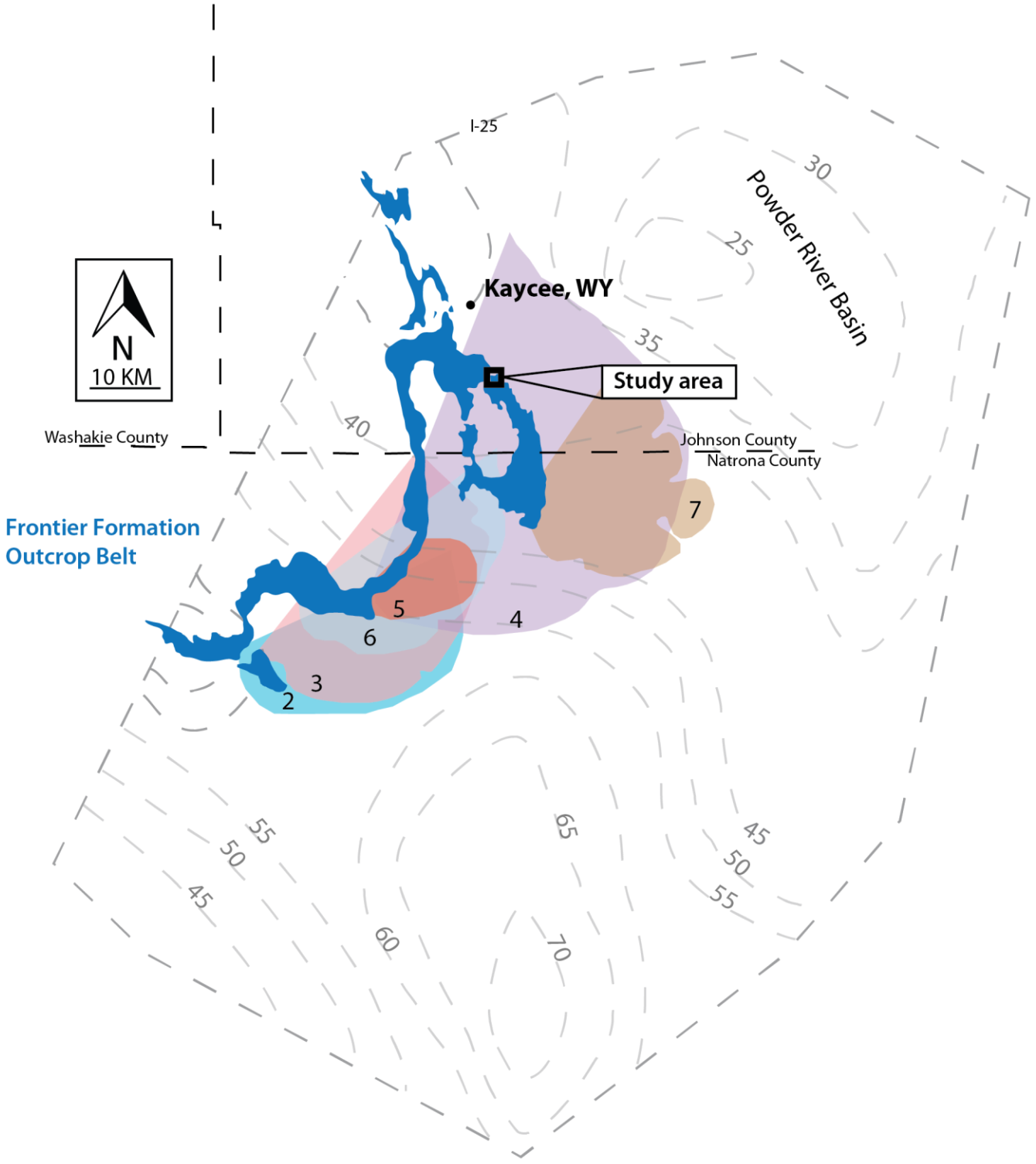

Figure 2: *Wall Creek Member isopach and approximate parasequence sandstone pinch-outs. Total WCM isopach contours are shown in grey. The pinch-out of correlated outcrop-subsurface parasequences (2-7) of Bhattacharya et al. 2003, Sadeque, 2006; etc. are highlighted and labeled. PS2 is oldest and PS7 is youngest. Note that WCM thickness decreases from north to south. Also note the laterally shifting character of WCM sandstones, indicative of a deltaic source. Parasequences tend to amalgamate in the northern, low-accommodation regions of deposition. Figure modified from Sadeque, 2006.*

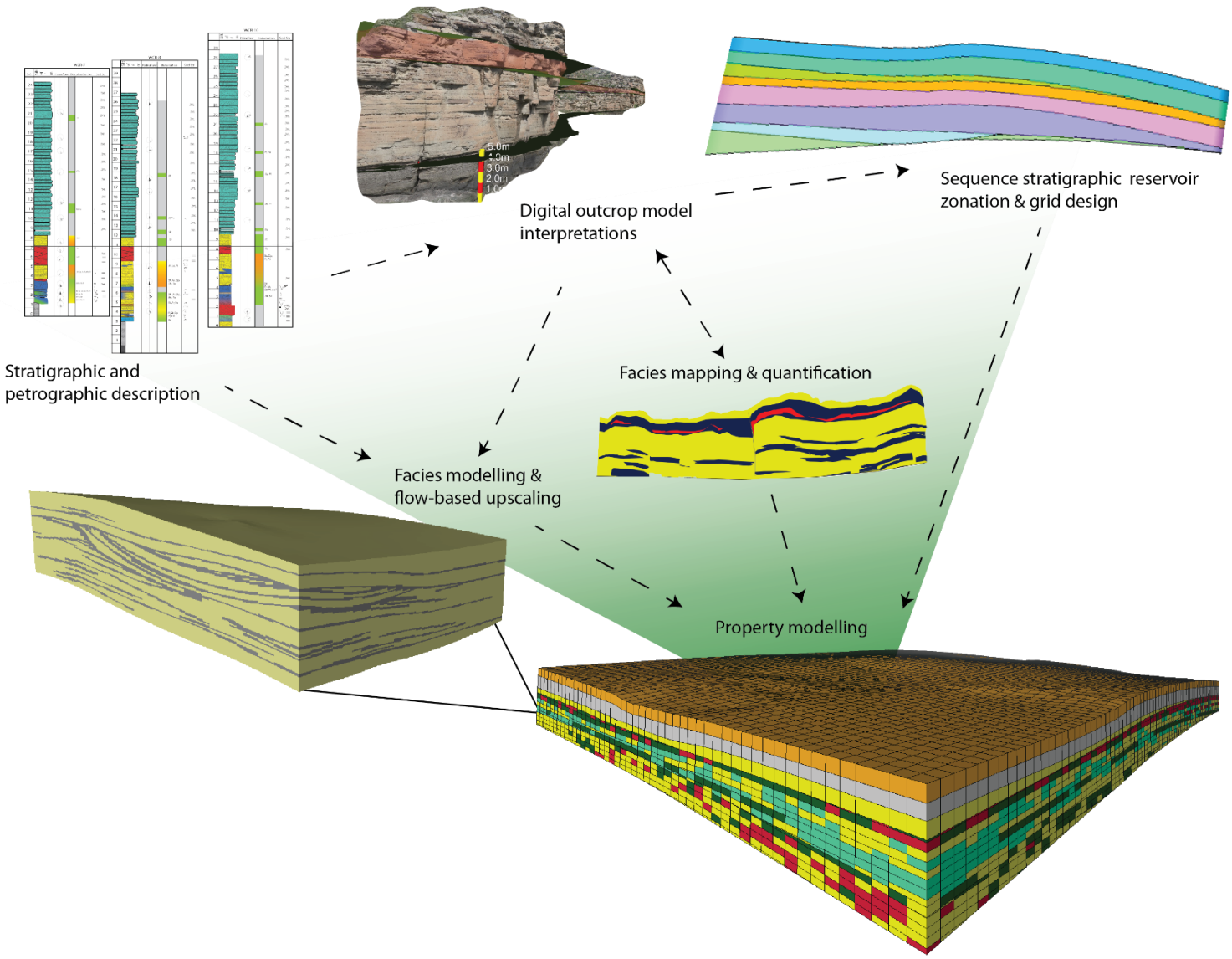

Figure 3: *Generalized workflow to capture detailed facies architecture in high resolution Petrel geomodel. Stratigraphic description in the field and lab (**top left**) constrain stratigraphic interpretations made in a digital outcrop model using Virtual Reality Geological Studio (**top center**). Major sequence stratigraphic surfaces are interpolated in Petrel to create the geomodel framework (**top right**). Flow based upscaling of bed- scale geocellular models provides effective permeability properties for the upscaled geomodel (**left center**). Photograph based facies quantification of all each zone at all outcrops in the study location provides the spatial statistics needed to distribute upscaled properties across the geomodel (**right center and bottom right**).*

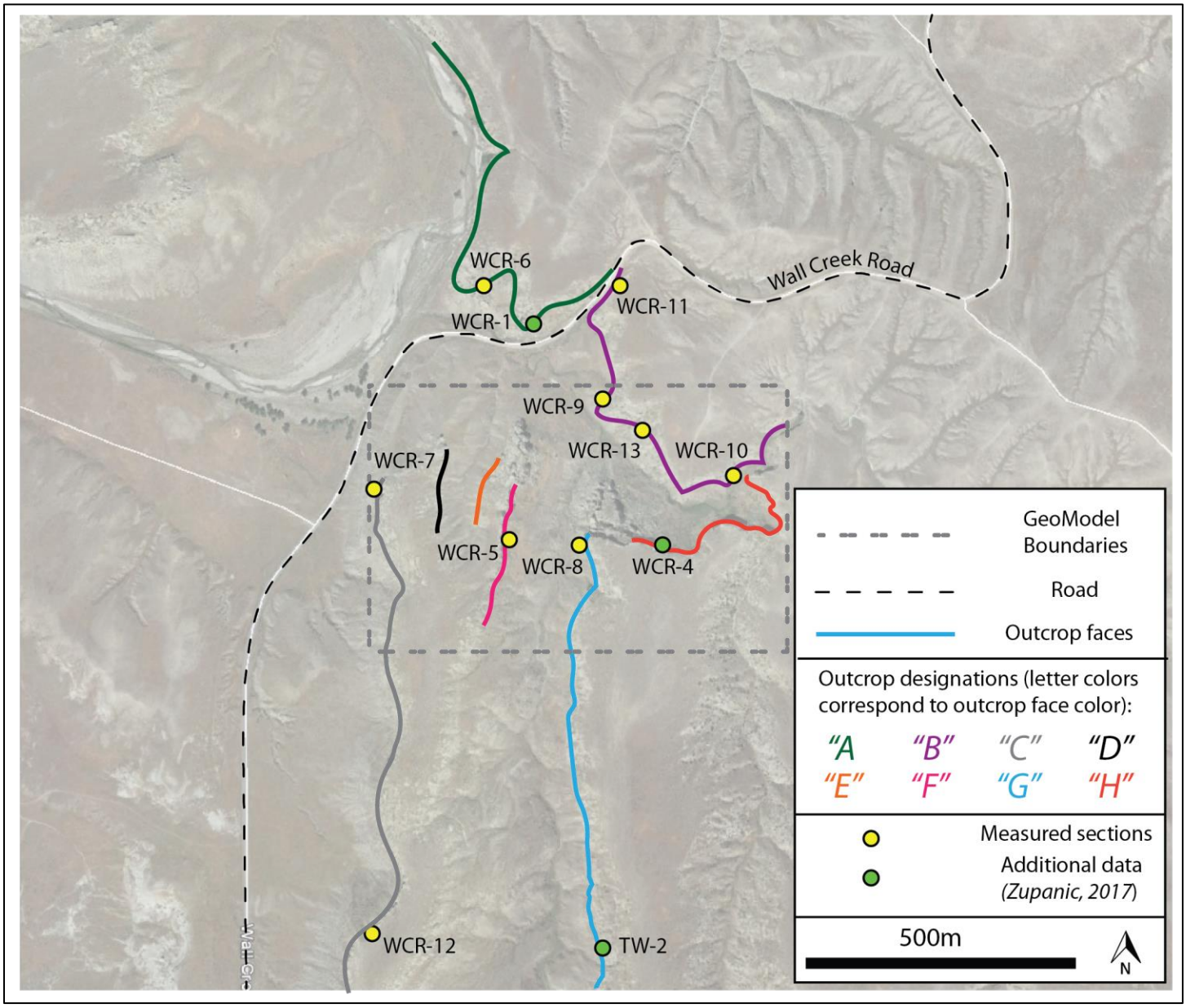

Figure 4: *Map of the study location and Geomodel boundary. The locations of measured sections as well as the outcrop letter designations (A-H) are shown. The northernmost two outcrops are designated "A" and "B". After this, "C"-"H" designations are sequentially given to outcrops in a west-east order. Note that the highest concentration of outcrop faces lie within the geomodel boundaries, providing the best constraint for modelling parameters.*

Wall Creek Member Sandstone Facies

	Facies	Description	Bioturbation	Facies Association
1.1	Continuous (100s m), thinly interbedded sandstone and siltstone.	Tabular, sharp-based sandstone interbedded with thin siltstone and mudstone drapes. Beds have massive, plane-parallel, and ripple-laminated bedding, with clear Bouma sequences. Beds have clinoformal geometries and are often amalgamated. Carbonaceous plant material is common.	BI: 0-2. (Sk, Oph, Pl, Th, Pa)	FA1, FA4
1.2	Discontinuous (10s m), thinly interbedded sandstone and siltstone.	Lenticular to tabular bedded sandstone with massive to planar bedding, interbedded with thin siltstone/mudstone drapes. Sharp based, sometimes erosional bed boundaries. Pinch and swell beds geometries with scour surfaces present.	BI: 2-3. (Sk, Oph, Ar, Pl, Th, Td, Tb, Pa, Ro)	FA2
2.1	Swaley cross-stratified sandstone (SCS)	Very fine to fine-grained, tan to red sandstone with multiple orders of truncating low-angle, planar lamina sets. Commonly scour underlying sediments; Common basal lag of pebbles, shells, ammonites, concentrated plant detritus and rip-up clasts.	BI: 0-2. (Sk, Oph, Ar)	FA1, FA2, FA3, FA4
2.2	Hummocky cross-stratified sandstone (HCS)	Very fine to fine-grained, tan to red sandstone with antiformal planar lamination. Beds are typically 5-15 cm thick and exhibit sharp basal contacts. Often associated with SCS.	BI: 0-2. (Sk, Oph, Ar)	FA1, FA2, FA3, FA4
2.3	Low-angle planar sandstone	Very fine to fine-grained, tan to red sandstone with low-angle, planar lamination, often with ripple-capped bedding planes. Often preferentially cemented in the field, associated with SCS.	BI: 0-2. (Sk, Oph, Ar)	FA1, FA2, FA3, FA4
3	Planar and trough cross-bedded sandstone	Fine to medium-grained, cross-bedded sandstone with rare mud draped foresets; rare mud chips on foresets. Beds range from 5-30 cm thick.	BI: 0-2. (Sk, Oph, Ar)	FA3, FA4
4	Heterolithic, wavy and flaser bedding	Mud-rich cm-scale interbedded mud and sand beds. Associated with heterolithic trough cross bedding and thick (2-10) cm mud beds.	BI: 0-2. (Pl, Pa)	FA5
5	Heterolithic trough and planar cross-bedded sandstone	Tan, reddish, and grey sandstone with common mud-draped foresets and bed boundaries. Deposited in lenticular aggradational beds 10-30 cm thick. Rip up clasts sometimes present. Reactivation surfaces and ripples present.	BI: 0-1. (Sk)	FA5

Figure 5: *Wall Creek Member lithofacies*

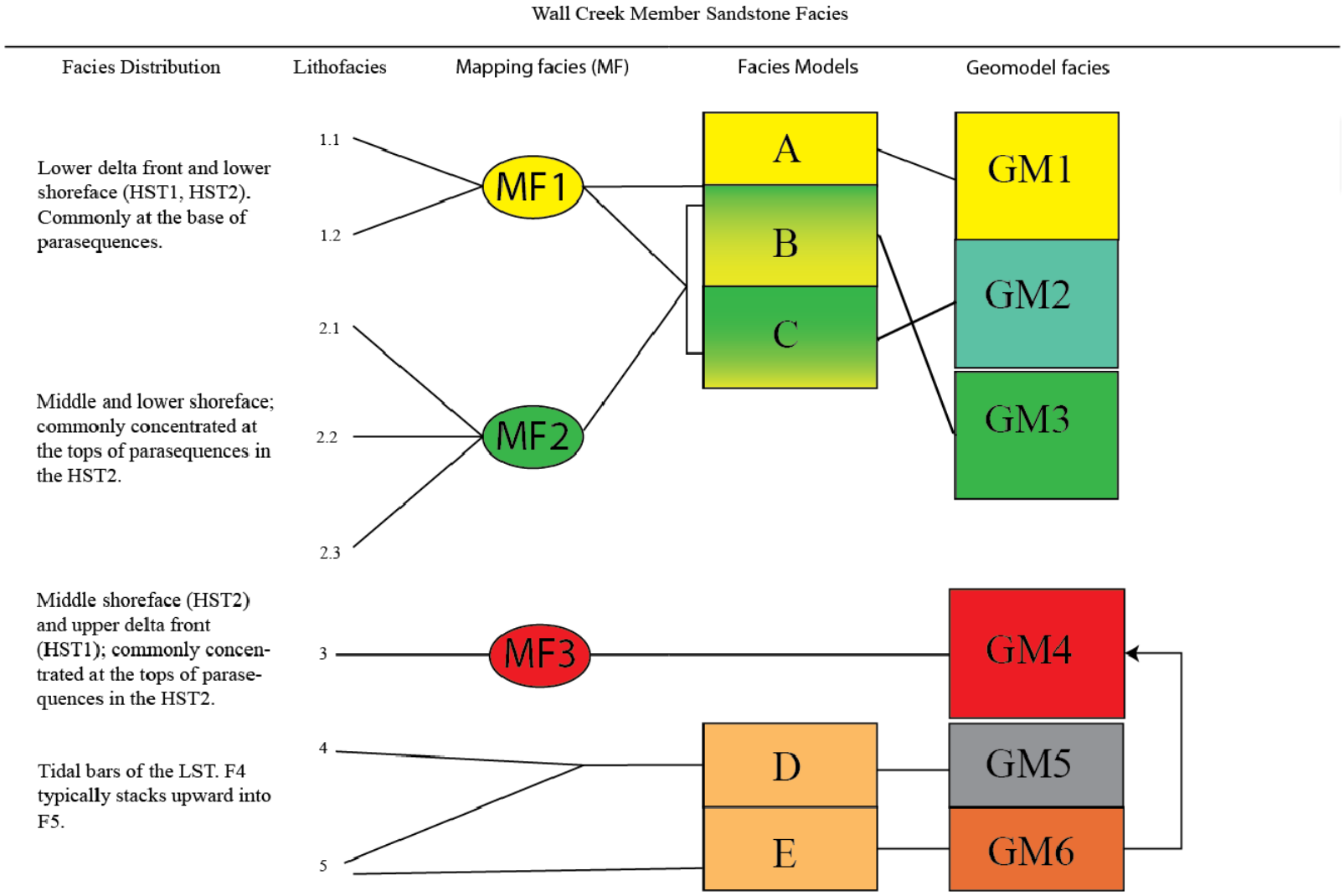

Figure 5 (cont.): *Lithofacies and equivalent mapping facies (MF). Tidal facies 4 and 5 are found in the upper part of the WCM and were not mapped. Results of flow simulation of facies models A-E provided property inputs for upscaled geomodel facies (GM) in the field-scale geomodel. GM3 has greater proportions of F2 than FM2. Lithofacies 3 is very similar to lithofacies 5, FM4 was populated with properties from facies model E simulation results.*

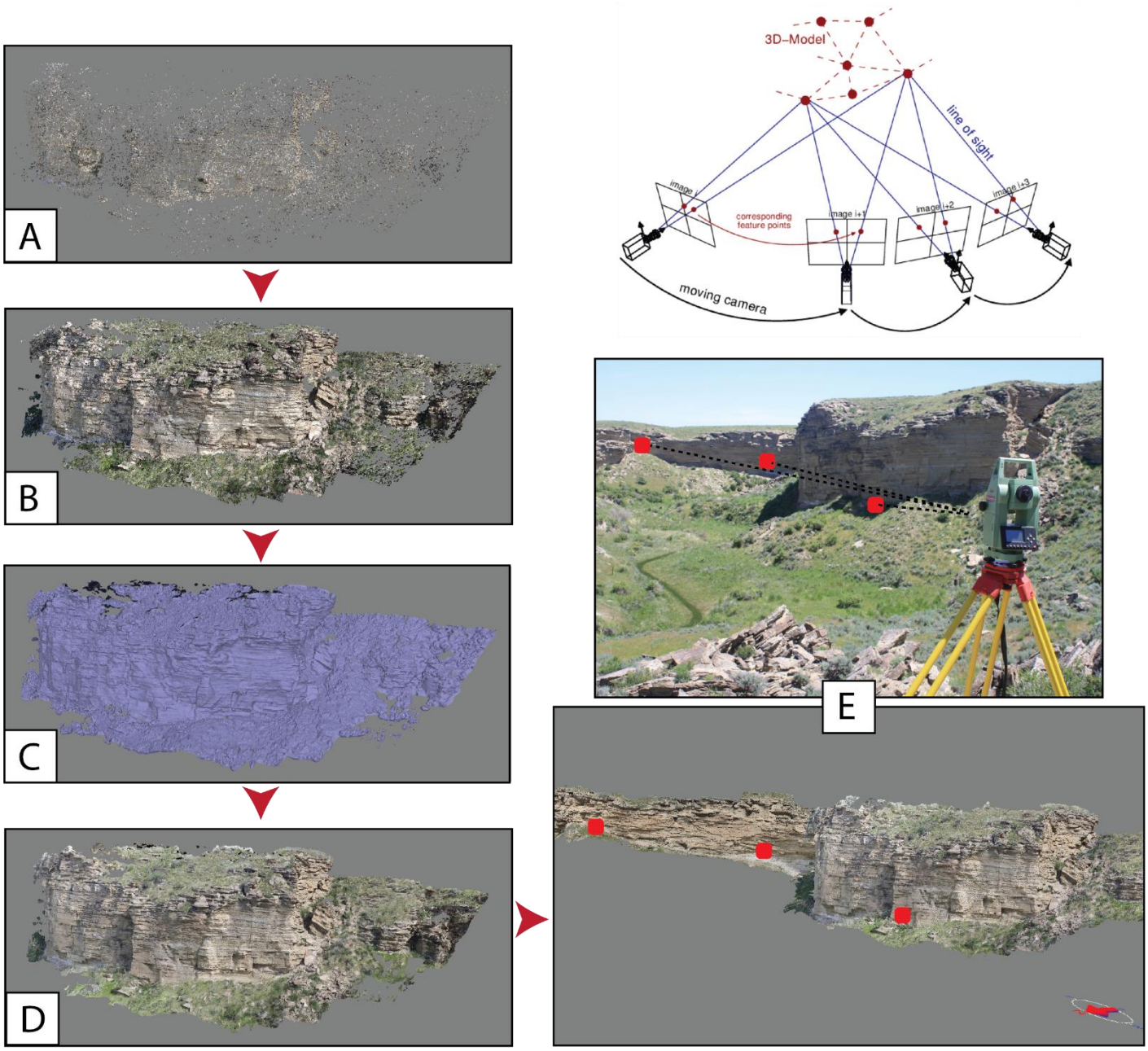

Figure 6: *Photogrammetric process used to build digital outcrop models. Top right: Illustration of photogrammetric principles. A 3D representation of the target object is calculated as a function of angular variation between photographs taken from different perspectives. Source: Theia-sfm.org (2016). Top left to bottom right images show the workflow to produce the 28 sub-models. After points are matched between all image data (**A**), a dense 3D point cloud is generated (**B**). Points are then connected to form a Triangular Irregular Network (TIN) (**C**). A photographic texture is then draped over the TIN (**D**). Finally, digital outcrop model points (bottom right) are assigned coordinates gathered during the total station survey of ground control points (**E**).*

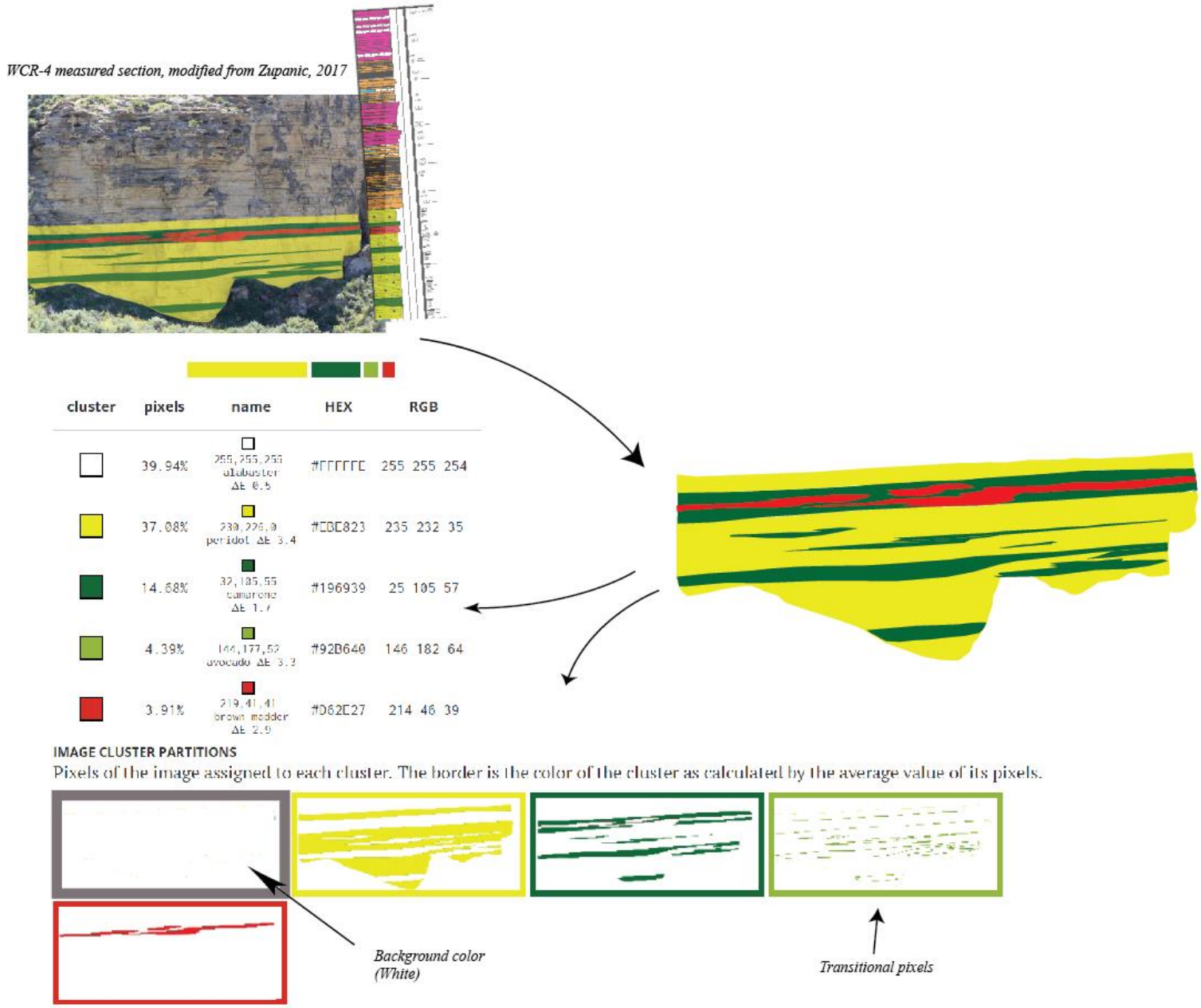

Figure 7: *Facies quantification process. Top left: Measured sections and high-resolution photos constrained facies maps at all outcrops. Maps were imported into the image analysis software, which calculated image statistics, including color proportions. Facies proportions were normalized for the three primary map facies and their respective colors. Background colors such as white (39.94% in this example) were disregarded, and percentage values of transitional pixel clusters (i.e. "avocado") were split between the two primary colors (yellow and green). This process was repeated for each zone of the geomodel at all outcrops, and provided the primary statistical input for facies proportions and spatial trends*

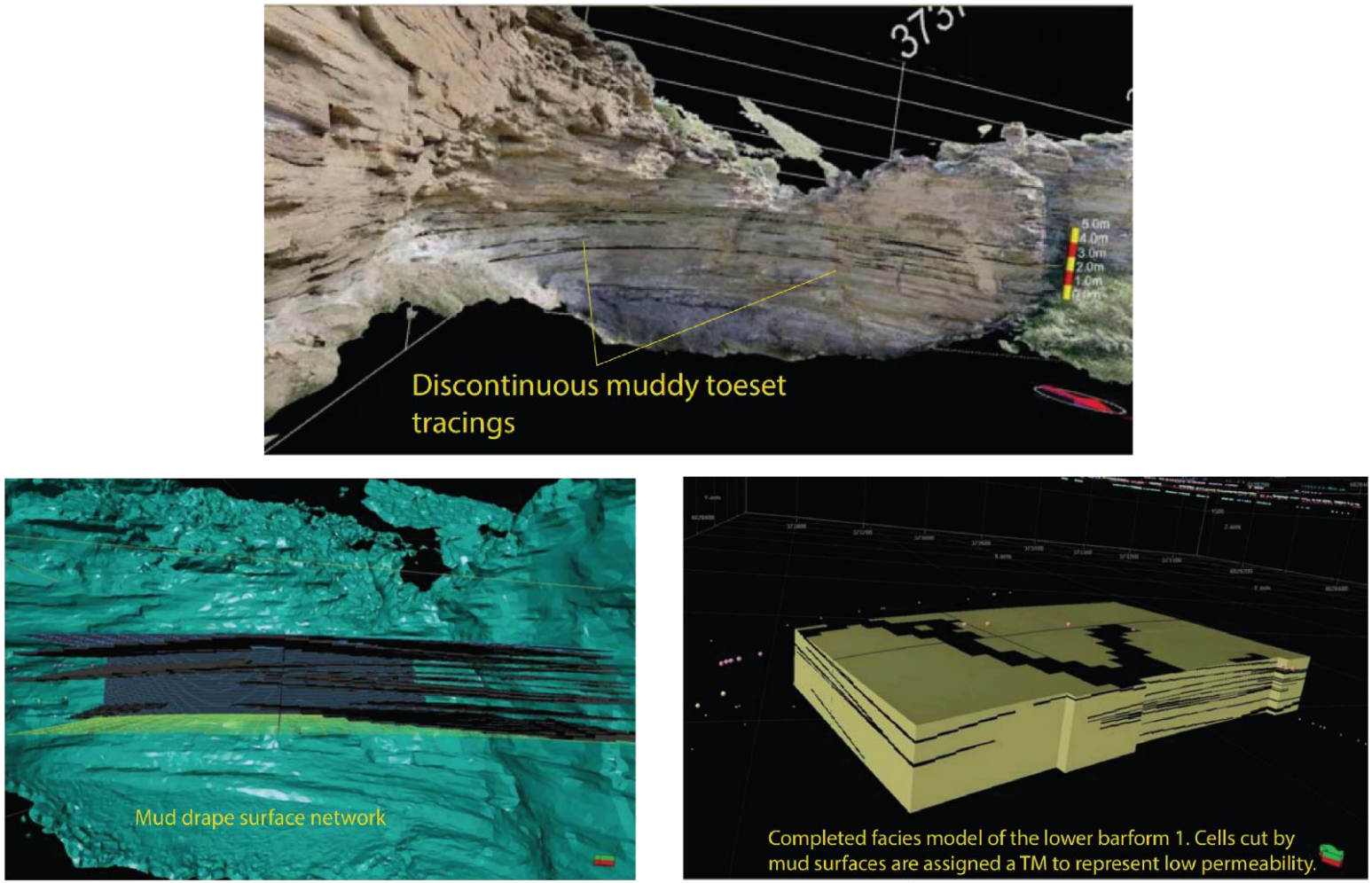

Figure 8: *Facies modelling process, shown here for model "D". Top: fine-grained thin beds are traced in a three-dimensionally exposed outcrop location. These polylines are then imported into Petrel, and used to condition surfaces that with average thin-bed dimensions according the field-wide measurements. Surfaces are given planar or parabolic trends to match observed facies characteristics. Geological rules are applied so younger beds truncate older beds, ultimately creating a network of cells representing realistic bed geometries. These cells are then applied a Transmissibility Multiplier to represent low permeability values.*

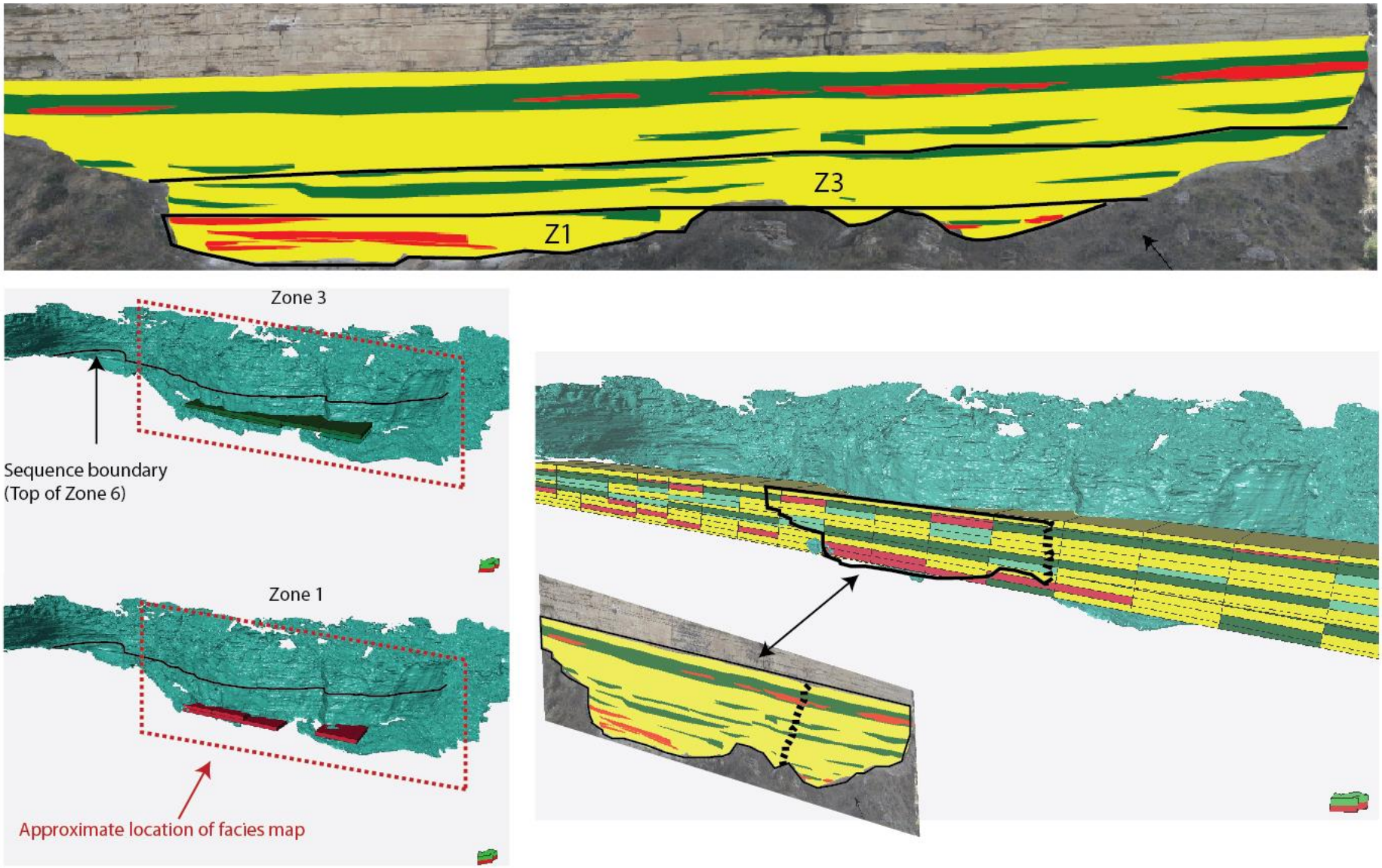

Figure 9: *Illustration of upscaling process for zones 1 and 3 at the WCR outcrop "H". Polylines traced in VRGS, intersecting non-background facies (F3 in zone 1 and F2 in zone 3) were imported into Petrel. These point sets were assigned Petrel facies codes and upscaled; stochastic simulation of each zone incorporated this hard data. Above, a Petrel geomodel cross-section of the same outcrop shows the similarities between the facies map and final geocellular representation after property distribution. Note that the outcrop bends toward and away from the photopanorama (as can be seen in the teal DOM), so the Petrel cross-section cuts oblique to the facies diagram.*

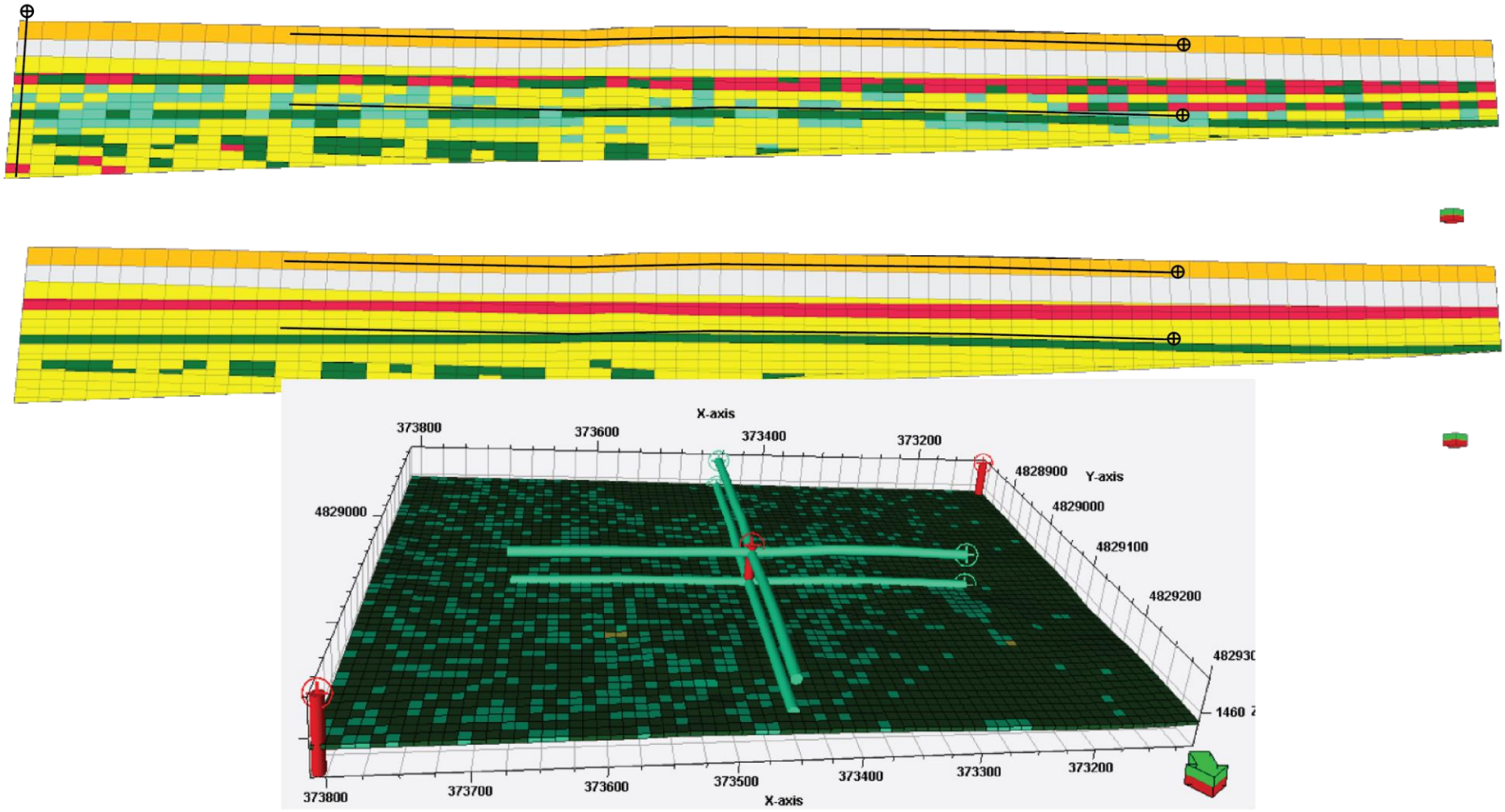

Figure 10: *Geocellular models flattened on Surface D, illustrating the well configurations used in final flow simulation.* ***Top:*** *Detailed outcrop model incorporating all facies architecture observations and upscaled cells, and the proxy "subsurface" model capturing parasequence-scale architecture. Note the black lines showing the horizons that the lateral and vertical wells penetrate.* ***Bottom:*** *3D illustration of lateral (teal) and vertical (red) well configurations. The vertical well on the bottom left (NE) is the same as that shown on the left side of the geomodel cross sections.*

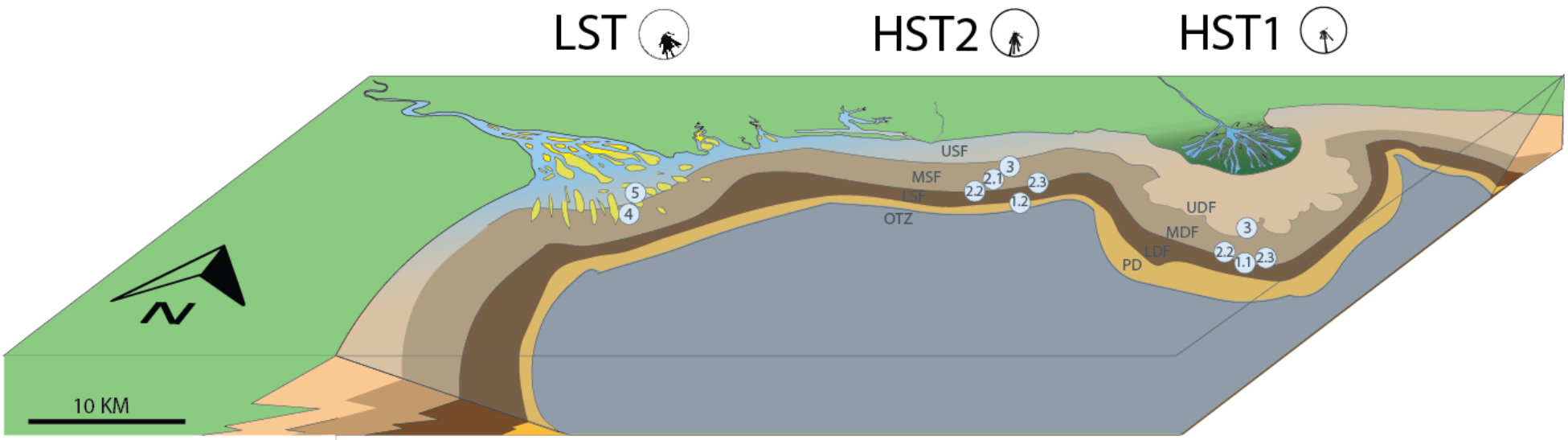

Figure 11: *Conceptual block diagram illustrating depositional setting of lithofacies and their position within the three systems tracts. The stratigraphic packages from the base of the WCM to its top include a fluvial-dominated delta HST1 (right), a storm-wave dominated shoreface HST2 (center), and a LST tidal delta (left).*

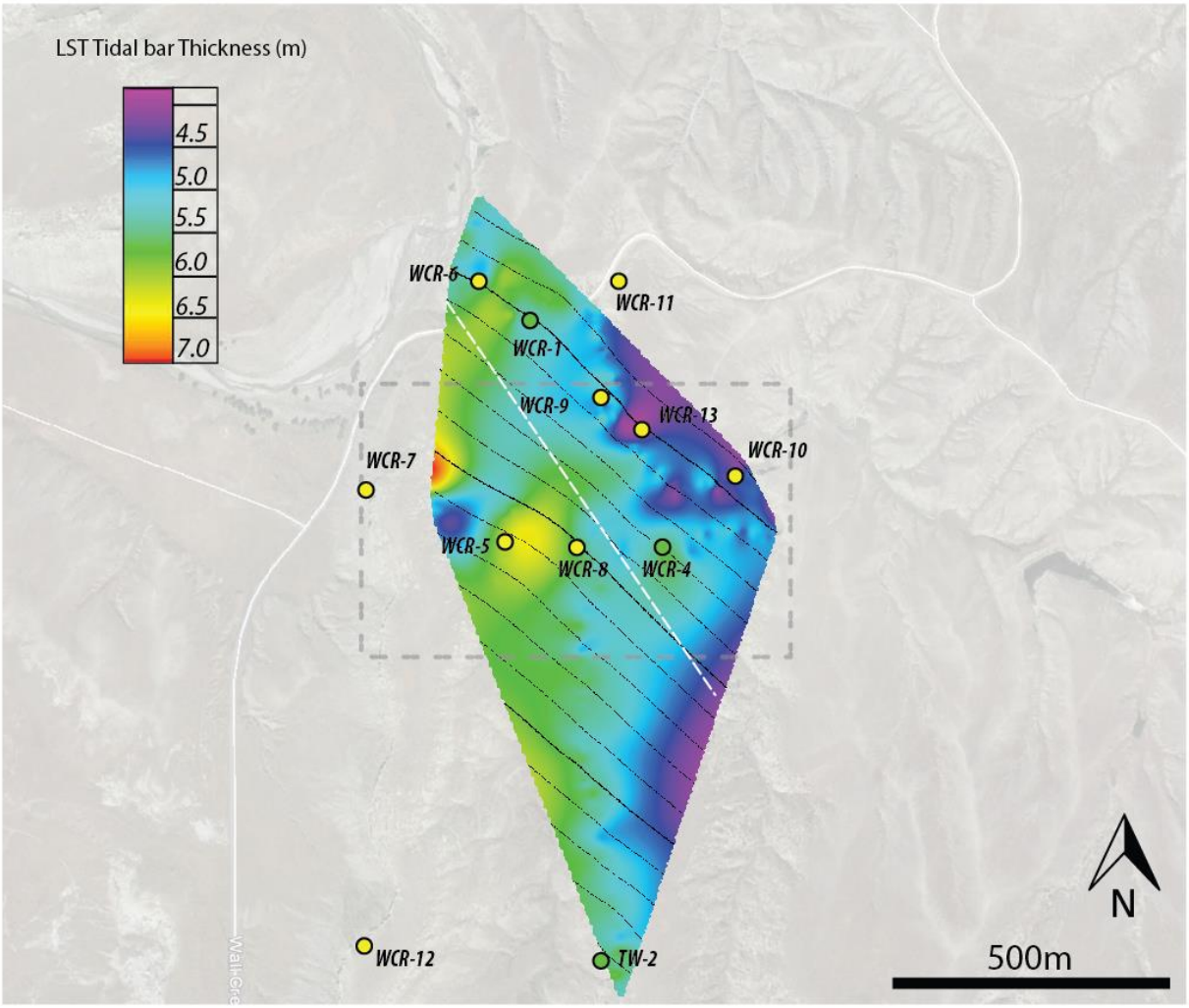

***Figure 12**: Isopach of the lowermost tidal bar in the LST succession. Note the gradual westward to southwestward thickening of the bar, perpendicular to the white dashed line. This bar is divided into zones 7 and 8 in the field-scale geomodel.*

Figure 13: *Stratigraphic expression of Surface A. Top: Telephoto of surface WCR-13. The basal package below the surface (Zone 1 of geomodel) is interpreted as a fluvial-dominated delta lobe, which thickens by 1 meter in just 30 meters laterally. Overlying beds belonging to the northern delta lobe onlap this horizon. Bottom: Sedimentological characteristics of Surface A at WCR-9, the left-most part of the outcrop shown above. The lens cap rests on the thick, fine-grained bed delineating surface A. Note the anomalously heavy bioturbation present at this surface, which is largely composed of Thalassinoides of the glossifungites ichnofacies. The assemblage of trace fossils located along this surface is some of the largest observed in the field, signaling a period of nondeposition associated with delta lobe abandonment.*

Figure 14: *Interpreted telephoto and bedding diagram of the WCR-6 section. Clinoforms of the basal HST1 delta are truncated by surface B, interpreted as a transgressive surface of erosion (TSE). The transgressive systems tract separating the underlying HST1 from the HST2 shoreface is locally absent, and the TSE is merged with the maximum flooding surface (MFS).*

Figure 15: *Surface C (black dashed line) at WCR-5. Note the abrupt transition between a horizon of interbedded F1 and thick F2 deposits, to the overlying F1 beds. The contact representing this parasequence flooding surface is often highly transitional but can be clearly seen in all facies diagrams (this surface marks the top of Zone 3). F1 deposits dominate Zone 4, while F1 is only a minimal component of much of Zone 3.*

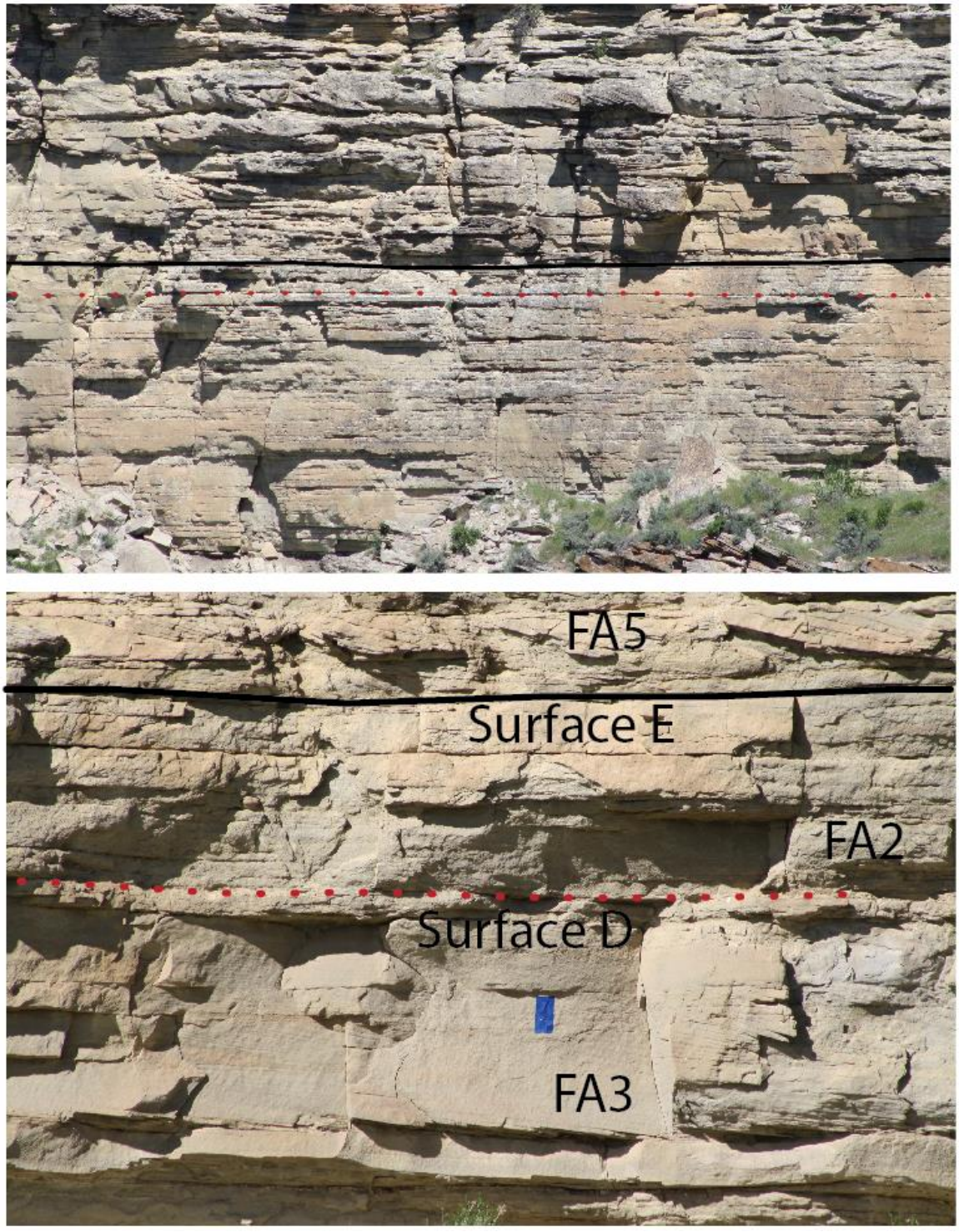

Figure 16: *Stratigraphic expression of Surface D (dashed red line) and E (solid black line). Note Surface D's very sharp, planar expression in the top telephoto. Surface D is a flooding surface that separates cross-bedded facies of FA3 from overlying, interbedded sandstone and siltstone deposits of FA2. Surface E is the regional sequence boundary that separates the underlying shoreface deposits from the overlying tidal deposits of FA5.*

Figure 17: *Surface F tidal bar parasequence boundary.* ***Top:*** *Illustration of regional weathering pattern associated with Surface E. The coarser-grained, better cemented F5 bar top facies lie just below the surface (dashed black line). Above the surface, beds are made up of a high proportion of mud-rich F4, which is consistently more weathered.* ***Bottom:*** *Beds of F4 and F5 directly above the bar top surface, which is often covered, but locally exposed the base of the Jacob's Staff.*

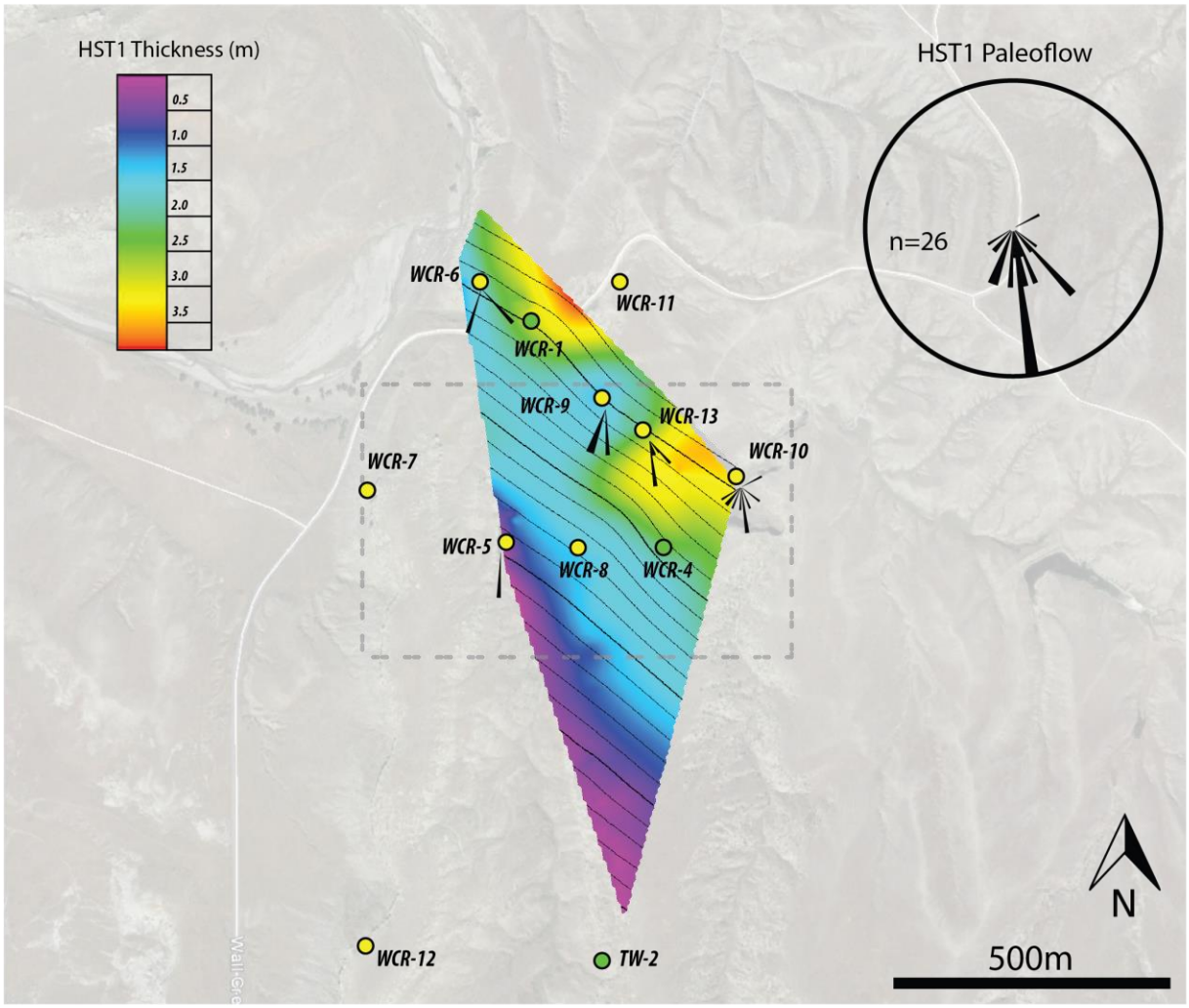

Figure 18: *Isopach of the basal HST1. Note the westward pinch-out of the package as well as its two distinct depocenters, interpreted to represent two fluvial-dominated delta lobes. The inter-lobe thinning at WCR-9 corresponds to the lateral pinching-out of the southern lobe, and was identified in the field based on its heavily bioturbated, fine-grained character and overlying onlapping bed geometries (see HST1-PS1 surface). Paleoflow from this interval suggests a general source to the north. WCR-10 and the area just east of WCR-4 (Eastern Outcrop "H") are located in the more axial position on the southern lobe. These localized areas preserve a significantly increased proportion of trough cross-bedded facies, indicative of greater unidirectional fluvial energy. Note that the geomodel primarily captures the southern delta lobe, but the sole paleoflow measurement in WCR-5 deposits suggests a possible northern lobe source.*

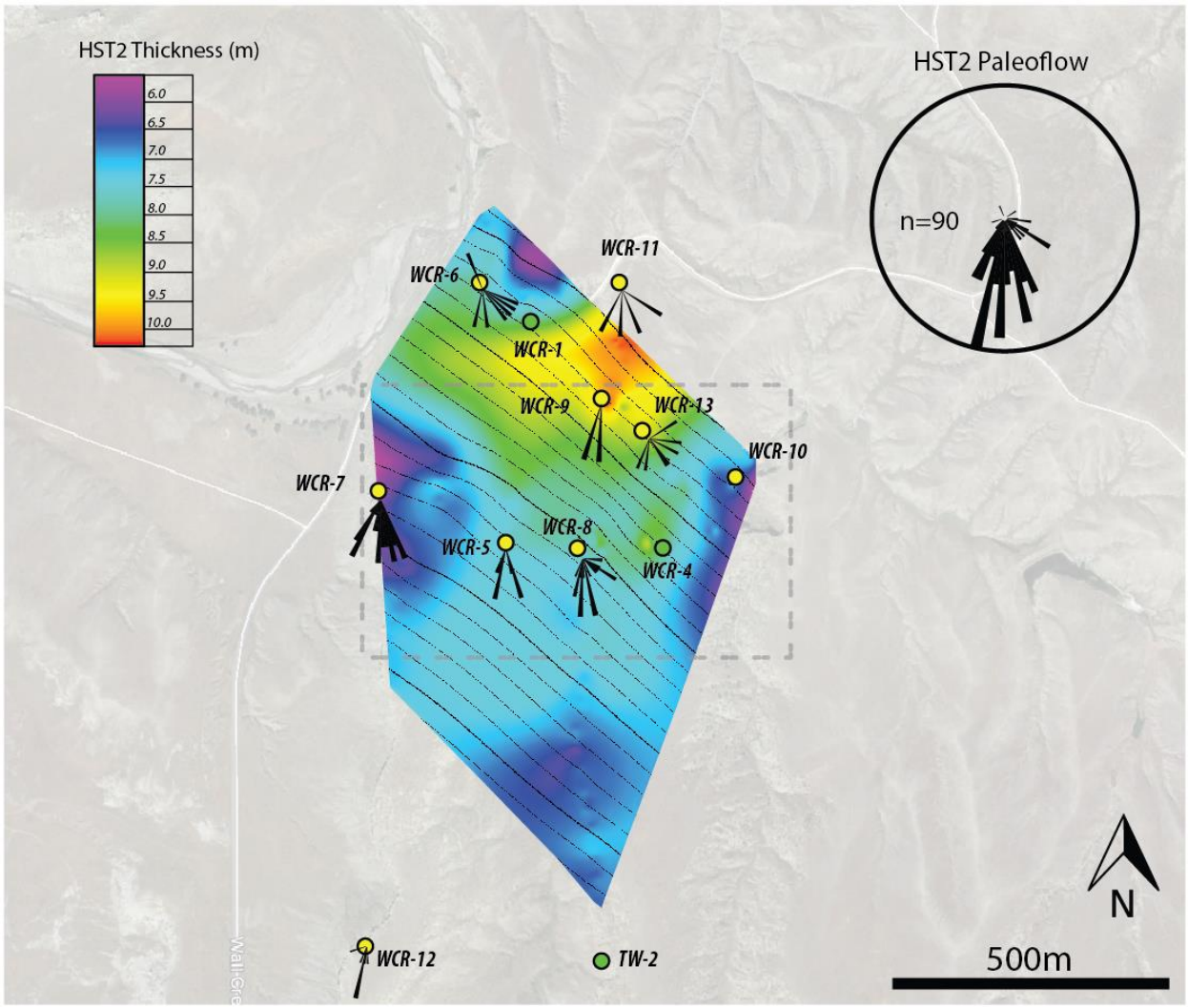

Figure 19: *Isopach of the HST2, interpreted to represent a storm-wave dominated shoreface succession. Note the westward thinning toward WCR-7, similar to the underlying HST1. Additionally, note that depocenter of the HST2 corresponds to the inter-lobe low of the HST`1, demonstrating a compensational stacking pattern. Thinning of the HST2 occurs at the thickest points of deltaic sedimentation. Again, paleoflow data shows a dominantly southerly to southwesterly direction.*

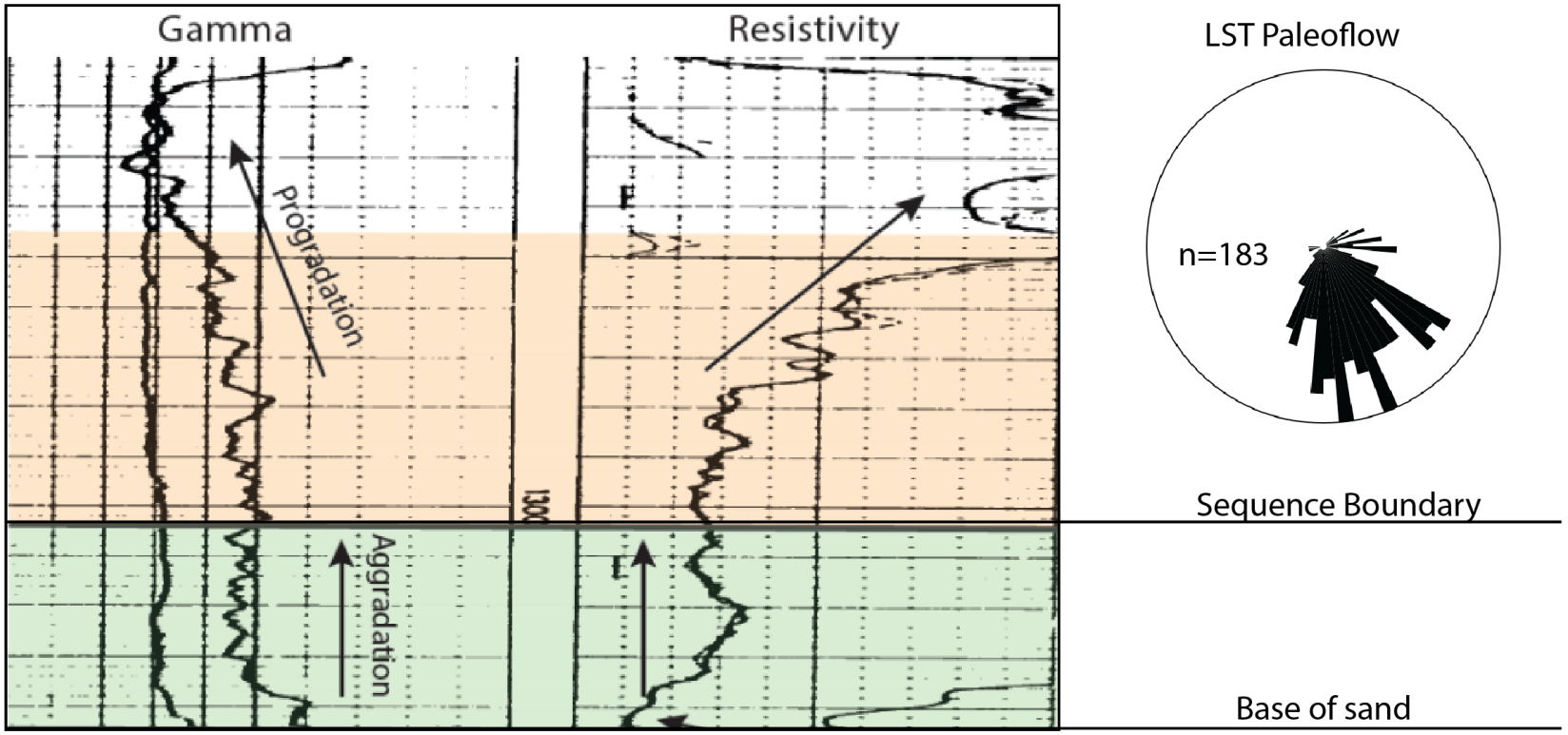

Figure 20: *Lowstand Systems Tract subsurface expression and aggregate paleoflow data. Due to erosion at the surface, the top of the WCM could not be mapped in the field area to produce an isopach. In this figure, note the highly progradational nature of the LST, supporting a regressive deltaic interpretation. The well is taken from Waldo Lynch-Aquitine Oil Company, No. 1 Federal, and annotated figure is modified from Zupanic, 2017.*

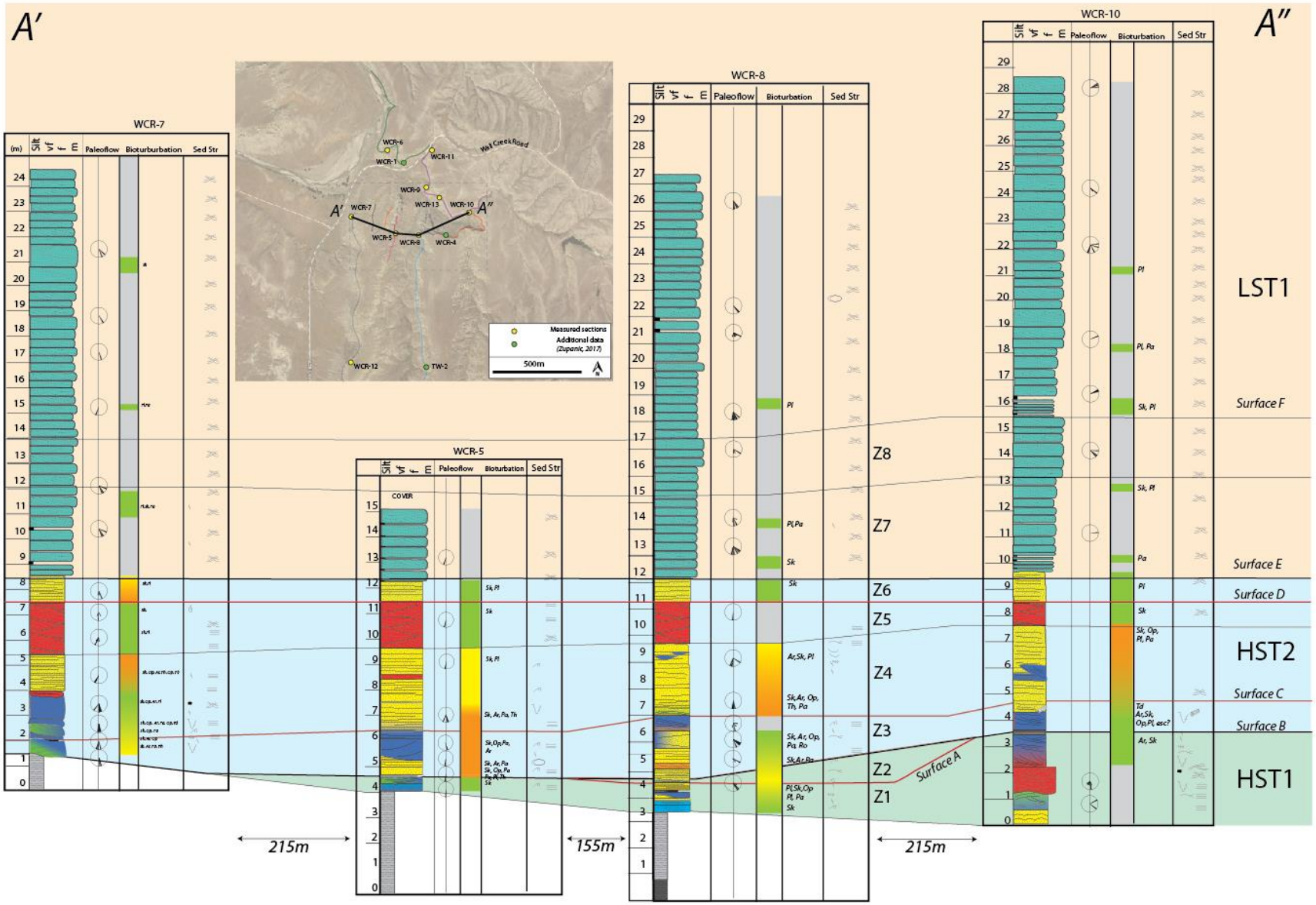

Figure 21: *W-E cross section, showing the 8 geomodel zones (Z1-Z8), divided on the basis of sequence stratigraphic surfaces and regional, intra-parasequence facies transitions. The surfaces and their position within the three systems tracts (HST1, HST2, and LST) are shown.*

Figure 22: *Isopachs of zones 1-4. Note that the colors are not to scale between each map. All values are shown in meters.*

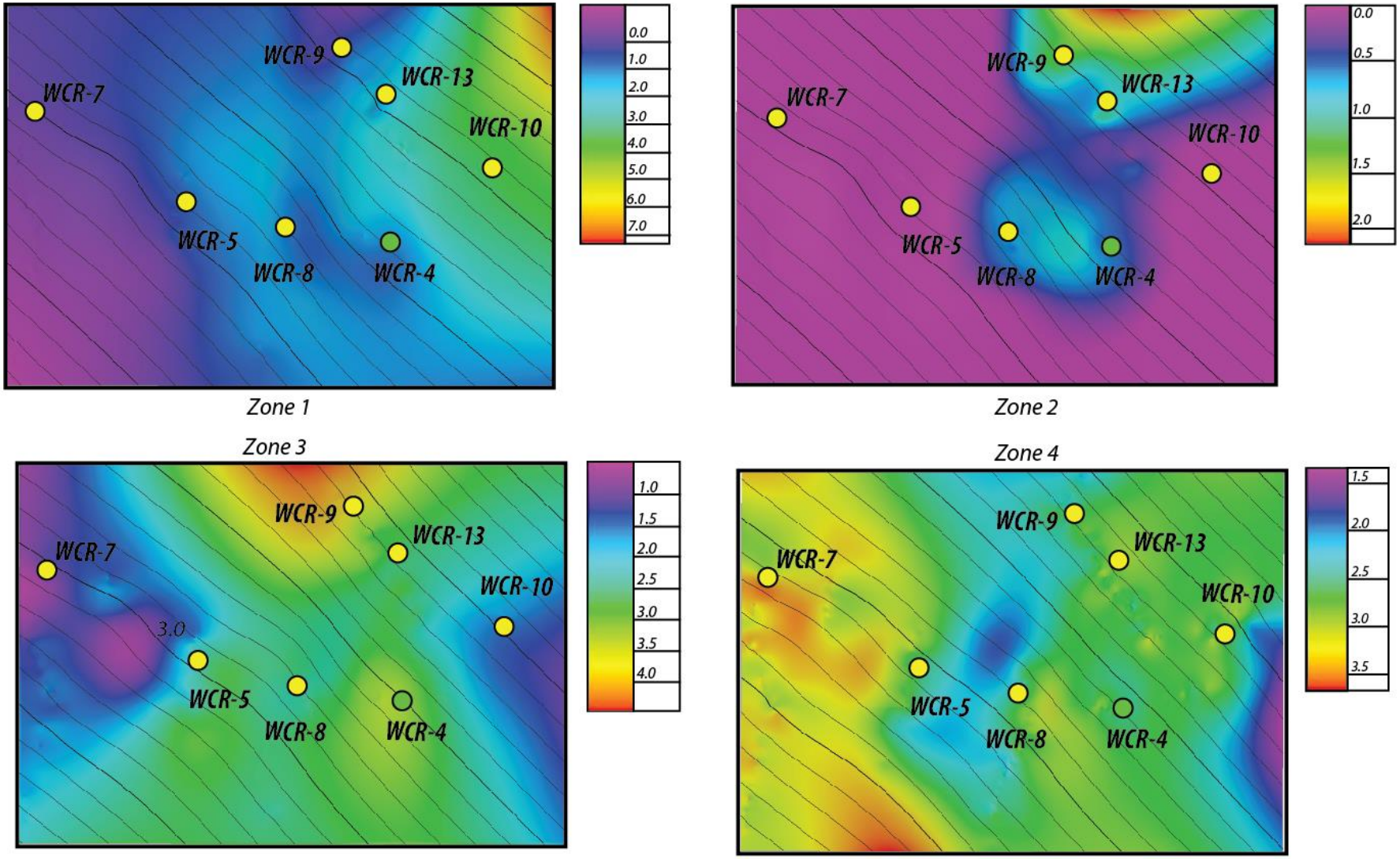

Figure 22 cont.: *Isopachs of zones 5-8. Note that the colors are not to scale between each map. All values are shown in meters. The homogenous zone 8 isopach is present as basal surface of zone 8 is identical to its upper surface, but 2 m lower in all locations.,*

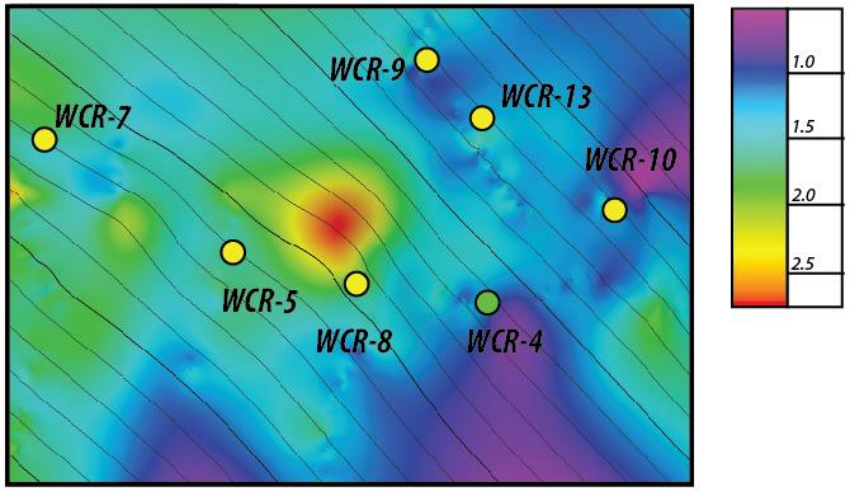

Zone 5

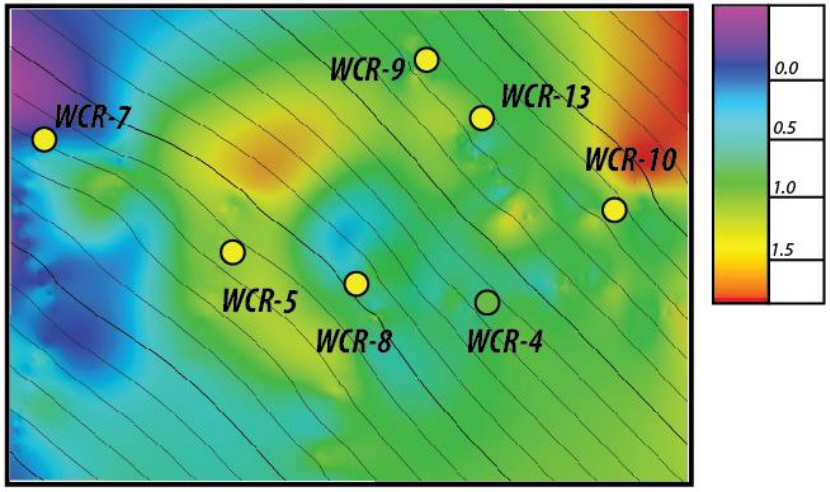

Zone 6

Zone 7

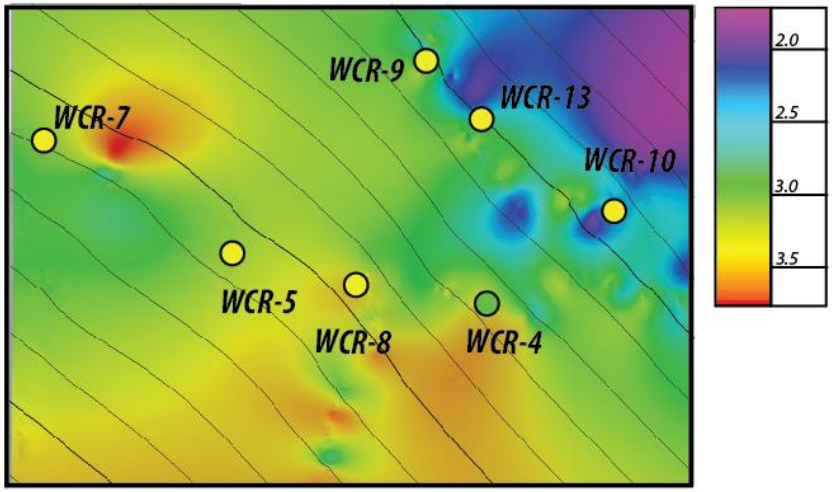

Zone 8

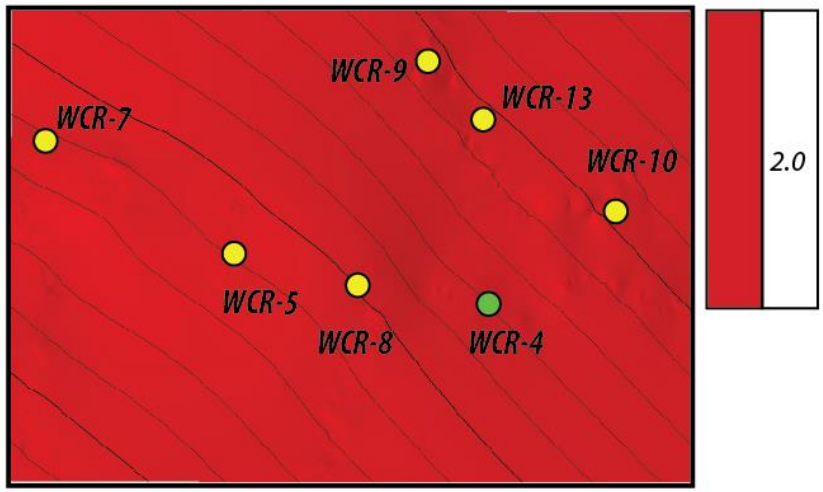

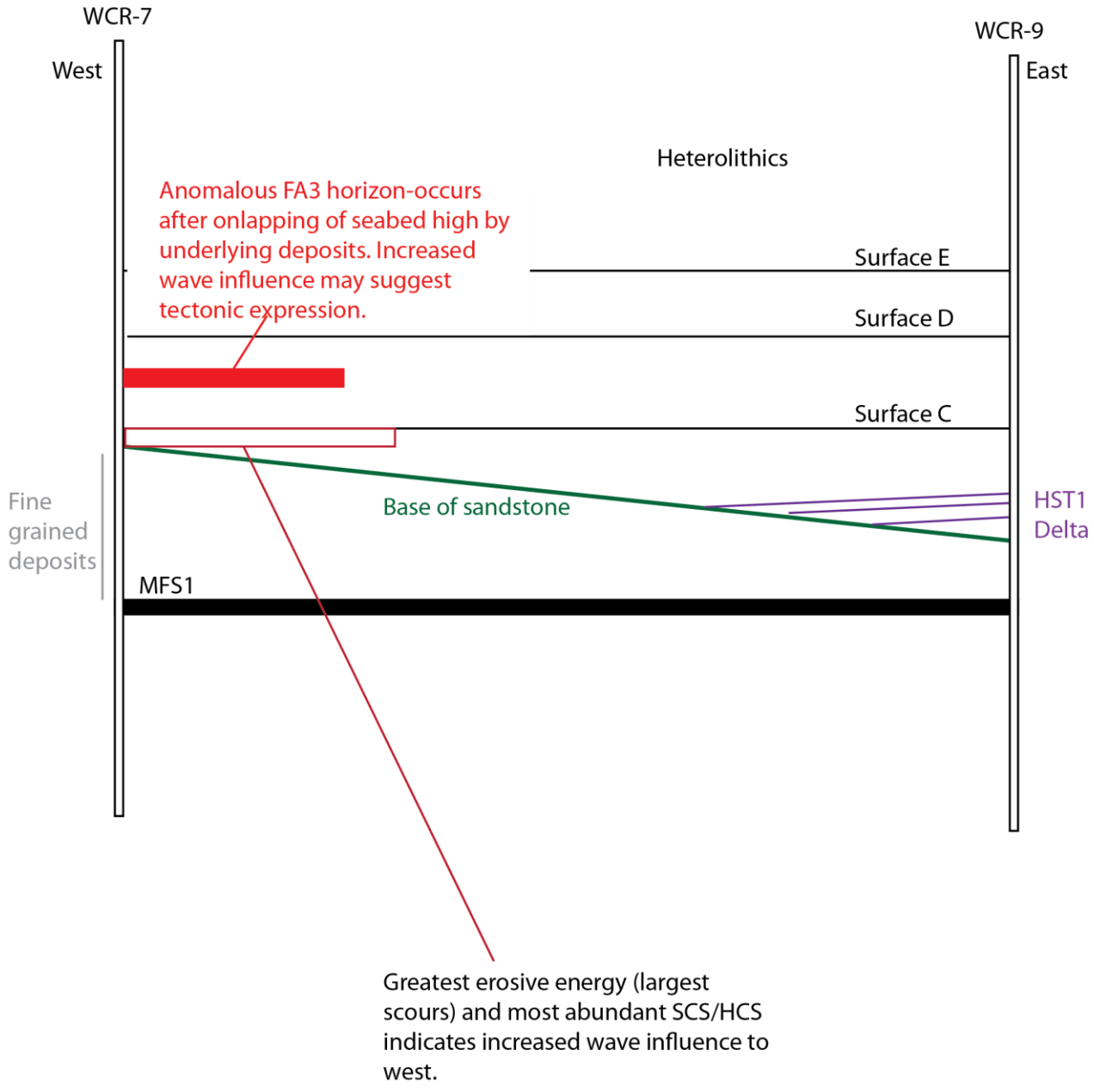

Figure 23: *W-E schematic diagram between WCR-7 and WCR-9. The underlying MFS (Zupanic, 2017) is 2m below the lower contact of the sandstone at WCR-9 and over 5m below the sandstone at WCR-7. A thicker package of sediment overlying this horizon in the west may have reduce the local accommodation space, causing the abrupt pinch-out of the HST1 delta and the HST2-PS1. The anomalous horizon of FA3 within HST2-PS2, as well as the increased storm wave influence associated with the uppermost horizon of the HST2-PS1, are not fully explained by this model. Slight tectonic adjustment may be a possible mechanism for these facies relationships.*

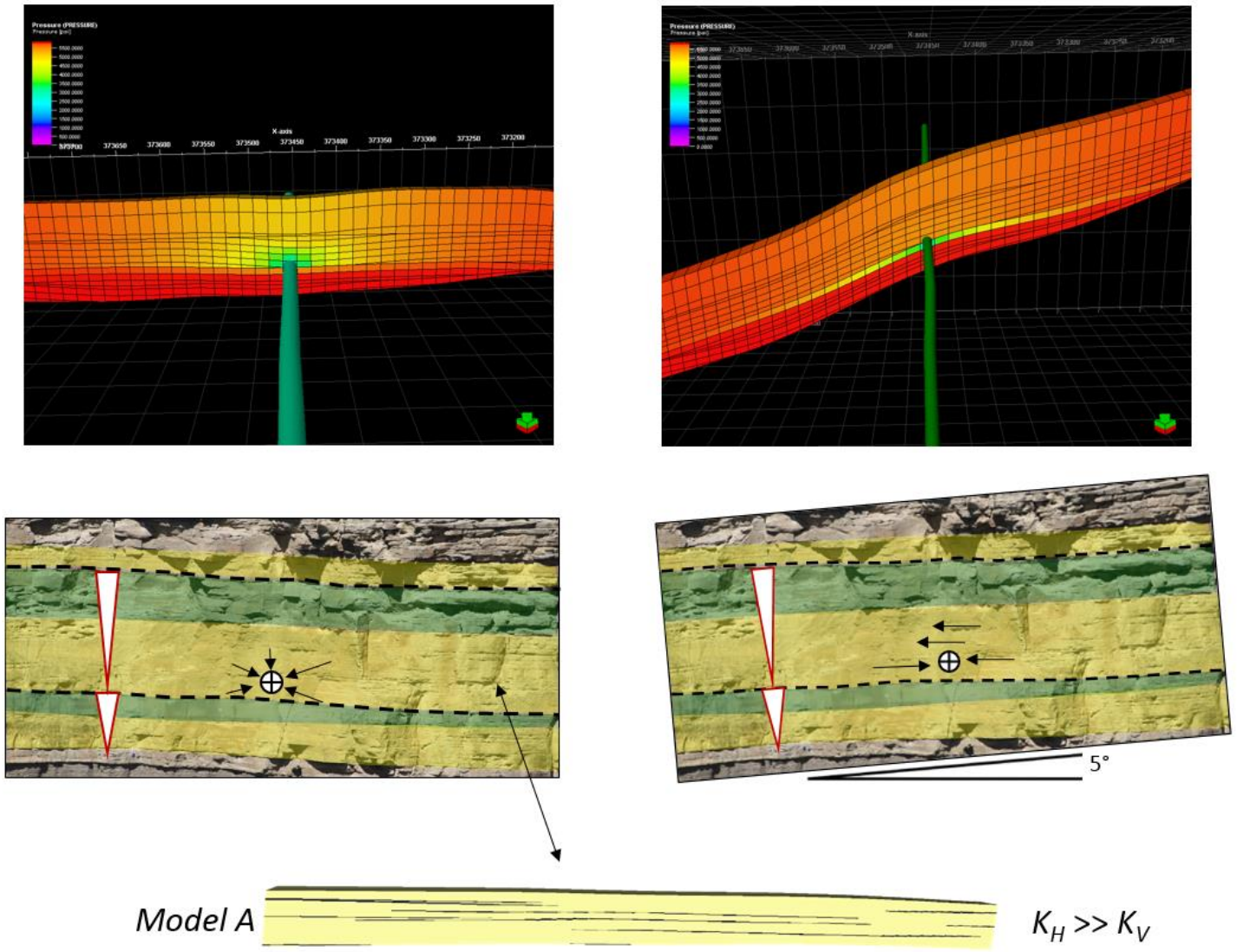

Figure 24: *Pressure distribution at five years around the N-S HST well in the flattened and tilted geomodels. Wave-dominated facies of the lower shoreface (upscaled model A results) are sensitive to minimal structural dip, and gravity drainage is superior to pressure drive in the tilted model example.*

IX. Tables

Table A

Tilted Models

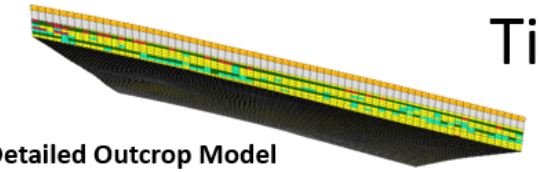

Detailed Outcrop Model

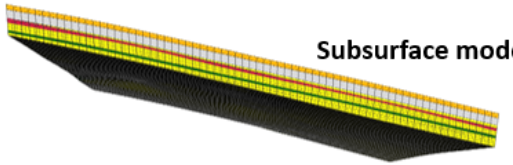

Subsurface model

TM=0 (Thin-bed impermeability); **unfractured** lateral wells

Well orientation	Well placement	
	Upper Horizon (LST)	Lower Horizon (HST)
North-South	21,554 stb	4,372 stb
West-East	22,824 stb	4,677 stb

stb = stock tank barrels at 5 years

TM=0.5 (High transmissibility); **unfractured** laterals

Well orientation	Well placement	
	Upper Horizon (LST)	Lower Horizon (HST)
North-South	38,500 stb (**+78.6%**)	40,051 stb (**+816%**)
West-East	40,620 stb (**+77.9%**)	44,123 stb (**+843%**)

Isotropic, high *K*; **unfractured** lateral wells

Well orientation	Well placement	
	Upper Horizon (LST)	Lower Horizon (HST)
North-South	41,649 stb (**+8.2%**)	39,588 stb (**-1.1%**)
West-East	43,770 stb (**+7.8%**)	41,175 stb (**-6.7%**)

- **Left: TM=0.5 ±** values indicate variation from **TM=0 results**
  - Lower and upper zones not communicating at TM=0
- **Above: Proxy ±** values indicate variation from **TM=0.5 results**
  - Interspersed high energy facies not present in subsurface model

Table B

Lateral wells with fractures

Tilted Models

Well orientation	Well placement TM=0	
	Upper Horizon (LST)	Lower Horizon (HST)
North-South	28,947 stb (+30%)	5,079 stb (+16%)
West-East	33,069 stb (+45%)	10,655 stb (+128%)

Well orientation	Well placement TM=0.5	
	Upper Horizon (LST)	Lower Horizon (HST)
North-South	45,493 stb (+18%)	41,888 stb (+4.5%)
West-East	48,824 stb (+20%)	43,307 stb (-1.8%)

Well orientation	Well placement PROXY	
	Upper Horizon (LST)	Lower Horizon (HST)
North-South	48,726 stb (+17%)	41,600 stb (+5%)
West-East	52,183 stb (+19%)	42,335 stb (+2.8%)

Flattened Models

Well orientation	Well placement TM=0	
	Upper Horizon (LST)	Lower Horizon (HST)
North-South	29,320 stb (+35%)	6,368 stb (+23%)
West-East	34,280 stb (+50%)	7,579 stb (+140%)

Well orientation	Well placement TM=0.5	
	Upper Horizon (LST)	Lower Horizon (HST)
North-South	45,490 stb (+18%)	42,004 stb (+3.8%)
West-East	50,077 stb (+22%)	45,471 stb (+1.6%)

Well orientation	Well placement PROXY	
	Upper Horizon (LST)	Lower Horizon (HST)
North-South	48,672 stb (+17%)	40,779 stb (+2.7%)
West-East	53,473 stb (+21%)	43,244 stb (+3.1%)

± values indicate variation relative to equivalent simulation **without** artificial fractures

- Greatest increase in production for W-E trending wells in HST, at TM=0.

Table C

Flattened Models

Outcrop Model

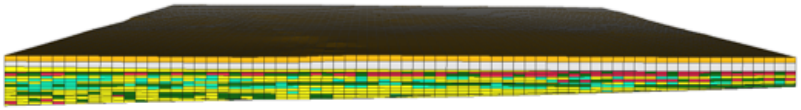

Subsurface Model

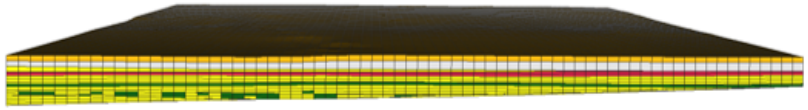

TM=0 (Thin-bed impermeability); **unfractured** lateral wells

Well orientation	Well placement	
	Upper Horizon (LST)	Lower Horizon (HST)
North-South	21,684 stb (**+0.6%**)	5,167 stb (**+18%**)
West-East	22,910 stb (**+0.4%**)	3,152 stb (**-32.6%**)

TM=0.5 (High transmissibility); **unfractured** lateral wells

Well orientation	Well placement	
	Upper Horizon (LST)	Lower Horizon (HST)
North-South	38,562 stb (**+0.2%**)	40,446 stb (**+0.9%**)
West-East	40,899 stb (**-0.6%**)	44,749 stb (**+1.4%**)

Isotropic *K*; **unfractured** lateral wells

Well orientation	Well placement	
	Upper Horizon (LST)	Lower Horizon (HST)
North-South	41,687 stb (**+.09%**)	39,684 stb (**+0.2%**)
West-East	44,092 stb (**+0.7%**)	41,912 stb (**+1.7%**)

- **± values** indicate variation from equivalent structural model results
- Overall, structure has very little impact on fluid flow in the LST
  - **Structure important in HST wells at TM=0**

X. Appendices

Appendix A: Stratigraphic Sections

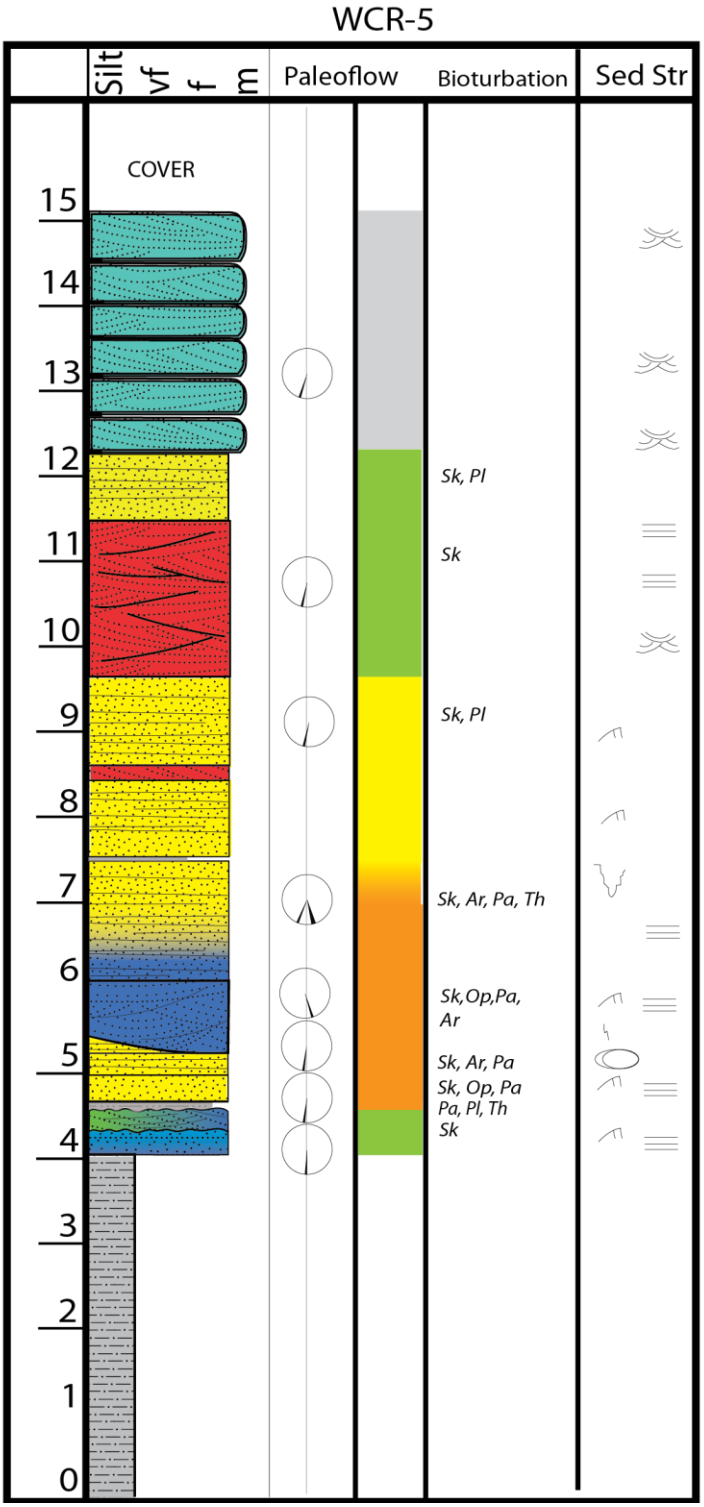

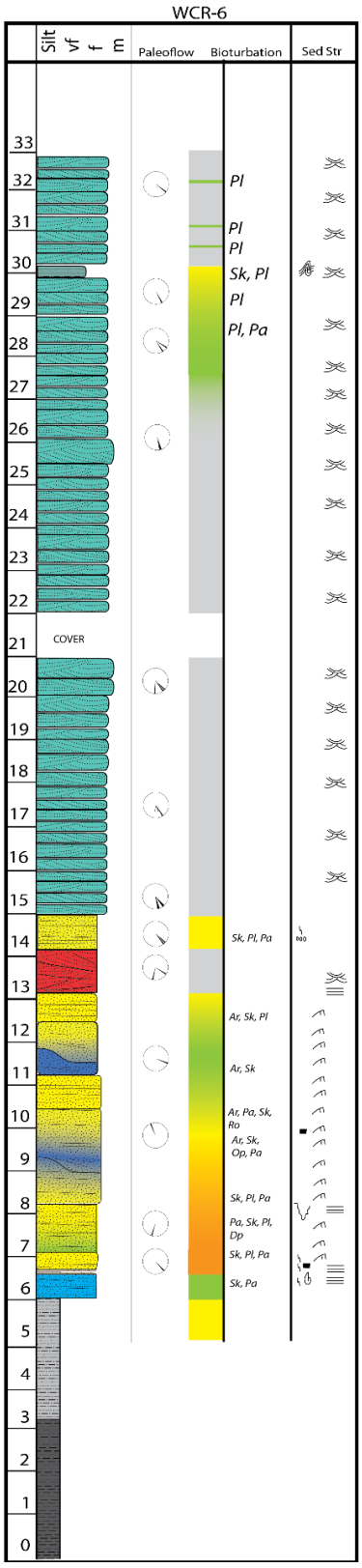
WCR-6
Silt
vf
f
m
Paleoflow
Bioturbation
Sed Str
COVER
Pl
Pl
Pl
Sk, Pl
Pl
Pl, Pa
Sk, Pl, Pa
Ar, Sk, Pl
Ar, Sk
Ar, Pa, Sk, Ro
Ar, Sk, Op, Pa
Sk, Pl, Pa
Pa, Sk, Pl, Dp
Sk, Pl, Pa
Sk, Pa

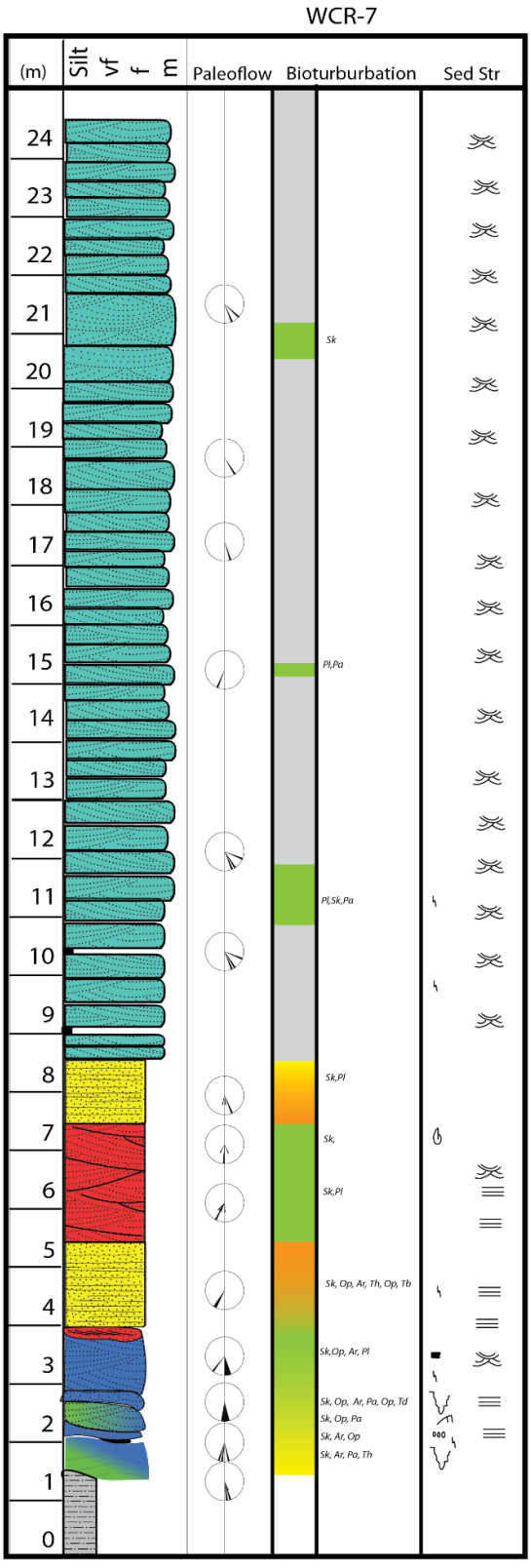
WCR-7
(m)
Silt
vf
f
m
Paleoflow
Bioturburbation
Sed Str
24
23
22
21
20
19
18
17
16
15
14
13
12
11
10
9
8
7
6
5
4
3
2
1
0
Sk
Pl,Pa
Pl,Sk,Pa
Sk,Pl
Sk,
Sk,Pl
Sk, Op, Ar, Th, Op, Tb
Sk,Op, Ar, Pl
Sk, Op, Ar, Pa, Op, Td
Sk, Op, Pa
Sk, Ar, Op
Sk, Ar, Pa, Th

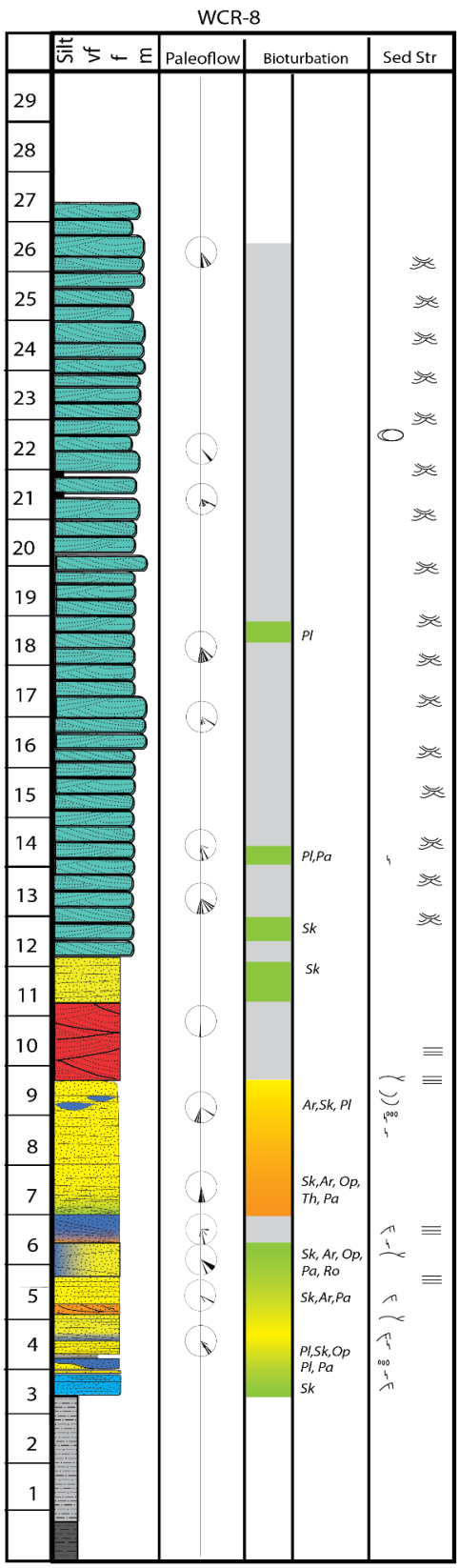
WCR-8
Silt
vf
f
m
Paleoflow
Bioturbation
Sed Str
29
28
27
26
25
24
23
22
21
20
19
18
17
16
15
14
13
12
11
10
9
8
7
6
5
4
3
2
1
Pl
Pl,Pa
Sk
Sk
Ar,Sk, Pl
Sk,Ar, Op,
Th, Pa
Sk, Ar, Op,
Pa, Ro
Sk,Ar,Pa
Pl,Sk,Op
Pl, Pa
Sk

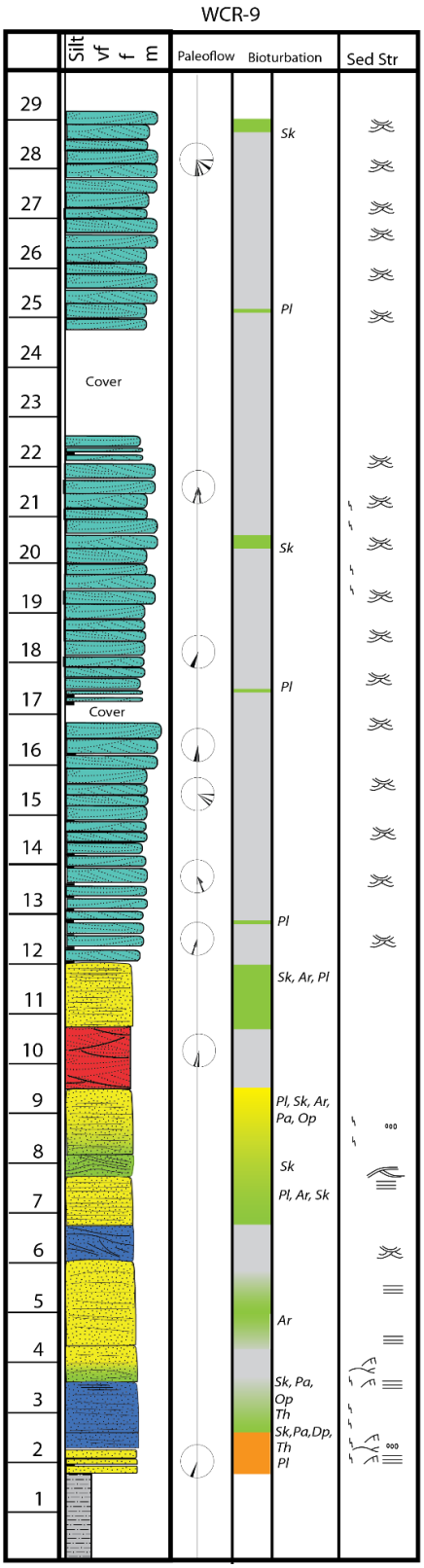
WCR-9
Silt
vf
f
m
Paleoflow
Bioturbation
Sed Str
29
28
27
26
25
24
23
22
21
20
19
18
17
16
15
14
13
12
11
10
9
8
7
6
5
4
3
2
1
Cover
Cover
Sk
Pl
Sk
Pl
Pl
Sk, Ar, Pl
Pl, Sk, Ar, Pa, Op
Sk
Pl, Ar, Sk
Ar
Sk, Pa, Op Th
Sk,Pa,Dp, Th Pl

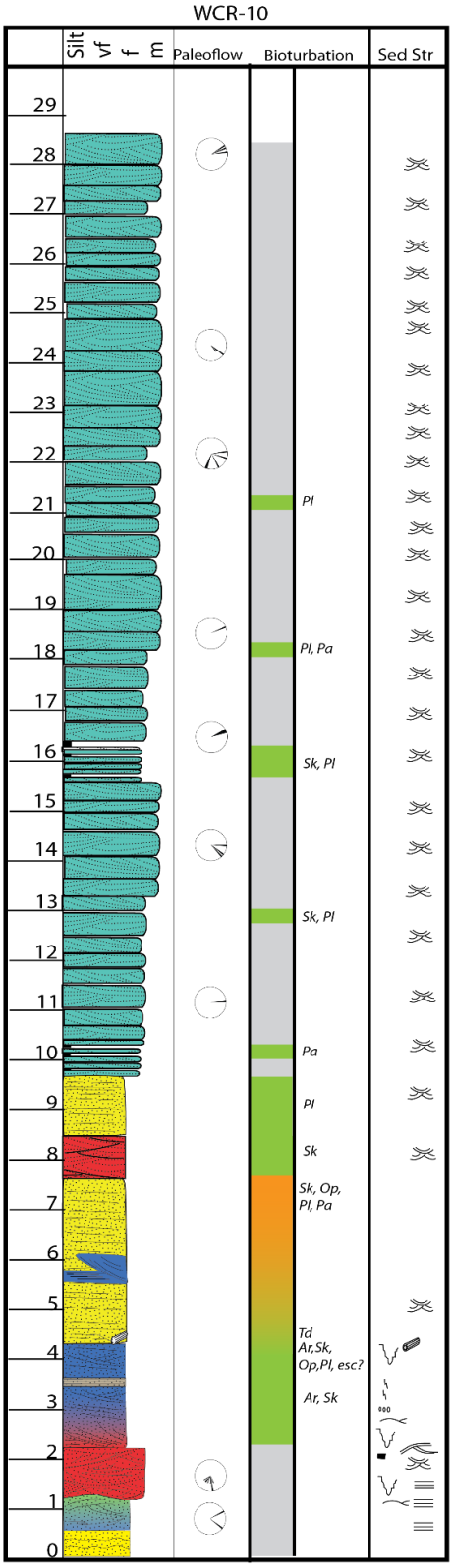
WCR-10
Silt
vf
f
m
Paleoflow
Bioturbation
Sed Str
29
28
27
26
25
24
23
22
21
20
19
18
17
16
15
14
13
12
11
10
9
8
7
6
5
4
3
2
1
0
Pl
Pl, Pa
Sk, Pl
Sk, Pl
Pa
Pl
Sk
Sk, Op, Pl, Pa
Td Ar,Sk, Op,Pl, esc?
Ar, Sk

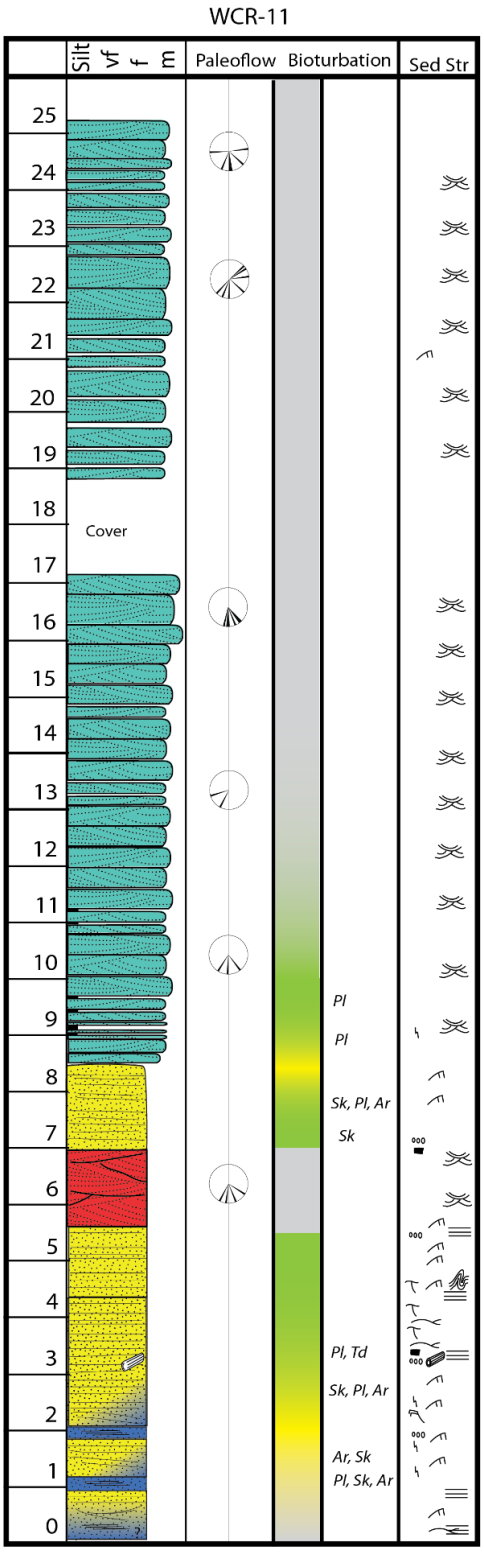
WCR-11
Silt
vf
f
m
Paleoflow
Bioturbation
Sed Str
25
24
23
22
21
20
19
18
17
16
15
14
13
12
11
10
9
8
7
6
5
4
3
2
1
0
Cover
Pl
Pl
Sk, Pl, Ar
Sk
Pl, Td
Sk, Pl, Ar
Ar, Sk
Pl, Sk, Ar

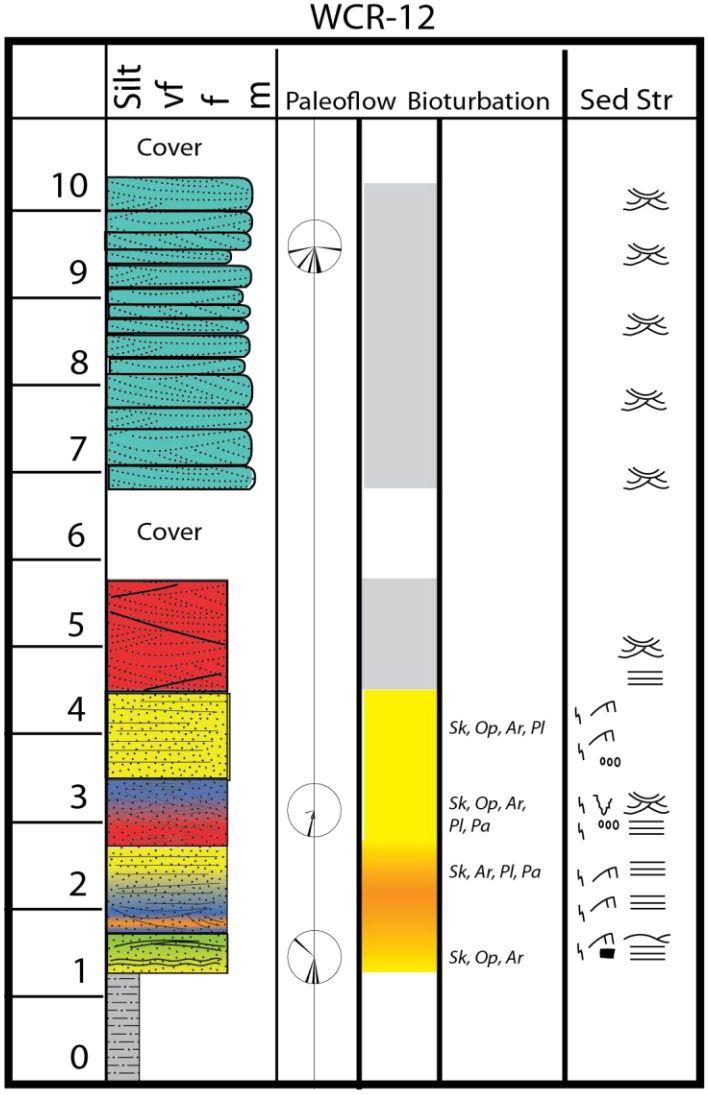
WCR-12
Silt
vf
f
m
Paleoflow
Bioturbation
Sed Str
Cover
10
9
8
7
6
Cover
5
4
3
2
1
0
Sk, Op, Ar, Pl
Sk, Op, Ar, Pl, Pa
Sk, Ar, Pl, Pa
Sk, Op, Ar

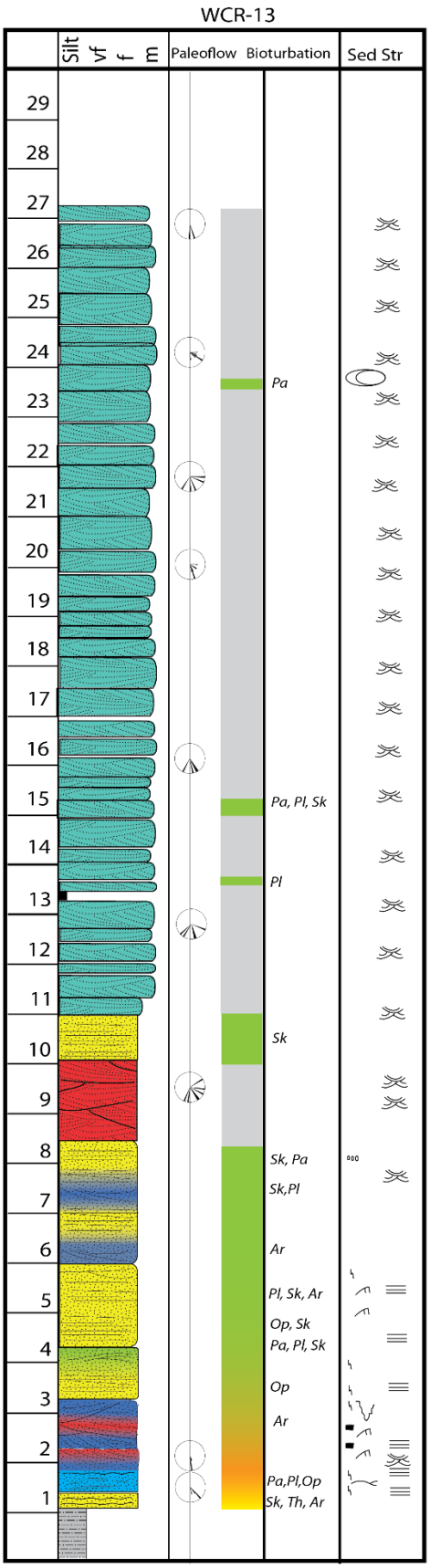
WCR-13
Silt
vf
f
m
Paleoflow
Bioturbation
Sed Str
29
28
27
26
25
24
23
22
21
20
19
18
17
16
15
14
13
12
11
10
9
8
7
6
5
4
3
2
1
Pa
Pa, Pl, Sk
Pl
Sk
Sk, Pa
Sk,Pl
Ar
Pl, Sk, Ar
Op, Sk
Pa, Pl, Sk
Op
Ar
Pa,Pl,Op
Sk, Th, Ar

Appendix B: Ground Control Points

Outcrop	GCP#	X	Y	Z	X Error	Y Error	Z Error
A	1	373455.4	4829448	1440.821	0.353237	-0.723563	-0.011209
	2	373409.1	4829426	1435.502	-0.353237	0.723563	0.011209
B	3	373695.5	4829093	1447.855	0.035528	-0.312325	0.006903
	4	373717.2	4829084	1437.866	0.08568	-0.243176	0.006283
	5	373727.9	4829101	1437.889	0.045621	-0.221298	-0.101354
	6	373622.1	4829106	1440.862	0.098357	-0.747546	0.002479
	7	373565.1	4829190	1439.97	0.12132	-0.034812	0.088006
	8	373545.8	4829296	1439.609	0.146799	0.372675	0.010869
	9	373533	4829396	1437.891	-0.533216	1.186481	-0.013187
C	10	373131	4829164	1471.477	0.167309	-0.157434	0.825606
	11	373120.3	4829120	1475.285	0.467851	-0.433548	-1.119516
	12	373134.3	4829021	1480.944	1.185716	0.2817	0.3215
	13	373130.4	4828934	1488.079	1.397847	0.517319	-0.941907
	14	373131.6	4829157	1483.271	-1.529119	-0.202218	0.76744
	15	373126.6	4829112	1490.72	-1.66501	-0.505877	0.16433
	16	373136.1	4828941	1495.868	-0.024594	0.500022	-0.049557
D	17	373218.7	4829128	1470.756	-0.178984	0.045878	-0.037411
	18	373231.4	4829189	1462.082	-0.10614	-0.17277	0.518903
	19	373229.2	4829176	1463.456	-0.154907	-0.295119	0.395372
	20	373211.1	4829140	1481.236	0.14497	0.028729	0.083325
	21	373218.6	4829182	1479.572	0.303659	-0.127419	0.453302
	22	373221.5	4829095	1476.752	0.063662	0.289818	-0.594038
	23	373230.4	4829074	1471.874	0.067944	0.353093	-0.901754
	24	373207.2	4829127	1481.521	-0.140203	-0.12221	0.082302
E	25	373306.2	4829147	1470.475	-0.41059	2.102811	0.3307
	26	373327.2	4829179	1468.398	-0.307507	0.588255	-0.134864
	27	373357	4829199	1469.04	3.752695	-6.634395	-1.002027
	28	373288.6	4829137	1463.14	-1.919608	1.958825	0.841234
	29	373314.1	4829168	1461.1	-1.098385	1.205669	0.375561
	30	373349.2	4829214	1454.71	-0.204046	0.437026	-0.342458
	31	373354.9	4829231	1453.13	0.187442	0.341809	-0.068145
F	32	373271	4828894	1493.623	1.648648	2.971353	-0.153608
	33	373310.5	4828979	1480.263	0.659244	1.363821	0.224736
	34	373318.7	4829019	1481.456	-0.00251	0.373971	-0.116245

	35	373325	48290661	1479.173	-0.495138	-0.79699	-0.371248
	36	373341.7	4829107	1479.477	-1.097857	-1.938124	-0.589498
	37	373317.8	4828996	1472.341	0.542919	1.113095	0.342881
	38	373323.4	4829042	1467.623	0.075956	-0.185112	0.112072
	39	373367	4829126	1457.807	-1.332363	-2.902013	0.55091
G	40	373472.5	4829031	1458.284	-1.134605	0.308153	-0.219578
	41	373478.4	4828979	1463.145	-0.5973	-0.0751	-0.185123
	42	373438.6	4828881	1473.4	0.1663	-0.410519	0.27876
	43	373416	4828727	1478.96	0.947786	0.452059	0.128178
	44	373487.6	4828995	1483.13	-0.357042	-0.00404	-0.138499
	45	373437.6	4828865	1489.52	1.045698	-0.18442	0.149976
	46	373481.3	4828945	1479.47	-0.07	-0.086036	-0.013714
H	47	373774.4	4829076	1446.421	-0.643149	-0.1684	0.045609
	48	373796.7	4829050	1453.128	-0.474642	0.045989	0.350217
	49	373800.1	4828992	1445.578	-0.14317	0.230494	-0.07115
	50	373733.6	4829009	1448.236	0.041044	-0.053675	0.002115
	51	373672.9	4829010	1446.379	0.14886	-0.272947	-0.2724
	52	373580.7	4828992	1456.093	1.071057	0.21854	-0.786776
				Average Error (m)	0.5748	0.7126	0.3095
	Average Error with outcrop "E" omitted (m)				**0.4852**	**0.52**	**0.2879**

Appendix C: Outcrop facies diagrams

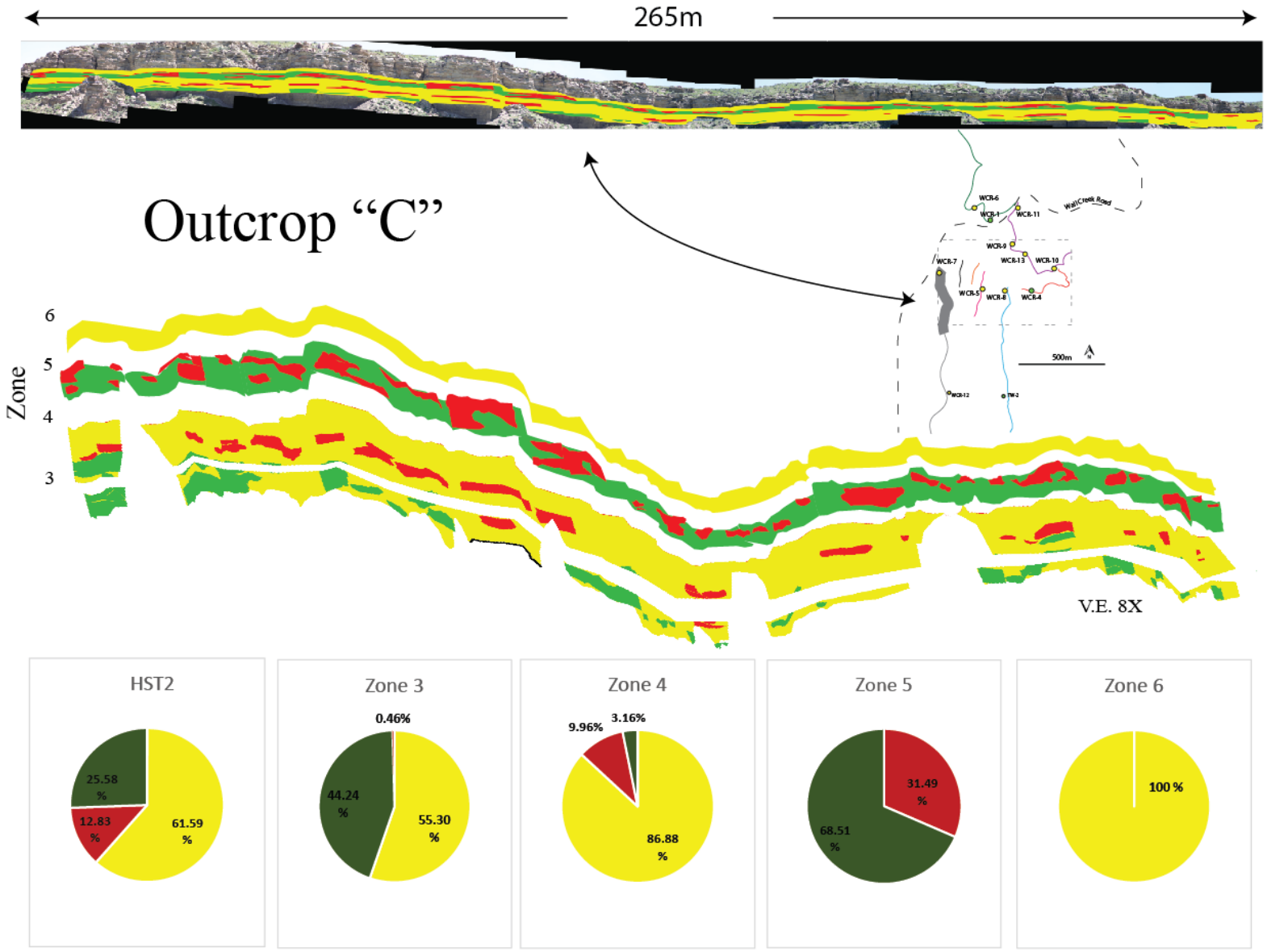

Outcrop “ D”

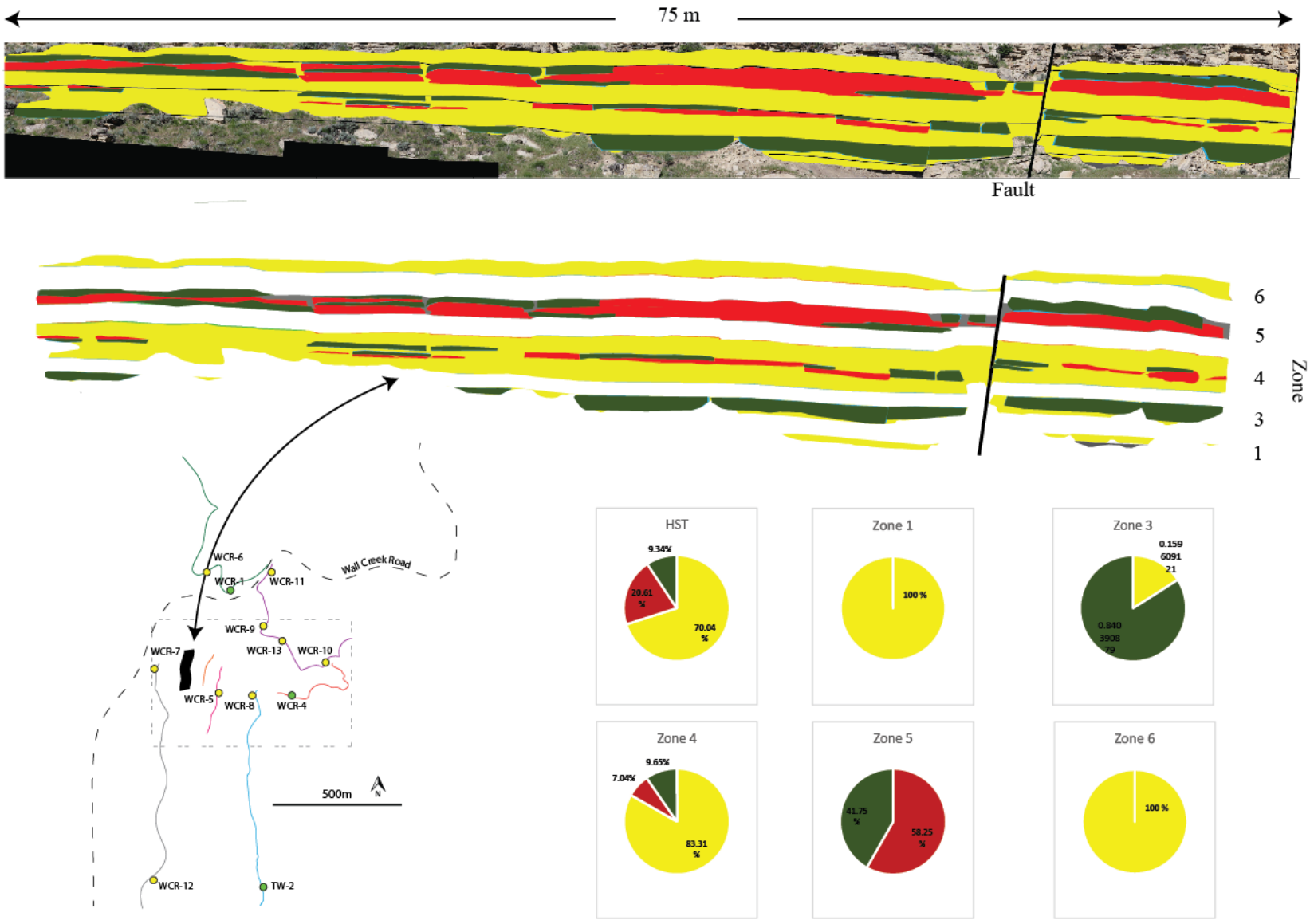
75 m
Fault
6
5
4
3
1
Zone
WCR-6
WCR-1
WCR-11
Wall Creek Road
WCR-9
WCR-13
WCR-10
WCR-7
WCR-5
WCR-8
WCR-4
500m
WCR-12
TW-2
HST
9.34%
20.61 %
70.04 %
Zone 1
100 %
Zone 3
0.159
6091
21
0.840
3908
79
Zone 4
9.65%
7.04%
83.31 %
Zone 5
41.75 %
58.25 %
Zone 6
100 %

Outcrop “ F”

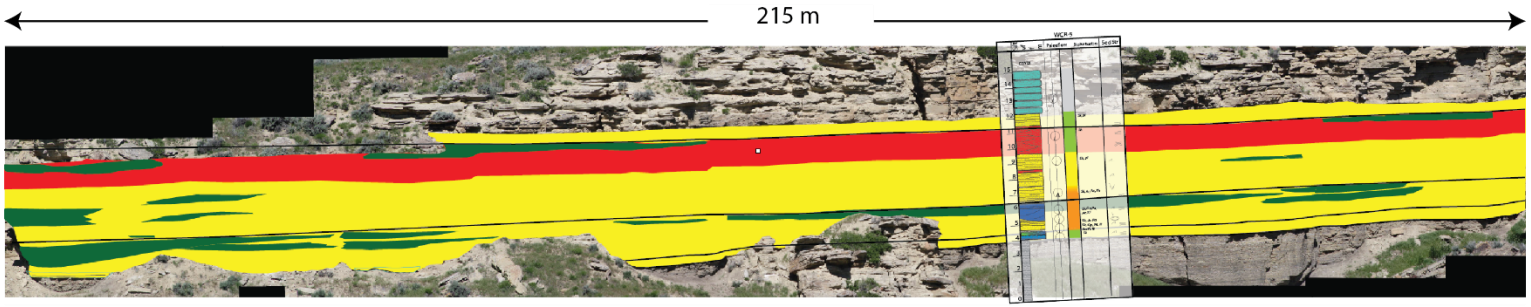
215 m


6
5
4
3
1
Zones

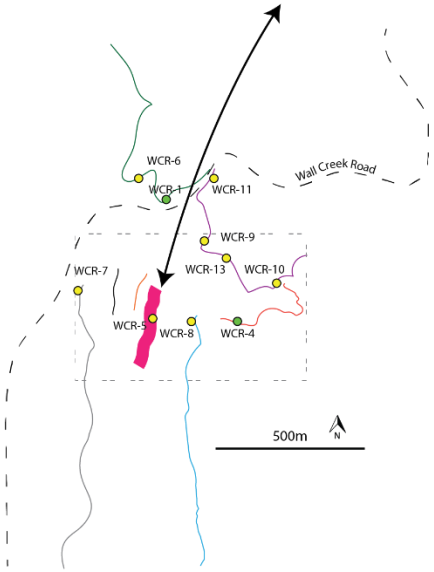
WCR-6
WCR-1
WCR-11
Wall Creek Road
WCR-9
WCR-7
WCR-13
WCR-10
WCR-5
WCR-8
WCR-4
500m
N

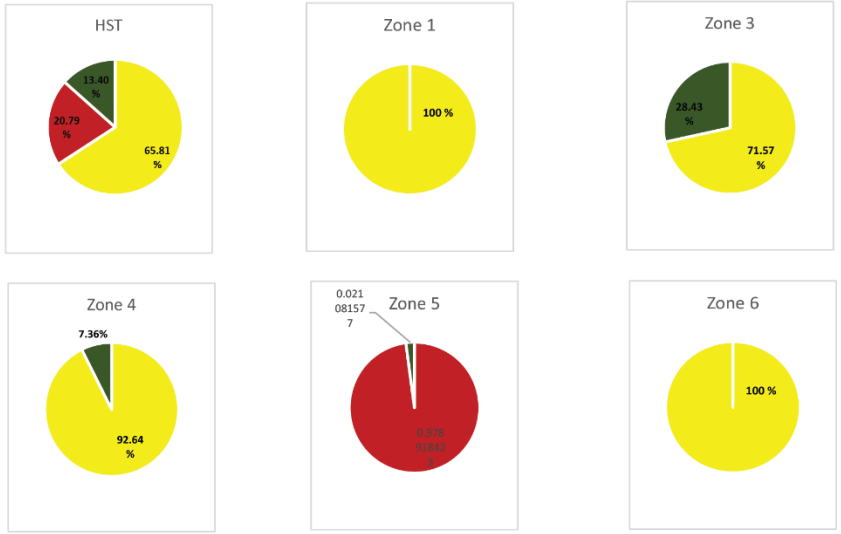
HST
13.40 %
20.79 %
65.81 %
Zone 1
100 %
Zone 3
28.43 %
71.57 %
Zone 4
7.36%
92.64 %
Zone 5
0.021 08157 7
0.978 91842 3
Zone 6
100 %

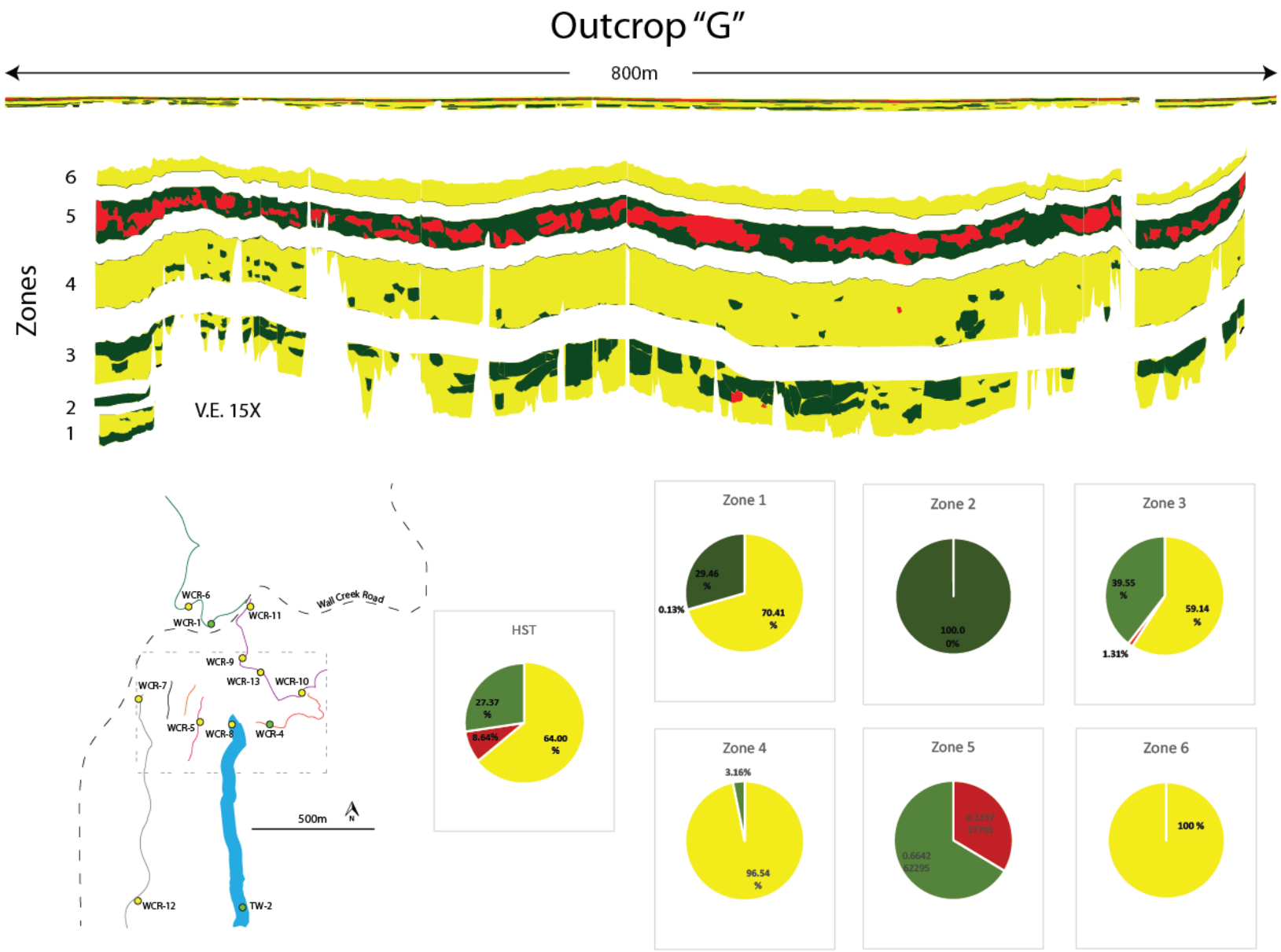
Outcrop "G"
800m
Zones
6
5
4
3
2
1
V.E. 15X
WCR-6
WCR-1
WCR-11
Wall Creek Road
WCR-9
WCR-13
WCR-10
WCR-7
WCR-5
WCR-8
WCR-4
500m
N
WCR-12
TW-2
HST
27.37 %
8.64%
64.00 %
Zone 1
29.46 %
0.13%
70.41 %
Zone 2
100.0
0%
Zone 3
39.55 %
1.31%
59.14 %
Zone 4
3.16%
96.54 %
Zone 5
0.3357
37705
0.6642
62295
Zone 6
100 %

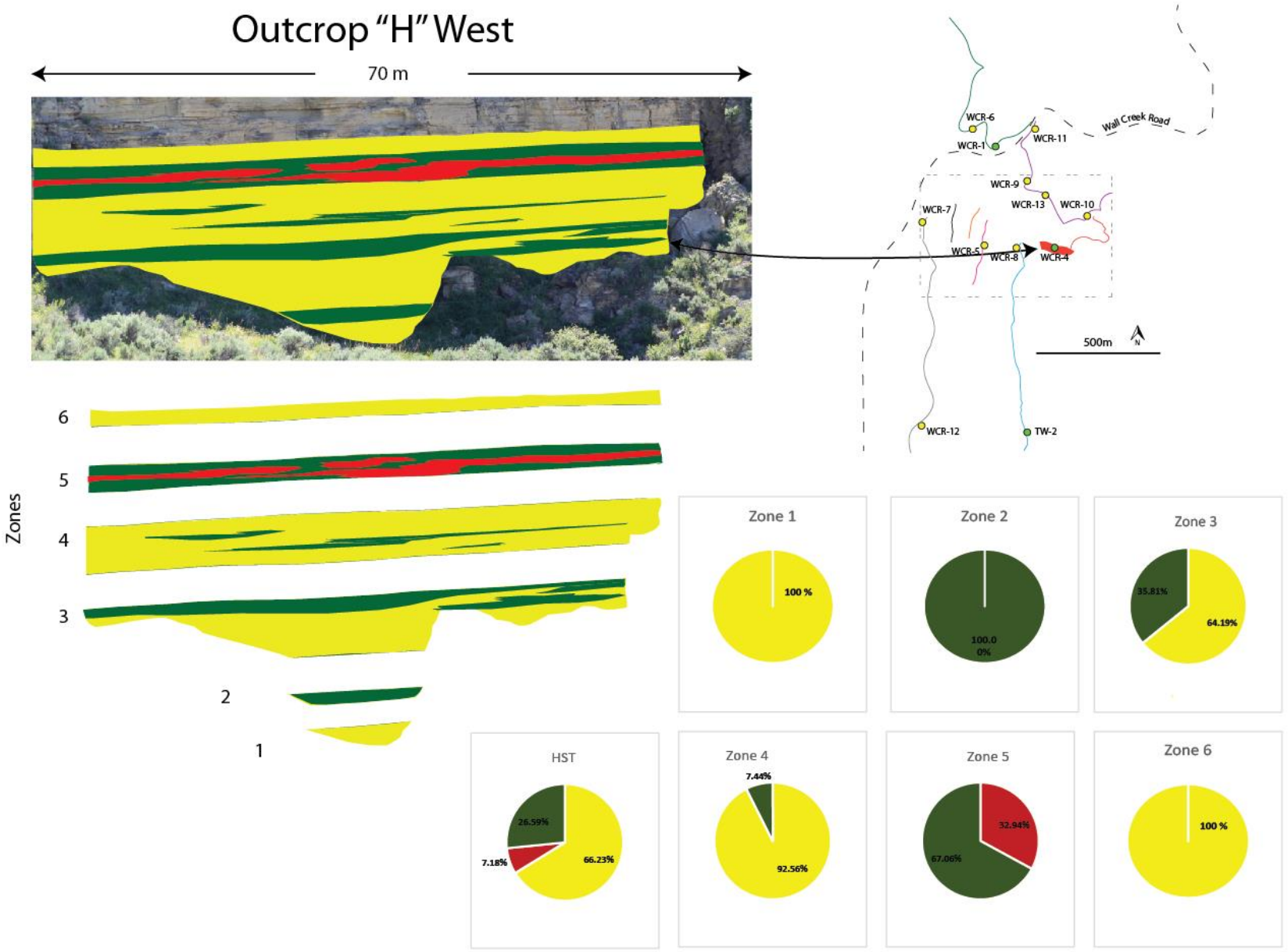
Outcrop "H" West
70 m
WCR-6
WCR-1
WCR-11
Wall Creek Road
WCR-9
WCR-13
WCR-10
WCR-7
WCR-5
WCR-8
WCR-4
500m
WCR-12
TW-2
Zones
6
5
4
3
2
1
Zone 1
100 %
Zone 2
100.0
0%
Zone 3
35.81%
64.19%
HST
26.59%
7.18%
66.23%
Zone 4
7.44%
92.56%
Zone 5
32.94%
67.06%
Zone 6
100 %

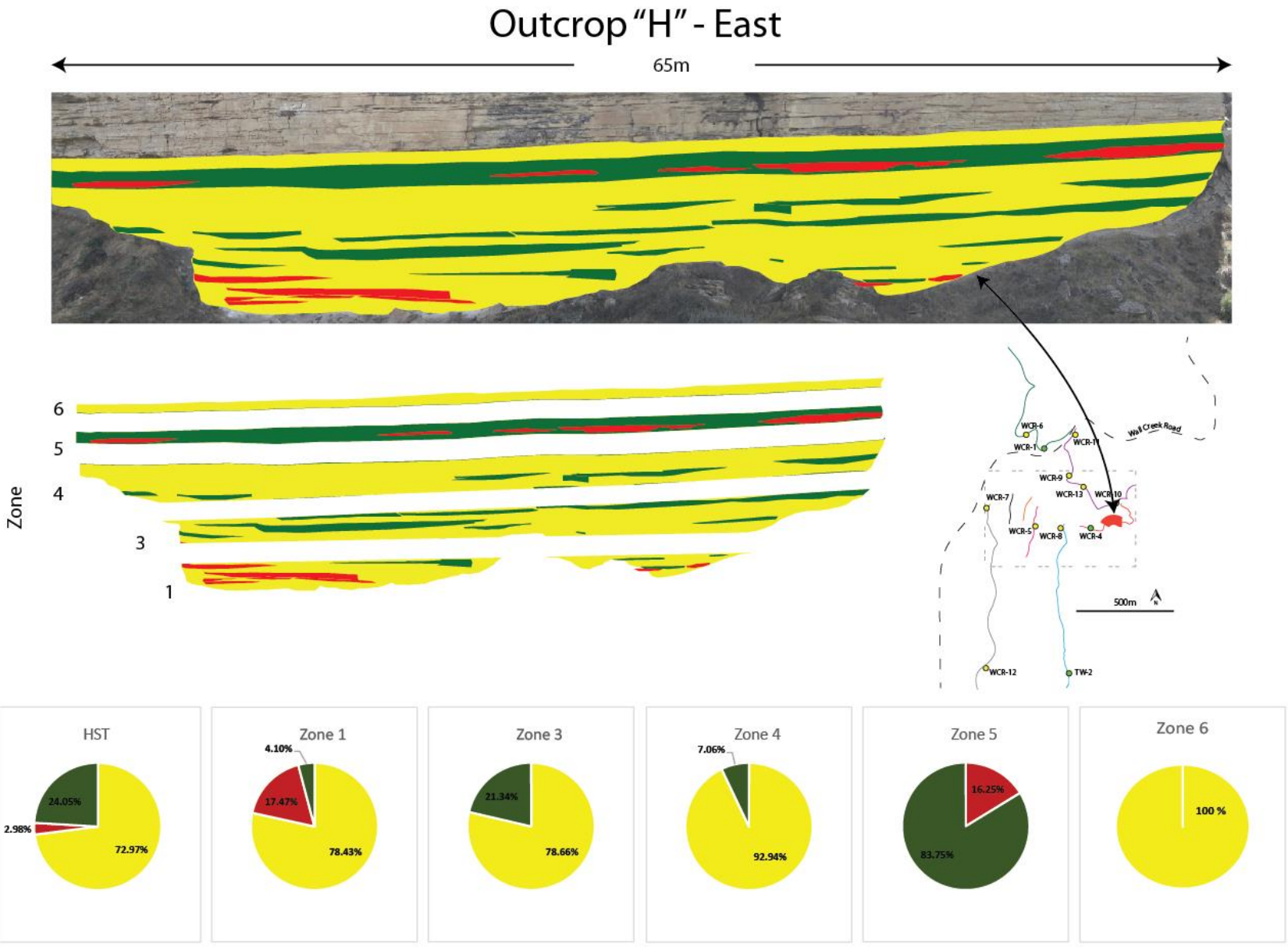
Outcrop "H" - East
65m
Zone
6
5
4
3
1
WCR-6
WCR-1
WCR-11
Wall Creek Road
WCR-9
WCR-13
WCR-10
WCR-7
WCR-5
WCR-8
WCR-4
500m
WCR-12
TW-2
HST
24.05%
2.98%
72.97%
Zone 1
4.10%
17.47%
78.43%
Zone 3
21.34%
78.66%
Zone 4
7.06%
92.94%
Zone 5
16.25%
83.75%
Zone 6
100 %

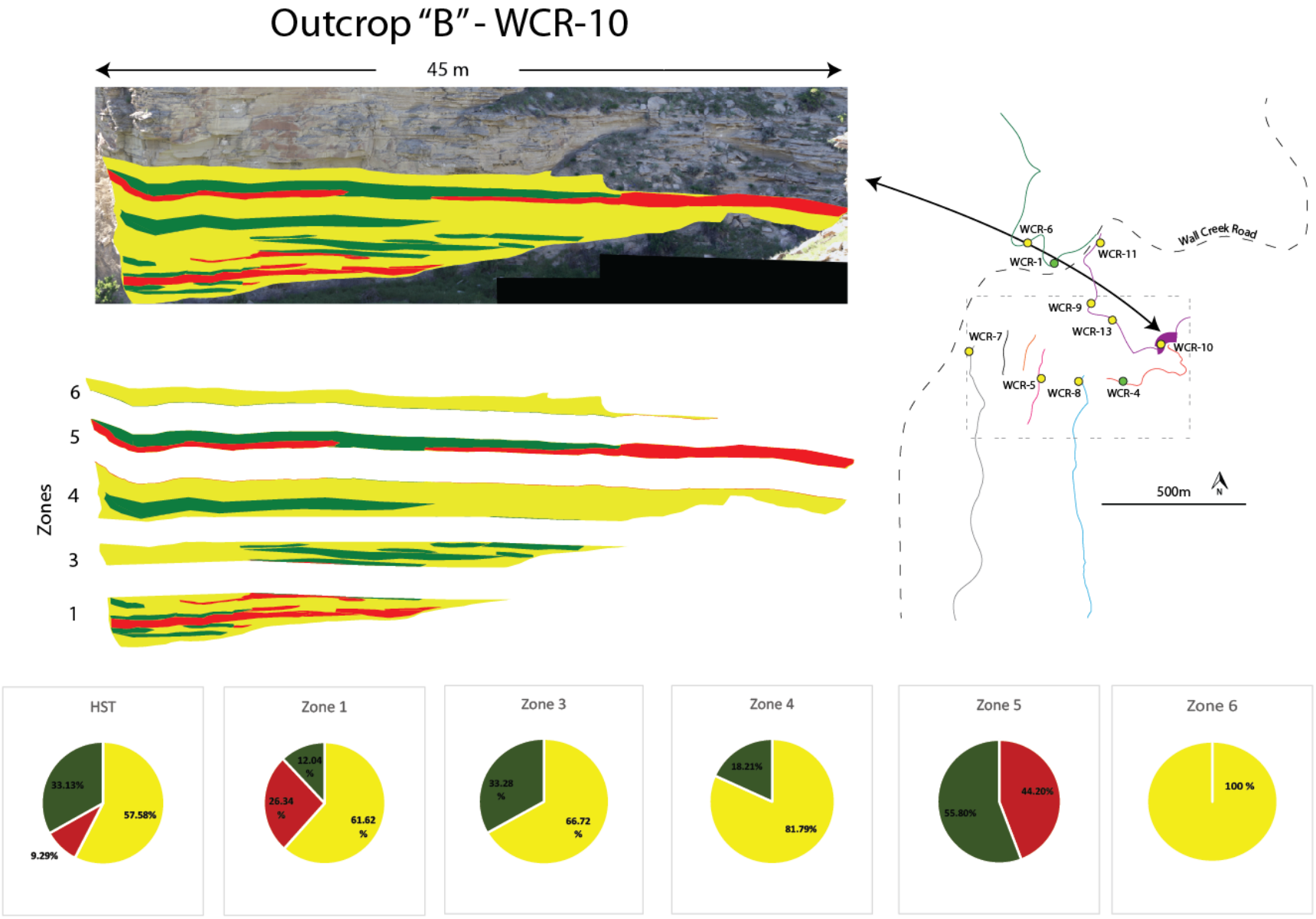
Outcrop "B" - WCR-10
45 m
Zones
6
5
4
3
1
WCR-6
WCR-1
WCR-11
Wall Creek Road
WCR-9
WCR-13
WCR-7
WCR-10
WCR-5
WCR-8
WCR-4
500m
N
HST
33.13%
57.58%
9.29%
Zone 1
12.04 %
26.34 %
61.62 %
Zone 3
33.28 %
66.72 %
Zone 4
18.21%
81.79%
Zone 5
55.80%
44.20%
Zone 6
100 %

Outcrop "B" - South

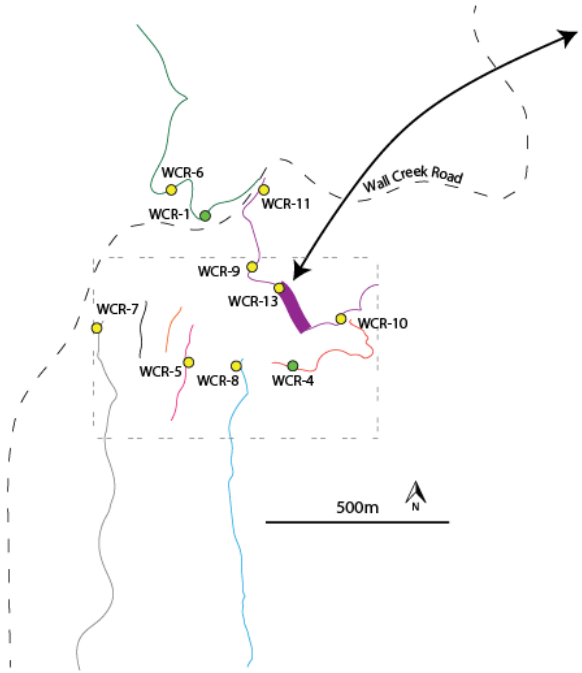

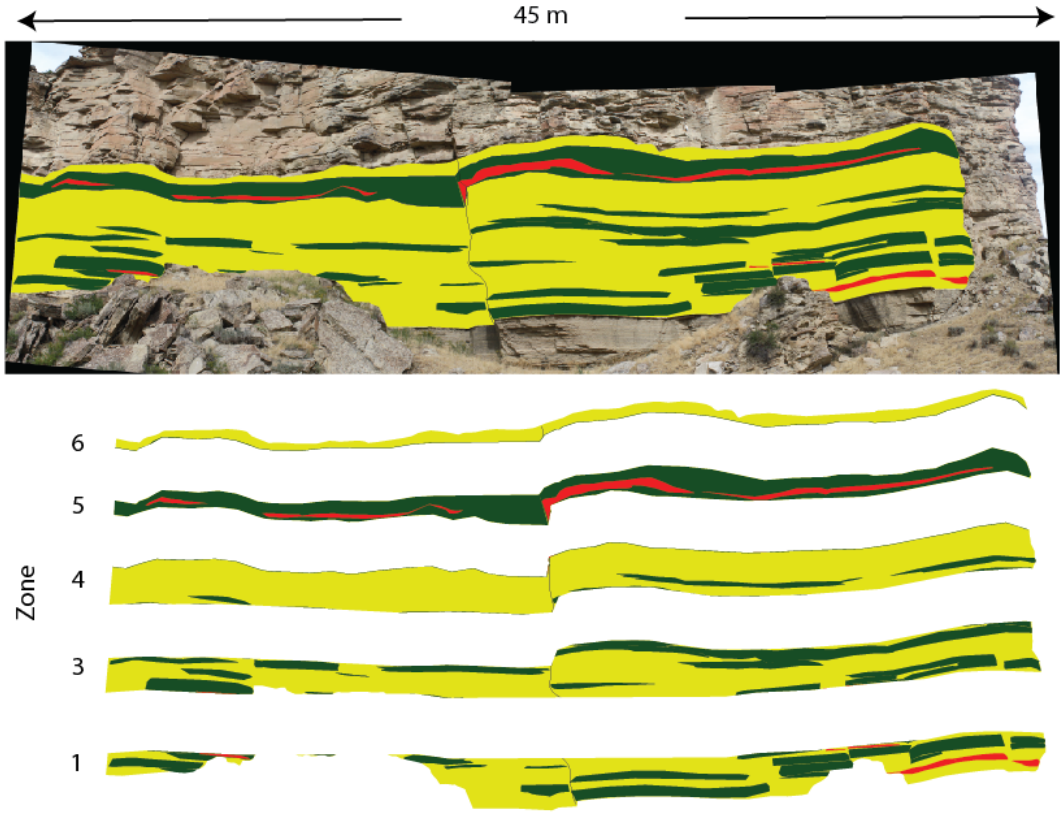

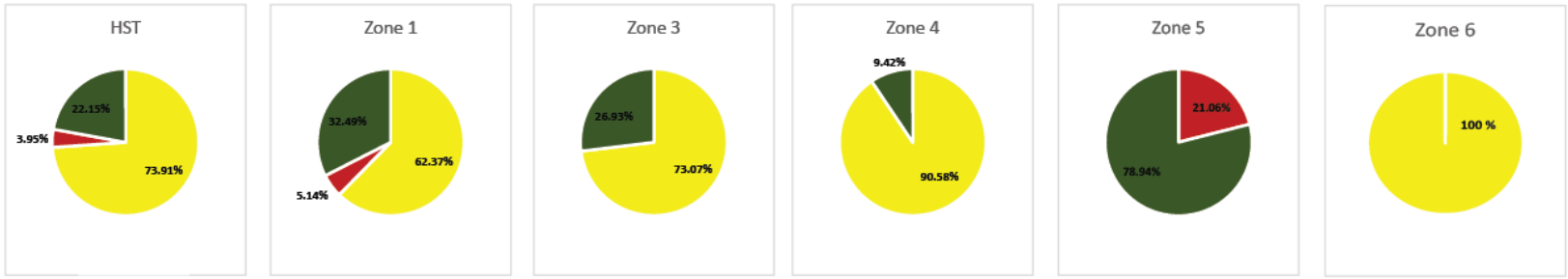

Outcrop "B" - North

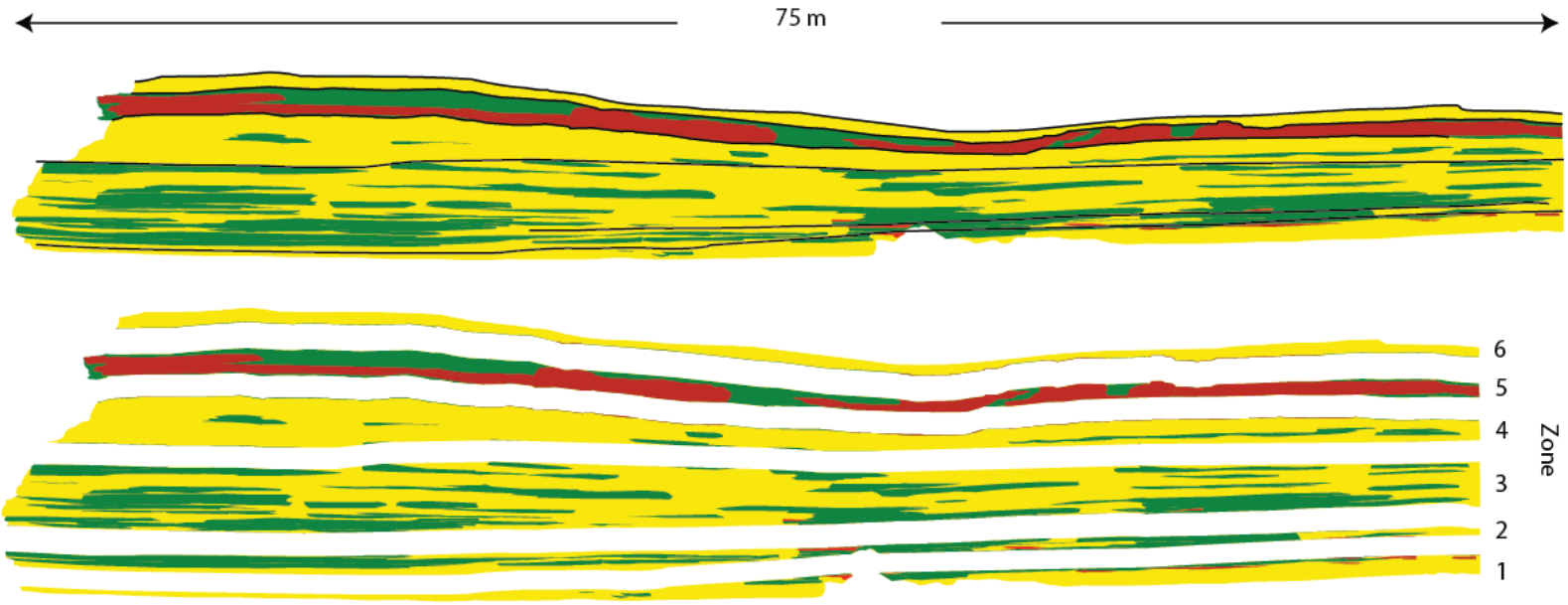

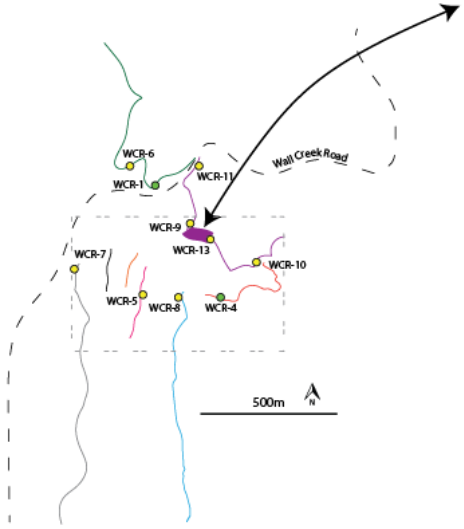

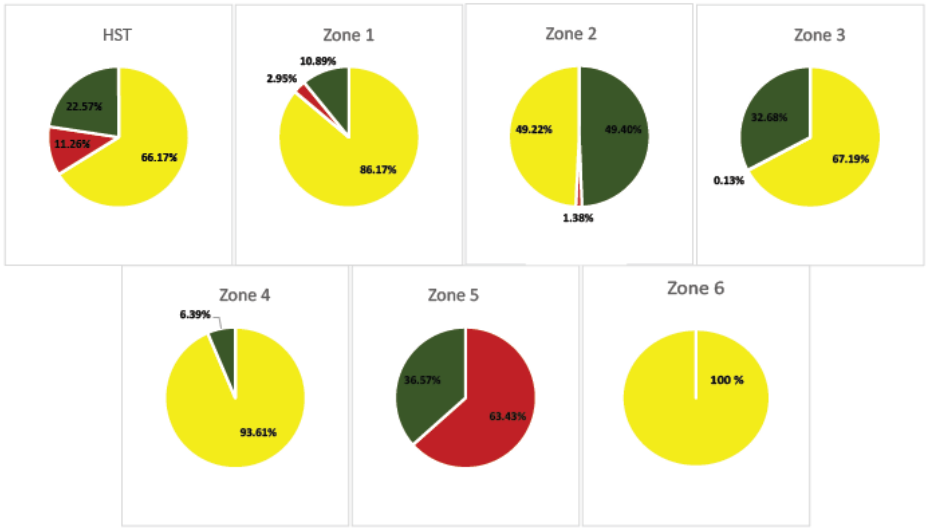

Appendix D: Modelling Workflow and Facies Model figures

Example of Agisoft Photoscan pre-processing. *The original photo is on the left. On the right, the same photo is shown, with a mask covering vegetation, sky, and undesired background. This method reduces the pixel data processing load during the photogrammetric model building process. In this example, pixel data was reduced by ~40%. This process was performed when necessary for each outcrop photograph.*

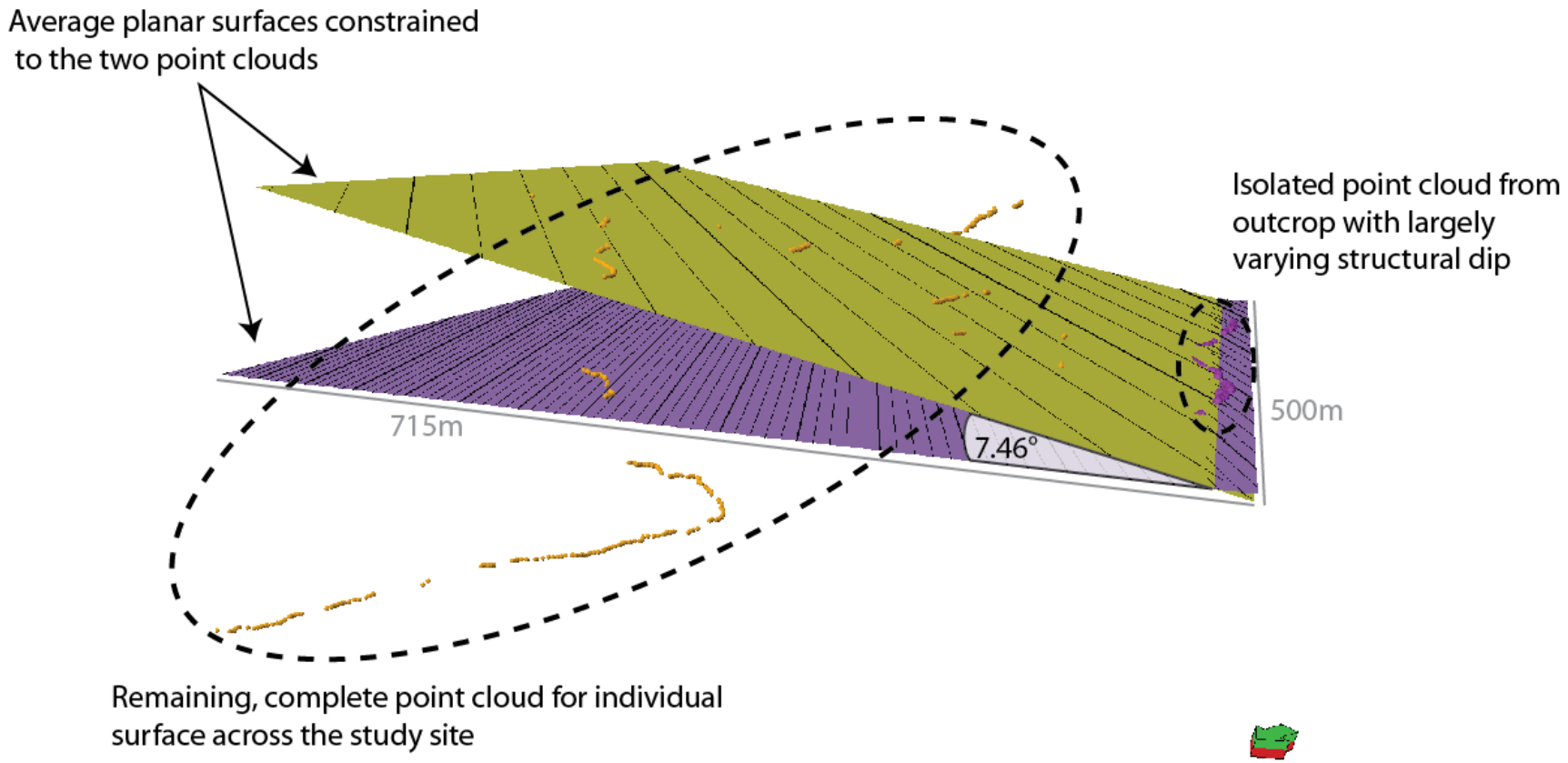

Structural restoration process used to adjust stratigraphic data points imported from DOM outcrops of dramatically varying plunge and/or dip. *In this example, the western outcrop points (purple) were isolated, rotated about their barycenter by 7.46 °, and spliced back into the original point cloud. Such corrections minimized artificial thinning or thickening of stratigraphic intervals between outcrop data sources.*

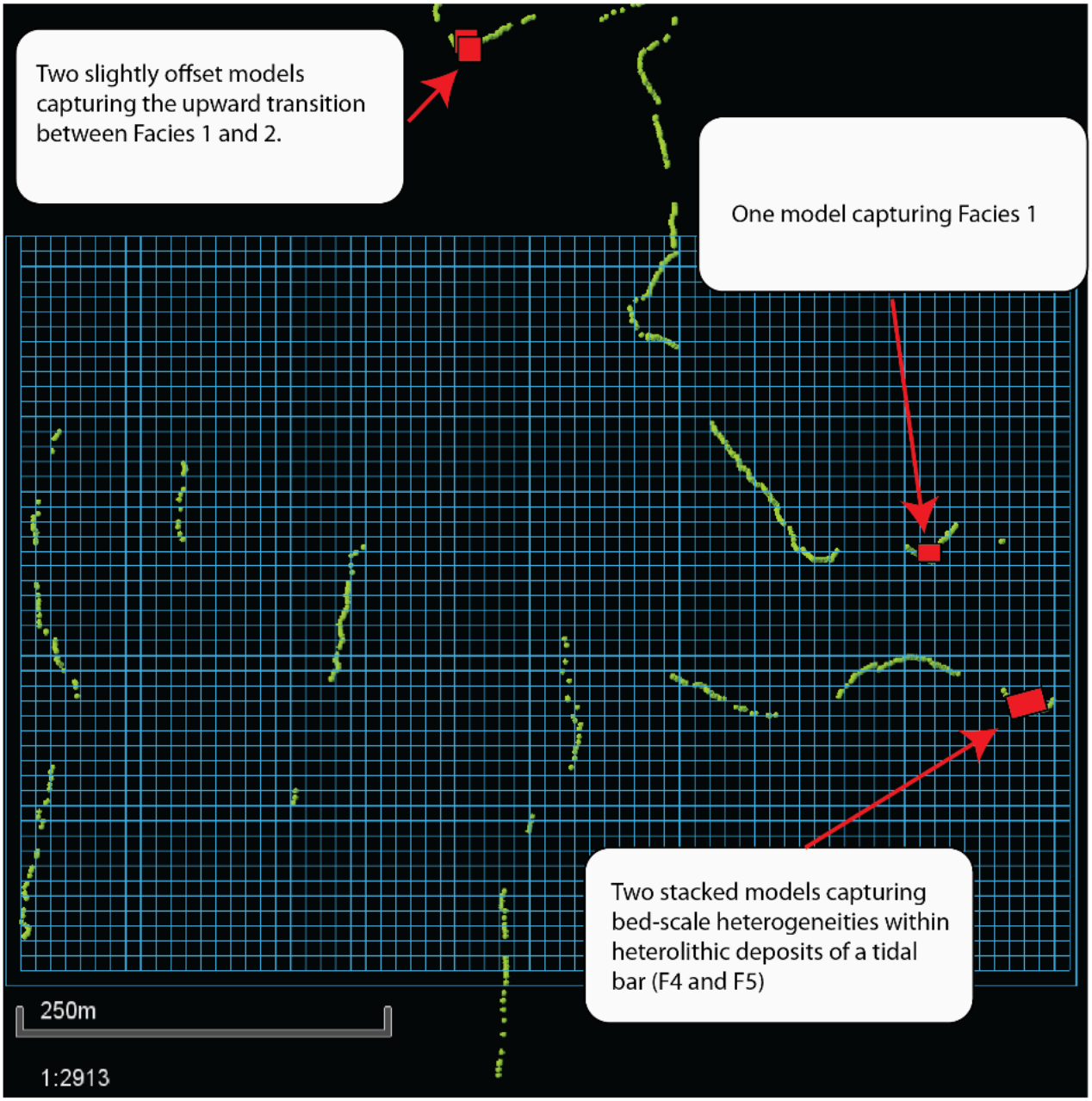

Location of nested, high resolution facies models, shown by the red boxes. *The outline of outcrops is shown by the green point set, marking a horizon correlated across the study area. The blue grid represents the final geomodel and its internal cell dimensions.*

Model A

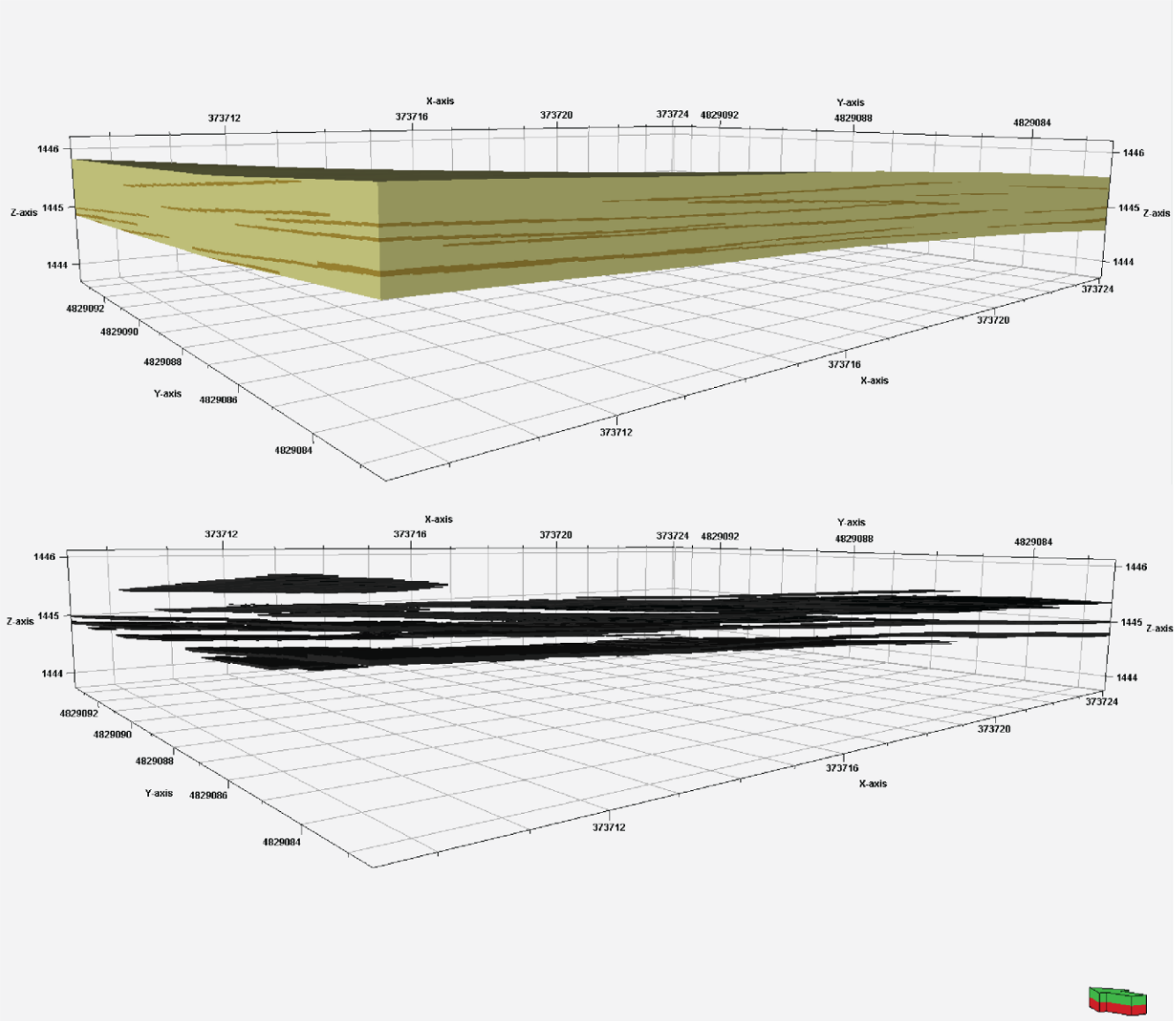

Model A, representing a bedset of F1. *Note the largely horizontal bedding, which contrasts with more complicated scouring bedforms captured in models B-E. Flow simulation of this model provides results for Petrel Geomodel Facies 1, which makes up a vast majority of the final model.*

Models B and C

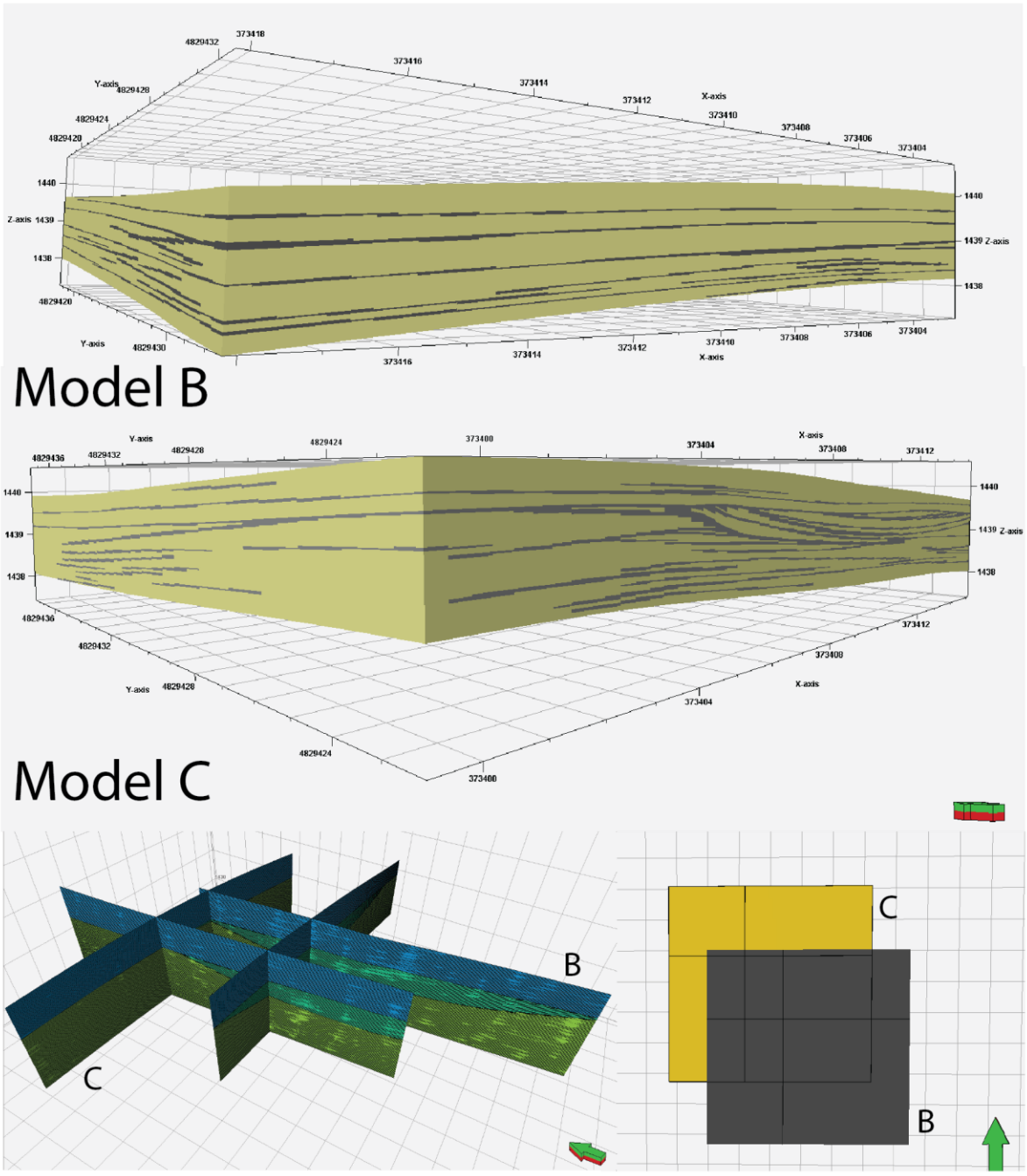

Models B and C, capturing F1 stacking upward into erosive F2 deposits. *Model B and C are shown in the top two images. Their slightly offset nature, shown in the bottom two images, causes a slight variation in F1:F2 proportion. Note that an entire scour bed (middle, teal zone) is captured in Model B, while it is only partially captured in Model C. Model B results educated GM3, while Model C inputs were used in GM2.*

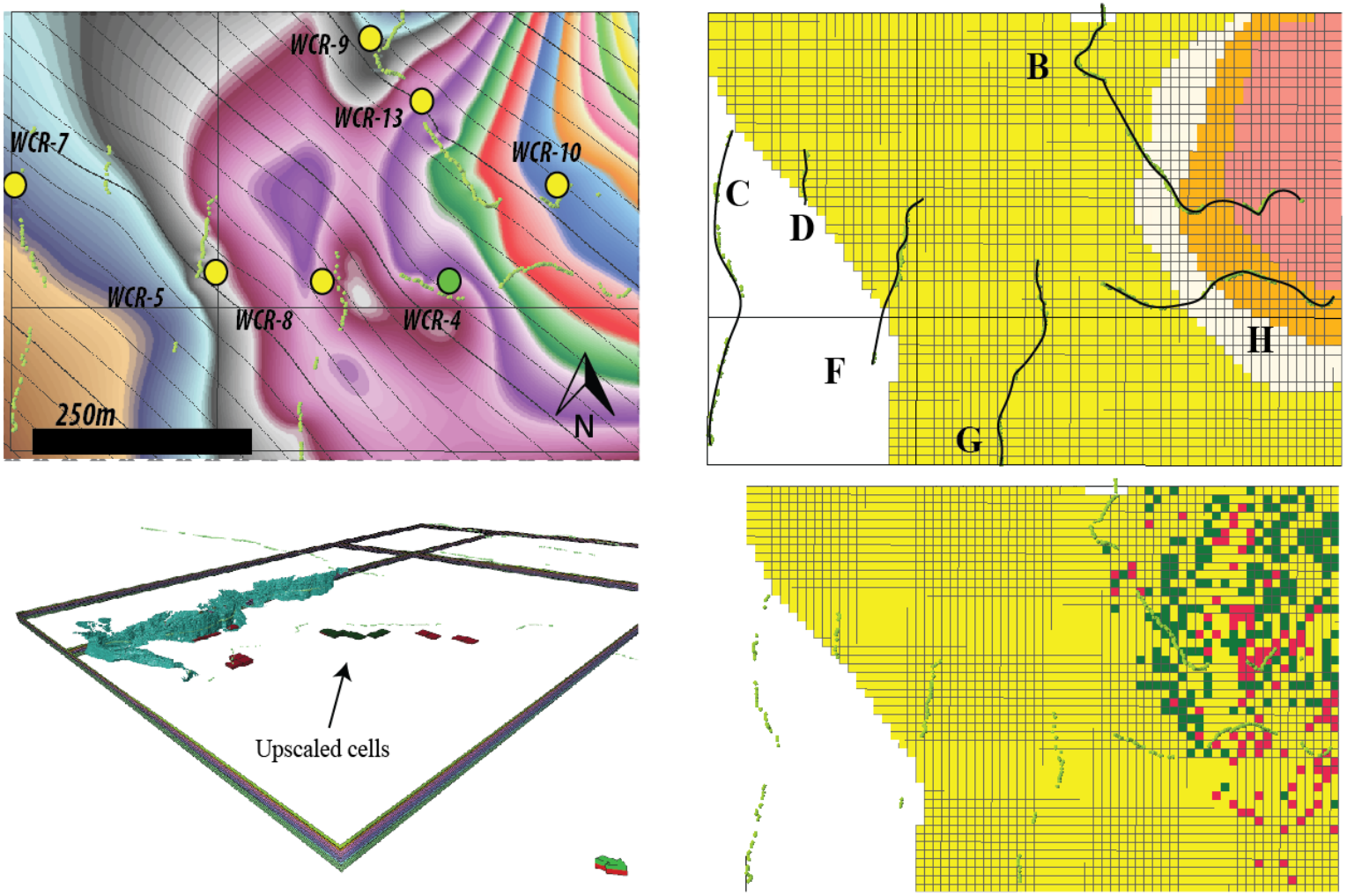

Model building procedure for Zone 1-HST1, capturing facies heterogeneity within a fluvial delta system. *Truncated Gaussian with Trends algorithm is used to populate facies belts contoured to delta lobe isopach geometries (**top left and right**). Facies statistics for outcrops within the contoured facies belts are used to populate their respective belt; for example, facies statistics gathered at WCR-4 and WCR-13 outcrops (outcrops "H-West" and "B-North") condition the white facies belt, while outcrop "B-WCR-10" and "H-East" are used to populate the red colored belt, seen above.* ***Bottom left:*** *a point set representing the location of non-background facies (F2 and F3) condition an upscaled data set before distribution of facies throughout the entire model.* ***Bottom right:*** *An underlying trend representing facies proportion statistics gathered from all facies proportion statistics is applied. Combined with upscaled cell data and accurate deltaic lobe geometries, this procedure outputs a final property model representing both field observations and the interpreted depositional model.*

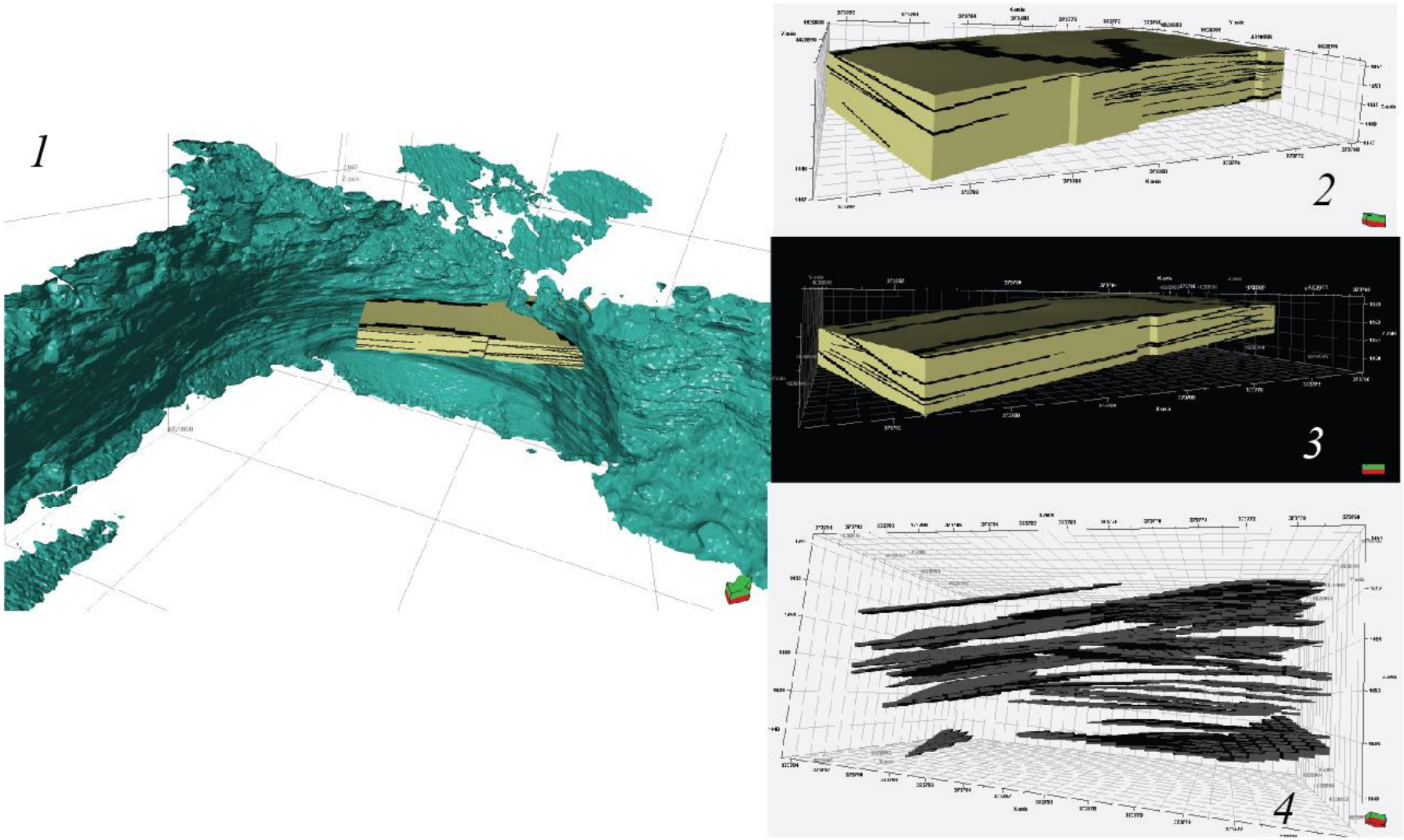

Stacked models D and E, representing fine-grained networks within F4 and F5 of a tidal bar. *Clockwise from left: 1) 3D exposed outcrop used to condition facies models. 2) Model D, representing the basal 3m of the bar, and 3) Model E, representing the coarser grained upper 2m of the same bar. 4) Shale network with transmissibility multiplier applied,*

Appendix E: Subsurface Facies Data from Powder River Basin

Location and name of well are proprietary

Sandstone Facies	Permeability (Klinkenberg) (mD)	Permeability (air) (mD)	Porosity (%)
1	***	***	2.54
1	.020	.052	3.51
1	.001	.006	4.76
1	.002	.007	2.91
1	***	***	3.29
2	.002	.008	4.51
2	.001	.006	4.65
2	.001	.005	4.03
2	.002	.008	4.03
2	.003	.012	5.78
3 and 5	.001	.007	3.25
3 and 5	.004	.014	3.15
3 and 5	.002	.007	5.19
3 and 5	.003	.011	5.01
3 and 5	.001	.005	4.75
3 and 5	.002	.009	4.97
3 and 5	.001	.005	5.07
3 and 5	.001	.006	4.52
3 and 5	.002	.009	4.86
3 and 5	.002	.010	4.63
3 and 5	.002	.008	5.20
3 and 5	.001	.007	4.52
3 and 5	.002	.010	4.74
3 and 5	.002	.009	4.38
3 and 5	.002	.008	4.52
3 and 5	.003	.010	4.94
3 and 5	.002	.008	4.92
3 and 5	.002	.007	4.35
3 and 5	.003	.013	4.55
3 and 5	.002	.009	4.95
3 and 5	.002	.009	4.88
3 and 5	.003	.011	4.84
3 and 5	.002	.008	5.43
3 and 5	.003	.013	4.73
3 and 5	.002	.008	5.07
3 and 5	.002	.008	5.06
3 and 5	.001	.004	4.28
3 and 5	.003	.011	5.03
3 and 5	.002	.009	5.51
5	.001	.005	4.31
5	.002	.007	5.16
5	.001	.004	4.79

5		.005		.017		5.28
5		.001		.007		4.83
5		.001		.006		4.99
5		.003		.011		4.80
5		.002		.010		5.15
5		.008		.025		5.52
5		.002		.008		5.13
5		.002		.007		4.38
5		.002		.008		4.70
5		.002		.007		5.50
5		.002		.008		5.36
5		.002		.009		4.99
5		.002		.007		4.82
5		.001		.006		4.75
5		.001		.006		4.20
5		.003		.011		5.10
5		.002		.010		5.05
5		.002		.007		5.27
5		.002		.008		5.45
5		.001		.005		5.42
5		.003		.011		4.78
5		.003		.012		4.53
5		.018		.047		3.53
4 and 5		.002		.010		5.25
4 and 5		.002		.007		4.72
4 and 5		.002		.007		4.84
4 and 5		.002		.010		4.65
4 and 5		.001		.007		5.08
4 and 5		.001		.005		2.67

Appendix F:

Facies Model Flow Simulation Results

Model A

A. Geocellular model and fluid simulation parameters

Height	0.97009312	m	3.18	ft
Width	11.1	m	36.42	ft
Length	14.7	m	48.23	ft
Area	163.17	m2	1756.35	ft2
Permeability	0.0015	md		
Porosity	0.0329	%		
β =	1.0358	rb/stb		
μ =	0.2421	cp		

B. Scenario 1

Case	**Transmissibility Multiplier**	**P2**	**P1**	ΔP	**q**	**PermX**	% Reduction
		(psi)	**(psi)**	**(psi)**	**(bbl/day)**	**(md)**	
1	0	7866	366	7500	0.1106	0.0014	9.75
2	0.3	7866	366	7500	0.1161	0.0014	5.28
3	0.5	7866	366	7500	0.1180	0.0015	3.75
4	0.7	7866	366	7500	0.1198	0.0015	2.25
5	1	7866	366	7500	0.1226	0.0015	0.00
Case	**Transmissibility Multiplier**	**P2**	**P1**	ΔP	**q**	**PermY**	% Reduction
		(psi)	**(psi)**	**(psi)**	**(bbl/day)**	**(md)**	
1	0	7866	366	7500	0.1940	0.0014	8.73
2	0.3	7866	366	7500	0.2049	0.0014	3.62
3	0.5	7866	366	7500	0.2082	0.0015	2.09
4	0.7	7866	366	7500	0.2114	0.0015	0.57
5	1	7866	366	7500	0.2126	0.0015	0.00
Case	**Transmissibility Multiplier**	**P2**	**P1**	ΔP	**q**	**PermZ**	% Reduction
		(psi)	**(psi)**	**(psi)**	**(bbl/day)**	**(md)**	
1	0	7866	366	7500	0.4789	0.0000	97.88
2	0.3	7866	366	7500	19.6960	0.0011	12.97
3	0.5	7866	366	7500	21.2327	0.0011	6.18
4	0.7	7866	366	7500	21.9984	0.0012	2.79
5	1	7866	366	7500	22.6303	0.0012	0.00

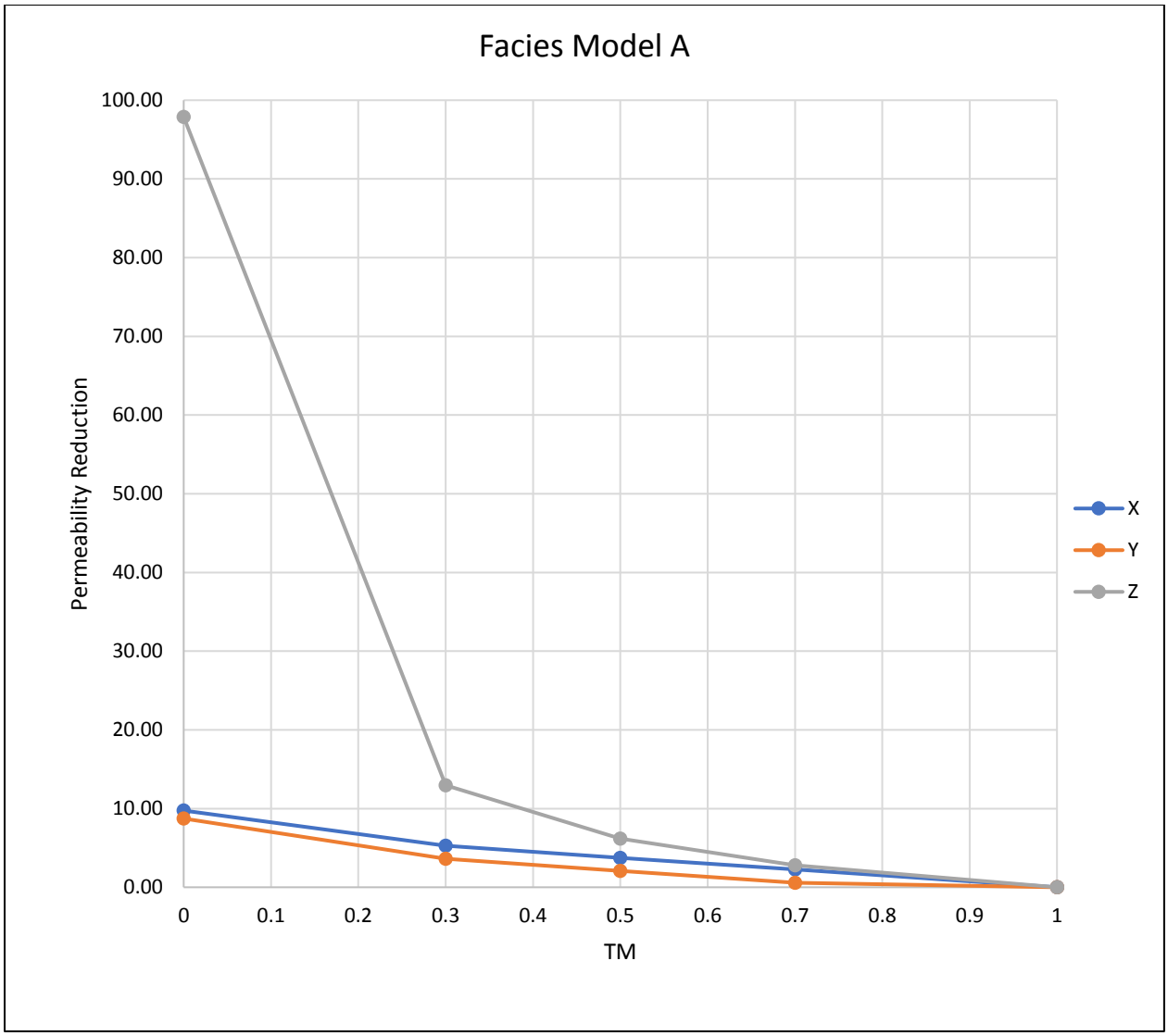

Facies Model "A" fluid simulation results. Baseline permeability input (TM=1) =0.0015 mD.

Model B – Scenario 1

C. Geocellular model and fluid simulation parameters

Height	2.4048128	m	7.89	ft
Width	15.5	m	50.85	ft
Length	15.9	m	52.17	ft
Area	37.275	m2	401.22	ft2
	F1		F2	
Permeability	0.0015	md	0.003	md
Porosity	0.0329	%	0.0578	%
β =	1.0358	rb/stb		
μ =	0.2421	cp		

D. Results

Case	**Transmissibility Multiplier**	**P2**	**P1**	ΔP	**q**	**PermX**	% Reduction
		(psi)	**(psi)**	**(psi)**	**(bbl/day)**	**(md)**	
1	0	7866	366	7500	0.2846	0.0011	31.12
2	0.3	7866	366	7500	0.3640	0.0014	11.92
3	0.5	7866	366	7500	0.3782	0.0015	8.47
4	0.7	7866	366	7500	0.3923	0.0015	5.06
5	1	7866	366	7500	0.4132	0.0016	0.00
Case	**Transmissibility Multiplier**	**P2**	**P1**	ΔP	**q**	**PermY**	% Reduction
		(psi)	**(psi)**	**(psi)**	**(bbl/day)**	**(md)**	
1	0	7866	366	7500	0.3036	0.0011	31.81
2	0.3	7866	366	7500	0.3905	0.0014	12.29
3	0.5	7866	366	7500	0.4064	0.0015	8.72
4	0.7	7866	366	7500	0.4220	0.0015	5.21
5	1	7866	366	7500	0.4452	0.0016	0.00
Case	**Transmissibility Multiplier**	**P2**	**P1**	ΔP	**q**	**PermZ**	% Reduction
		(psi)	**(psi)**	**(psi)**	**(bbl/day)**	**(md)**	
1	0	7866	366	7500	0.0000	0.0000	100.00
2	0.3	7866	366	7500	17.5344	0.0015	24.40
3	0.5	7866	366	7500	20.2815	0.0018	12.56
4	0.7	7866	366	7500	21.8196	0.0019	5.93
5	1	7866	366	7500	23.1950	0.0020	0.00

Model B – Scenario 2

E. Geocellular model and fluid simulation parameters

Height	2.404813	m	7.89	ft
Width	15.5	m	50.85	ft
Length	15.9	m	52.17	ft
Area	37.275	m2	401.22	ft2
	F1		F2	
Permeability	0.0015	md	0.002	md
Porosity	0.0329	%	0.0451	%
β =	1.0358	rb/stb		
μ =	0.2421	cp		

F. Results

Case	**Transmissibility Multiplier**	**P2**	**P1**	ΔP	**q**	**PermX**	% Reduction
		(psi)	**(psi)**	**(psi)**	**(bbl/day)**	**(md)**	
1	0	7866	366	7500	0.2353	0.0009	29.73
2	0.3	7866	366	7500	0.2952	0.0011	11.84
3	0.5	7866	366	7500	0.3066	0.0012	8.41
4	0.7	7866	366	7500	0.3180	0.0012	5.03
5	1	7866	366	7500	0.3348	0.0013	0.00
Case	**Transmissibility Multiplier**	**P2**	**P1**	ΔP	**q**	**PermY**	% Reduction
		(psi)	**(psi)**	**(psi)**	**(bbl/day)**	**(md)**	
1	0	7866	366	7500	0.2464	0.0009	31.44
2	0.3	7866	366	7500	0.3154	0.0012	12.24
3	0.5	7866	366	7500	0.3281	0.0012	8.69
4	0.7	7866	366	7500	0.3407	0.0012	5.19
5	1	7866	366	7500	0.3593	0.0013	0.00
Case	**Transmissibility Multiplier**	**P2**	**P1**	ΔP	**q**	**PermZ**	% Reduction
		(psi)	**(psi)**	**(psi)**	**(bbl/day)**	**(md)**	
1	0	7866	366	7500	0.0001	0.0000	100.00
2	0.3	7866	366	7500	15.1539	0.0013	24.15
3	0.5	7866	366	7500	17.4991	0.0015	12.41
4	0.7	7866	366	7500	18.8089	0.0017	5.85
5	1	7866	366	7500	19.9779	0.0018	0.00

Model B – Scenario 3

G. Geocellular model and fluid simulation parameters

Height	2.404813	m	7.89	ft
Width	15.5	m	50.85	ft
Length	15.9	m	52.17	ft
Area	37.275	m2	401.22	ft2
	F1		F2	
Permeability	0.0015	md	0.001	md
Porosity	0.0329	%	0.0403	%
β =	1.0358	rb/stb		
μ =	0.2421	cp		

H. Results

Case	**Transmissibility Multiplier**	**P2**	**P1**	ΔP	**q**	**PermX**	% Reduction
		(psi)	**(psi)**	**(psi)**	**(bbl/day)**	**(md)**	
1	0	7866	366	7500	0.1836	0.0007	27.92
2	0.3	7866	366	7500	0.2250	0.0009	11.63
3	0.5	7866	366	7500	0.2336	0.0009	8.26
4	0.7	7866	366	7500	0.2421	0.0009	4.94
5	1	7866	366	7500	0.2547	0.0010	0.00
Case	**Transmissibility Multiplier**	**P2**	**P1**	ΔP	**q**	**PermY**	% Reduction
		(psi)	**(psi)**	**(psi)**	**(bbl/day)**	**(md)**	
1	0	7866	366	7500	0.1888	0.0007	30.66
2	0.3	7866	366	7500	0.2392	0.0009	12.16
3	0.5	7866	366	7500	0.2488	0.0009	8.62
4	0.7	7866	366	7500	0.2583	0.0009	5.15
5	1	7866	366	7500	0.2723	0.0010	0.00
Case	**Transmissibility Multiplier**	**P2**	**P1**	ΔP	**q**	**PermZ**	% Reduction
		(psi)	**(psi)**	**(psi)**	**(bbl/day)**	**(md)**	
1	0	7866	366	7500	0.0001	0.0000	100.00
2	0.3	7866	366	7500	10.9267	0.0010	23.70
3	0.5	7866	366	7500	12.5813	0.0011	12.14
4	0.7	7866	366	7500	13.5016	0.0012	5.71
5	1	7866	366	7500	14.3198	0.0013	0.00

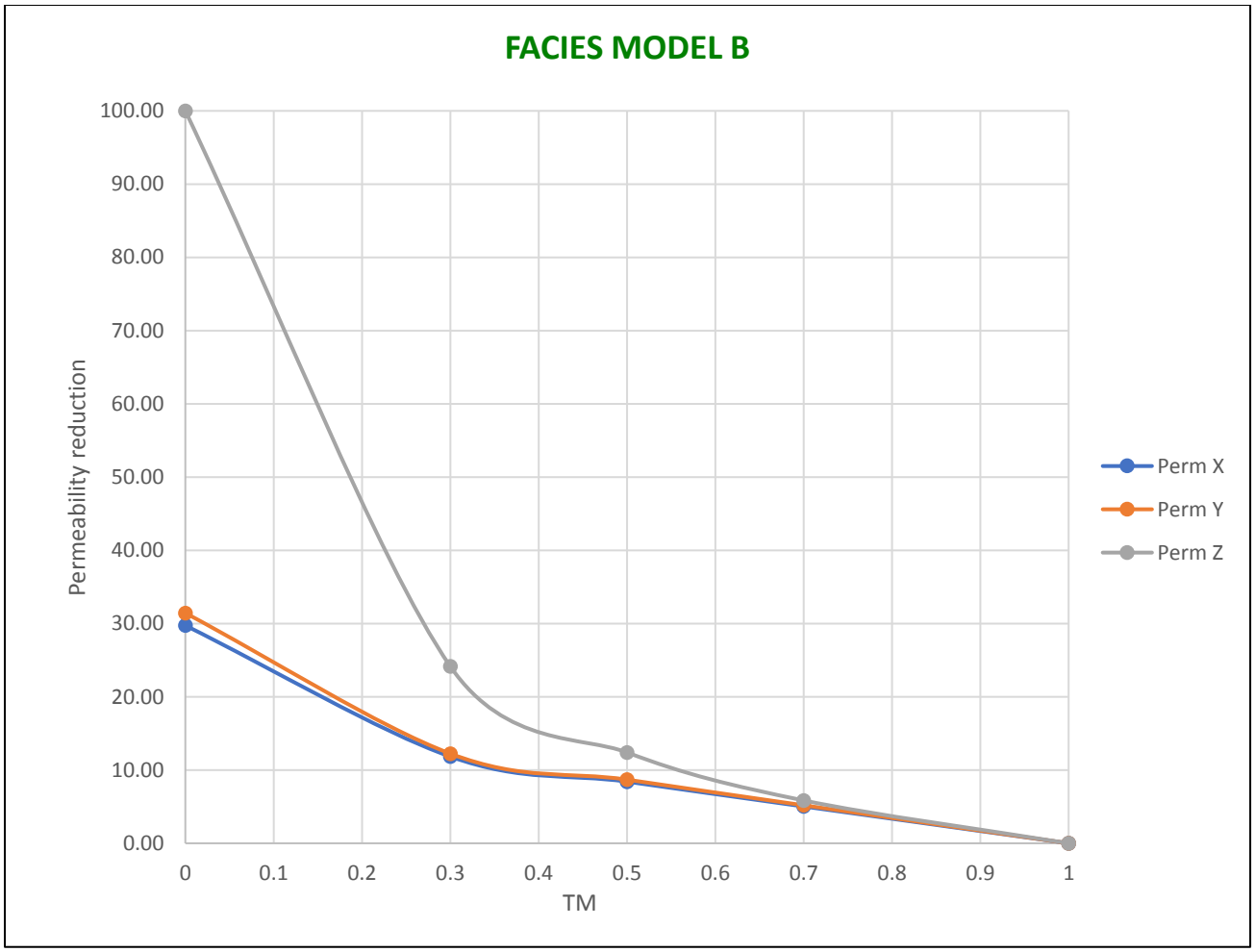

Facies Model "B" fluid simulation results. Baseline permeability input (TM=1) =0.0015 mD for F1 cells, which make up the lower ~1/2 of the grid, and 0.002 mD for F2 cells, which form the upper part of the grid.

Model C – Scenario 1

I. Geocellular model and fluid simulation parameters

Height	2.404813	m	7.89	ft
Width	15.5	m	50.85	ft
Length	15.9	m	52.17	ft
Area	39.102	m2	420.89	ft2
	F1		F2	
Permeability	0.0015	md	0.003	md
Porosity	0.0329	%	0.0578	%
β =	1.0358	rb/stb		
μ =	0.2421	cp		

J. Results

Case	**Transmissibility Multiplier**	**P2**	**P1**	ΔP	**q**	**PermX**	% Reduction
		(psi)	**(psi)**	**(psi)**	**(bbl/day)**	**(md)**	
1	0	7866	366	7500	0.3303	0.0012	24.17
2	0.3	7866	366	7500	0.3904	0.0014	10.38
3	0.5	7866	366	7500	0.4035	0.0015	7.38
4	0.7	7866	366	7500	0.4164	0.0015	4.41
5	1	7866	366	7500	0.4356	0.0016	0.00
Case	**Transmissibility Multiplier**	**P2**	**P1**	ΔP	**q**	**PermY**	% Reduction
		(psi)	**(psi)**	**(psi)**	**(bbl/day)**	**(md)**	
1	0	7866	366	7500	0.3489	0.0012	25.30
2	0.3	7866	366	7500	0.4176	0.0015	10.61
3	0.5	7866	366	7500	0.4320	0.0015	7.53
4	0.7	7866	366	7500	0.4462	0.0016	4.49
5	1	7866	366	7500	0.4671	0.0016	0.00
Case	**Transmissibility Multiplier**	**P2**	**P1**	ΔP	**q**	**PermZ**	% Reduction
		(psi)	**(psi)**	**(psi)**	**(bbl/day)**	**(md)**	
1	0	7866	366	7500	0.0000	0.0000	100.00
2	0.3	7866	366	7500	19.4536	0.0018	23.65
3	0.5	7866	366	7500	22.4071	0.0021	12.06
4	0.7	7866	366	7500	24.0409	0.0022	5.65
5	1	7866	366	7500	25.4803	0.0024	0.00

Model C – Scenario 2

K. Geocellular model and fluid simulation parameters

Height	2.404813	m	7.89	ft
Width	15.5	m	50.85	ft
Length	15.9	m	52.17	ft
Area	39.102	m2	420.89	ft2
	F1		F2	
Permeability	0.0015	md	0.0451	md
Porosity	0.0329	%	0.379	%
β =	1.0358	rb/stb		
μ =	0.2421	cp		

L. Results

Case	Transmissibility Multiplier	P2	P1	ΔP	q	PermX	% Reduction
		(psi)	(psi)	(psi)	(bbl/day)	(md)	
1	0	7866	366	7500	0.2655	0.0010	23.96
2	0.3	7866	366	7500	0.3128	0.0012	10.40
3	0.5	7866	366	7500	0.3233	0.0012	7.40
4	0.7	7866	366	7500	0.3337	0.0012	4.42
5	1	7866	366	7500	0.3492	0.0013	9.00
Case	**Transmissibility Multiplier**	**P2**	**P1**	ΔP	**q**	**PermY**	% Reduction
		(psi)	(psi)	(psi)	(bbl/day)	(md)	
1	0	7866	366	7500	0.2756	0.0010	26.29
2	0.3	7866	366	7500	0.3339	0.0012	10.69
3	0.5	7866	366	7500	0.3456	0.0012	7.58
4	0.7	7866	366	7500	0.3570	0.0012	4.52
5	1	7866	366	7500	0.3739	0.0013	0.00
Case	**Transmissibility Multiplier**	**P2**	**P1**	ΔP	**q**	**PermZ**	% Reduction
		(psi)	(psi)	(psi)	(bbl/day)	(md)	
1	0	7866	366	7500	0.0000	0.0000	100.00
2	0.3	7866	366	7500	17.0507	0.0016	23.23
3	0.5	7866	366	7500	19.5671	0.0018	11.90
4	0.7	7866	366	7500	20.9837	0.0019	5.52
5	1	7866	366	7500	22.2102	0.0021	0.00

Model C – Scenario 3

M. Geocellular model and fluid simulation parameters

Height	2.404813	m	7.89	ft
Width	15.5	m	50.85	ft
Length	15.9	m	52.17	ft
Area	39.102	m2	420.89	ft2
	F1		F2	
Permeability	0.0015	md	0.0403	md
Porosity	0.0329	%	0.0329	%
β =	1.0358	rb/stb		
μ =	0.2421	cp		

N. Results

Case	**Transmissibility Multiplier**	**P2**	**P1**	ΔP	**q**	**PermX**	% Reduction
		(psi)	**(psi)**	**(psi)**	**(bbl/day)**	**(md)**	
1	0	7866	366	7500	0.2004	0.0007	23.49
2	0.3	7866	366	7500	0.2347	0.0009	10.40
3	0.5	7866	366	7500	0.2425	0.0009	7.39
4	0.7	7866	366	7500	0.2503	0.0009	4.42
5	1	7866	366	7500	0.2619	0.0010	0.00
Case	**Transmissibility Multiplier**	**P2**	**P1**	ΔP	**q**	**PermY**	% Reduction
		(psi)	**(psi)**	**(psi)**	**(bbl/day)**	**(md)**	
1	0	7866	366	7500	0.2010	0.0007	28.24
2	0.3	7866	366	7500	0.2499	0.0009	10.78
3	0.5	7866	366	7500	0.2586	0.0009	7.65
4	0.7	7866	366	7500	0.2673	0.0009	4.56
5	1	7866	366	7500	0.2800	0.0010	0.00
Case	**Transmissibility Multiplier**	**P2**	**P1**	ΔP	**q**	**PermZ**	% Reduction
		(psi)	**(psi)**	**(psi)**	**(bbl/day)**	**(md)**	
1	0	7866	366	7500	0.0000	0.0000	100.00
2	0.3	7866	366	7500	12.5598	0.0012	22.31
3	0.5	7866	366	7500	14.3436	0.0013	11.28
4	0.7	7866	366	7500	15.3174	0.0014	5.26
5	1	7866	366	7500	16.1673	0.0015	0.00

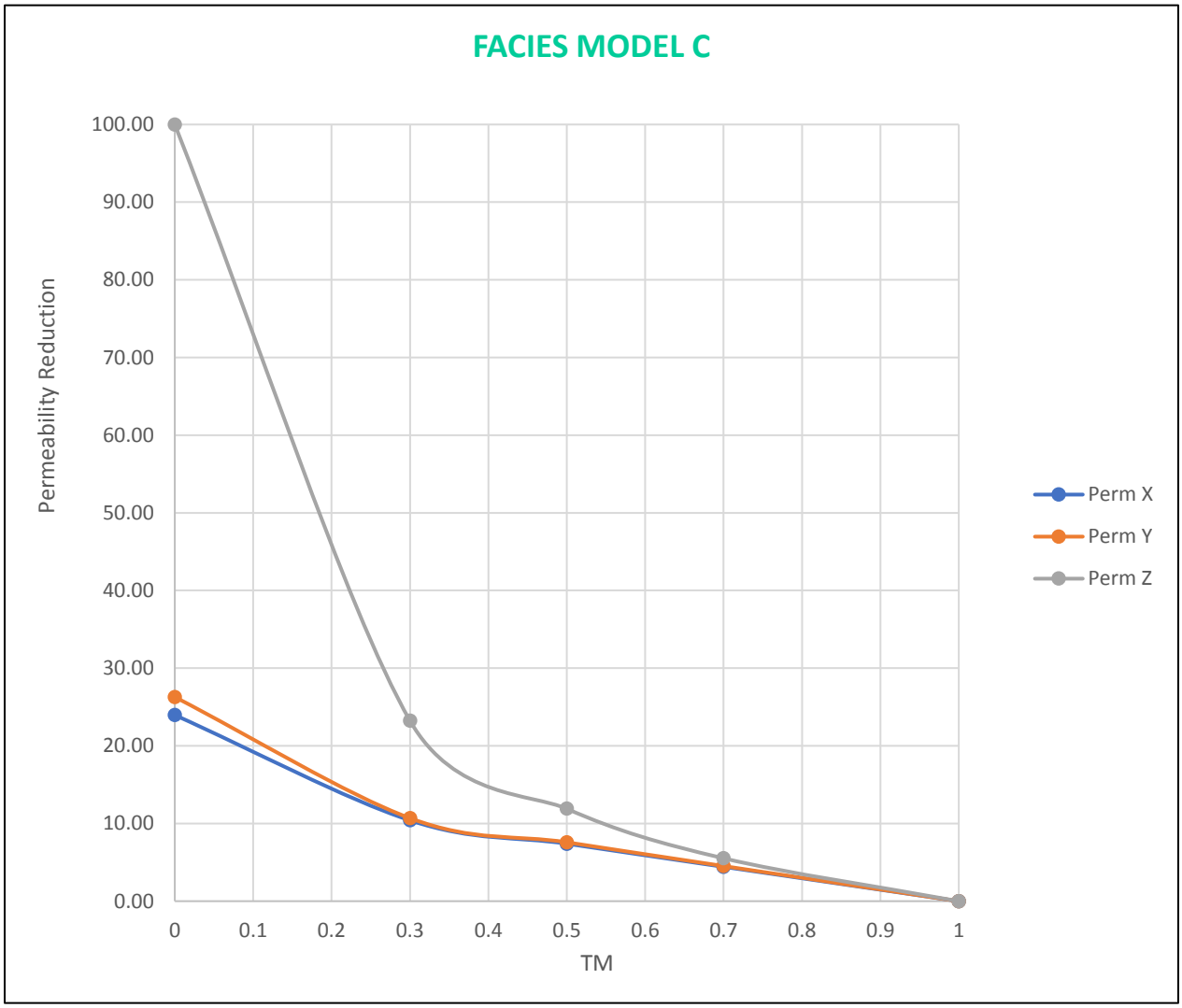

Facies Model "C" fluid simulation results. Baseline permeability input (TM=1) =0.0015 mD for F1 cells, which make up the lower ~1/2 of the grid, and 0.002 mD for F2 cells, which form the upper part of the grid.

Model D – Scenario 1

O. Geocellular model and fluid simulation parameters

Height	3	m	9.84	ft
Width	14.5	m	47.57	ft
Length	22.5	m	73.62	ft
Area	43.5	m2	468.23	ft2
Permeability	0.179	md		
Porosity	6.65	%		
β =	1.03584253	rb/stb		
μ =	0.2421	cp		

P. Results

Case	**Transmissibility Multiplier**	**P2**	**P1**	ΔP	**q**	**PermX**	**%Reduction**
		(psi)	**(psi)**	**(psi)**	**(bbl/day)**	**(md)**	
1	1	6866	366	6500	32.7112	0.1765	
2	0	6866	366	6500	27.6483	0.1492	15.47762044
3	1	7866	366	7500	37.8064	0.1768	
4	0	7866	366	7500	31.9548	0.1495	15.47769848
Case	**Transmissibility Multiplier**	**P2**	**P1**	ΔP	**q**	**PermY**	**%Reduction**
		(psi)	**(psi)**	**(psi)**	**(bbl/day)**	**(md)**	
5	1	6866	366	6500	83.1272	0.1863	
6	0	6866	366	6500	71.7745	0.1609	13.65702701
7	1	7866	366	7500	96.0780	0.1866	
8	0	7866	366	7500	82.9566	0.1612	13.65698382
Case	**Transmissibility Multiplier**	**P2**	**P1**	ΔP	**q**	**PermZ**	**%Reduction**
		(psi)	**(psi)**	**(psi)**	**(bbl/day)**	**(md)**	
9	1	6866	366	6500	1071.1771	0.1028	
10	0	6866	366	6500	363.6545	0.0349	66.05094504
11	1	7866	366	7500	1238.1425	0.1030	
12	0	7866	366	7500	420.3386	0.0350	66.05086749

Model D – Scenario 2

Q. Geocellular model and fluid simulation parameters

Height	3	m	9.84	ft
Width	14.5	m	47.57	ft
Length	22.5	m	73.62	ft
Area	43.5	m2	468.23	ft2
Permeability	0.179	md		
Porosity	6.65	%		
β =	1.03584253	rb/stb		
μ =	0.2421	cp		

R. Results

Case	Transmissibility Multiplier	q	PermX	Percent Decrease	Percentage from Tm=1
		(bbl/day)	(md)		
LTM0	0	27.6483	0.1492	15.48	84.52
LTM10	0.1	30.07573891	0.1623	8.06	91.94
LTM20	0.2	30.3893	0.1640	7.10	92.90
LTM30	0.3	30.6890	0.1656	6.18	93.82
LTM40	0.4	30.9838	0.1672	5.28	94.72
LTM50	0.5	31.2758	0.1688	4.39	95.61
LTM60	0.6	31.5658	0.1704	3.50	96.50
LTM70	0.7	31.8541	0.1719	2.62	97.38
LTM80	0.8	32.1411	0.1735	1.74	98.26
LTM90	0.9	32.4267	0.1750	0.87	99.13
LTM100	1	32.7112	0.1765	0.00	100.00
Case	**Transmissibility Multiplier**	**q**	**PermY**	**Percent Decrease**	**Percentage from Tm=1**
		(bbl/day)	(md)		
LTM0Y	0	71.7745	0.1609	13.66	86.34
LTM10Y	0.1	75.95269775	0.1702	8.63	91.37
LTM20Y	0.2	76.8284	0.1722	7.58	92.42
LTM30Y	0.3	77.6619	0.1741	6.57	93.43
LTM40Y	0.4	78.4760	0.1759	5.60	94.40
LTM50Y	0.5	79.2763	0.1777	4.63	95.37
LTM60Y	0.6	80.0653	0.1795	3.68	96.32
LTM70Y	0.7	80.8442	0.1812	2.75	97.25

LTM80Y	0.8	81.6138	0.1829	1.82	98.18
LTM90Y	0.9	82.3746	0.1846	0.91	99.09
LTM100Y	1	83.1272	0.1863	0.00	100.00
Case	**Transmissibility Multiplier**	**q**	**Permz**	**Percent Decrease**	**Percentage from Tm=1**
		(bbl/day)	**(md)**		
LTM0Z	0	363.6545	0.0349	66.05	33.95
LTM10Z	0.1	778.0860596	0.0747	27.36	72.64
LTM20Z	0.2	889.6206	0.0854	16.95	83.05
LTM30Z	0.3	947.1244	0.0909	11.58	88.42
LTM40Z	0.4	983.0851	0.0943	8.22	91.78
LTM50Z	0.5	1008.0852	0.0967	5.89	94.11
LTM60Z	0.6	1026.6960	0.0985	4.15	95.85
LTM70Z	0.7	1041.2360	0.0999	2.80	97.20
LTM80Z	0.8	1053.0128	0.1010	1.70	98.30
LTM90Z	0.9	1062.8220	0.1020	0.78	99.22
LTM100Z	1	1071.1771	0.1028	0.00	100.00

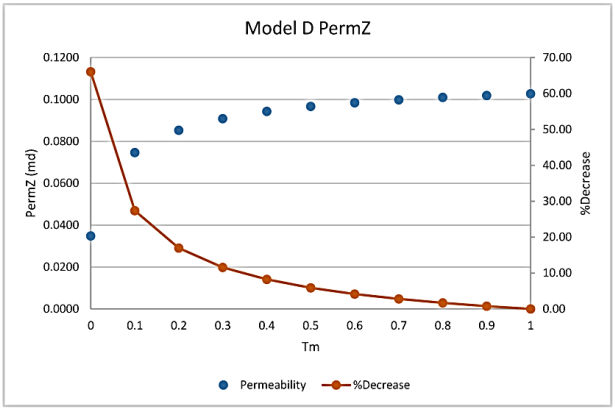

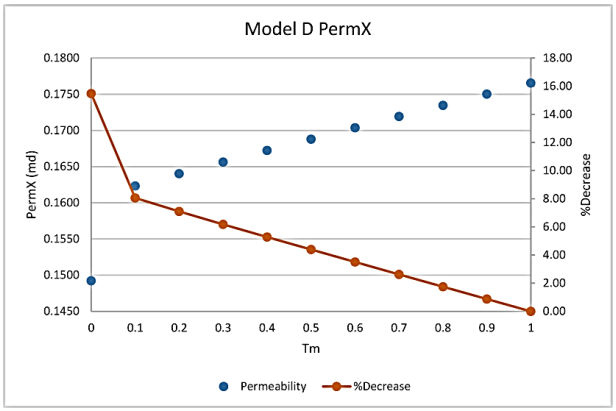

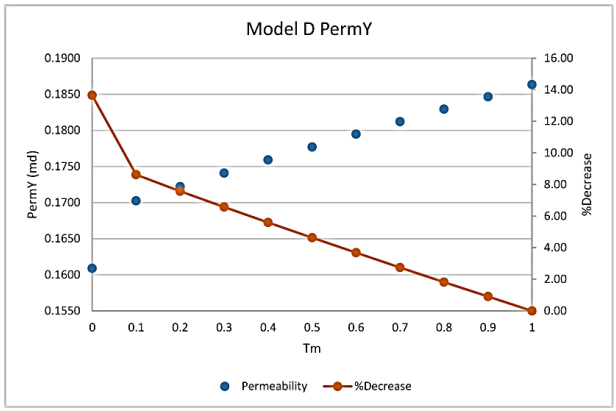

Model D – Scenario 3

S. Geocellular model and fluid simulation parameters

Height	3	m	9.84	ft
Width	14.5	m	47.57	ft
Length	22.5	m	73.62	ft
Area	43.5	m2	468.23	ft2
	Case 1	Case 2	Case 3	
Permeability	0.002	0.003	0.002	md
Porosity	4.74	4.91	4.29	%
β =	1.03584253	rb/stb		
μ =	0.2421	cp		

T. Results

Case	Transmissibility Multiplier	P2	P1	ΔP	q	PermX	%Reduction
1x	0	6866	366	6500	0.3091	0.0017	15.47731075
2X	0	6866	366	6500	0.4636	0.0025	15.47763434
3X	0	6866	366	6500	0.3091	0.0017	15.47731075
Case	**Transmissibility Multiplier**	**P2**	**P1**	ΔP	**q**	**PermX**	**%Reduction**
1x	0	6866	366	6500	0.8024	0.0018	13.65701364
2X	0	6866	366	6500	1.2036	0.0027	13.65702799
3X	0	6866	366	6500	0.8024	0.0018	13.65701364
Case	**Transmissibility Multiplier**	**P2**	**P1**	ΔP	**q**	**PermX**	**%Reduction**
1x	**0**	**6866**	**366**	**6500**	4.065450193	0.000390073	66.05094421
2X	0	6866	366.0000	6500.0000	6.098175055	0.000585109	66.05094551
3X	0	6866	366.0000	6500.0000	4.0655	0.000390078	66.05052826

Model E – Scenario 1

U. Geocellular model and fluid simulation parameters

Height	2	m	6.56	ft
Width	14	m	45.93	ft
Length	24	m	78.74	ft
Area	28	m2	301.39	ft2
Permeability	0.179	md		
Porosity	0.067	%		
β =	1.035843	rb/stb		
μ =	0.2421	cp		

V. Results

Case	Transmissibility Multiplier	P2	P1	ΔP	q	PermX	%Reduction
		(psi)	(psi)	(psi)	(bbl/day)	(md)	
1	1	6866	366	6500	20.2985	0.1815	
2	0	6866	366	6500	13.5553	0.1212	33.22005046
3	1	7866	366	7500	23.3750	0.1812	
4	0	7866	366	7500	15.6224	0.1211	33.16588073
Case	Transmissibility Multiplier	P2	P1	ΔP	q	PermY	%Reduction
		(psi)	(psi)	(psi)	(bbl/day)	(md)	
5	1	6866	366	6500	59.2037	0.1802	
6	0	6866	366	6500	36.1655	0.1101	38.91345055
7	1	7866	366	7500	68.4270	0.1805	
8	0	7866	366	7500	41.7999	0.1103	38.91324536
Case	Transmissibility Multiplier	P2	P1	ΔP	q	PermZ	%Reduction
		(psi)	(psi)	(psi)	(bbl/day)	(md)	
9	1	6866	366	6500	2601.004639	0.161546684	
10	0	6866	366	6500	267.1582642	0.016593024	89.7287
11	1	7866	366	7500	3006.266846	0.161821619	

Model E Scenario 2

W. Geocellular model and fluid simulation parameters

Height	2	m	6.56	ft
Width	14	m	45.93	ft
Length	24	m	78.74	ft
Area	28	m2	301.39	ft2
Permeability	0.179	md		
Porosity	0.067	%		
β =	1.035843	rb/stb		
μ =	0.2421	cp		

X. Results

Case	Transmissibility Multiplier	q	PermX	Percentage decrease	Percentage from Tm=1
		(bbl/day)	(md)		
UTM0	0	13.55530262	0.121235172	33.22005046	66.77994954
UTM10	0.1	17.40388298	0.155655894	14.26008997	85.73991003
UTM20	0.2	17.74390221	0.158696939	12.58499147	87.41500853
UTM30	0.3	18.07222939	0.161633413	10.96749364	89.03250636
UTM40	0.4	18.39616394	0.164530602	9.371636031	90.62836397
UTM50	0.5	18.71741104	0.167403754	7.789018089	92.21098191
UTM60	0.6	19.03663254	0.170258789	6.216379229	93.78362077
UTM70	0.7	19.35416985	0.173098762	4.6520375	95.3479625
UTM80	0.8	19.67022896	0.175925514	3.094978096	96.9050219
UTM90	0.9	19.98495865	0.178740376	1.544468056	98.45553194
UTM100	1	20.29846191	0.18154427	0	100
Case	Transmissibility Multiplier	q	PermY	Percentage decrease	Percentage from Tm=1
		(bbl/day)	(md)		
UTM0Y	0	36.16551208	0.11006459	38.91345055	61.08654945
UTM10Y	0.1	50.33961487	0.153201455	14.97221535	85.02778465
UTM20Y	0.2	51.45970917	0.156610303	13.08028318	86.91971682
UTM30Y	0.3	52.4874382	0.15973805	11.34436361	88.65563639
UTM40Y	0.4	53.48405457	0.16277111	9.660995901	90.3390041
UTM50Y	0.5	54.46310425	0.165750709	8.007299789	91.99270021
UTM60Y	0.6	55.4295311	0.168691891	6.374924685	93.62507531

UTM70Y	0.7	56.38568115	0.171601798	4.759907948	95.24009205
UTM80Y	0.8	57.33289719	0.174484515	3.159981495	96.8400185
UTM90Y	0.9	58.27203751	0.177342655	1.573695603	98.4263044
UTM100Y	1	59.20372391	0.18017811	0	100
Case	Transmissibility Multiplier	q	PermX	Percentage decrease	Percentage from Tm=1
		(bbl/day)	(md)		
UTM0Z	0	267.1582642	0.016593024	89.72865099	9.209234002
UTM10Z	0.1	1313.661865	0.081590673	49.49405911	45.28334377
UTM20Z	0.2	1746.702271	0.108486527	32.84509206	60.21071439
UTM30Z	0.3	2000.824463	0.124269889	23.07493677	68.97058091
UTM40Z	0.4	2170.138184	0.134785853	16.56538588	74.80700779
UTM50Z	0.5	2291.705811	0.142336338	11.8915139	78.99757524
UTM60Z	0.6	2383.50293	0.148037797	8.362219188	82.16192111
UTM70Z	0.7	2455.405762	0.152503634	5.597793821	84.64048941
UTM80Z	0.8	2513.322266	0.15610079	3.371096373	86.63693387
UTM90Z	0.9	2561.016357	0.159063039	1.53741676	88.28100075
UTM100Z	1	2601.004639	0.161546684	0	89.65944

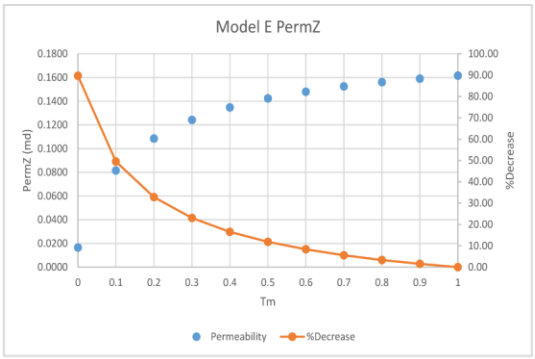

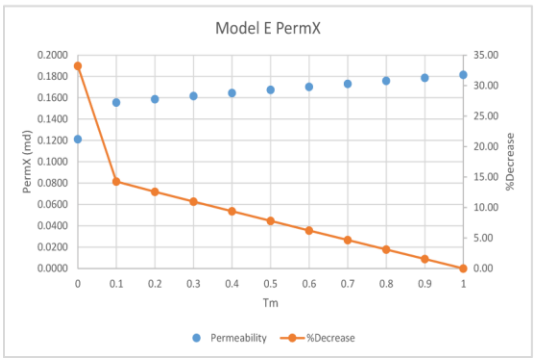

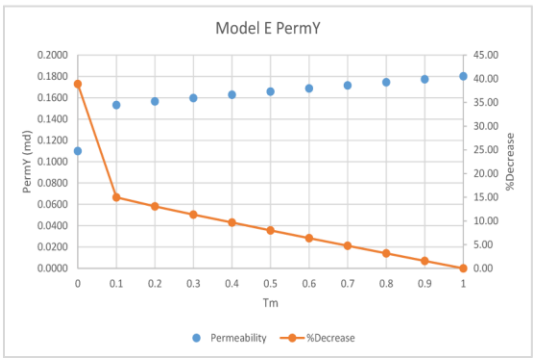

Model E - Scenario 3

Y. Geocellular model and fluid simulation parameters

Height	2	m	6.56	ft
Width	14	m	45.93	ft
Length	24	m	78.74	ft
Area	28	m2	301.39	ft2
	Case 1	Case 2	Case 3	
Permeability	0.002	0.003	0.002	md
Porosity	4.74	4.91	4.29	%
β =	1.03584253	rb/stb		
μ =	0.2421	cp		

Z. Results

1X	**0**	**6866**	**366**	**6500**	**0.151622**	**0.001356**	**33.18411**
2X	0	6866	366	6500	0.227328	0.002033	33.21509
3X	0	6866	366	6500	0.151622	0.001356	33.18411
Case	Transmissibility **Multiplier**	P2	P1	ΔP	q	PermX	%**Reduction**
1X	0	6866	366	6500	0.40431	0.00123	38.91345
2X	**0**	**6866**	**366**	**6500**	**0.606465**	**0.001846**	**38.91345**
3X	0	6866	366	6500	0.40431	0.00123	38.91345
Case	Transmissibility **Multiplier**	P2	P1	ΔP	q	PermX	%Reduction
1X	0	6866	366	6500	2.986678	0.000186	89.72865
2X	**0**	**6866**	**366**	**6500**	**4.480016**	**0.000278**	**89.72865**
3X	0	6866	366	6500	2.986677	0.000186	89.72865

Appendix G: Field-scale geomodel simulation

Lateral well nomenclature legend

Structurally dipping?	**Proxy Model?**	**Well configuration**	**Well placement**	**Orientation**	**Fracture?**	**TM**
D (Dipping, only included for structural models. Flattened models have no notation)	(Px) only included for proxy model	L (Lateral)	U(Upper)	W (W-E trending)	F (Fractured; no notation if unfractured)	0
			L (lower)	N (N-S trending)		0.5

Vertical well nomenclature legend

Structurally dipping?	**Proxy model?**	**Well configuration**	**Well placement**	**Well completion**	**TM**
D (Dipping, only included for structural models. Flattened models have no notation)	(Px) Only included for proxy model	V (Vertical)	C (Center)	U (upper zone)	0
			SW (Southwest)	A (All zones)	0.5
			NE (Northeast)		

Outcrop geomodel simulation results (Dipping)

Lateral well arrangements

Dynamic data: Field Water produc		Dynamic data: Field Water production		Dynamic data: Field Water production c		Dynamic data: Field Water prod	
Date	**DFracNSLTm5 I**	**Date**	**DFracWELTm5 Uni**	**Date**	**DFracNSUTm5 Uni**	**Date**	**DFracWEUTr**
1/1/2018	0	1/1/2018	0	1/1/2018	0	1/1/2018	0
1/2/2018	336.2979736	1/2/2018	319.3535461	1/2/2018	173.2501984	1/2/2018	158.4842224
1/5/2018	714.1879273	1/5/2018	690.673645	1/5/2018	583.5419312	1/5/2018	539.6738892
1/14/2018	1511.710693	1/14/2018	1481.059326	1/14/2018	1567.656494	1/14/2018	1458.771973
2/10/2018	3361.077148	2/10/2018	3308.306396	2/10/2018	3891.025635	2/10/2018	3640.211426
5/2/2018	7442.99707	5/2/2018	7320.126953	5/2/2018	8867.392578	5/2/2018	8414.918945
1/1/2019	15596.01953	1/1/2019	15387.02539	1/1/2019	18123.51758	1/1/2019	17775.3418
1/1/2020	24227.44336	1/1/2020	24175.39063	1/1/2020	27371.33984	1/1/2020	27721.46094
1/1/2021	31078.09766	1/1/2021	31392.875	1/1/2021	34487.92188	1/1/2021	35759.07031
1/1/2022	36839.88281	1/1/2022	37661.32813	1/1/2022	40378.03906	1/1/2022	42661.75781
1/1/2023	41888.31641	1/1/2023	43307.59766	1/1/2023	45493.97266	1/1/2023	48824.41797
DLLNF0.5		DLLWF0.5		DLUNF0.5		DLUWF0.5	
Dynamic data: Field Water produc		Dynamic data: Field Water production		Dynamic data: Field Water production c		Dynamic data: Field Water prod	
Date	**DNSLTm5 Unit:**	**Date**	**DWELTm5 Unit: ST**	**Date**	**DNSUTm5 Unit: ST**	**Date**	**DWEUTm5 U**
1/1/2018	0	1/1/2018	0	1/1/2018	0	1/1/2018	0
1/2/2018	451.5419006	1/2/2018	462.4710083	1/2/2018	153.5720367	1/2/2018	146.5252838
1/5/2018	931.0604858	1/5/2018	958.149231	1/5/2018	496.611084	1/5/2018	481.9530945
1/14/2018	1860.518188	1/14/2018	1923.648438	1/14/2018	1268.420898	1/14/2018	1242.676392
2/10/2018	3817.7771	2/10/2018	3953.26001	2/10/2018	3002.765137	2/10/2018	2947.876221
5/2/2018	7755.910645	5/2/2018	8054.506348	5/2/2018	6694.224121	5/2/2018	6586.183105
1/1/2019	15285.16895	1/1/2019	16041.15625	1/1/2019	14008.94238	1/1/2019	13960.12891
1/1/2020	23289.61133	1/1/2020	24796.54297	1/1/2020	21889.73438	1/1/2020	22198.77539
1/1/2021	29728.45508	1/1/2021	32055.16016	1/1/2021	28259.17383	1/1/2021	29087.71094
1/1/2022	35207.56641	1/1/2022	38395.54688	1/1/2022	33691.49219	1/1/2022	35135.82813
1/1/2023	40051.23047	1/1/2023	44123.48047	1/1/2023	38500.38672	1/1/2023	40620.58203
DLLN0.5		DLLW0.5		DLUN0.5		DLUW0.5	
Dynamic data: Field Water produc		Dynamic data: Field Water production		Dynamic data: Field Water production c		Dynamic data: Field Water prod	
Date	**DFracNSLTm0 I**	**Date**	**DFracWELTm0 Uni**	**Date**	**DFracNSUTm0 Uni**	**Date**	**DFracWEUTr**
1/1/2018	0	1/1/2018	0	1/1/2018	0	1/1/2018	0
1/2/2018	17.46575165	1/2/2018	16.87888527	1/2/2018	104.6207886	1/2/2018	100.060791
1/5/2018	57.05627441	1/5/2018	55.12321472	1/5/2018	348.907196	1/5/2018	335.5745544
1/14/2018	142.6927795	1/14/2018	144.5704651	1/14/2018	915.2005615	1/14/2018	887.5458374
2/10/2018	334.1785278	2/10/2018	374.1373596	2/10/2018	2234.638428	2/10/2018	2205.184326
5/2/2018	755.0491943	5/2/2018	983.3143921	5/2/2018	5108.773926	5/2/2018	5217.999023
1/1/2019	1647.62439	1/1/2019	2599.118408	1/1/2019	10760.61328	1/1/2019	11491.24023
1/1/2020	2683.156982	1/1/2020	4789.330078	1/1/2020	16721.31641	1/1/2020	18361.46875
1/1/2021	3568.747803	1/1/2021	6842.822266	1/1/2021	21456.76172	1/1/2021	23958.53125
1/1/2022	4357.404297	1/1/2022	8788.757813	1/1/2022	25446.42188	1/1/2022	28771.36328
1/1/2023	5079.900391	1/1/2023	10655.78809	1/1/2023	28947.33008	1/1/2023	33069.83203
DLLNF0		DLLWF0		DLUNF0		DLUWF0	
Dynamic data: Field Water produc		Dynamic data: Field Water production		Dynamic data: Field Water production c		Dynamic data: Field Water prod	
Date	**DNSLTm0 Unit:**	**Date**	**DWELTm0 Unit: ST**	**Date**	**DNSUTm0 Unit: ST**	**Date**	**DWEUTm0 U**
1/1/2018	0	1/1/2018	0	1/1/2018	0	1/1/2018	0
1/2/2018	8.01325321	1/2/2018	9.26511002	1/2/2018	67.02841949	1/2/2018	67.05391693
1/5/2018	23.83298302	1/5/2018	27.81166649	1/5/2018	225.1327667	1/5/2018	226.3127289
1/14/2018	59.36922455	1/14/2018	67.08300781	1/14/2018	579.2059326	1/14/2018	581.8272705
2/10/2018	148.4010925	2/10/2018	162.756485	2/10/2018	1374.273071	2/10/2018	1373.931885
5/2/2018	381.8666992	5/2/2018	410.8990479	5/2/2018	3135.473877	5/2/2018	3137.543701
1/1/2019	1011.270264	1/1/2019	1078.431641	1/1/2019	6945.532715	1/1/2019	7041.976563
1/1/2020	1892.116943	1/1/2020	2016.42041	1/1/2020	11396.72949	1/1/2020	11723.16895
1/1/2021	2741.692871	1/1/2021	2924.983398	1/1/2021	15185.31641	1/1/2021	15794.27832
1/1/2022	3565.991943	1/1/2022	3809.578369	1/1/2022	18527.04492	1/1/2022	19453.4082
1/1/2023	4372.621094	1/1/2023	4677.593262	1/1/2023	21554.30469	1/1/2023	22824.44727
DLLN0		DLLW0		DLUN0		DLUW0	

Outcrop geomodel simulation results (Dipping)

Vertical well arrangements

Date	DVertSWTm0 U	Date	DVertCTm0 U	Date	DVertNETm0 U	Date	DVertSW
1/1/2018	0	1/1/2018	0	1/1/2018	0	1/1/2018	0
1/2/2018	0.436713	1/2/2018	0.44036	1/2/2018	0.44117	1/2/2018	2.80791
1/5/2018	1.634343	1/5/2018	1.66755	1/5/2018	1.65122	1/5/2018	10.0234
1/14/2018	4.837491	1/14/2018	5.08661	1/14/2018	4.84247	1/14/2018	26.4484
2/10/2018	13.41955	2/10/2018	14.8335	2/10/2018	13.1657	2/10/2018	62.3089
5/2/2018	36.66005	5/2/2018	43.0711	5/2/2018	35.2771	5/2/2018	145.431
1/1/2019	100.9666	1/1/2019	125.821	1/1/2019	95.7129	1/1/2019	350.638
1/1/2020	192.5839	1/1/2020	247.622	1/1/2020	181.354	1/1/2020	623.707
1/1/2021	281.9918	1/1/2021	368.641	1/1/2021	264.767	1/1/2021	880.078
1/1/2022	369.537	1/1/2022	488.578	1/1/2022	346.383	1/1/2022	1124.76
1/1/2023	455.8854	1/1/2023	607.947	1/1/2023	426.86	1/1/2023	1361.63
DVSWU0		DVCU0		DVNEU0		DVSWA0	
Dynamic data: Field Water		Dynamic data: Field Wate		Dynamic data: Field Wate		Dynamic data: Field V	
Date	DVertNEATm5 U	Date	DVertCATm5 U	Date	DVertSWATm5	Date	DVertNET
1/1/2018	0	1/1/2018	0	1/1/2018	0	1/1/2018	0
1/2/2018	8.91196	1/2/2018	10.201	1/2/2018	13.0728	1/2/2018	0.6556
1/5/2018	26.55242	1/5/2018	30.5984	1/5/2018	31.7314	1/5/2018	2.48975
1/14/2018	58.52862	1/14/2018	73.2867	1/14/2018	59.6895	1/14/2018	7.57538
2/10/2018	122.3141	2/10/2018	177.149	2/10/2018	114.665	2/10/2018	21.7426
5/2/2018	266.646	5/2/2018	446.81	5/2/2018	240.256	5/2/2018	61.3351
1/1/2019	614.9468	1/1/2019	1164.34	1/1/2019	543.607	1/1/2019	172.579
1/1/2020	1071.242	1/1/2020	2157.98	1/1/2020	940.708	1/1/2020	331.528
1/1/2021	1495.727	1/1/2021	3110.94	1/1/2021	1310	1/1/2021	486.628
1/1/2022	1898.418	1/1/2022	4033	1/1/2022	1660.26	1/1/2022	638.424
1/1/2023	2286.534	1/1/2023	4934.38	1/1/2023	1997.78	1/1/2023	788.078
DVNEA0.5		DVCA0.5		DVSWA0.5		DVNE0.5	
Dynamic data: Field Water		Dynamic data: Field Wate		Dynamic data: Field Wate		Dynamic data: Field V	
Date	DVertNEATm0 U	Date	DVertCATm0 U	Date	DVertCTm5 U	Date	DVertSWT
1/1/2018	0	1/1/2018	0	1/1/2018	0	1/1/2018	0
1/2/2018	3.720773	1/2/2018	3.27439	1/2/2018	0.65731	1/2/2018	0.65537
1/5/2018	13.17381	1/5/2018	11.8899	1/5/2018	2.52859	1/5/2018	2.49889
1/14/2018	34.46119	1/14/2018	33.6141	1/14/2018	7.9063	1/14/2018	7.64545
2/10/2018	80.7926	2/10/2018	89.9042	2/10/2018	23.5435	2/10/2018	21.8597
5/2/2018	187.6429	5/2/2018	241.538	5/2/2018	69.2838	5/2/2018	60.942
1/1/2019	448.9065	1/1/2019	658.919	1/1/2019	203.889	1/1/2019	169.233
1/1/2020	794.1633	1/1/2020	1249.05	1/1/2020	402.181	1/1/2020	322.765
1/1/2021	1116.937	1/1/2021	1821.7	1/1/2021	599.196	1/1/2021	471.94
1/1/2022	1424.106	1/1/2022	2380.13	1/1/2022	794.418	1/1/2022	617.522
1/1/2023	1720.82	1/1/2023	2929.22	1/1/2023	988.683	1/1/2023	760.743
DVNEA0		DVCA0		DVCU0.5		DVSWU0.5	

Subsurface proxy geomodel simulation results (Dipping)

Lateral and vertical well arrangements

Dynamic data: Field Water produc		Dynamic data: Field Water productio		Dynamic data: Field Water production		Dynamic data: Field Water produ	
Date	**DPxFracNSL Un**	**Date**	**DPxFracWEL Unit**	**Date**	**DPxFracNSU Unit:**	**Date**	**DPxFracWEU**
1/1/2018	0	1/1/2018	0	1/1/2018	0	1/1/2018	0
1/2/2018	97.48137665	1/2/2018	90.71984863	1/2/2018	186.872467	1/2/2018	169.5239258
1/5/2018	342.3638001	1/5/2018	320.6585999	1/5/2018	626.1243286	1/5/2018	574.7616577
1/14/2018	957.9553223	1/14/2018	902.7127686	1/14/2018	1679.910156	1/14/2018	1551.40625
2/10/2018	2509.724854	2/10/2018	2369.637939	2/10/2018	4171.997559	2/10/2018	3873.53833
5/2/2018	6219.814941	5/2/2018	5884.516113	5/2/2018	9503.576172	5/2/2018	8956.167969
1/1/2019	14204.32129	1/1/2019	13604.28027	1/1/2019	19407.21484	1/1/2019	18930.77734
1/1/2020	23030.53906	1/1/2020	22456.74219	1/1/2020	29307.88477	1/1/2020	29563.13281
1/1/2021	30178.48047	1/1/2021	29894.35742	1/1/2021	36932.68359	1/1/2021	38175.12109
1/1/2022	36251.02734	1/1/2022	36423.20703	1/1/2022	43244.76172	1/1/2022	45577.52734
1/1/2023	41600.44531	1/1/2023	42335.16797	1/1/2023	48725.97266	1/1/2023	52182.70703
D(Px)LLNF		D(Px)LLWF		D(Px)LUNF		D(Px)LUWF	

Dynamic data: Field Water produc		Dynamic data: Field Water productio		Dynamic data: Field Water production		Dynamic data: Field Water produ	
Date	**DPxNSL Unit: S**	**Date**	**DPxWEL Unit: ST**	**Date**	**DPxNSU Unit: STB**	**Date**	**DPxWEU Unit**
1/1/2018	0	1/1/2018	0	1/1/2018	0	1/1/2018	0
1/2/2018	122.1517334	1/2/2018	113.5461044	1/2/2018	168.4570465	1/2/2018	158.4304047
1/5/2018	413.2043152	1/5/2018	388.4031982	1/5/2018	539.6242065	1/5/2018	516.9915772
1/14/2018	1098.39856	1/14/2018	1047.459351	1/14/2018	1372.849487	1/14/2018	1327.878906
2/10/2018	2708.422119	2/10/2018	2604.235596	2/10/2018	3251.074219	2/10/2018	3151.598389
5/2/2018	6306.564941	5/2/2018	6100.431152	5/2/2018	7255.569824	5/2/2018	7056.224609
1/1/2019	13757.64746	1/1/2019	13502.6123	1/1/2019	15186.17676	1/1/2019	14993.6416
1/1/2020	21982.16992	1/1/2020	21966.25977	1/1/2020	23717.65234	1/1/2020	23881.06836
1/1/2021	28703.8457	1/1/2021	29117.82813	1/1/2021	30602.47461	1/1/2021	31318.98438
1/1/2022	34469.09375	1/1/2022	35432.12891	1/1/2022	36466.09375	1/1/2022	37851.01563
1/1/2023	39588.45313	1/1/2023	41175.80078	1/1/2023	41649.89844	1/1/2023	43770.61328
D(Px)LLN		D(Px)LLW		D(Px)LUN		D(Px)LUW	

Dynamic data: Field Water produc		Dynamic data: Field Water productio		Dynamic data: Field Water production		Dynamic data: Field Water produ	
Date	**DPxVertNEA Un**	**Date**	**DPxVertCA Unit:**	**Date**	**DPxVertSWA Unit:**	**Date**	**DPxVertNE U**
1/1/2018	0	1/1/2018	0	1/1/2018	0	1/1/2018	0
1/2/2018	4.66555977	1/2/2018	4.66605711	1/2/2018	4.01059055	1/2/2018	0.70273751
1/5/2018	16.20784569	1/5/2018	16.66819382	1/5/2018	13.86395264	1/5/2018	2.66892576
1/14/2018	41.79081726	1/14/2018	46.86349106	1/14/2018	35.50823975	1/14/2018	8.1267395
2/10/2018	98.40098572	2/10/2018	126.0586548	2/10/2018	83.17472839	2/10/2018	23.35020447
5/2/2018	232.2222595	5/2/2018	340.8261108	5/2/2018	195.8672485	5/2/2018	65.99477386
1/1/2019	564.8634644	1/1/2019	933.1855469	1/1/2019	476.6361389	1/1/2019	186.1824341
1/1/2020	1008.119873	1/1/2020	1770.977295	1/1/2020	851.5107422	1/1/2020	358.2579346
1/1/2021	1424.352417	1/1/2021	2583.829834	1/1/2021	1203.959473	1/1/2021	526.3679199
1/1/2022	1821.610229	1/1/2022	3376.277344	1/1/2022	1540.594482	1/1/2022	691.031311
1/1/2023	2206.160889	1/1/2023	4155.192871	1/1/2023	1866.61853	1/1/2023	853.4714356
D(Px)VNEA		D(Px)VCA		D(Px)VSWA		D(Px)VNEU	

Dynamic data: Field Water produc		Dynamic data: Field Water production cumulative	
Date	**DPxVertC Unit:**	**Date**	**DPxVertSW Unit: STB**
1/1/2018	0	1/1/2018	0
1/2/2018	0.70509738	1/2/2018	0.70353419
1/5/2018	2.71236134	1/5/2018	2.67756081
1/14/2018	8.49064541	1/14/2018	8.17370033
2/10/2018	25.3361721	2/10/2018	23.38359642
5/2/2018	74.72836304	5/2/2018	65.42930603
1/1/2019	220.3638306	1/1/2019	182.5283051
1/1/2020	435.1425781	1/1/2020	349.0306702
1/1/2021	648.6665039	1/1/2021	511.060791
1/1/2022	860.319397	1/1/2022	669.3410645
1/1/2023	1070.986694	1/1/2023	825.1611328
D(Px)VCU		D(Px)VSWU	

Outcrop geomodel simulation results (Flattened)

Lateral well arrangements

Date	FracNSUTm0	Date	FracWEUTm0	Date	WEUTm0 Unit	Date	NSUTm
1/1/2018	0	1/1/2018	0	1/1/2018	0	1/1/2018	0
1/2/2018	103.4	1/2/2018	107.92	1/2/2018	67.862	1/2/2018	67.54
1/5/2018	347.4	1/5/2018	363.42	1/5/2018	229.84	1/5/2018	228.3
1/14/2018	917.2	1/14/2018	963.29	1/14/2018	591.64	1/14/2018	589.2
2/10/2018	2248	2/10/2018	2385.5	2/10/2018	1394.2	2/10/2018	1396
5/2/2018	5158	5/2/2018	5589.4	5/2/2018	3172.6	5/2/2018	3174
1/1/2019	10905	1/1/2019	12139	1/1/2019	7094.8	1/1/2019	7005
1/1/2020	16960	1/1/2020	19227	1/1/2020	11789	1/1/2020	11476
1/1/2021	21757	1/1/2021	24969	1/1/2021	15868	1/1/2021	15282
1/1/2022	25788	1/1/2022	29892	1/1/2022	19533	1/1/2022	18641
1/1/2023	29320	1/1/2023	34280	1/1/2023	22910	1/1/2023	21684
LUNF0		**LUWF0**		**LUW0**		**LUN0**	

Dynamic data: Field Water p		Dynamic data: Field Water pr		Dynamic data: Field Water pr		Dynamic data: Field	
Date	**WELTm0 Unit**	**Date**	**NSLTm0 Unit:**	**Date**	**FracWELTm0**	**Date**	**FracNS**
1/1/2018	0	1/1/2018	0	1/1/2018	0	1/1/2018	0
1/2/2018	4.691	1/2/2018	9.3462	1/2/2018	13.995	1/2/2018	17.22
1/5/2018	14.47	1/5/2018	28.32	1/5/2018	47.063	1/5/2018	57.03
1/14/2018	36.87	1/14/2018	69.849	1/14/2018	125.54	1/14/2018	146.8
2/10/2018	94.33	2/10/2018	173.05	2/10/2018	319.93	2/10/2018	358.7
5/2/2018	250.1	5/2/2018	445.3	5/2/2018	802.45	5/2/2018	855.3
1/1/2019	687.5	1/1/2019	1185.4	1/1/2019	1989	1/1/2019	1971
1/1/2020	1319	1/1/2020	2226.7	1/1/2020	3530.7	1/1/2020	3295
1/1/2021	1939	1/1/2021	3233.6	1/1/2021	4952.9	1/1/2021	4433
1/1/2022	2549	1/1/2022	4211.2	1/1/2022	6293.5	1/1/2022	5445
1/1/2023	3152	1/1/2023	5167.8	1/1/2023	7579	1/1/2023	6368
LLW0		**LLN0**		**LLWF0**		**LLNF0**	

Dynamic data: Field Water p		Dynamic data: Field Water pr		Dynamic data: Field Water pr		Dynamic data: Field	
Date	**WEUTm5 Unit**	**Date**	**NSUTm5 Unit:**	**Date**	**WELTm5 Unit**	**Date**	**NSLTm**
1/1/2018	0	1/1/2018	0	1/1/2018	0	1/1/2018	0
1/2/2018	146.1	1/2/2018	151.07	1/2/2018	571.55	1/2/2018	450
1/5/2018	483.2	1/5/2018	493.27	1/5/2018	1125.1	1/5/2018	935.5
1/14/2018	1249	1/14/2018	1266.6	1/14/2018	2158.3	1/14/2018	1877
2/10/2018	2965	2/10/2018	3002.2	2/10/2018	4279.7	2/10/2018	3861
5/2/2018	6626	5/2/2018	6690.1	5/2/2018	8476	5/2/2018	7853
1/1/2019	14049	1/1/2019	14002	1/1/2019	16538	1/1/2019	15469
1/1/2020	22345	1/1/2020	21894	1/1/2020	25339	1/1/2020	23550
1/1/2021	29283	1/1/2021	28281	1/1/2021	32629	1/1/2021	30044
1/1/2022	35375	1/1/2022	33733	1/1/2022	38996	1/1/2022	35566
1/1/2023	40899	1/1/2023	38562	1/1/2023	44749	1/1/2023	40446
LUW0.5		**LUN0.5**		**LLW0.5**		**LLN0.5**	

Dynamic data: Field Water p		Dynamic data: Field Water pr		Dynamic data: Field Water pr		Dynamic data: Field	
Date	**FracWEUTm5**	**Date**	**FracNSUTm5**	**Date**	**FracWELTm5**	**Date**	**FracNS**
1/1/2018	0	1/1/2018	0	1/1/2018	0	1/1/2018	0
1/2/2018	166.2	1/2/2018	170.92	1/2/2018	423.97	1/2/2018	354
1/5/2018	569.9	1/5/2018	580.36	1/5/2018	928.83	1/5/2018	743.4
1/14/2018	1545	1/14/2018	1564.9	1/14/2018	1943.3	1/14/2018	1548
2/10/2018	3845	2/10/2018	3881.5	2/10/2018	4088.3	2/10/2018	3396
5/2/2018	8818	5/2/2018	8829.6	5/2/2018	8444.2	5/2/2018	7469
1/1/2019	18444	1/1/2019	18052	1/1/2019	16849	1/1/2019	15626
1/1/2020	28606	1/1/2020	27301	1/1/2020	25890	1/1/2020	24278
1/1/2021	36795	1/1/2021	34436	1/1/2021	33287	1/1/2021	31151
1/1/2022	43817	1/1/2022	40350	1/1/2022	39701	1/1/2022	36934
1/1/2023	50077	1/1/2023	45490	1/1/2023	45471	1/1/2023	42004
LUWF0.5		**LUNF0.5**		**LLWF0.5**		**LLNF0.5**	

Outcrop geomodel simulation results (Flattened)

Vertical well arrangements

Date	VertSWTm5 Unit	Date	VertCTm5 U	Date	VertNET	Date	VertNEATm5 Uni
1/1/2018	0	1/1/2018	0	1/1/2018	0	1/1/2018	0
1/2/2018	0.652357	1/2/2018	0.6572	1/2/2018	0.66	1/2/2018	5.68894
1/5/2018	2.488111	1/5/2018	2.5283	1/5/2018	2.49	1/5/2018	19.1201
1/14/2018	7.615609	1/14/2018	7.9067	1/14/2018	7.57	1/14/2018	46.9535
2/10/2018	21.78733	2/10/2018	23.549	2/10/2018	21.7	2/10/2018	105.245
5/2/2018	60.78707	5/2/2018	69.315	5/2/2018	61.3	5/2/2018	238.821
1/1/2019	168.9634	1/1/2019	204.03	1/1/2019	173	1/1/2019	564.434
1/1/2020	322.4663	1/1/2020	402.51	1/1/2020	331	1/1/2020	993.688
1/1/2021	471.7066	1/1/2021	599.74	1/1/2021	486	1/1/2021	1394.37
1/1/2022	617.4255	1/1/2022	795.19	1/1/2022	638	1/1/2022	1775.28
1/1/2023	760.8414	1/1/2023	989.7	1/1/2023	787	1/1/2023	2142.93
VSWU0.5		VCU0.5		VNEU0.5		VNEA0.5	
Dynamic data: Field Water pr		Dynamic data: Field Wate		Dynamic data: Field		Dynamic data: Field Water pr	
Date	VertCATm5 Unit:	Date	VertSWATm	Date	VertSW	Date	VertCTm0 Unit: S
1/1/2018	0	1/1/2018	0	1/1/2018	0	1/1/2018	0
1/2/2018	6.661671	1/2/2018	4.3211	1/2/2018	0.44	1/2/2018	0.44497
1/5/2018	22.17333	1/5/2018	14.717	1/5/2018	1.66	1/5/2018	1.68424
1/14/2018	57.74224	1/14/2018	36.594	1/14/2018	4.9	1/14/2018	5.1355
2/10/2018	146.4397	2/10/2018	82.699	2/10/2018	13.6	2/10/2018	14.9727
5/2/2018	380.3834	5/2/2018	189.23	5/2/2018	37.1	5/2/2018	43.4712
1/1/2019	1012.057	1/1/2019	451.72	1/1/2019	102	1/1/2019	126.987
1/1/2020	1894.639	1/1/2020	800.34	1/1/2020	195	1/1/2020	249.919
1/1/2021	2745.325	1/1/2021	1127.3	1/1/2021	285	1/1/2021	372.067
1/1/2022	3571.153	1/1/2022	1439.1	1/1/2022	374	1/1/2022	493.123
1/1/2023	4380.429	1/1/2023	1740.8	1/1/2023	461	1/1/2023	613.608
VCA0.5		VSWA0.5		VSWU0		VCU0	
Dynamic data: Field Water pr		Dynamic data: Field Wate		Dynamic data: Field		Dynamic data: Field Water pr	
Date	VertNETm0 Unit:	Date	VertSWATm	Date	VertCAT	Date	VertNEATm0 Uni
1/1/2018	0	1/1/2018	0	1/1/2018	0	1/1/2018	0
1/2/2018	0.444715	1/2/2018	2.8559	1/2/2018	3.31	1/2/2018	3.76377
1/5/2018	1.663669	1/5/2018	10.181	1/5/2018	12	1/5/2018	13.3141
1/14/2018	4.87589	1/14/2018	26.812	1/14/2018	33.9	1/14/2018	34.7821
2/10/2018	13.24823	2/10/2018	63.061	2/10/2018	90.7	2/10/2018	81.4317
5/2/2018	35.4776	5/2/2018	147.02	5/2/2018	244	5/2/2018	188.906
1/1/2019	96.19428	1/1/2019	354.25	1/1/2019	665	1/1/2019	451.457
1/1/2020	182.178	1/1/2020	630.02	1/1/2020	1260	1/1/2020	798.145
1/1/2021	265.8835	1/1/2021	888.97	1/1/2021	1837	1/1/2021	1122.07
1/1/2022	347.752	1/1/2022	1136.2	1/1/2022	2400	1/1/2022	1430.19
1/1/2023	428.4488	1/1/2023	1375.5	1/1/2023	2954	1/1/2023	1727.7
VNEU0		VSWA0		VCA0		VNEA0	

Subsurface proxy geomodel simulation results

Lateral and vertical well arrangements

Date	PxVertSW	Date	PxVertC U	Date	PxVertNE U	Date	PxVertSWA
1/1/2018	0	1/1/2018	0	1/1/2018	0	1/1/2018	0
1/2/2018	0.698	1/2/2018	0.703	1/2/2018	0.7015	1/2/2018	3.9698
1/5/2018	2.657	1/5/2018	2.706	1/5/2018	2.6646	1/5/2018	13.747
1/14/2018	8.115	1/14/2018	8.474	1/14/2018	8.1147	1/14/2018	35.292
2/10/2018	23.24	2/10/2018	25.29	2/10/2018	23.319	2/10/2018	82.857
5/2/2018	65.08	5/2/2018	74.62	5/2/2018	65.908	5/2/2018	195.48
1/1/2019	181.8	1/1/2019	220.1	1/1/2019	185.9	1/1/2019	476.44
1/1/2020	347.9	1/1/2020	434.7	1/1/2020	357.62	1/1/2020	851.95
1/1/2021	509.6	1/1/2021	648.1	1/1/2021	525.32	1/1/2021	1205.3
1/1/2022	667.7	1/1/2022	859.6	1/1/2022	689.51	1/1/2022	1542.9
1/1/2023	823.4	1/1/2023	1070	1/1/2023	851.44	1/1/2023	1870.1
(Px)VSWU		(Px)VCU		(Px)VNEU		(Px)VSWA	
Dynamic data: Field Wate		Dynamic data: Field Wa		Dynamic data: Field Water		Dynamic data: Field Water p	
Date	PxVertCA I	Date	PxVertNE/	Date	PxWEU Unit	Date	PxNSU Unit:
1/1/2018	0	1/1/2018	0	1/1/2018	0	1/1/2018	0
1/2/2018	4.643	1/2/2018	4.653	1/2/2018	157.49	1/2/2018	164.61
1/5/2018	16.6	1/5/2018	16.17	1/5/2018	517.18	1/5/2018	533.03
1/14/2018	46.72	1/14/2018	41.74	1/14/2018	1332.5	1/14/2018	1364.5
2/10/2018	125.8	2/10/2018	98.38	2/10/2018	3166.6	2/10/2018	3238.2
5/2/2018	340.4	5/2/2018	232.3	5/2/2018	7096.3	5/2/2018	7231.7
1/1/2019	932.7	1/1/2019	565.1	1/1/2019	15092	1/1/2019	15154
1/1/2020	1771	1/1/2020	1008	1/1/2020	24048	1/1/2020	23695
1/1/2021	2584	1/1/2021	1425	1/1/2021	31544	1/1/2021	30597
1/1/2022	3377	1/1/2022	1821	1/1/2022	38127	1/1/2022	36482
1/1/2023	4157	1/1/2023	2206	1/1/2023	44092	1/1/2023	41687
(Px)VCA		(Px)VNEA		(Px)LUW		(Px)LUN	
Dynamic data: Field Wate		Dynamic data: Field Wa		Dynamic data: Field Water		Dynamic data: Field Water p	
Date	PxWEL Uni	Date	PxNSL Un	Date	PxFracWEU	Date	PxFracNSU
1/1/2018	0	1/1/2018	0	1/1/2018	0	1/1/2018	0
1/2/2018	123.5	1/2/2018	118.2	1/2/2018	176.91	1/2/2018	182.88
1/5/2018	416.2	1/5/2018	406.6	1/5/2018	604.56	1/5/2018	618.8
1/14/2018	1106	1/14/2018	1096	1/14/2018	1637.4	1/14/2018	1668.5
2/10/2018	2717	2/10/2018	2715	2/10/2018	4077.8	2/10/2018	4145.3
5/2/2018	6307	5/2/2018	6321	5/2/2018	9356.9	5/2/2018	9435.5
1/1/2019	13853	1/1/2019	13778	1/1/2019	19601	1/1/2019	19292
1/1/2020	22449	1/1/2020	22017	1/1/2020	30461	1/1/2020	29189
1/1/2021	29701	1/1/2021	28757	1/1/2021	39235	1/1/2021	36830
1/1/2022	36098	1/1/2022	34543	1/1/2022	46765	1/1/2022	43166
1/1/2023	41912	1/1/2023	39684	1/1/2023	53474	1/1/2023	48672
(Px)LLW		(Px)LLN		(Px)LUWF		(Px)LUNF	
Dynamic data: Field Wate		Dynamic data: Field Water production cumulative					
Date	PxFracWEI	Date	PxFracNSL Unit: STB				
1/1/2018	0	1/1/2018	0				
1/2/2018	97.04	1/2/2018	91.01				
1/5/2018	339.3	1/5/2018	320.6				
1/14/2018	946.5	1/14/2018	899.8				
2/10/2018	2469	2/10/2018	2369				
5/2/2018	6098	5/2/2018	5916				
1/1/2019	14016	1/1/2019	13667				
1/1/2020	23049	1/1/2020	22338				
1/1/2021	30616	1/1/2021	29411				
1/1/2022	37247	1/1/2022	35447				
1/1/2023	43244	1/1/2023	40779				
(Px)LLWF		(Px)LLNF					

Appendix H: F1 and F4/F5 Thin bed statistics used for facies model A-E parameters

	A			B and C			D			E	
Lithofacies	Strike	Dip	Lithofacies	Strike	Dip	Lithofacies	Strike	Dip	Lithofacies	Strike	Dip
F1	6.45	2	F1	1.1	0.9	F4/F5	7.6	4.6	F4/F5	5.7	4.67
F1	7.2	2.2	F1	1.5	1.1	F4/F5	9.3	6.8	F4/F5	6	4.94
F1	8.7	2.2	F1	2.5	1.2	F4/F5	9.7	7.3	F4/F5	6	5.4
F1	9	2.5	F1	2.7	1.3	F4/F5	11	7.4	F4/F5	7.84	6.4
F1	9.1	2.6	F1	2.8	1.4	F4/F5	11.4	7.7	F4/F5	9.2	6.9
F1	9.7	2.8	F1	2.8	1.7	F4/F5	11.5	8.6	F4/F5	9.4	6.9
F1	10	2.8	F1	3.14	1.7	F4/F5	12.3	9.6	F4/F5	9.7	7.1
F1	10.9	3.2	F1	3.2	1.8	F4/F5	12.8	9.6	F4/F5	12.6	7.2
F1	11.3	3.2	F1	3.3	1.8	F4/F5	12.8	9.8	F4/F5	13.4	7.6
F1	12.3	3.3	F1	3.65	1.9	F4/F5	13.4	9.8	F4/F5	13.4	7.7
F1	13.2	3.5	F1	3.7	2.2	F4/F5	13.5	10.1	F4/F5	14.2	9
F1	13.37	3.8	F1	4	2.3	F4/F5	13.7	10.7	F4/F5	15.6	9.1
F1	15.1	3.9	F1	4.2	2.5	F4/F5	14.2	11.8	F4/F5	17.2	9.4
F1	22.2	4.1	F1	4.7	3.2	F4/F5	15.9	12.4	F4/F5	17.5	10.3
F1	24.2	4.4	F1	4.9	3.4	F4/F5	17.1	13.4	F4/F5	17.7	10.4
F1		4.5	F1	5.35	3.5	F4/F5	17.39	13.9	F4/F5	18.1	10.4
F1		4.8	F1	5.5	3.8	F4/F5	18.4	14.2	F4/F5	19.5	11.5
F1		5.2	F1	7.1	4	F4/F5	18.7	14.6	F4/F5		11.5
F1		5.2	F1	7.28	4.1	F4/F5	19.2	14.8	F4/F5		12.8
F1		5.6	F1	7.86	4.6	F4/F5		14.9	F4/F5		14.2
F1		5.8	F1	8.11	4.6	F4/F5		14.92	F4/F5		17.4
F1		5.8	F1	8.16	5	F4/F5		15.4	F4/F5		25.2
F1		6	F1	8.3	5.2	F4/F5		16			
F1		6.1	F1	9.6	5.3	F4/F5		16.85			
F1		6.4	F1	9.8	5.6	F4/F5		19			
F1		6.5	F1	10	5.8	F4/F5		19.9			
F1		6.7	F1	12.1	6.2	F4/F5		23.3			
F1		6.9	F1	13.6	6.2						
F1		7.39	F1	15.4	6.45						
F1		7.4	F1	15.8	6.7						
F1		7.5	F1	18.6	6.8						
F1		7.6	F1	19.3	7.4						
F1		7.7	F1	20	7.7						
F1		8.2	F1	22.7	7.8						
F1		8.3	F1	22.8	8.1						
F1		8.7	F1	24.8	8.3						
F1		9.5	F1	37.2	9.7						
F1		10	F1		10						
F1		10.4	F1		11.5						
F1		11	F1		12.2						
F1		11.4	F1		13.4						
F1		11.8	F1		13.9						
F1		12.1	F1		14.7						
F1		15.9	F1		16.1						
F1		17.5	F1		16.6						
F1		18.1	F1		20.7						
F1		19.7	F1		21.6						
F1		19.9	F1		28.8						
F1		20.4									
F1		26.4									
Averages	12.18133333	7.9778		9.663513514	7.098958333		13.67842105	12.49518519		12.53176471	9.818636364

Appendix I: Non-Background facies lateral extents, used for variogram range estimation

Zone 1					
Geomodel Facies	Delta X	Delta Y	Final 2D length	AVG	Mediian
3	5.16	4.65	6.946085228	6.314760608	6.946085228
3	2.15	1.91	2.875865087		
3	0.5	1.73	1.800805375		
3	3	9.69	10.14377149		
3	5.21	6.7	8.487290498		
3	2.95	5.08	5.874427632		
3	4.95	6.38	8.075078947		
				AVG	Median
4	1.08	2.11	2.370337529	8.035290433	6.125659148
4	2.46	5.61	6.125659148		
4	3.02	4.4	5.336703102		
4	4.01	9.48	10.29322593		
4	4.17	10.27	11.08430422		
4	4.24	7.38	8.511286624		
4	6.64	14.21	15.68482388		
4	8.97	1.54	9.10123618		
4	3.9	1.37	4.133630366		
4	5.56	1.54	5.769332717		
4	3.75	2.13	4.312702169		
Zone 3					
Facies	Delta X	Delta Y	Final 2D length		
3	5.32	13.2	14.23173918		
3	6.51	28.44	29.17556683		
3	9.54	12.71	15.89200113		
3	33.38	10.63	35.03171848		
3	16.53	3.11	16.82001784		
3	7.86	3.18	8.478915025		
3	12.31	22.82	25.92852676		
3	3.02	12.65	13.00549499		
3	10.18	67.93	68.6885529		
3	14	81.47	82.66414519		
3	34.93	344.02	345.7887582		
3	34.72	14.23	37.52294365		
3	10.38	11.87	15.7683639		
3	4.42	4.61	6.386587508		
3	6.41	20.27	21.2593744		
3	7.14	8.89	11.40226732		
3	1.19	7.18	7.277946139		

3	1.33	12.07	12.14305563	AVG	Median
3	4.2	6.86	8.043606156	21.67344352	11.77200068
3	1.9	8.51	8.71952407		
3	1.87	12.1	12.24364733	AVG X	Med X
				7.183018868	4.91
2	6.29	10.24	12.01755799		
2	4.91	6.37	8.042698552	AVG Y	Med Y
2	2.17	6.17	6.540473989	21.67344352	11.77200068
2	1.38	4.06	4.288123133		
2	0.76	6.03	6.077705159		
2	0.34	3.7	3.715588782		
2	0.85	6.63	6.684265105		
2	0.8	12.25	12.27609466		
2	1.58	16.57	16.64515846		
2	0.39	7.18	7.190584121		
2	1.49	24.31	24.35561947		
2	1.13	6.18	6.282459709		
2	8.57	7.44	11.34894268		
2	3.65	2.42	4.379372101		
2	2.93	2.01	3.553167601		
2	2.34	7.2	7.570706704		
2	7.49	7.13	10.34103476		
2	6.09	6.32	8.776702114		
2	12.33	22.59	25.73590877		
2	11.62	12.34	16.94992625		
2	3.07	2.85	4.188961685		
2	4.64	7.99	9.239572501		
2	4.06	17.82	18.27665177		
2	1.32	9.45	9.541745123		
2	1.51	8.82	8.948323865		
2	7.11	4.79	8.572992476		
2	12.98	5.09	13.94232764		
2	10.3	5.7	11.77200068		
2	10.06	7.88	12.77881059		
2	10.86	24.54	26.83563303		
2	10.13	14.38	17.58980671		
2	0.41	7.75	7.760837584		
Zone 4					
Facies	Delta X	Delta Y	Final 2D length		
3	210.23	163.3	266.2020716	AVG	Median
3	8.65	4.93	9.956274404	11.19326604	10.33399381
3	8.29	9.84	12.86661183		
3	3.45	15.98	16.34817727	AVG X	MED X
3	4.16	7.36	8.454300681	5.047222222	3.61

3	4.91	6.37	8.042698552		
3	2.17	6.17	6.540473989	AVG Y	MED Y
3	2.74	15.5	15.74031766	9.05	6.865
3	3.51	20.65	20.94618342		
3	0.76	11.97	11.99410272		
3	1.01	4	4.125542389		
3	2.2	3.71	4.313247037		
3	1.78	3.9	4.287003616		
3	3.71	18.69	19.05466347		
3	0.72	6.18	6.221800383		
3	6.07	10.08	11.76653305		
3	20.16	7.97	21.67824947		
3	9.32	5.28	10.71171321		
3	7.24	4.32	8.430895563		
		Zone 5			
Facies	Delta X	Delta Y	Final 2D length		
4	2.89	6.05	6.704819162	AVG	Median
4	0.16	6.89	6.891857514	14.663	10.74475327
4	3.11	9.94	10.41516683		
4	1.14	6.63	6.727295147	AVG X	MED X
4	0.54	5.61	5.635929382	9.8522	2.605
4	1.48	12.57	12.6568282		
4	0.3	5.9	5.907622195	AVG Y	MED Y
4	1.2	9.73	9.803718682	12.545	9.425
4	6.45	15.52	16.80693012		
4	2.18	12.48	12.66896997		
4	1.21	16.57	16.6141205		
4	3.23	13.31	13.69631337		
4	1.23	4.75	4.906668931		
4	0.78	3.98	4.055712021		
4	2.06	11.13	11.31903264		
4	0.79	3.25	3.344637499		
4	4.11	12.46	13.12035442		
4	0.74	9.4	9.42908267		
4	9.44	0.26	9.44357983		
4	4.15	7.22	8.327718775		
4	2.15	42.87	42.92387914		
4	4.44	45.76	45.9748975		
4	2.74	9.33	9.72401666		
4	1.59	7.97	8.127053587		
4	1.81	9.31	9.484313365		
4	4.12	19.92	20.34160269		
4	1.2	5.31	5.443904849		
4	0.31	11.07	11.07433971		

4	0.05	7.61	7.610164256		
4	0.73	7.7	7.734526488		
4	3.36	37.58	37.72990856		
4	3.7	0.68	3.76196757		
4	46.63	21.07	51.16934434		
4	9.61	13.29	16.4004939		
4	13.89	3.04	14.21877984		
4	4.87	13.34	14.20114432		
4	3.28	11.89	12.33411934		
4	6.68	9.45	11.57259262		
4	28.68	43.42	52.03689845		
4	2.47	6.78	7.215906042		
4	14.26	6.46	15.65500559		
4	11.62	19.41	22.62238935		
3	6.44	10.83	12.60009921	AVG	Median
3	2.56	22.73	22.87370761	13.873	12.60009921
3	2.7	5.52	6.144949145	AVG X	MED X
				9.1999	2.7
				AVG Y	MED Y
				13.027	10.83

Appendix J: F2 SCS Scour dimensions

F2 Scour dimensions			
		Strike	Dip
		13.14	
			48.78
		11.78	>9.5
		8	12.7
		24.2	
		40	
			75
			20.18
			17.75
			7.4
			41
			>19
			38
	Averages	19.424	32.60125
Highest confidence measurements			19.806

Appendix K: Integrated measured sections and maps; *Zupanic, 2017*

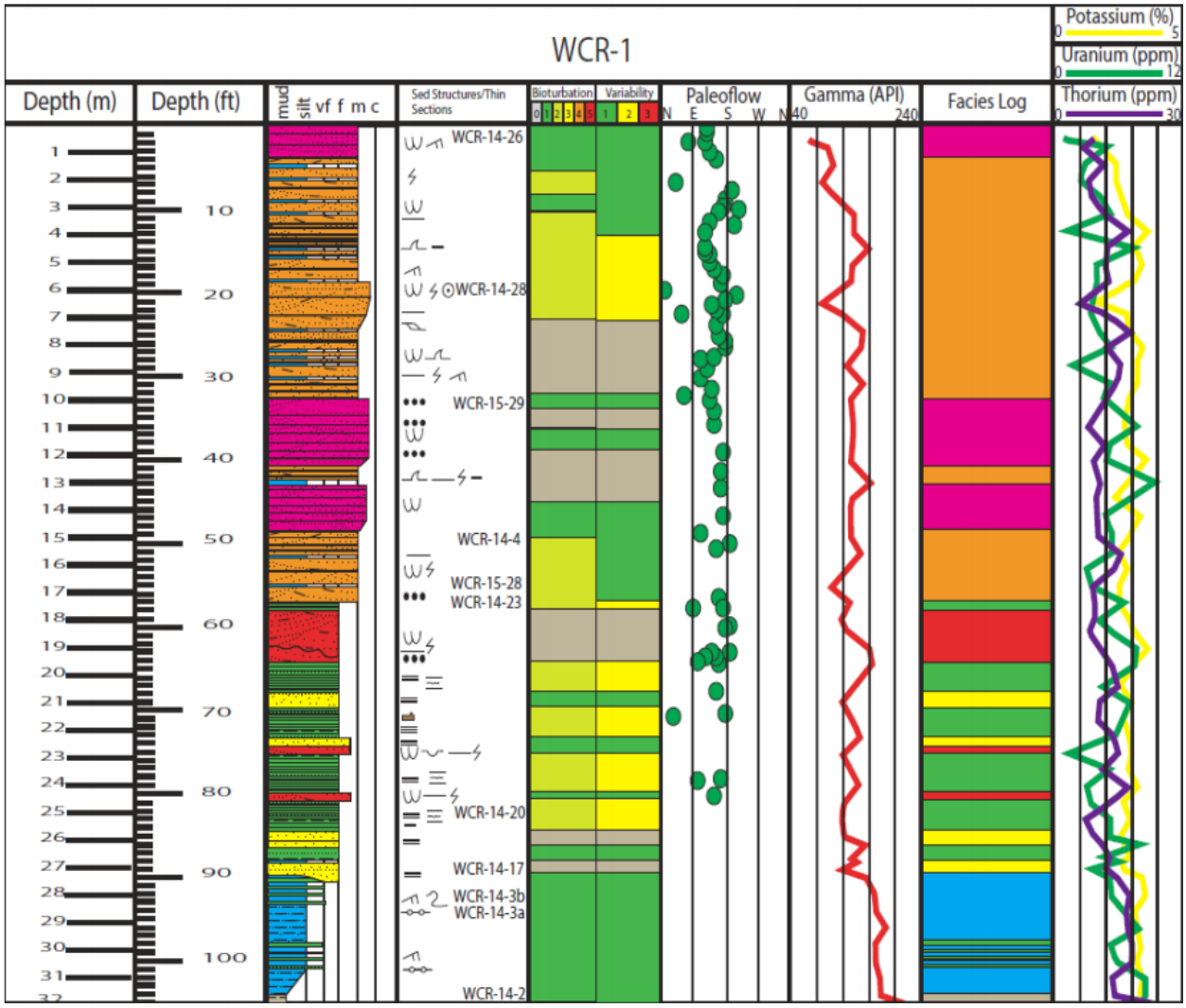

WCR-1 stratigraphic section

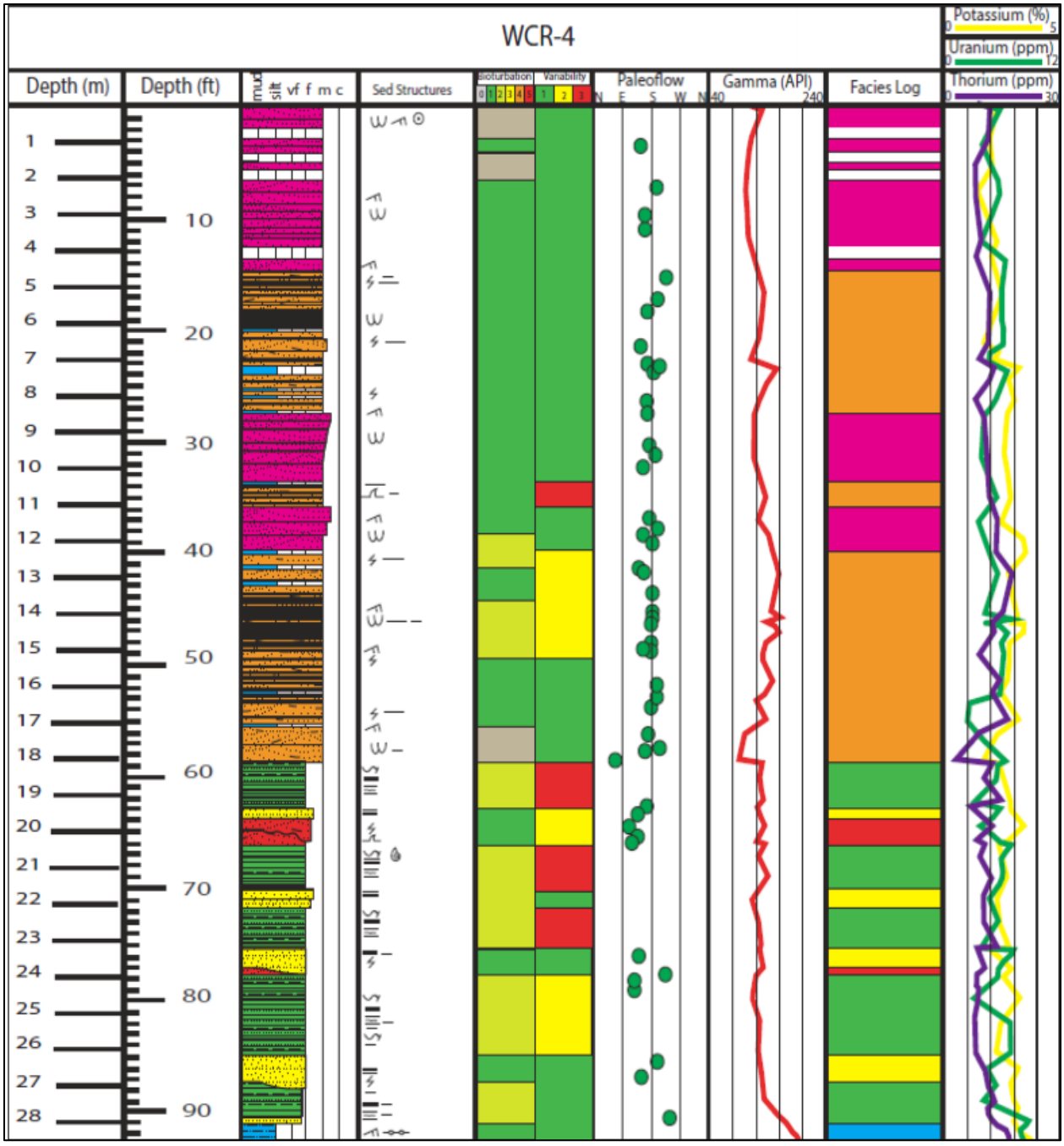

WCR-4 stratigraphic section

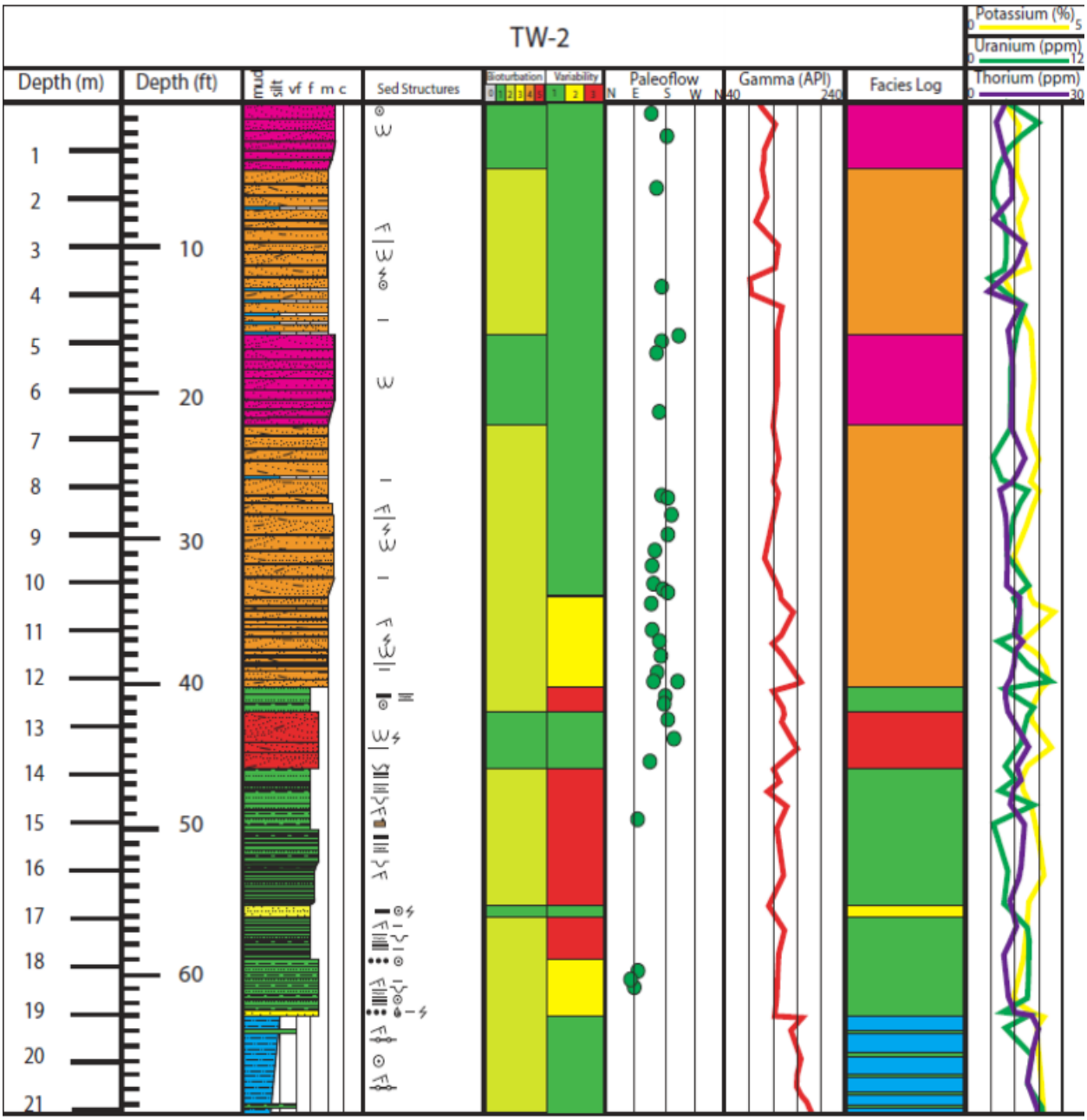

TW-2 stratigraphic section

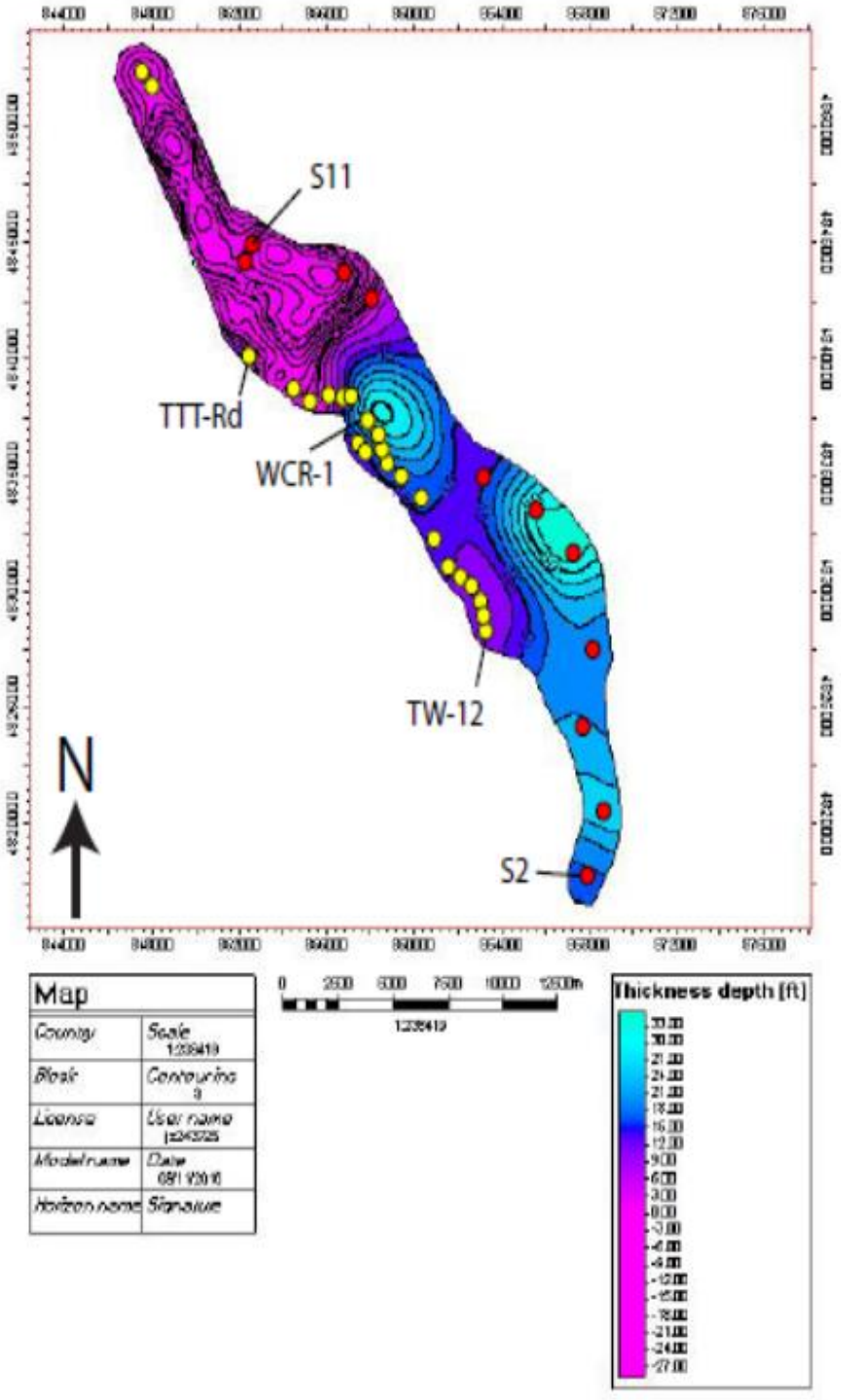

HST2 (Zupanic, 2017) regional isopach. Note a WCM depocenter exists at the WCR locality. The river-dominated HST1 was not differentiated in this map and is the source of the local thickness accumulation.